UNIVERSITÄTSKLINIKUM HAMBURG-EPPENDORF

Institut für Neuroimmunologie und Multiple Sklerose

Prof. Dr. Manuel A. Friese

Establishing a local immune tolerance to protect neurons against inflammatory neurodegeneration

Dissertation

zur Erlangung des Doktorgrades Dr. rer. biol. hum. an der Medizinischen Fakultät der Universität Hamburg

vorgelegt von

Lisa Katharina Cornelia Unger
aus Helmstedt

Hamburg, 2024

Angenommen von der Medizinischen Fakultät
der Universität Hamburg am 08.07.2024

Veröffentlicht mit Genehmigung der Medizinischen Fakultät der Universität Hamburg

Prüfungsausschuss, der Vorsitzende: Prof. Dr. Manuel A. Friese

Prüfungsausschuss, zweiter Gutachter: Prof. Dr. Boris Fehse

Table of Contents

I. List of Figures

II. List of Tables

1. Introduction

1.1. Multiple sclerosis

Multiple sclerosis (MS) is an immune-mediated disease of the central nervous system (CNS) and the most frequent reason for neurological disabilities in young adults with an average disease onset of 30 years. A majority of people with MS experience reoccurring neurological symptoms, which are caused by inflammatory lesions in the CNS that initially still completely resolve[1]. Although a number of disease modifying treatments (DMTs) are available, MS remains an incurable disease with a life expectancy that is seven years shorter than of healthy individuals. Moreover, it is accompanied by a substantially reduced quality of life[2]. MS is generally thought to be an autoimmune disease with peripheral activation of T and B lymphocytes that infiltrate the CNS[1,3]. Yet, an alternative hypothesis suggests an initiation of the disease within the CNS with subsequent peripheral immune cell activation[4,5]. To date a total of 2.9 million people are diagnosed with MS worldwide and compared to 2.3 million people in 2013 the numbers are rising[6].

The typical bouts of disease activity are caused by CNS-infiltrating immune cells, which drive neuronal demyelination, degeneration and astrogliosis by forming local inflammatory hotspots, which are observable as lesions in magnetic resonance imaging (MRI)[7]. The spectrum of clinical manifestations depends on the lesion's location and ranges from cognitive to physical disabilities including visual disturbances, fatigue, spasticity, loss of balance, tremor and intestinal as well as urinary system dysfunction[1,3,8]. In addition to the MRI, the diagnosis and disease activity assessment is supported by the analysis of oligoclonal bands and IgG elevation in the cerebrospinal fluid (CSF), which is acquired by lumbar punction and reflects the inflammatory activity in the CNS[9]. Neurofilament light chain is an established biomarker for neurodegeneration and elevated in people with MS, up to 6 years before clinical onset. However, the search for an MS-specific biomarker for early disease diagnosis and disease activity evaluation remains ongoing[10,11]. Clinically, the degree of disability is monitored via the expanded disability status scale (EDSS) score for the systematic assessment of the degree of patient morbidity[12].

1.1.1. Etiology and epidemiology

The predominant manifestation of MS is relapsing-remitting MS (RRMS) and is diagnosed in 85% of people with MS. RRMS is characterized by relapses that cause neurological symptoms, which can initially resolve completely. Over a span of 10–20 years post-diagnosis, around 80% of those with RRMS transition to secondary progressive MS (SPMS), marked by a gradual neurological decline and CNS atrophy, which occurs independently of relapses. About 10–

15% of people with MS do not present with relapses, but directly experience a primary progressive form of MS (PPMS) from disease onset[13–15].

Although the cause of MS remains unknown, several risk factors have been identified that favor MS development. Women have a 3-fold increased risk of being affected compared to men[16,17] and lifestyle factors like childhood obesity[18,19] or smoking[20–23] favor MS development, while pregnancy appears to protect from new relapses, especially in the second and third trimester[24,25]. The risk of developing MS varies geographically, showing a lower incidence nearer to the equator, which is manifested during the first two decades of life[26,27]. Environmental factors like viral infections and sun exposure-derived vitamin D levels are discussed as a contributing factor to this association, as reduced vitamin D levels favor disease development[28,29], potentially by reduced reprogramming of type 17 T helper (Th17) cells towards a more tolerogenic state[30]. Moreover, viral infections are associated with a higher MS risk. A prominent example is an association between Epstein–Barr Virus (EBV) infections and MS, as EBV appears to be required but not sufficient to develop disease[31]. Moreover, several genetic variants have been identified as predisposing factors, indicating a heritable component of MS[32,33]. This was initially observed in a study that identified an increased MS risk in siblings of an affected monozygotic twin (17% age-adjusted risk for the unaffected twin, compared to a risk of 0.5% in the general population)[34–36]. The majority of genetic variants that has been identified to be connected to MS susceptibility, affects immune related genes. Gene variants within the human leukocyte antigen (HLA) complex, which encode for the major histocompatibility complex (MHC), and specifically HLA-DRB1*15:01 contribute to disease susceptibility[37–40]. On a cellular level this variant is associated with an enhanced peripheral self-activation of autoreactive type 1 T helper (Th1) cells by memory B cells[41]. Moreover, the combination of carrying HLA-DRB1*15:01 with being infected with EBV, is associated with a synergistically increased likelihood of developing MS. This correlation was shown for individuals with high Epstein–Barr nuclear antigen 1 (EBNA1) titers[42] and predisposition for infectious mononucleosis[43,44]. A possible explanation is provided by the finding, that EBV utilizes MHCII as a co-receptor for virus entry into B cells[45,42].

1.1.2. Immunopathology

MS immunopathology is characterized by an interplay of multiple immune cell types that contribute to disease progression. A key event is the migration of autoreactive T cells into the CNS by crossing the blood–brain barrier (BBB)[46], which gets disrupted during the disease course of MS[47–49]. This disruption involves the downregulation of laminin in the basement membrane or the selective loss of claudin leading to abnormalities in tight junctions, as observed in experimental autoimmune encephalomyelitis (EAE)[50]. Moreover, leukocyte derived cytokines further induce the expression of endothelial adhesion molecules[51] and Th17

cells can weaken the BBB integrity by disrupting tight junctions by secretion of interleukin- (IL-)17 and IL-22[52,53].

Once T cells infiltrate the CNS, they initiate the release of proinflammatory cytokines such as tumor necrosis factor alpha (TNF-α), interferon gamma (IFN-γ), and granulocyte-macrophage colony-stimulating factor (GM-CSF), which facilitate the recruitment of blood-derived myeloid cells and neutrophils[54,55]. This in turn enforces CNS inflammation by further releasing inflammatory factors and reactivating autoreactive T cells. These cells subsequently activate CNS-infiltrating macrophages and microglia, the brain resident antigen presenting cells (APCs)[56], which are present in active lesions, but also in normal-appearing white and grey matter[57]. Moreover, autoreactive T cells are reported to enhance myelopoiesis in the bone marrow with an augmented output of neutrophils and monocytes that invade the CNS and amplify inflammatory brain injury[58].

Different stages of MS are accompanied by predominant activity of different immune cell subsets[1,59], however an overshooting immune reaction due to a disturbed immune tolerance to self is a hallmark of MS pathogenesis[1,3]. Early lesions typically comprise of cluster of differentiation (CD)8^+ T cells, $CD4^+$ T cells, especially Th1 and Th17 subtypes[53,60,61], B cells, plasma cells and macrophages. Among infiltrating T cells, $CD8^+$ T cells have been found to be the predominating population in MS lesions[62]. Additionally, an underrepresentation of regulatory T cells (Treg) in CNS infiltrates may exacerbate inflammation and contribute to disease progression in MS[63,64]. As MS progresses, the inflammatory infiltrates within the CNS become more widespread and diffuse[57]. In addition to elevated levels of B cells and plasma cells in the affected areas, this progression is accompanied by an increased contribution of the innate immune system with activation of microglia and macrophages[65]. This in turn leads to a diffuse reduction of myelin, axonal injury and astrogliosis. Activated astrocytes further promote microglia activation by secreting inflammatory molecules such as GM-CSF[66,67]. Also neurons participate in regulation of inflammation, for instance by upregulation of the anti-inflammatory checkpoint programmed death ligand 1 (PD-L1), thus inhibiting T cell activity[68]. On the other hand, neurons and oligodendrocytes downregulate the antiphagocytic surface protein OX-2 membrane glycoprotein (CD200) and thereby enhance microglial activation while astrocytes show an CD200 upregulation[69,70].

1.1.3. Disease modifying treatments

Despite effective treatment options to reduce relapses during RRMS by targeting the peripheral immune system, MS remains an incurable disease. Especially for the interference with primary and secondary disease progression treatment options are limited. Most current therapies are acting on immune cells in the periphery and are designed to initiate an immune phenotype shift, inhibit immune cell egress from the LN or inhibit BBB transmigration and CNS

infiltration[71]. DMTs, which aim to reduce relapse frequency are categorized in three groups based on their efficacy[72]. The first group contains drugs that reduce relapses by 30–50% compared to placebo including interferon-beta (IFN-β), dimethyl fumarate, glatiramer acetate and teriflunomide[72]. IFN-β gained approval as the initial medication for MS treatment in 1993 and acts by inhibiting the proliferation of inflammatory cells and their trafficking into the CNS[73,74]. Dimethyl fumarate acts by reducing inflammation and oxidative stress, thereby aiding to protect neurons from damage[75]. Glatiramer acetate functions by shifting the balance from pro-inflammatory T cells towards Treg, and by the inhibition of APCs[76] and teriflunomide inhibits the dihydroorotate dehydrogenase, a mitochondrial enzyme necessary for *de novo* pyrimidine synthesis and thereby interference with T and B cell proliferation[77]. The second group of drugs reduces the relapse rate by 50–60%[72]. It contains cladribine, which reduces circulating lymphocytes by interference with DNA synthesis, and sphingosine-1-phosphate receptor (S1PR) modulators including fingolimod and siponimod, which limit the egress of lymphocytes from the lymph node[78]. The third group of highly active agents consists of monoclonal antibodies, which target specific molecules on immune cells and reduce the relapse rate by over 60% compared to placebo or more than 40% compared to category 1 drugs[72]. Alemtuzumab targets CD52 which is present on the surface of lymphocytic cells[79], while ocrelizumab binds to CD20 found on B cells[80]. Additionally, natalizumab acts by binding to the integrin very late antigen-4 (VLA-4), thus impeding the migration of lymphocytes across the BBB[81]. Despite being very effective, these therapeutics harbor the risk of severe side effects like progressive multifocal leukoencephalopathy (PML) for natalizumab. PML is a progressive, fatal demyelinating disease, which is caused by a reactivation of the JC virus, and predominantly presents in people that suffer from immunodeficiency or are receiving immunosuppressive therapy[82]. For the treatment of the progredient forms of MS, to date only the B cell depleting anti-CD20 ocrelizumab is clinically approved[80]. However, a phase 3 trial of siponimod, also showed a reduction of the risk of disability progression[83]. Moreover, the treatment of RRMS with the fingolimod, alemtuzumab, or natalizumab are reducing the risk of conversion from RRMS to SPMS[84].

1.1.4. Animal models

Substantial knowledge about MS disease pathophysiology and treatment options, has been acquired in animal models[85]. The most commonly employed animal model for MS is experimental autoimmune encephalomyelitis (EAE) and can be performed in a range of different species including rhesus monkeys, guinea pigs, rats, and mice[86–88]. However, EAE experiments are predominantly carried out in mice, where they are immunized with myelin antigens such as myelin oligodendrocyte glycoprotein (MOG) or proteolipid protein (PLP) alongside an adjuvant, inducing an autoimmune reaction against myelin. In C57BL/6 mice,

MOG_{35-55} is frequently utilized as the antigen for inducing EAE. More specifically by subcutaneous injection of an emulsion of the myelin epitopes and complete Freund's adjuvant containing *Mycobacterium tuberculosis*, the immune system is activated and $CD4^+$ T cells get primed against myelin. This active immunization ultimately results in the generation of autoreactive, CNS-infiltrating T cells, which are subsequently causing neuroinflammation and can be further enhanced by administration of pertussis toxin (PTX). Motor impairments and weight loss are prominent features reflecting the progression of the autoimmune response against myelin and often manifest as weakness, altered coordination and paralysis, primarily affecting the hind limbs[86–88].

The EAE animal model recapitulates neuroinflammation as observed in MS, however it does not reproduce all aspects of MS pathophysiology[89]. For example, EAE induces neuroinflammation by targeting a specific antigen, whereas despite substantial scientific efforts the autoantigen responsible for MS remains unidentified. Moreover, in classical C57BL/6 EAE, CNS-infiltrating immune cells are mainly localized in the spinal cord, while in MS mostly the brain is affected by inflammation[89]. Finally, EAE is induced by priming of $CD4^+$ T cells, which therefore dominate disease activity, while MS is characterized by a bias towards $CD8^+$ T cells, at least in MS lesions[90]. Therefore, not all findings from the mouse model can be transferred to the human pathophysiology. However, the EAE mouse model provided mechanistic evidence that VLA-4 blocking, effectively prevents the accumulation of leukocytes in the CNS[91,92], which led to the development of natalizumab as a potent therapeutic to treat RRMS[81]. Specific aspects of MS pathophysiology can be recapitulated by the utilization of different immunization regimes and mouse strains. Adoptive transfer of primed T cells from donor mice into naïve recipient mice, allows precise control over the timing and genetic features of the transferred autoreactive T cell population[93]. To investigate the relapsing-remitting nature of MS, SJL mice are commonly used due to their genetic predisposition for relapsing-remitting disease courses. Notably, SJL females often exhibit more pronounced relapses than males, making it an attractive model to study sex differences, as seen in MS[94]. Additionally, two mouse models focusing on the neurodegenerative aspects of MS include the cuprizone-induced demyelination model, where demyelination is accompanied by predominant $CD8^+$ T cell infiltration[95,96], and the Theiler's murine encephalomyelitis virus (TMEV) model, which triggers CNS demyelination through TMEV virus infection, resulting in an immune-mediated inflammatory response targeting myelin[97,98].

1.2. The immune system

The immune system operates through a series of coordinated events and cellular interactions involving various immune cell populations and humoral immune response mechanisms to defend the body against non-self, including pathogens such as bacteria, viruses, and fungi, as

well as neoplastic cells[99]. The balance between identification of potential threats, while maintaining tolerance towards endogenous, healthy cells is crucial for an effective defense against pathogens. The majority of immune cells develop from hematopoietic stem cells in the bone marrow, followed by differentiation into myeloid and lymphoid progenitor cells[100]. Immune cells of the myeloid lineage comprise of erythrocytes, megakaryocytes, and innate immune cells such as granulocytes, mast cells, macrophages, and dendritic cells (DCs). Immune cells of the lymphoid lineage include T cells, B cells, and natural killer (NK) cells and are predominantly involved in the adaptive immune response[99].

The first line of defense in host immunosurveillance is the innate immune system that detects pathogens through genetically encoded pattern recognition receptors (PRRs) expressed on myeloid cells, natural killer cells and DCs[99]. Toll-like receptors (TLRs) are among the key PRRs, utilized by these cells to recognize specific pathogen-associated molecular patterns (PAMPs), as well as damage-associated molecular patterns (DAMPs)[101]. This interaction initiates an inflammatory response with the release of chemokines and cytokines, signaling molecules that attract other immune cells to the site of infection. For example in physiological conditions TLR-2 recognizes lipopeptides of bacterial origin, but also viral components including the EBV-encoded dUTPase[102,103]. TLRs however also play a role in MS immunopathology, as ligation of TLR2 on CNS-infiltrating DCs, induces the production of IL-1, IL-6 and IL-12, which drive the differentiation of naïve T cells into pathogenic Th1 and Th17 cells[104]. Following their recognition, pathogenic structures are engulfed and phagocytosed by APCs, such as DCs, macrophages and B cells. This process serves the destruction of pathogens, and moreover contributes to the activation of the adaptive immune system, by antigen presentation on MHC molecules[105]. DCs, crucial for antigen presentation and immune regulation, are further subdivided based on their origin and function. Different DC subsets exist, however most DCs develop from the common DC progenitor cells, which give rise to classical DCs (cDCs). They either reside in lymphatic organs and receive antigens by lymphatic drainage or transfer from other cells, while migratory cDCs reside in parenchymal tissues and must migrate to LNs to prime naïve T cells[106].

In contrast to the innate immune system, which provides immediate, non-specific defense mechanisms against a wide range of pathogens, the adaptive immune system offers a highly specific response to antigens that is conserved over time as immunological memory[99]. This enables enhanced protection upon subsequent exposures and is facilitated by T cells and B cells that are equipped with a wide variety of specific receptors. A key function of B cells is their differentiation into plasma cells, which then produce antibodies and support the humoral immune response[107]. These antibodies can neutralize pathogens, mark them for destruction by other immune cells, or activate the complement system to enhance their clearance. To initiate B cell activation, the B cell receptor needs to bind to a corresponding antigen.

Specifically, the antigen is first presented on MHCII by follicular DCs in secondary lymphatic organs including the lymph nodes and the spleen[107]. Secondly, the antigen has to be presented on MHCII by follicular T helper cells (Tfh) that were activated with the same antigen[108]. Additional signals that are required for B cell activation and differentiation, include co-stimulation provided by the interaction of CD40 on B cells with CD40 ligand (CD40L) on Tfh[107,108]. This interaction stimulates B cell activation and differentiation by promoting the release of cytokines such as IL-2, IL-4, and IL-6. Additionally, IL-4 and IL-10 derived from Th2 cells contribute to B cell differentiation and activation. In addition to their role in assisting B cells to become activated, T cells differentiate into diverse subtypes, each serving distinct functions[109,110]. These specialized T cell subsets are crucial for safeguarding the body against a wide range of pathogens or neoplastic cells.

1.2.1. Specialized T cell subsets

The spectrum of pathogens that can attack the organism contains an immense heterogeneity and ranges from intracellular virus infections to intracellular and extracellular bacteria and parasites, and even cancerous cells. T cells, as part of the adaptive immune system play a critical role in recognizing these different invaders and initiate the corresponding defense machinery[99]. Yet, the differing type of pathogen, their cellular localization, and mechanisms to evade the host immunosurveillance, requires specialized T cell subsets to fulfill distinct functions[99]. T cells are broadly categorized by the expression of either CD4 or CD8 as co-receptor to stabilize TCR–MHC binding for antigen recognition and activation[111,112]. $CD4^+$ helper T cells recognize antigens, presented on MHCII, and coordinate immune responses by activating other immune cells, producing cytokines, and assisting in the development of antibody responses. $CD8^+$ cytotoxic T cells recognize antigens, presented on MHCI and directly target and eliminate infected or neoplastic cells[105]. Additionally there are unconventional T cell subsets, including γδT cells, NK T cell and MAIT cells[113–116].

To fulfill specialized functions, effector $CD4^+$ T cells (Teff) differentiate into subtypes upon activation under the influence of distinct transcription factors and cytokines[109,110]. Among these subsets are Tfh, which play a critical role in supporting B cell activation and antibody production with the main transcription factor B-cell lymphoma 6 protein (Bcl-6)[117]. Th1 cells are crucial for combating intracellular pathogens such as viruses and certain bacteria and primarily secrete IFN-γ and IL-2 as their main effector cytokines. They differentiate under the influence of transcription factor T-box transcription factor TBX21 (T-bet)[118]. Type 2 T helper (Th2) cells which express the transcription factor GATA3, primarily secrete IL-4 and IL-10 and are involved in activating B-cell mediated antibody production, thereby aiding in immune responses against extracellular pathogens[119]. Th17 cells, distinguished by their secretion of IL-17, crucially contribute to combating extracellular pathogens, guided in their differentiation by the

transcription factor RAR-related orphan receptor gammat (RORγt), while also promoting tissue inflammation and contributing to the pathogenesis of autoimmune diseases[120]. To balance the inflammatory activity of Teff, Treg are equipped to suppress excessive immune responses and differentiate under the influence the transcription factor Forkhead box P3 (FoxP3) in the thymus. Treg maintain immune tolerance primarily through secretion of anti-inflammatory cytokines like IL-10 and transforming growth factor-beta (TGF-β). Moreover, they express cytotoxic T-lymphocyte-associated Protein 4 (CTLA-4), which acts as an inhibitory signal, by binding the co-stimulation molecules CD80/86 on DCs. Finally, via high expression of the IL-2R (CD25), they can reduce IL-2 concentrations and thereby limit Teff activation and proliferation[121].

1.2.2. Immune tolerance

While T cells are crucial for host defense, they can contribute to autoimmunity by mistakenly attacking the body's own cells and tissues. Under physiological conditions this is prevented by the elimination of self-reacting T cells in the thymus, in a process called central immune tolerance[122,123]. As a first step, CD4 and CD8 double positive T cell progenitors, get positively selected in the cortex of the thymus, based on their binding affinity towards MHCI and MHCII, which are expressed by the cortical thymic epithelial cells (cTECs)[111]. A stronger binding to MHCII favors $CD4^+$ T cell polarization, in contrast to preferred MHCI binding, which induces $CD8^+$ T cell polarization[124]. The resulting single positive T cells for either CD4 or CD8, are further selected, in a process called negative selection, localized in the medulla of the thymus. Here, the single positive T cells are presented with endogenous antigens by MHC molecules on the surface of medullary thymic epithelial cells (mTECs). The expression for peripheral tissue-specific antigens, is promoted by a critical transcriptional regulator, the autoimmune regulator (AIRE)[125–127]. In addition to mTECs, DCs present self-antigens to developing T cells in the thymus[128]. Thymocytes that recognize self-antigens with a too high affinity either undergo negative selection and are deleted or acquire a regulatory phenotype (Treg) under the influence of the transcription factor Foxp3[129,130]. T cells which fail to recognize the endogenous antigens, get selected as mature T cells and are released into the periphery. The process of positive and negative selection during central immune tolerance in the thymus aims to prevent the generation of autoreactive T cells by ensuring the ability to distinguish self from foreign antigens. However, this mechanism is not perfect and needs to be complemented by additional peripheral immune tolerance pathways that control T cells by inhibitory cues, and prevent their activation[122]. This second arm of immune tolerance is orchestrated by co-inhibitory signals or the suppressive effects of Treg.

For T cell activation to occur, three separate signals are required[131]. Firstly, the T cell receptor must recognize the cognate antigen presented on MHCII for $CD4^+$ T helper cells, or

on MHCI for $CD8^+$ cytotoxic T cells. CD4 and CD8 function as a co-receptor to stabilize the TCR–MHC interaction and thereby promote T cell activation. Secondly, co-stimulation is necessary through the interaction of CD28 with CD80/86, which is localized on APCs. Co-stimulation can also occur through the binding of CD40L with CD40 on B cells or DCs. As a third signal, stimulation via cytokines, such as IL-2, IL-6, IL-7, or IL-21, is required to activate T cells[131]. Activated T cells upregulate the alpha chain of the IL-2 receptor (IL-2Rα) also known as CD25, which is particularly upregulated in response to antigenic stimulation and IL-2 signaling. This enhances sensitivity towards IL-2, which plays a central role in T cell proliferation, survival, and differentiation[132]. Moreover, activated T cells express elevated surface levels of the early activation marker CD69. It participates in T cell migration, retention within tissues, and modulating effector functions during immune responses[133–135]. Expression of CD44 on the cell surface of activated T cells has various functions including cell adhesion, migration, activation and lymphocyte activation and proliferation[136].

To counteract T cell activation and prevent an excessive immune response, the immune system relies on co-inhibitory immune checkpoints[131]. These include programmed cell death protein 1 (PD-1) on T cells, which interacts with PD-L1 on APCs. CTLA-4, which is upregulated by activated T cells as well as constitutively expressed by Treg, competes with CD28 for CD80/86 binding on APCs with higher affinity[137]. Another mechanism to dampen T cell activity is mediated through signaling by lymphocyte-activation gene 3 (LAG3), which is structurally similar to CD4 and negatively regulates T cells by competing with CD4 for MHCII binding. Exhausted T cells exhibit elevated levels of PD-1 and LAG3[138]. Moreover, soluble mediators like TGF-β and IL-10 play a significant role in T cell inhibition, particularly sourced from Treg[121]. However, immune tolerance extends beyond the adaptive immune system, as the innate immune system also contributes regulatory mechanisms. For example, tolerogenic DCs release anti-inflammatory signals such as IL-10 that promote the differentiation of Treg. Moreover, these cells also modulate myeloid cell behavior, steering them towards a state of tissue repair and regeneration, thus attenuating inflammation[121].

1.3. Targeting the central nervous system

Targeting immune cells outside the CNS presents an effective approach to control relapses in RRMS. However, existing treatments fall short in addressing the persistent inflammation in the CNS that fuels progressive disease development. The ongoing neuroinflammation triggers irreversible neurodegeneration, leading to clinical symptoms. Delivering anti-inflammatory agents directly to the site of CNS damage, offers new potential for treating progressive MS. Thus, directly equipping neurons with means to suppress the immune system and foster a tolerogenic environment, may not only intervene in neurodegeneration but also minimize side

effects from peripheral anti-inflammatory treatments. Yet, the challenge lies in specifically targeting the CNS and in surpassing the protective nature of the BBB.

1.3.1 Blood–brain barrier

The BBB is composed of endothelial cells that serve to separate the brain from the bloodstream, tightly regulating the passage of ions, molecules, and cells. This barrier plays a crucial role in protecting the CNS from neurotoxins, maintaining brain homeostasis, regulating neurotransmitter levels, and preventing plasma macromolecules from entering the brain[139]. Endothelial cells lining the capillary lumen of blood vessels are interconnected by tight junctions, which are sealed by proteins such as claudins, occludins, and junctional adhesion molecules, thereby restricting paracellular transport[140,141]. Surrounding these endothelial cells is a basal lamina containing pericytes, which in turn are enveloped by astrocytes[139,50,142].

Small lipophilic molecules with a molecular weight of less than 500 Da can pass through the BBB via passive diffusion[143]. However, larger hydrophilic proteins rely on different active transport mechanisms. Carrier-mediated transcytosis involves influx and efflux transporters and is crucial for transporting glucose and amino acids across the BBB. Another active transport mechanism is receptor-mediated transcytosis, which facilitates the passage of insulin, leptin, and iron transferrin. Alternatively, adsorptive-mediated transcytosis occurs through electrostatic interactions[144]. In a healthy brain, only a few immune cells infiltrate, with minimal presence of neutrophils and lymphocytes. In conditions such as MS and stroke, immune cells breach into the CNS via diapedesis. This process involves multiple sequential steps, including initial tethering of immune cells to endothelial cells, followed by rolling along the endothelium, subsequent crawling to find suitable entry points, arrest, and finally, the transmigration of immune cells across the endothelial barrier into the CNS parenchyma[145]. Endothelial cells express adhesion molecules such as vascular cell adhesion molecule 1 (VCAM-1) and intercellular adhesion molecule 1 (ICAM-1), which interact with lymphocyte function-associated antigen 1 (LFA-1) and VLA-4 integrin on T cells[145].

1.3.2. Neuronal gene delivery with adeno-associated viruses

Various strategies have been investigated to develop targeted interventions for the CNS in both research and clinical settings. Delivering treatments across the BBB depends on the biochemical properties of the compound being used. Passive diffusion without an additional vehicle is typically restricted to small molecules, which may also exhibit biological activity in the periphery, potentially leading to off-target effects. This not only poses an issue for clinical treatments but also for investigating the function of proteins of interest in preclinical animal models.

Adeno-associated virus (AAV)-mediated gene transfer has become a valuable tool to introduce proteins of interest into murine cells due to their broad tropism spectrum and present a non-invasive, quick, and relatively cost-effective way, to study the role of delivered cargo *in vivo*. AAVs were discovered in the 1960s and are small (~25 nm diameter) non-enveloped single stranded DNA viruses of the family Parvoviridae[146,147]. They are non-pathogenic to mammalian cells and cannot replicate on their own but require a helper virus like adeno virus[148] or herpes simplex virus[149] to provide essential replication proteins. AAVs possess an icosahedral protein capsid, which consists of three types of subunits (VP1, VP2, and VP3) and they carry a rep gene, which encodes proteins for viral replication and a cap gene, which encodes for the three capsid subunits, flanked by two inverted terminal repeats (ITRs). The ITRs function as the recognition sequence for encapsidation and origin of genome replication. To deliver specific genetic information for research and clinical treatments, recombinant AAVs (rAAVs) have been developed by replacing the genetic information between the ITRs with an expression cassette, encoding a transgene under the control of a promoter[150]. They have a packaging capacity of 4.7 kb including the ITRs[151]. Several naturally occurring serotypes with distinct cellular tropisms have been described, whereas the serotypes AAV1–9 are the most well understood. Multiple AAV serotypes are able to transduce CNS cells, but only AAV9 can penetrate the BBB after intravenous administration, which provides a non-invasive method to target cells of the CNS. Nevertheless, this crossing occurs with limited effectiveness, showing a preference for infecting astrocytes and exhibiting notable transduction of cells in peripheral tissues, such as hepatocytes[152,153]. The delivered genomic information persists as double-stranded circular episome, that forms concatemers in the nucleus[154]. Only up to 1% of the delivered genetic information gets integrated into the host genome[155]. The lack of integration poses a benefit for research and as vehicle for clinical applications, as it can affect the expression of the delivered transgenes, as well as the expression of neighboring genes. AAVs infect the cells by adhesion to cell-surface glycans and by binding to specific receptors that mediate receptor-mediated endocytosis. Several receptors like GPR108[156] or the AAV receptor (AAVR) have been identified. AAVR contains an array of five immunoglobulin (Ig)-like polycystic kidney disease domains (PKD1–5)[157]. Although the primary receptor for some serotypes has not been identified, PDK2 was discovered to interact with AAV9 to enter the cell[158]. This knowledge was for example harnessed to increase transduction efficiency in many diverse cell types via the generation of a transgenic mouse line, which tissue specifically overexpresses AAVR[159]. Interestingly, sex differences in AAV transduction efficiency have been reported. Female mice showed a higher transduction of the brain after systemic AAV9 injection compared to male mice and a lower liver transduction[160,161].

Although AAV9 can penetrate the BBB after intravenous administration, it also transduces a great number of cells in the peripheral tissues and is therefore inefficient in

specifically targeting CNS cells. Intracranial injection of AAV2 and AAV9 are widely used in research to transduce CNS cells, however intravenous administration facilitates a minimal invasive, broader and more uniform transduction of the CNS[162]. During the past decade, several organ and cell type specific engineered AAV serotype variants have been developed that revolutionized the field of neuronal gene therapy. By directed evolution of the VP1 position of the AAV9 capsid, new AAV variants were developed that were selected for crossing the BBB after intravenous administration. Namely AAV-PHP.B which transduced the CNS 40-fold compared with its AAV9 ancestor and the enhanced version AAV-PHP.eB were developed by the Gradinaru group[163–165] and since then applied for neuronal gene delivery *in vivo*[166]. Three groups have independently identified the receptor Ly6a to bind to AAV-PHP.eB and facilitate BBB penetration, which is a glycophosphatidylinositol (GPI)-anchored surface protein highly expressed in the microvascular endothelial cells of C57BL/6 mice[167–169]. These novel serotypes transduce the majority of CNS-resident cells, but additional capsids have been developed with a cellular tropism, biased towards a specific cell population, like the AAV.CAP-B10 serotype with a neuronal bias[170]. Targeting a specific cell type can be either achieved by choosing a serotype with tropism for the cell of interest or by choosing a cell type specific promoter. For delivering genetic material specifically to neurons, promoters like the human Synapsin 1 (*hSyn1*) promoter or the mouse calcium/calmodulin-dependent protein kinase type II subunit alpha (*CaMKIIα*) promoter are commonly used[171].

1.4 Immune evasion

Given that MS pathophysiology is characterized by an excessive immune response targeting self-antigens, a promising approach is to reverse autoimmunity by inducing immune tolerance. Many invading pathogens, such as parasites or viruses, have evolved defense strategies to evade the immune system, leading to inadequate innate and adaptive immune responses. Additionally, various tissues own mechanisms to evade immune detection and maintain local immune tolerance. For example, during pregnancy, the immune system exhibits tolerance towards the fetus, and tumors develop mechanisms to establish a tolerogenic microenvironment and evade immunosurveillance.

1.4.1 Escape from host immunosurveillance

Parasites possess different strategies to evade the immune system[172]. One example is molecular mimicry where the parasite encodes proteins, that share similarity to host antigens and therefore evade recognition by the host[173]. *Plasmodium falciparum* erythrocyte membrane protein 1 (PfEMP1) contains a 14 amino acid motif that is identical to part of the heparin-binding domain of the host vitronectin[174]. Additionally, viruses utilize strategies such as the inhibition

of interferon response by the influenza virus. PB2, a subunit of the influenza virus RNA polymerase, interacts with the mitochondrial antiviral signaling protein MVAS and thereby inhibits MAVS-mediated IFN-β expression[175,176]. Human cytomegalovirus (HCMV) interferes with antigen processing and transport and therefore with MHCI presentation[177]. Also, EBV acquired several mechanisms for immune modulation and causes long term latent infection in B cells. One such mechanism is the production of a viral homolog of IL-10 (vIL-10), which displays 82% homology to human IL-10. EBV persists in memory B cells, and not only releases vIL-10, but also induces IL-10 production in the host, which is however not as potent as the human version[178,179]. Moreover, EBNA1 induces CXCL12 secretion to recruit regulatory T cells and to create an immunosuppressive microenvironment[180]. EBNA1 has also been proposed to trigger cross reacting antibody production against glial cell adhesion molecule (GlialCAM), a protein expressed by CNS-resident glial cells. This molecular mimicry has been proposed as a potential contributing factor in MS disease development[42,181,182].

A selection of proteins, which are used by the immune system to mediate immune tolerance are also used by cancer cells to escape the immune system. Tumor cells shape a tolerogenic microenvironment to protect themselves from being detected by the immune system and evade anti-proliferative signaling. This is achieved by either downregulation of proteins like MHCI to inhibit recognition by and the attack of $CD8^+$ T cells, or by upregulation of immune checkpoints like PD-L1[183], CD200[184] or LAG-3[185]. Another strategy for immune evasion by cancer cells is the induction of immunosuppressive cells and the inhibition of DC maturation by secreting anti-inflammatory molecules like IL-10, TGF-β and growth differentiation factor 15 (GDF-15)[186,187]. Moreover, tumor cells express vascular endothelial growth factors (VEGF), which induce tumor microvasculature and are capable of suppressing antigen presentation and stimulating the activity of Treg cells as well as tumor-associated macrophages[188]. Inhibiting immune checkpoints with monoclonal antibodies, like anti-PD-1/anti-PD-L1 or anti-CTLA4 agents emerged to be a potent immunotherapy of cancer. In contrast to the treatment of cancer, which follows the goal to foster immune activity towards malignant cells, MS treatment aims for silencing of the dysregulated immune system, which is targeting the CNS[189]. Consequently, an interference with the progressing neuroinflammation in MS requires the equipment of neurons with inhibitory effector proteins, such as PD-L1, CD200, GDF-15 or IL-10 to create a tolerogenic milieu, similar to the tumor microenvironment as proposed in Figure 1.1.

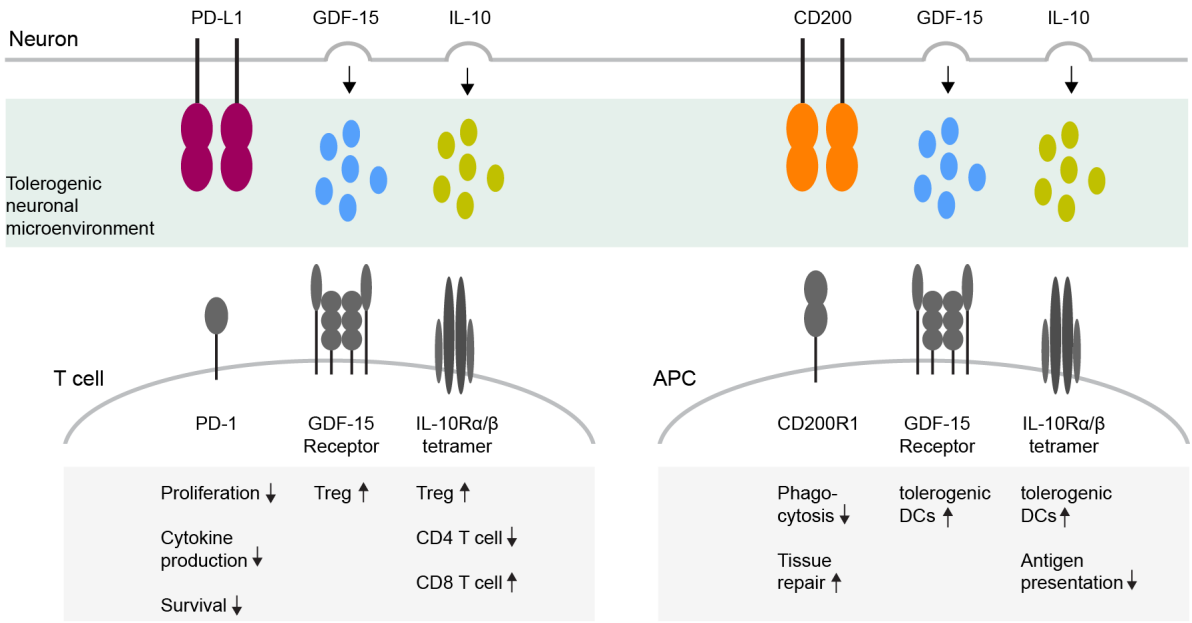

Figure 1.1: Equipped neuron expressing the effector proteins PD-L1, CD200, GDF-15 and IL-10 to mediate a local immune tolerance.
rAAV-mediated neuronal expression of the surface proteins PD-L1 and CD200 as well as the secreted molecules GDF-15 and IL-10 to equip neurons with anti-inflammatory defense mechanisms against the inflammatory attack in MS. A selection of predominant effects via the respective cognate receptors on T cells and APCs is shown. PD-L1 signals mainly via its receptor PD-1 on T cells, which inhibits T cell proliferation, cytokine production and survival. CD200 acts mainly antiphagocytic via CD200R1 on APCs. The immune cell receptor that mediates anti-inflammatory effects of GDF-15 remains unidentified, however direct immune effects are described including the increase of Treg and tolerogenic DCs. IL-10 signals via a tetrameric receptor consisting of IL-10Rα and IL-10Rβ subunits and mediates Treg expansion and an increase of tolerogenic DCs. Moreover, it reduces antigen presentation on APCs and $CD4^+$ T cell proliferation, while it acts stimulating on $CD8^+$ T cells.

1.4.2 Surface proteins PD-L1 and CD200

PD-L1 is a type I single pass transmembrane protein of 32.8 kDa and was first described by Dong *et al.* in 1999 as B7-H1[190]. It is also known as CD274 and is expressed by T cells, B cells, DCs and macrophages, some cancer cells and gets upregulated by CNS cells during inflammation[191]. It functions as a negative T cell regulator by inhibition of TCR-mediated responses via its receptor PD-1, which is expressed on the cell surface of activated T cells, B cells, DC, monocytes, and natural killer cells[192]. It mediates programmed cell death in antigen specific T cells and reduction of apoptosis in DCs. Upon PD-L1 binding to PD-1, two tyrosine motifs in PD-1 become phosphorylated: an immunoreceptor tyrosine-based switch-motif (ITSM) and an immunoreceptor tyrosine-based inhibitory motif (ITIM). These motifs recruit phosphatases, including Src homology region 2 -containing protein tyrosine phosphatase 2 (SHP2), to the ITSM in the PD-1 tail. These phosphatases then inhibit downstream signaling of co-stimulatory signals such as CD28, leading to direct inhibition of T cell proliferation via the transcription factor basic leucine zipper transcriptional factor ATF-like (BATF)[191]. PD-L1 is mostly described as a co-inhibitory signal for T cells, however more recent studies identified PD-L1–PD-1 interaction between astrocytes and microglia. PD-L1 is crucial to maintain self-

tolerance visible in the fact that *Pd1*$^{-/-}$ mice develop lupus-like glomerulonephritis and arthritis starting at 6 months of age[193]. Also, several studies have linked PD-L1 to MS and EAE. PD-L1 is upregulated in MS lesions and is proposed to be a compensatory protective mechanism[68]. This is in line with findings from the EAE mouse model, where the lack of PD-L1–PD-1 signaling worsened the EAE phenotype. *Pdl1*$^{-/-}$ mice develop a more severe EAE phenotype[194] and also a PD-1 blockade resulted in more severe disease with increased CNS lymphocyte infiltration[195]. Moreover, PD-L1 on astrocytes is required to resolve inflammation in EAE via interaction with PD1 on microglia[196]. PD-L1–PD-1, but not PD-L2–PD-1 interactions, regulate the severity of EAE[197]. But not only the interference with this pathway leads to a worsened EAE disease course, also the activation of PD-1 signaling via the treatment with PD-L1 Fc Fusion protein ameliorates EAE[198]. This finding was revalidated *in vitro,* and B7-H1-Ig suppressed the Th17 differentiation of human CD4$^+$ T cells from healthy control subjects and people with MS[198].

CD200 is a type I single pass transmembrane protein that contains two immunoglobulin superfamily domains of 31.2 kDa and was first described in humans by McCaughan *et al.* in 1987[199]. It is expressed by the somas, axons, dendrites and synapses of neurons, endothelial cells[200], cancer cells and T cells. CD200 acts antiphagocytic mainly via binding to the CD200R1, which is expressed on myeloid cells, like microglia, macrophages and DCs, but also on B and T cells[201]. Anti-inflammatory signaling is mediated via the inhibition of NF-kB. Moreover, CD200 can interact with and transduce signaling through activation of the fibroblast growth factor receptor (FGFR), thereby inducing neuritogenesis and promoting neuronal survival in primary neurons[202]. *Cd200*$^{-/-}$ mice have a normal life-span and show no obvious behavioral changes, but display an increased number of more activated myeloid cells[203]. While PD-L1 is upregulated in active MS lesions, CD200 is downregulated in the center of chronic active and inactive MS lesions[70]. A decrease in CD200 protein expression was also observed from the onset of clinical signs in EAE[204]. CD200 seems to be critical in EAE, as the lack of CD200 results in a more rapid onset of EAE[203] and an antibody-mediated blockade of CD200R leads to an aggravated clinical course of EAE[205]. The stimulation of CD200–CD200R1 interaction was beneficial during EAE as the subcutaneous administration of CD200-Fc during the chronic stages of EAE, reduced disease severity, demyelination, and axonal damage[206].

1.4.3 Soluble molecules GDF-15 and IL-10

GDF-15 is a cytokine belonging to the TGF-β superfamily and biologically active as a dimer after secretion. It consists of 25 kDa per dimer, has a half-life of about 3 hours in humans[207] and was first described in 1997 by multiple research groups in parallel and therefore known under different names before it got renamed to GDF-15 by Böttner *et al*. in 1999[208]. Former names like macrophage inhibitory cytokine (MIC-1)[209] and placental transforming growth factor

beta (PTGF)[210], hint towards an anti-inflammatory activity on macrophages and abundant expression by the placenta. The overall highest physiological GDF-15 expression occurs during pregnancy, which is essential to maintain the pregnancy and can also be measured in the CSF[211,212]. However, it is also elevated in other tissues in pathological conditions, like during bacterial infection[213] and by cancer cells[214,215]. GDF-15 signals via the brainstem-restricted receptor Glial Cell Line-Derived Neurotrophic Factor family receptor alpha-like (GFRAL) through its co-receptor Rearranged during transfection (RET)[216–218].

GDF-15 is involved in multiple physiological processes, for instance the induction of anorexia and cachexia via GFRAL. This ability of reducing body weight is subject to clinical trials, harnessing its metabolic property to pharmacologically treat obesity[219]. Various anti-inflammatory mechanisms for GDF-15 have been proposed, by directly acting on immune cells[220], by functioning as an immune cell repellent[214], or by more indirect anti-inflammatory mechanisms, such as the inhibition of T cell stimulation and cytotoxic T lymphocyte activation by DCs[221]. GDF15 induces immunosuppression via CD48 stimulation on Treg in hepatocellular carcinoma[222], and GDF-15 is reported to shift DCs towards a more tolerogenic state[223]. Additionally, *Gdf15*$^{-/-}$ mice display a stronger inflammatory reaction to LPS, highlighting the importance of GDF-15 in balancing immune cell activation[224]. Yet the receptor, which mediates these anti-inflammatory effects has not been identified as GDF-15 shows direct effects on immune cell types that do not express GFRAL[220]. A role as a neurotrophic factor has been suggested based on characterization of *Gdf15*$^{-/-}$ mice, which are viable but show loss of motor axons and significant impairment of rotarod skills[225]. Moreover, GDF-15 is reported to be associated with MS severity[226] and GDF-15 is increased in stable MS[227]. To date there are no reports about the role of GDF-15 in EAE. However, the increase in GDF-15 levels during pregnancy, together with the observed protective effect of pregnancy against new relapses in MS, suggests a potential protective role for GDF-15 in this condition[211,227,212].

IL-10 is a non-covalently linked homo-dimeric type II cytokine of 37 kDa and was first described in the 1980s as cytokine synthesis inhibitory factor (CSIF), secreted by Th2 clones[228]. It has a half-life of 2.7–4.5 h upon subcutaneous injection in humans[229]. A great number of immune cells have been identified, which can produce and respond to IL-10, such as the regulatory T cell subsets Treg and Tr1 cells, B cells, T cells, DCs, macrophages and microglia. IL-10 signals via the IL-10 receptor (IL-10R) and reprograms pro-inflammatory immune cells towards an anti-inflammatory phenotype but is also required as a survival signal for T cells[230]. IL-10R forms a transmembrane hetero-tetramer, consisting of two IL-10 receptor α-subunits (IL-10Rα), which are exclusive for IL-10 and two IL-10 receptor β-subunits (IL-10Rβ), which are shared between members of the IL-10 cytokine family like IL-19, IL-20, IL-22, IL-26, and IL-29. Upon IL-10 binding, the downstream recruitment of a Janus (Jak) kinase/ tyrosine kinase (Tyk) phosphorylates signal transducer and activator of transcription 3

(STAT3), which homodimerizes, translocates to the nucleus and binds to IL-10 responsive genes. This in turn inhibits the transcription of NF-κB-mediated expression of pro-inflammatory proteins like IL-6, TNF, and IL-1.

Multiple anti-inflammatory effects for IL-10 have been reported[231,232] like the inhibition of antigen presentation via downregulation of MHCII and CD80/86 on macrophages and DCs[186], the suppression of $CD4^+$ proliferation, the induction of Treg and Tr1 cells, a promotion of $CD8^+$ T cell exhaustion[233] and conversion of Th17 cells via a production switch from IL-17 to IL-10[234,235]. Although IL-10 is thought of as a tolerogenic cytokine, a pro-inflammatory role of IL-10 has also been reported[232,236,237]. For example $CD8^+$ T cell proliferation, B cell expansion and mast cell and NK cell induction have been described[237]. The nature of IL-10 effects is not only determined by the immune cell populations involved, but also changes in absolute levels of IL-10 protein can shift an inhibitory effect towards an activating effect. Low and intermediate IL-10 levels lead to more inhibitory effects like the exhaustion of $CD8^+$ T cells, which results in tumor growth[238] and a promotion of $CD8^+$ T cell memory formation, which causes a reduced anti-viral response[233]. In contrast, high levels of IL-10 stimulate an increased cytotoxicity of $CD8^+$ T cells, which leads to tumor shrinkage[239]. Moreover, several studies have linked IL-10 to MS, however due to conflicting results in preclinical studies it has been difficult to harness IL-10 for therapy[240]. Serum IL-10 is associated with the risk of experiencing a second relapse[241]. And people with PPMS that possess a low IL-10 expression haplotype showed a trend towards a worse clinical outcome[242]. The regulatory function of IL-10 is reported to be impaired in people with MS[243]. In the EAE mouse model, an increase of IL-10 mRNA expression was observed in the CNS during the recovery phase[244]. While *Il10*$^{-/-}$ mice are unable to recover from EAE and develop a more severe phenotype, transgenic mice with T cells that constitutively overexpress IL-10, do not develop disease[245]. Also, intracerebral injection of IL-10 encoding adenovirus protected from EAE[246].

1.5 Aims

MS immunopathology is characterized by the infiltration of autoreactive immune cells into the CNS, which causes irreversible neuronal damage as the disease progresses. This thesis will investigate the potential of localized anti-inflammatory treatments to resolve persistent CNS inflammation by establishing a local immune tolerance in direct neuronal proximity. In an attempt to protect neurons against inflammation-induced degeneration, the rAAV-mediated neuron-specific delivery of the immunomodulatory molecules PD-L1, CD200, GDF-15 and IL-10 will be explored to limit inflammatory damage in EAE.

To achieve this, the following aims were addressed:

1. Establishment of neuron-specific transgene delivery for the use as neuroprotective treatment in EAE.

2. Exploration of the immune evasion proteins PD-L1, CD200, GDF-15 and IL-10 to counteract neuroinflammatory damage in EAE.

3. Mechanistic analysis of immune modulation by effector proteins.

4. Biotechnological engineering of the genetic delivery system to achieve temporal and spatial control of protein expression.

2 Materials and methods

2.1 Materials

2.1.1 Laboratory animals

Six- to twelve-week-old female C57BL/6 were housed at 55–65% humidity at 18–23 °C with a 12 h light/dark cycle at the University Medical Center Hamburg-Eppendorf (UKE) in the Center for Molecular Neurobiology Hamburg (ZMNH). All experiments were approved by the local ethics committee (Behörde für Justiz und Verbraucherschutz Hamburg, Tierversuchsantrag N093/2020 and ORG 946).

Table 2.1: Mouse strains

Mouse strain	Official symbol	Origin
C57BL/6	C57BL/6	The Jackson Laboratory

2.1.2 Cell lines

Table 2.2: Cell lines

Cell line		Origin
Neuro-2a cells	ACC 148	DSMZ-German Collection of Microorganismen and Cell Cultures GmbH

2.1.3 Reagents

Table 2.3: Reagents for animal experiments

Reagent	Company
CO_2/O_2 gas mixture (80% CO_2, 20% O_2)	SOL Deutschland
CO_2 gas (100%)	SOL Deutschland
DietGel Recovery	Clear H2O
Freund's adjuvant, incomplete	BD Biosciences
Hanks Balanced Salt Solution without Ca^{2+}, Mg^{2+} (HBSS)	Thermo Fisher Scientific
Isofluoran CP 1 mg ml^{-1}	CP Pharma
Ketanet RS 25 mg ml^{-1} (Ketamine)	Pfizer Pharma
Mouse/rat $MOG_{35–55}$ peptide	Peptides & elephants
Mycobacterium tuberculosis	BD Biosciences
Paraformaldehyde (PFA)	Carl Roth
PBS (1×)	Pan-Biotech
Pertussis toxin, from Bordetella pertussis	Calbiochem (Merck)
Rompun R 2% (Xylazine)	Bayer

Table 2.4: Reagents for cell culture

Reagent	Company
Brefeldin A Solution (1,000×)	BioLegend

Bromodeoxyuridine (BrdU)	BioLegend
b-Mercaptoethanol	Sigma-Aldrich
Doxycycline-hydrochloride	Sigma-Aldrich
Ethylenediaminetetraacetic acid (EDTA) 0.5 M	Thermo Fisher Scientific
Fetal calf serum (FCS)	Sigma-Aldrich
Glutamax	Thermo Fisher Scientific
N-2-Hydroxyethylpiperazine-*N*'-2-ethane sulphonic acid (HEPES)	Thermo Fisher Scientific
Lipofectamine 2000	Invitrogen
Ionomycin	Santa Cruz
Minocyclin-hydrochloride	Sigma-Aldrich
Mouse/rat $MOG_{35–55}$ peptide	Peptides & elephants
Non-essential amino acids (NEAA)	Thermo Fisher Scientific
OptiMEM	Gibco
Dulbecco´s Phosphate Buffered Saline (1×) (PBS)	Pan-Biotech
Dulbecco´s Phosphate Buffered Saline (10×) (PBS 10×)	Pan-Biotech
Penicillin and streptomycin	Thermo Fisher Scientific
Percoll (1.13 g ml^{-1})	GE Healthcare
Phorbol 12-myristate 13-acetate (PMA)	Sigma-Aldrich
Poly-D-Lysine hydrobromide (PDL)	Sigma-Aldrich
Sodium pyruvate	Thermo Fisher Scientific
Trypanblue solution	Sigma Aldrich
TrypLE Express solution	Gibco
Trypsin + EDTA	Thermo Fisher Scientific
Ultra-LEAF Purified Anti-CD28 (Clone 37.51)	BioLegend
Ultra-LEAF Purified Anti-CD3 (Clone 145-2C11)	BioLegend
Venor®GeM Advance Test Kit	Minerva Biolabs

Table 2.5: Reagents for nuclei isolation

Reagent	**Company**
ddH_2O	Generated in house
Bovine serum albumin (BSA)	Merck
Ethylenediaminetetraacetic acid (EDTA) 0.5 M	Thermo Fisher Scientific
Glycerol	Sigma-Aldrich
Nonident® P40 (NP-40)	Sigma-Aldrich
Magnesium Chloride $MgCl_2$	Merck
Potassium chloride KCl	Sigma Aldrich
Sodium Chloride NaCl	Sigma-Aldrich
Sucrose	Sigma-Aldrich
Tris	Roche
β-Glycerophosphat Dinatriumsalz Hydrat	Sigma-Aldrich

Table 2.6: Reagents for flow cytometry

Reagent	**Company**
Alexa Fluor 750 live/dead	Thermo Fisher Scientific
BD FACS Clean Solution	BD Biosciences
BD FACS Flow (20 l)	BD Biosciences
BD FACS Rinse Solution	BD Biosciences
BD Trucount tubes	BD Biosciences
Brilliant Stain Buffer	BD Biosciences
Bovine serum albumin (BSA)	Merck

Calcium Chloride $CaCl_2$	Sigma Aldrich
Collagenase A	Roche
ddH_2O	Generated in house
DNase I	Merck
eBioscience™ Foxp3/Transcription Factor Staining Buffer Set	Thermo Fisher Scientific
Na_2EDTA	Thermo Fisher Scientific
Fixation Buffer	BioLegend
Hoechst 33342	Thermo Fisher Scientific
Intracellular Staining Permeabilization Wash Buffer (10×)	BioLegend
Potassium bicarbonate $KHCO_3$	Sigma-Aldrich
Magnesium Chloride $MgCl_2$	Merck
Ammonium chloride NH_4Cl	Merck
Dulbecco´s Phosphate Buffered Saline (1×) (PBS)	Pan-Biotech
Precision Count Beads	BioLegend
RPMI 1640 medium	Pan-Biotech
Sodium azide (NaN_3)	Carl Roth
True-Phos™ Perm Buffer	BioLegend
TruStain FcX™ (anti-mouse CD16/32) Antibody	BioLegend
Ultracomp eBeads™ compensation-beads	Thermo Fisher Scientific
V500 live/dead stain	Thermo Fisher Scientific
Zombie Violet™ Fixable Viability Kit	BioLegend

Table 2.7: Reagents for BCA assay and western blot

Reagent	**Company**
4-12% Bis Tris Plus Gel	Thermo Fisher Scientific
Bolt™ Antioxidant	Thermo Fisher Scientific
4× Bolt™ LDS Sample Buffer	Thermo Fisher Scientific
20X Bolt™ MOPS SDS running buffer	Thermo Fisher Scientific
Bolt™ Blot Transfer buffer (20×)	Thermo Fisher Scientific
Bovine serum albumin (BSA)	Merck
cOmplete™, EDTA-free Protease Inhibitor	Roche
ddH_2O	Generated in house
Ethylenediaminetetraacetic acid (EDTA) 0.5 M	Thermo Fisher Scientific
Methanol	Carl Roth
Sodium Chloride NaCl	Sigma-Aldrich
Nitrocellulose Membrane 0.45 µm	Invitrogen
Nonident® P40 (NP-40)	Sigma-Aldrich
Dulbecco´s Phosphate Buffered Saline (1×) (PBS)	Pan-Biotech
PhosSTOP EASYpack	Roche
Pierce™ BCA Protein Assay Kit	Thermo Fisher Scientific
Pierce™ Bovine Serum Albumin Standard Ampules, 2 mg ml^{-1}	Thermo Fisher Scientific
Sodium Dodecyl Sulfate (SDS)	Carl Roth
Sodium deoxycholate (DOC)	Sigma-Aldrich
Spectra Multicolor High Range Protein Ladder	Thermo Fisher Scientific
Tris	Roche
Triton-X® 100	Carl Roth
TWEEN 20	Sigma Aldrich
WesternSure® Chemiluminescence Substrate	LI-COR

Table 2.8: Reagents and kits for molecular cloning

Reagent	Company
Agarose Ultrapure	Thermo Fisher Scientific
Ampicillin	Carl Roth
ddH_2O	Generated in house
dNTP (1 mM)	Thermo Fisher Scientific
FastDigest BshTI	Thermo Fisher Scientific
FastDigest KpnI	Thermo Fisher Scientific
FastDigest HindIII	Thermo Fisher Scientific
FastDigest MunI	Thermo Fisher Scientific
FastDigest Pfl23II	Thermo Fisher Scientific
FastDigest SacI	Thermo Fisher Scientific
GeneRuler 1 kb DNA Ladder	Thermo Fisher Scientific
Nucleo Spin Gel and PCR cleanup kit	Machery Nagel
Nucleo Spin Plasmid easy pure kit	Machery Nagel
Nucleo Bond Xtra Midi kit	Machery Nagel
NucleoBond Xtra Midi Plus EF, Midi kit	Machery Nagel
Q5 High-Fidelity DNA Polymerase	New England Biolabs
RotiSafe	Carl Roth
SOC outgrowth medium.f	New England Biolabs
Stbl3 Chemically competent bacteria	Invitrogen
Top 10 Chemically competent bacteria	Invitrogen
T4 Ligase	New England Biolabs
T4 Polynucleotide Kinase	New England Biolabs

Table 2.9: Reagents for immunocytochemistry and immunohistochemistry

Reagent	Company
High Precision Microscope Cover Glasses	Marienfeld
Hoechst 33342	Invitrogen
Immu-Mount	Thermo Fisher Scientific
Microscope slides	Carl Roth
Normal Donkey Serum	Merck
PAP pen 2 mm tip width (Liquid Blocker)	Sigma–Aldrich
Paraformaldehyd (PFA)	Sigma–Aldrich
Superfrost Plus™ Adhesion Microscope Slides	Thermo Fisher Scientific
Tissue-Tek® O.C.T.™	Weckert
Triton-X® 100	Carl Roth

Table 2.10: Reagents for IL-10 protein analysis

Name	Company
cOmplete™, EDTA-free Protease Inhibitor	Roche
Dulbecco´s Phosphate Buffered Saline (1×) (PBS)	Pan-Biotech
Ethylenediaminetetraacetic acid (EDTA), 0.5 M	Thermo Fisher Scientific
ELISA MAX™ Deluxe Set Mouse IL-10	BioLegend
Phenylmethylsulfonyl fluoride (PMSF)	Abcam
Sodium Chloride NaCl	Sigma-Aldrich
Sodium deoxycholate (DOC)	Sigma-Aldrich
Sulfuric acid (H_2SO_4)	Carl Roth
Triethylene glycol diamine tetraacetic acid (EGTA)	Thermo Fisher Scientific
Tris	Roche

Triton-X® 100	Carl Roth

2.1.4 Antibodies

Table 2.11: Primary antibodies for immunocytochemistry, immunohistochemistry and western blot

Antigen	Clone	Host Species	Dilution ICC	Dilution IHC	Dilution WB	Company
CD200/OX2	OX-90	Rat	1:100	1:100		BioLegend
CD274/ PD-L1	EPR20529	Rabbit			1:1000	Abcam
GDF-15	0297	Mouse	1:200			Evitria
GFP	Polyclonal	Chicken		1:1000		Abcam
GFP	Polyclonal	Rabbit		1:300		Thermo Fisher Scientific
IL-10	JES5-16E3	Rat	1:100	1:100		BioLegend
MAP2	Polyclonal	Chicken	1:2500			Abcam
NeuN	Polyclonal	Chicken	1:300			Millipore
NeuN	Polyclonal	Guinea pig	1:300			Synaptic Systems
Vinculin	hVin-1	Mouse			1:1000	Sigma Aldrich

Table 2.12: Primary antibodies for flow cytometry

Antigen	Clone	Fluorophore	Dilution	Company
BrdU	3D4	FITC	1:20	BioLegend
CD3e	500A2	BUV737	1:100	BD Biosciences
CD4	GK1.5	BUV395	1:200	BD Biosciences
CD8a	53-6.7	BV785	1:200	BioLegend
CD8a	53-6.7	PerCP/Cy5.5	1:200	BioLegend
CD11b	M1/70	BUV395	1:200	BD Biosciences
CD11b	M1/70	BV510	1:200	BioLegend
CD11c	N418	PE-Cy7	1:300	BioLegend
CD19	6D5	BV510	1:200	BioLegend
CD19	6D5	BV605	1:100	BioLegend
CD19	6D5	BV650	1:400	BioLegend
CD25	PC61	PE	1:100	BioLegend
CD44	IM7	BV650	1:100	BioLegend
CD45	30-F11	FITC	1:200	BioLegend
CD69	H1.2F3	BV785	1:100	BioLegend
CD274/PD-L1	10F.9G2	APC	1:100	BioLegend
CD279/PD-1	29F.1A12	BV421	1:100	BioLegend
CD200/OX2	OX-90	AF647	1:100	BioLegend
F4/80	BM8	BV421	1:100	BioLegend
FoxP3	FJK-16s	APC	1:300	Invitrogen
IFN-γ	XMG1.2	BV786	1:50	BioLegend
IL-4	11B11	PE-Cy7	1:50	BioLegend
IL-10	JES5-16E3	APC	1:100	BioLegend
IL-17a	TC11-18H10.1	APC	1:100	BioLegend

LFA-1	H155-78	PE-Cy7	1:100	BioLegend
Ly6G	1A8	APC-Cy7	1:200	BioLegend
MHC II	M5/114.15.2	BV711	1:400	BioLegend
NeuN	EPR12763	AF647	1:500	Abcam
NK1.1	PK136	PE	1:300	Invitrogen
pSTAT3	13A3-1	PE	1:20	BioLegend
TCRβ	H57-597	BUV737	1:100	BD Biosciences
TNF-α	MP6-XT22	PE	1:50	BioLegend

Table 2.13: Secondary antibodies

Reactivity	**Host species**	**Fluorophore**	**Method**	**Dilution**	**Company**
Chicken	Donkey	AF488	ICC/IHC	1:500	Jackson Immuno Research
Chicken	Donkey	Cy3	ICC/IHC	1:500	Abcam
Chicken	Donkey	AF647	ICC/IHC	1:500	Abcam
Mouse	Goat	HRP	WB	1:15000	LI-COR
Rabbit	Goat	HRP	WB	1:10000	LI-COR
Rabbit	Donkey	AF488	ICC/IHC	1:500	Abcam
Rat	Donkey	AF555	ICC/IHC	1:500	Abcam
Rat	Donkey	AF647	ICC/IHC	1:500	Abcam
Guinea pig	Donkey	Cy3	ICC/IHC	1:500	Abcam

2.1.5 Plasmids, rAAVs, primers and oligonucleotides

Table 2.14: Generated plasmids and rAAVs

Plasmid	**Abbreviation**	**rAAV**	**Serotype**
CAG-NLS-EGFP (Addgene #104061)	*CAG*-EGFP	AAV-PHP.eB:*CAG*	AAV-PHP.eB
		AAV.CAP-B10:*CAG*	AAV.CAP-B10
hSyn1-2×NLS-EGFP	*hSyn1*-EGFP (3.1.1, 3.1.2)	AAV-PHP.eB:*hSyn1* (3.1.1, 3.1.2)	AAV-PHP.eB
	Control (3.2.1 onwards)	AAV-Control (3.2.1 onwards)	AAV-PHP.eB
hSyn1-2×NLS-EGFP-P2A-PDL1	PDL1	AAV-PDL1	AAV-PHP.eB
hSyn1-2×NLS-EGFP-P2A-CD200	CD200	AAV-CD200	AAV-PHP.eB
hSyn1-2×NLS-EGFP-P2A-GDF15	GDF15	AAV-GDF15	AAV-PHP.eB
hSyn1-2×NLS-EGFP-P2A-IL10	IL10	AAV-IL10	AAV-PHP.eB
hSyn1-2×NLS-EGFP-P2A-GPI-1×IL10	GPI-1×IL10		
hSyn1-2×NLS-EGFP-P2A-GPI-2×IL10	GPI-2xIL10	AAV-GPI-2×IL10	AAV-PHP.eB
hSyn1-2×NLS-EGFP-P2A-tmPDL1-1×IL10	tmPDL1-1×IL10		
hSyn1-2×NLS-EGFP-P2A-tmPDL1-2×IL10	tmPDL1-2xIL10	AAV-tmPDL1-2×IL10	AAV-PHP.eB

hSyn1-2×NLS-EGFP-P2A-tmIL2ra-1×IL10	tmIL2ra-1×IL10		
hSyn1-2×NLS-EGFP-P2A-mIL2ra-2×IL10	tmIL2ra-2xIL10		
TRE-2×NLS-EGFP	*TRE*-Ctrl		
TRE-2×NLS-EGFP-P2A-IL10	*TRE*-IL10	AAV-*TRE*-IL10	AAV-PHP.eB
hSyn1-2×NLS-mSc	*hSyn1*-mSc		
hSyn1-2×NLS-mSc-P2A-rtTA	*hSyn1*-rtTA		
ihSyn1-2×NLS-mSc-P2A-rtTA	*ihSyn1*-rtTA	AAV-*ihSyn1*-rtTA	AAV-PHP.eB

Table 2.15: Addgene and Takara plasmids

Plasmid number	**Name**	**Company**
#118025	*hSyn1*-2xNLS-mTurquoise2	Addgene
#107012	pUNO mouse CD274 + 3'UTR WT full length	Addgene
#104061	*CAG*-NLS-EGFP	Addgene
#104056	pAAV-*TRE*-eYFP	Addgene
#99120	pAAV-*ihSyn1*-tTA	Addgene
#631168	*pCMV*-Tet3G from Tet-On 3G Inducible Expression System	Takara

Table 2.16: PCR primers 5'→ 3'

Label	**Gene**	**RE**	**Sequence**
P1_fwd	EGFP	BshTI	GCCACCGGTGTGAGCAAGGGCGAGGAGCT
P1_rev	EGFP	MunI	GACCAATTGCTTGTACAGCTCGTCCATGCCG
P2_fwd	PD-L1	Pfl23II	ATCCGTACGAGGATATTTGCTGGCATTATATTCACAG
P2_rev	PD-L1	SacI	AAATGATACACAATTCGAGGAGACGTAAGAGCTCGCA
P3_fwd	CD200	Pfl23II	ACACGTACGGGCAGTCTGGTATTCAGGAGACC
P3_rev	CD200	SacI	GGATGCAAAGAATGAAATAAGAGCTCTAA
P4_fwd	GDF-15	Pfl23II	GTTCGTACGGCCCCGCCCGCGCTCC
P4_rev	GDF-15	SacI	GGGGCTGCCACTGCGCTTGAGAGCTCATC
P5_fwd	IL-10	Pfl23II	ATCCGTACGCCTGGCTCAGCACTGCTATGC
P5_rev	IL-10	SacI	AAGCATACATGATGATCAAAATGAAAAGCTAAGAGCTCGCC
P6_fwd	mScarlet	BshTI	GCCACCGGTGTGAGCAAGGGCGAGGCAGT
P6_rev	mScarlet	MunI	CGGCATGGACGAGCTGTACAAGCAATTGCCA

P7_fwd	rtTA	Pfl23II	CCACGTACGTCTAGACTGGACAAGAGC AAAGTCAT
P7_rev	rtTA	SacI	CCTTGACATGCTCCCCGGGTAAGAGCT CCAG

Table 2.17: Oligonucleotides 5'→ 3'

Label	Gene	RE	Sequence
O1_fwd	MCS	KpnI, BshTI, MunI, Pfl23II, SacI, SalI, HindIII	GGTACCCAAGTTAACGCGACCGGTGGA CAATTGGTCCGTACGGCTGAGCTCCAG GTCGACTCGAAGCTT
O1_rev	MCS	KpnI, BshTI, MunI, Pfl23II, SacI, SalI, HindIII	AAGCTTCGAGTCGACCTGGAGCTCAGC CGTACGGACCAATTGTCCACCGGTCGC GTTAACTTGGGTACC
O2_fwd	NLS	KpnI	CGCCACCATGGTTAAAAGGCCGGCGGC CACGAAAAAGGCCGGCCAGGCAAAAAA GAAAAAGA
O2_rev	NLS	BshTI	CCGGTCTTTTTCTTTTTTGCCTGGCCGG CCTTTTTCGTGGCCGCCGGCCTTTTAAC CATGGTGGCGGTAC
O3_fwd	NLS-P2A	MunI	AATTGCCCAAGAAAAAGCGGAAGGTGG GCGCAACAAACTTCTCTCTGCTGAAACA AGCCGGAGATGTCGAAGAGAATCCTGG ACCAC
O3_rev	NLS-P2A	Pfl23II	GTACGTGGTCCAGGATTCTCTTCGACAT CTCCGGCTTGTTTCAGCAGAGAGAAGTT TGTTGCGCCCACCTTCCGCTTTTTCTTG GGC
O4_fwd	NLS-P2A-STOP	MunI	AATTGCCCAAGAAAAAGCGGAAGGTGG GCGCAACAAACTTCTCTCTGCTGAAACA AGCCGGAGATGTCGAAGAGAATCCTGG ACCATAAC
O4_rev	NLS-P2A-STOP	Pfl23II	GTACGTTATGGTCCAGGATTCTCTTCGA CATCTCCGGCTTGTTTCAGCAGAGAGAA GTTTGTTGCGCCCACCTTCCGCTTTTTC TTGGGC

2.1.6 Solutions, buffers, and media

Table 2.18: Buffers and solutions

Name	Reagent	Concentrations/volume	Company
PBS with Ca^{2+} and Mg^{2+}	$CaCl_2$ (1 mM)	450 µl	Sigma Aldrich
	$MgCl_2$ (1 mM)	57.67 µl	Merck
	PBS	500 ml	Pan-Biotech
CNS digestion solution	Collagenase A	1 mg ml^{-1}	Sigma
	DNase I	0.1 mg ml^{-1}	Merck
	RPMI 1640 medium	50 ml	Pan-Biotech
ELISA wash buffer	PBS	1000 ml	Pan-Biotech
	TWEEN 20	0.05%	Sigma Aldrich

ELISA stop solution	H_2SO_4	1 M	Carl Roth
	ddH_2O	ad 500 ml	Generated in house
Erylysis buffer (pH 7.3 – 7.4)	$KHCO_3$	10 mM	Sigma-Aldrich
	NH_4Cl	0.15 M	Sigma-Aldrich
	EDTA 0.5 M	0.1 mM	Thermo Fisher Scientific
	ddH_2O	ad 500 ml	Generated in house
FACS buffer	BSA	2.5 g	Merck
	NaN_3	0.1 g	Carl Roth
	PBS	ad 500 ml	Pan-Biotech
Nuclei lysis buffer	NaCl	10 mM	Sigma Aldrich
	$MgCl_2$	5 mM	Merck
	NP-40	0,5%	Sigma Aldrich
	Tris	10 mM	Roche
	ddH_2O	ad 500 ml	Generated in house
Nuclei incubation buffer	BSA	1%	Merck
	EDTA 0.5 M	1 mM	Thermo Fisher Scientific
	Glycerol	5%	Sigma-Aldrich
	$MgCl_2$	2 mM	Merck
	KCl	25 mM	Sigma-Aldrich
	Sucrose	340 mM	Sigma-Aldrich
	β-Glycerophosphat Dinatriumsalz Hydrat	65 mM	Sigma-Aldrich
	ddH_2O	ad 500 ml	Generated in house
RIPA buffer	Tris, pH 8	50 mM	Roche
	NaCl	150 mM	Sigma-Aldrich
	EDTA 0.5 M	5 mM	Thermo Fisher Scientific
	SDS	0.1%	Carl Roth
	NP-40	1%	Sigma-Aldrich
	DOC	0.5%	Sigma-Aldrich
	ddH_2O	8.4 ml	Generated in house
	cOmplete™, EDTA-free Protease Inhibitor	1 Tablet	Roche
	PhosSTOP EASYpack	1 Tablet	Roche
TAE buffer (50×) (pH = 8.3)	Tris	242 g	Roche
	EDTA	18.6 g	Carl Roth
	100% Acetic acid	57.1 mL	Carl Roth
	ddH_2O	ad 1000 ml	Generated in house

TAE buffer (1×)	50× TAE buffer	40 mL	Generated in house
	ddH_2O	ad 2L	Generated in house
TBS (10×) (pH7.4-7.6)	NaCl	87.7 g	Sigma-Aldrich
	Tris	24.3 g	Roche
	ddH_2O	ad 1000 ml	Generated in house
TBS-T (1×)	TBS 10×	100 ml	Generated in house
	TWEEN 20	1 ml	Sigma Aldrich
	ddH_2O	ad 1000 ml	Generated in house
Tissue extraction buffer for ELISA	Tris-HCl, pH 7.4	100 mM	Roche
	NaCl	150 mM	Sigma-Aldrich
	EGTA	1 mM	Thermo Fisher Scientific
	EDTA 0.5 M	1 mM	Thermo Fisher Scientific
	Triton X-100	1%	Carl Roth
	DOC	0.5%	Sigma-Aldrich
	PMSF	1 mM	Abcam
	cOmplete™, EDTA-free Protease Inhibitor	1 Tablet	Roche
Tissue lysis buffer for fixed tissue (Thacker et al. 2020)	Tris, pH 7.4	500 mM	Roche
	NaCl	100 mM	Sigma-Aldrich
	EDTA 0.5 M	25 mM	Sigma-Aldrich
	SDS	2%	Carl Roth
	NP-40	1%	Thermo Fisher Scientific
	Triton X-100	1%	Carl Roth
	ddH_2O		Generated in house
	cOmplete™, EDTA-free Protease Inhibitor	1 Tablet	Roche
	PhosSTOP EASYpack	1 Tablet	Roche
Transfer buffer (1×)	Bolt™ Blot Transfer buffer (20X)	25 ml	Thermo Fisher Scientific
	Metanol	50 ml	Carl Roth
	Bolt Antioxidant	500 µl	Thermo Fisher Scientific
	ddH_2O	ad 500 ml	Generated in house

Table 2.19: Media

Name	**Reagent**	**Concentrations/volume**	**Company**
N2a culture medium	DMEM high glucose GlutaMAX	500 ml	Gibco

	FCS	10%	Sigma-Aldrich
	Penicillin-Streptomycin	1%	Gibco
	Amphotericin B	0,125 µg ml^{-1}	Gibco
Neuronal Growth Medium (NGM)	PNBM Primary Neuron Basal Medium	250 ml	Lanza
	PNGM Single Quots	1 Unit	Lanza
LB medium	LB Broth Base	20 g	Invitrogen
	ddH_2O	ad 1000 ml	
LB Agar plate	LB agar	32 g	Invitrogen
	NaCl	5 g	Carl Roth
	ddH_2O	ad 1000 ml	Generated in house
T cell medium	b-Mercaptoethanol	0.01%	Sigma-Aldrich
	FCS	10%	Sigma-Aldrich
	Penicillin and streptomycin	1%	Thermo Fisher Scientific
	HEPES	1%	Thermo Fisher Scientific
	NEAA	1%	Thermo Fisher Scientific
	Sodium pyruvate	1%	Thermo Fisher Scientific
	Glutamax	1%	Thermo Fisher Scientific
	RPMI 1640 medium	500 ml	Pan-Biotech

2.1.7 Devices

Table 2.20: Devices

Name	**Company**
ABI 3130 (Sanger sequencing)	Applied Biosystems
BD FACSymphony A3 analyzer	BD Biosciences
Bench Top Microcentrifuge	Eppendorf
Binocular Stereo Microscope	Leica
Biometra Low Voltage Power Supply	Analytik Jena
Centrifuge	Heraus
Chemical fume hood	Kugel medical
Computer	HP
Disposable Hemocytometer	NanoEnTEK
Electrophoretic system	Peqlab
Epifluorescence Microscope Eclipse Ts2R	Nikon
Eppendorf® Thermomixer Compact (1.5 ml block)	Sigma-Aldrich
Flex Cycler2	Analytik Jena
Freezer (−20 °C)	Liebherr
Freezer (−80 °C)	Heraus
Fridge (4 °C)	Liebherr
Fume hood	Belec Vario Lab
Gel iX Imager	INTAS Science Imaging
Glass douncer	Sigma-Aldrich

Homogenisator Dounce, 0.5 ml	Carl Roth
ImageQuant™LAS4000mini	GE Healthcare
Incubator (N2a cells)	Memmert
Incubator (primary neurons)	Thermo Fisher Scientific
KL1500	Schott AG
Laminar flow hood	Thermo Fisher Scientific
Light Microscope	Olympus
LSM 700 confocal laser scanning microscope	Zeiss
Microme HM 560 Cyrostat	Thermo Fisher Scientific
myFUGE Mini Microcentrifuge	Biozym
NanoDrop 1000 Spectrophotometer	Peqlab
Perfusion System	Ismatec
Pipettes	Eppendorf/Gilson
Rotator	GFL Gesellschaft für Laborbedarf
Sterile hood	Thermo Fisher Scientific
Spark™ 10M multimode microplate reader	Tecan
StainTray slide staining system	Sigma–Aldrich
Surgical instruments	FST Fine Scientific Tools
Tabletop centrifuge	Thermo Fisher Scientific
Water bath with shaker	GFL Gesellschaft für Laborbedarf

Table 2.21: Flow cytometer configuration of BD FACSymphony A3 analyzer

Laser	**Detector**	**Dichroic Mirror**	**Bandpass Filter**	**Fluorochrome**	**Other Fluorochromes**
355 nm	G	370 LP	379/28	BUV395	
	F	410 LP	450/50	DAPI	
		490 LP	515/30	Alternative: BUV496	
	E	550 LP	580/20	BUV563	
	D	600 LP	610/20	BUV615	
	C	630 LP	670/20	BUV661	
	B	690 LP	735/30	BUV737	
	A	770 LP	810/40	BUV805	
	H	410 LP	431/28	BV421	Pacific blue
405 nm	G	505 LP	525/50	BV510	AmCyan
	F	550 LP	585/15	BV570	
	E	595 LP	605/40	BV605	
	D	635 LP	677/20	BV650	
	C	685 LP	710/50	BV711	
	B	735 LP	750/30	BV750	
	A	770 LP	810/40	BV786	
	G		488/10	SSC	
	F	505 LP	530/30	Alexa 488	FITC
			513/17	Alternative: EGFP	
488 nm	E	600 LP	610/20	BB630	
	D	635 LP	670/30	BB660	
	C	685 LP	710/50	PerCP-Cy5.5	
	B	735 LP	750/30	BB755	
	A	770 LP	810/40	BB790	
	D	570 LP	586/15	PE	

561 nm	C	600 LP	610/20	PE-CF/Dazzle594	
	B	635 LP	670/30	PE-Cy5.5	
	A	750 LP	780/60	PE-Cy7	
637 nm	C	655 LP	670/30	Alexa 647	APC
	B	690 LP	730/45	Alexa700	
	A	750 LP	780/60	APC-Cy7	

2.1.8 Consumables

Table 2.22: Consumables

Name	**Company**
Butterfly cannula 25G, 80 mm	Sarstedt
CELLSTAR EASYstrainer (40 µm and 100 µm)	Greiner
Disposable hemocytometer	NanoEntek
Eppendorf tubes (0.2 ml, 0.5 ml, 1.5 ml, 2.5 ml)	Sarstedt
FACS tubes (5 ml)	Sarstedt
FACS tube with cell strainer cap	Thermo Fisher Scientific
Falcon tubes (15 ml and 50 ml)	Greiner
Liquid reservoir for multichannel pipettes	Integra
Multiwell plates (96-well, 24-well, 12-well, 6-well)	Greiner
Parafilm N	Carl Roth
PCR plate sealing tape	Sarstedt
Pipette tips	Sarstedt
Serological pipettes (2 ml, 5 ml, 10 ml and 25 ml)	Greiner, Sarstedt
Syringes and needles Braun	BD Biosciences
7 mm stainless steel bead	Qiagen
75 T flask, 25 T flask	Sarstedt

2.1.9 Software

Table 2.23: Software

Name	**Company**
Adobe Illustrator 2023	Adobe Inc.
FACSDiva™	BD Bioscience
FlowJo (Version 10)	BD Bioscience
Fiji ImageJ	Open source (https://imagej.nih.gov/ij/index.html)
Microsoft Office	Microsoft
Graphpad Prism (Version 10)	Graph Pad Software
R Studio	Posit Software
SparkControl plate reader software	Tecan
SDS 2.4	Thermo Fisher Scientific
TBase Client 4Dv12sql	4D Deutschland GmbH
Windows	Microsoft
Zen black	Zeiss

2.2 Methods

2.2.1 Molecular cloning

All plasmids used in this study were generated by molecular cloning, except when indicated otherwise. PCR primers, sequencing primers and oligonucleotides were ordered from Eurofins Genomics. Materials that were used for molecular cloning are listed in Table 2.8.

Restriction Digestion: Plasmids were incubated with the respective restriction enzyme at 37 °C for the maximum time until the enzyme exhibits star activity and heat inactivated according to its technical data sheet.

Polymerase chain reaction (PCR): DNA fragments of a respective gene sequence were amplified via polymerase chain reaction from template DNA. PCR primers were designed to introduce specific restriction enzyme recognition sequences, or additional short DNA sequences with an annealing temperature of 65 °C, which was calculated with OligoCalc (Table 2.16). 100 ng of template from plasmid DNA or 1 µl from complementary DNA (cDNA) were used as PCR template. The PCR steps were conducted in a thermocycler, starting with an initial denaturation step of 98 °C for 30 sec, which was followed by 35 cycles of 10 sec denaturation at 98 °C, 30 sec of primer annealing at 63 °C and elongation at 72 °C. These cycles were followed by a 2 min 72 °C final extension step. PCR products were purified by agarose gel electrophoresis and digested with the respective restriction enzymes to create sticky ends for ligation.

Agarose gel electrophoresis: PCR products and digested DNA fragments were visualized and isolated by agarose gel electrophoresis. The specific DNA fragments were separated in an electric field by size on a 1-3% agarose gel containing RotiSafe (1:5,000) for visualization under UV light. DNA bands of the correct size were purified with the Nucleo Spin Gel and PCR cleanup kit, according to the manufacturer's instructions.

Determination of DNA concentration: DNA concentrations were determined with a NanoDrop 1000 Spectrophotometer with measurement of absorbance at specific wavelengths and an absorbance ratio $A_{260/230}$ of 1.8 was considered as pure.

Ligation and transformation: Plasmids were generated by ligation of a digested vector and either a digested PCR product or annealed oligonucleotides with the T4 ligase according to the manufacturer's instructions. Vector and insert were used in a ratio of 1:3. A negative control of water replacing the insert DNA was prepared to address ligation background of potentially

religating vector. To ligate oligonucleotides into a vector, corresponding forward and reverse oligonucleotides were heated to 95 °C in ligation buffer for 5 min and slowly cooled down over 45 min to anneal. All oligonucleotides used in this study are listed in Table 2.17. Ligation mixes were transformed into Top10 chemically competent bacteria. After 15 min incubation time of 10 µl ligation mix with 50 µl bacteria, the transformation mix was heat shocked at 42 °C for 45 sec and incubated for 1 min on ice. 250 µl SOC medium were added and incubated at 37 °C for 45 min at 850 rpm. 150 µl were plated on an LB agar plate with ampicillin supplement and incubated at 37 °C overnight.

Identity verification of plasmids and DNA amplification: Three to six clones were picked with a 200 µl pipette tip and shaken for 16 h in 2 ml LB medium with ampicillin supplement (100 µg ml^{-1}) at 37 °C. The DNA was purified from the bacteria with the Nucleo Spin Plasmid easy pure kit, according to the manufacturer's instructions. The correct plasmid identity was validated with control digest of each individual clone and the characteristic DNA bands visualized by agarose gel electrophoresis. To verify the nucleotide sequence of regions that were amplified by PCR, the plasmid was analyzed by Sanger Sequencing. After identifying a correct plasmid, 200 µl of the corresponding mini preparation was added to 100 ml LB medium with ampicillin supplement (100 µg ml^{-1}) and shaken for 16 h at 37 °C. The DNA was isolated with the Nucleo Bond Xtra Midi Kit according to the manufacturer's instructions. Plasmids that were used for rAAV generation were purified with the endotoxin free NucleoBond Xtra Midi Plus EF, Midi kit.

Generation of constitutive delivery plasmids: To generate the constitutive delivery plasmids for PD-L1, CD200, GDF-15, IL-10, and memIL-10, pAAV-*hSyn1*-mTurquoise2 (Addgene #99125) was digested with KpnI and HindIII and a new multiple cloning site inserted (O1_fwd, O1_rev) by oligo ligation. Next, EGFP was amplified by PCR (P1_fwd, P1_rev) and vector and PCR product were digested with BshTI and MunI prior to ligation. An N-terminal NLS of the EGFP gene was added by digesting the vector with KpnI and BshTI, followed by oligo ligation (O2_fwd, O2_rev). A subsequent oligo ligation was used to add a C-terminal NLS of the EGFP as well as a P2A sequence after digestion with MunI and Pfl23II (O3_fwd, O3_rev). To generate the control constructs the last step was carried out by using oligos that also include a STOP codon C-terminal of the P2A sequence ((O4_fwd, O4_rev). These cloning steps resulted in *hSyn1*-2×NLS-EGFP-P2A and *hSyn1*-2×NLS-EGFP-P2A-STOP. The respective effector proteins were introduced via the restriction sites Pfl23II and SacI. For PD-L1 the Addgene plasmid #107012 served as a PCR template (P2_fwd, P2_rev), for CD200 (P3_fwd, P3_rev) and GDF-15 (P4_fwd, P4_rev) wild type N2a cell cDNA served as a

template, and for IL-10 murine regulatory T cell cDNA (P5_fwd, P5_rev). The different memIL-10 sequences were generated via gene synthesis and ordered from Twist Biosciences.

Generation of inducible delivery plasmids: First the response vector was cloned by digestion of the vector pAAV-*TRE*-mRuby2 (Addgene #99114), and the inserts *hSyn1*-2×NLS-EGFP-P2A-STOP and *hSyn1*-2×NLS-EGFP-P2A-IL10 with KpnI and HindIII and ligated, which resulted in *TRE*-2×NLS-EGFP-P2A-STOP and *TRE*-2×NLS-EGFP-P2A-IL10. To generate the neuron-specific delivery plasmid for the rtTA, first EGFP was replaced by mScarlet by PCR (P6_fwd, P6_rev). The vectors *hSyn1*-2×NLS-EGFP-P2A and *hSyn1*-2×NLS-EGFP-P2A-STOP and the PCR product were digested with BshTI and MunI and ligated to *hSyn1*-2×NLS-mSc-P2A and *hSyn1*-2×NLS-mSc-P2A-STOP. Next the rtTA was included by PCR of *pCMV*-Tet3G (#631168) (P7_fwd, P8_rev) and vector and insert digested with Pfl23II and SacI, resulting in *hSyn1*-2×NLS-mSc-P2A-rtTA. Moreover, this complete insert was transferred into a vector, which employs the self-enhancing *ihSyn1*. pAAV-*ihSyn1*-rTA (#99120) and *hSyn1*-2×NLS-mSc-P2A-rtTA were digested with KpnI and HindIII to receive *ihSyn1*-2×NLS-mSc-P2A-rtTA.

2.2.2 Neuro-2a cell culture

Neuro-2a (N2a) cells were cultured at 37 °C, in 5% CO_2 in N2a culture medium in a 75 T flask. The cells were split when reaching 80% confluency and were kept at low passage (≤ passage 20). To split the cells, the medium was removed, and the cells washed by adding 10 ml of phosphate buffered saline (PBS). The cells were incubated the with 4 ml TrypLE Express solution for 2 min and the cells detached by adding 6 ml of fresh N2a medium and pipetting up and down. After a centrifugation step (500*g*, 5 min, RT), the supernatant was removed, the cell pellet resuspended in 13 ml prewarmed N2a medium and pipetted into a new 75 T flask. The cells were regularly tested for contamination with mycoplasma with the Venor®GeM Advance Test Kit, according to the manufacturer's instructions.

2.2.3 Transient transfection of N2a cells

Correct protein delivery was tested in N2a cells by transient transfection. For western blot analysis a 6-well plate, for flow cytometry a 12-well plate and for immunocytochemistry a 24-well plate was used. N2a cells were washed with PBS and detached by addition of 4 ml TrypLE Express solution for 2 min and pipetting up and down with 6 ml of fresh N2a medium. The single cell suspension was diluted 1:1 with filtered Trypan-Blue in PBS (1:10), counted with a disposable hemocytometer and seeded at a cell density of 50,000 cells cm^{-2}. N2a cells were transiently transfected after 24 h of incubation at 37 °C with Lipofectamine 2000 at a cell

density of 50–70 % confluency, according to the manufacturer's instructions. OptiMEM was used to dissolve the transfection reagent and DNA. The supernatant was replaced with pre-warmed fresh N2a medium 6 h after transfection and the cells analyzed 24 h after transfection.

2.2.4 N2a–lymphocyte co-culture

N2a cells were seeded at a density of 80,000 cells cm^{-2} and transfected the following day. 24 h after transient transfection a single cell suspension of primary murine lymphocytes from a C57BL/6 wild type mouse was generated as described in 2.2.9. The cell suspension was centrifuged and resuspended in 5 ml of live/dead staining solution (1:1000 in PBS) in 15 ml falcon tubes and incubated at 4 °C for 20 min. Meanwhile the cells were counted with a disposable hemocytometer. The cells were washed with 10 ml cold PBS and centrifuged (1500 rpm, 5 min, 4 °C). The cell pellet was resuspended in T cell medium at a concentration of 3×10^6 cells ml^{-1} and 50 µl added to each well of a 96-well plate with the pre-seeded and transfected N2a cells in N2a cell medium. The N2a–lymphocyte co-culture was centrifuged (300*g*, 2 min, RT) to settle the lymphocytes to the well bottom onto the adherent N2a cells and incubated at 37 °C for 30 min. The cells were harvested and stained for flow cytometry analysis, according to the protocol for intracellular staining of phosphoproteins (2.2.10).

2.2.5 Primary neuronal cortical culture

Preparation: Cell culture plates were coated with Poly-D-Lysin (PDL) in PBS (1:500) overnight and washed twice with PBS, whereas for the last washing step the plate was incubated for 10 min at 37 °C. The PBS was replaced by PNGM culture medium and prewarmed at 37 °C until cell seeding.

Tissue dissection: A pregnant wild type C57BL/6 mouse was anesthetized with CO_2/O_2 gas mixture (80% CO_2, 20% O_2) and killed with a lethal dose of 100% CO_2. Embryos at day 16 (E16) of embryonic development were isolated from the uterus, placed in a petri dish with 25 ml cold Hanks Balanced Salt Solution without Ca^{2+}, Mg^{2+} (HBSS) and the embryo sack removed. After quickly decapitating the embryos, the heads were collected in 2 ml cold HBSS. To isolate the brains, the heads were pinned to a plate and the skull opened with one cut between the eyes and another along the longitudinal fissure. The brains were transferred with a spatula into 2 ml of fresh HBSS. Next, the meninges were removed under 4-10× magnification, the hemispheres separated from the brain stem and the cortical tissue isolated and collected in 10 ml cold HBSS.

Tissue dissociation: HBSS was removed and replaced with prewarmed 0.05% Trypsin + EDTA and incubated at 37 °C for 6 min. After the tissue settled down, the digestion solution was replaced by 1 ml prewarmed PNGM and dissolved by pipetting up and down with a 1,000 µl pipette, followed by another 15 times pipetting up and down with a Pasteur glass pipette for complete dissociation. The tube was filled up to 10 ml with prewarmed PNGM and counted with a disposable hemocytometer. For counting, the single cell suspension was diluted 1:1 with filtered Trypan-Blue in PBS (1:10) to visualize dead cells, which were excluded from the calculation. Primary cortical neurons were seeded at a cell density of 80,000 cells cm^{-2} and cultured in at 37 °C, in 5% CO_2.

2.2.6 Transduction of primary cortical neurons

Primary neuronal cultures were transduced at 7 days *in vitro* (DIV7) by dissolving an rAAV in prewarmed PNGM with a multiplicity of infection (MOI) of 50,000. The MOI was calculated based on the WPRE-specific titer.

2.2.7 AAV delivery and analysis of transduction efficiency in mice

rAAV production and delivery: rAAVs were produced at the UKE vector facility and vector genomes (vg) determined via qPCR. The rAAV-dosage was calculated by using the WPRE-specific titer. Primers for titer determination (WPRE: Fwd – CCGTTGTCAGGCAACGTG; Rev – AGCTGACAGGTGGTGGCAAT). rAAV dosages in the range of 10^{11}–10^{12} vg/animal were diluted in 100 µl PBS and injected retrobulbar into 8-week-old female C57BL/6 wild type mice. During the procedure the mice were anethetized with isoflurane. Full transgene expression was observed 2–4 weeks after rAAV-injection.

Nuclei isolation for analysis of transduction efficiency: Mice were anesthetized with CO_2/O_2 gas mixture (80% CO_2, 20% O_2) and killed with a lethal dose of 100% CO_2. Mice were intracardially perfused with 10 ml ice-cold PBS and the respective tissue harvested and postfixed in 4% PFA in PBS overnight. The transduction efficiency was quantified by flow cytometry as the frequency of $EGFP^+$ nuclei in $NeuN^+$ nuclei. Briefly, the tissue was homogenized in 2 ml cold nuclei lysis buffer and with a 5 ml glass douncer, first 25 times with a loose pestle, followed by 20 times with a tight pestle. After 5 min incubation on ice, the sample was centrifuged (500*g*, 5 min, 4 °C), the supernatant discarded, and the sample resuspended in 2 ml nuclei lysis buffer by vortexing. After 5 min incubation on ice the sample was centrifuged (500*g*, 5 min, 4 °C), and the cell pellet resuspended in 2 ml cold nuclei incubation buffer. After another centrifugation step (500*g*, 5 min, 4 °C), the cell pellet was resuspended in 500 µl nuclei incubation buffer and filtered through a cell strainer into a FACS tube. The cell strainer was

rinsed with an additional 500 µl of nuclei incubation buffer. The nuclei were centrifuged (1500*g*, 5 min, RT), stained with primary labelled rabbit anti-NeuN-AF647 (1:500) antibody and Hoechst (1:500) and incubated for 30 min. The nuclei were washed with 1 ml nuclei incubation buffer, centrifuged (500*g*, 5 min, RT), and resuspended in 300 µl nuclei incubation buffer for analysis with the BD FACSymphony A3 analyzer.

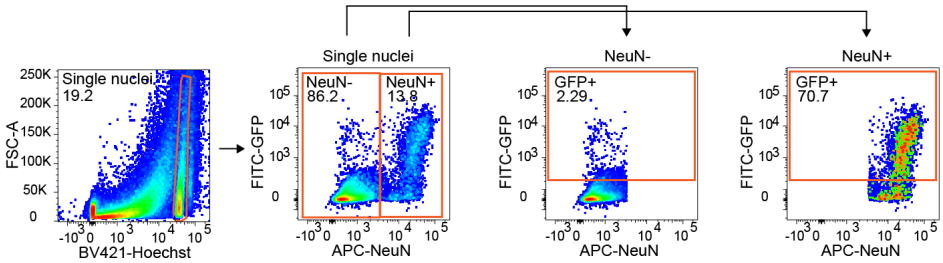

Figure 2.1: Gating Strategy for quantification of transduction efficiency.
Single nuclei were identified by gating Hoechst against the cell size (FSC-A) and further divided in NeuN$^-$ and NeuN$^+$ nuclei. The transduction efficiency was determined by gating GFP against NeuN in NeuN$^-$ and NeuN$^+$ nuclei. Gating is depicted in representative image of the thoracic spinal cord and analyzed analogous for the cortex. For the transduction efficiency in the peripheral organs, Liver, kidney, heart, spleen, and inguinal lymph nodes, NeuN was not included.

2.2.8 EAE induction and scoring

EAE Immunization: The mice were anesthetized with isoflurane and EAE was actively induced by administration of two subcutaneous 100 µl injections into each flank of a 1:1 emulsion of MOG_{35-55} peptide in PBS (2 mg ml^{-1}) and complete Freund's adjuvant with 2 mg ml^{-1} *Mycobacterium tuberculosis*. Moreover, 300 ng pertussis toxin solved in ddH_2O and diluted in 100 µl PBS, were injected intraperitoneally directly after the immunization and after 48 hours.

EAE scoring: Animal weight, general constitution and the clinical disease score were documented daily, starting six days after immunization for a maximum of 30 days. The score was determined according to the following 5-point scoring system: 0, no clinical deficits; 1, tail weakness; 2, hind limb paresis; 3, partial hind limb paralysis; 3.5, full hind limb paralysis; 4, full hind limb paralysis and forelimb paresis; 5, premorbid or dead. Animals were sacrificed when they reached one of the following termination criteria according to regulations of the Animal Welfare Act. Animals were sacrificed, when they reached a clinical score ≥ 4, when they had a clinical score of 3.5 for more than 7 days or when they lost more than 25% of their starting weight. For EAE experiments with neuronal PD-L1, CD200 and memIL-10 delivery, animals that did not get sick were excluded from the analysis. For EAE experiments with neuronal GDF-15 or IL-10 delivery, animals that did not get sick were included, because the treatment itself led to a complete reduction of the EAE phenotype. For all EAE experiments, missing data of animals which had to be sacrificed before day 30 after EAE induction due to reaching termination criteria, was imputed by calculation of the average group value.

Refinement: With the display of the first clinical EAE symptoms, the mouse cages were equipped with a fabric mat to provide additional grip, and thereby support mobility of affected mice in the cage. Additionally, mice were fed with recovery gel and food pellets that were pre-soaked with water directly in the cage, which was refilled daily to secure food and water access with decreasing mobility of the mice. Moreover, mice were injected subcutaneously with 200 µl of 0.9% NaCl solution, when losing ≥ 20% of their bodyweight, as a significant portion of observed weight loss in EAE animals is caused by dehydration.

2.2.9 Immune cell isolation from murine tissue

The mice were anesthetized with CO_2/O_2 gas mixture (80% CO_2, 20% O_2) and killed with a lethal dose of 100% CO_2. Mice were intracardially perfused with 10 ml ice-cold PBS and the respective tissue harvested.

Central nervous system: The complete brain and spinal cord were collected and transferred into 2 ml tubes with cold PBS and stored on ice. The tissue was mechanically dissociated with a scalpel, transferred into 50 ml falcon tubes with 5 ml CNS digestion solution and incubated in a shaking water bath at 37 °C for 45 min. The plunger of a 2 ml syringe was used to grind the tissue through a 70 µm cell strainer into a 50 ml falcon tube with and was rinsed with 20 ml cold PBS. The tissue was centrifuged (500*g*, 5 min, 4 °C) and resuspended in 4 ml Percoll B solution (1.33 ml 90% Percoll + 2,67 ml RPMI medium) and underlay with 2 ml Percoll A (1.56 ml 90% Percoll + 0.44 ml PBS). By mixing 10× PBS with Percoll (1:10) 90% Percoll was prepared. The gradient was centrifuged (2500 rpm, 30 min, 4 °C, acceleration 1, deceleration 1) and isolated immune cells were collected from the interphase with a 1000 µl pipette. The immune cells were washed with 15 ml cold PBS in a 15 ml falcon tube, centrifuged (1800 rpm for 10 min, 4 °C) and resuspended in 1 ml cold PBS.

Lymph nodes: Inguinal lymph nodes were collected and transferred into 2 ml tubes with cold PBS. To generate single cell suspensions, the tissue was grinded through a 40 µm cell strainer into a 50 ml falcon tube with the plunger of a 2 ml syringe and rinsed with 20 ml cold PBS. After centrifugation (500*g*, 5 min, 4 °C) the cell pellet was resuspended in 1 ml cold PBS and stored on ice.

Spleen: The spleen was collected and transferred into 2 ml tubes with cold PBS. To generate single cell suspensions, the tissue was grinded through a 40 µm cell strainer into a 50 ml falcon tube with the plunger of a 2 ml syringe and rinsed with 20 ml cold PBS. After centrifugation (500*g*, 5 min, 4 °C) an erylysis step was performed by addition of 3 ml erylysis buffer per

sample and incubation for 2 min at RT. The reaction was stopped by adding 20 ml of cold PBS. After centrifugation (500*g*, 5 min, 4 °C), the cell pellet was resuspended in 5 ml cold PBS and stored on ice.

2.2.10 Flow cytometry

All flow cytometry panels, were compensated by using Ultracomp eBeads™compensation-beads.

Surface staining: For the staining of surface antigens the samples were transferred into 5 ml FACS tubes with 2 ml cold PBS, centrifuged (1500*g*, 5 min, RT), and the cell pellet was resuspended in 50 µl of 2× master mix with live/dead stain (1:500) and Fc-block (1:250) in PBS. After incubation for 10 min at 4 °C, and addition of 50 µl 2× surface staining master mix in FACS buffer, containing the respective antibodies, samples were incubated for another 20 min at 4 °C in the dark. After washing the cells with 2 ml FACS buffer and centrifugation (1500*g*, 5 min, RT), cells were either resuspended in 300 µl FACS buffer for analysis with the BD FACSymphony A3 analyzer or it was proceeded with either the intracellular or intranuclear staining protocol.

Intracellular staining: Intracellular staining was performed by using the BioLegend intracellular staining kit. After live/dead and surface staining, the samples were fixed by adding 100 µl BioLegend fixation buffer and vortexing. The cells were incubated for 20 min at RT and washed with 1 ml Perm buffer. After centrifugation (1500*g*, 5 min, RT) the cells were resuspended in 100 µl intracellular antibody master mix in 1× Perm buffer and incubated for 30 min at RT. After another washing step with 1 ml Perm buffer and subsequent centrifugation, the cells were resuspended in 300 µl FACS buffer for analysis with the BD FACSymphony A3 analyzer.

Intranuclear staining: Intranuclear staining was performed by using the Foxp3/Transcription Factor Staining Buffer Set. After live/dead and surface staining, the samples were fixed by adding 200 µL fresh 1× FixPerm-Solution (4× FixPerm Conc diluted with FixPerm Diluent) and vortexed. The cells were incubated for 30 min at RT and washed with 1 ml Perm buffer. After centrifugation (1500*g*, 5 min, RT) the cells were resuspended in 100 µl intranuclear antibody master mix in 1× Perm buffer and incubated for 60 min at RT. After another washing step with 1 ml Perm buffer and subsequent centrifugation, the cells were resuspended in 300 µl FACS buffer for analysis with the BD FACSymphony A3 analyzer.

Intracellular staining of phosphoproteins: For the staining of intracellular phosphoproteins, the cells were harvested with a multichannel pipette and transferred to 0.4 ml of a prewarmed 1× Foxp3 Fixation/Permeabilization working solution, vortexed briefly and incubated for 30 min at RT. After 30 min the cells were shortly vortexed and resuspended in 0.4 ml of True-Phos Perm buffer pre-chilled to −20 °C and incubated for 60 min at 4 °C. The cells were centrifuged (1500*g*, 5 min, RT) and washed with 1 ml of 1× Perm/Wash buffer, centrifuged again (1500*g*, 5 min, RT) and resuspended in 50 µl antibody master mix in 1× Perm/Wash buffer. Cells were washed in 1 ml FACS buffer and resuspended in 300 µl FACS buffer for acquisition on the BD FACSymphony A3 analyzer.

2.2.11 Broad immune cell phenotyping

Single cell suspensions of isolated CNS-infiltrating immune cells were generated as described in 2.2.9 and stained as described in 2.2.10. For TruCount-based cell quantification 10% of the sample was used. The remaining sample was used for a broad phenotyping of CNS-infiltrating immune cells.

TruCount cell quantification: To quantify immune cell counts of CNS-infiltrating immune cells, 10% of the generated single cell suspension, were washed with 2 ml PBS and transferred to a TruCount tube. Cells were centrifuged (1500*g*, 5 min, RT) and resuspended in 100 µl of primary labelled anti-CD45-FITC (1:200) antibody and Fc receptor block in PBS for 30 min at 4 °C in the dark. Cells were centrifuged (1500*g*, 5 min, RT) and diluted with 300 µl FACS buffer for TruCount-based cell quantification. The total number of $CD45^+$ cells in the respective tissue was quantified as follows: $CD45^+$ cells = (total beads per tube / acquired beads) × (acquired $CD45^+$ cells × dilution factor of 10). Cell counts of individual cell populations were analyzed by initially gating on $CD45^+$ cells and relative calculation to the total number of $CD45^+$ cells.

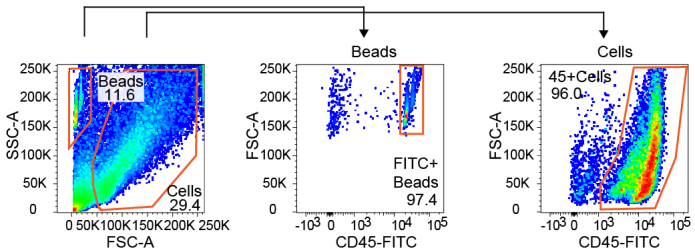

Figure 2.2: Gating Strategy for TruCount-based immune cell quantification.
Lymphocytes and beads were identified according to their size (FSC-A) and granularity (SSC-A). Beads were further gated against CD45-FITC to exclude cellular debris as the beads are detectable in multiple channels including the FITC channel. Cells were further gated against CD45-FITC, and negative cells excluded.

Broad phenotyping of CNS-infiltrating immune cells: The remaining sample was stained to identify CNS-infiltrating immune cells subsets according to the protocol for flow cytometry surface staining, followed by the protocol for intranuclear staining as described in 2.2.10.

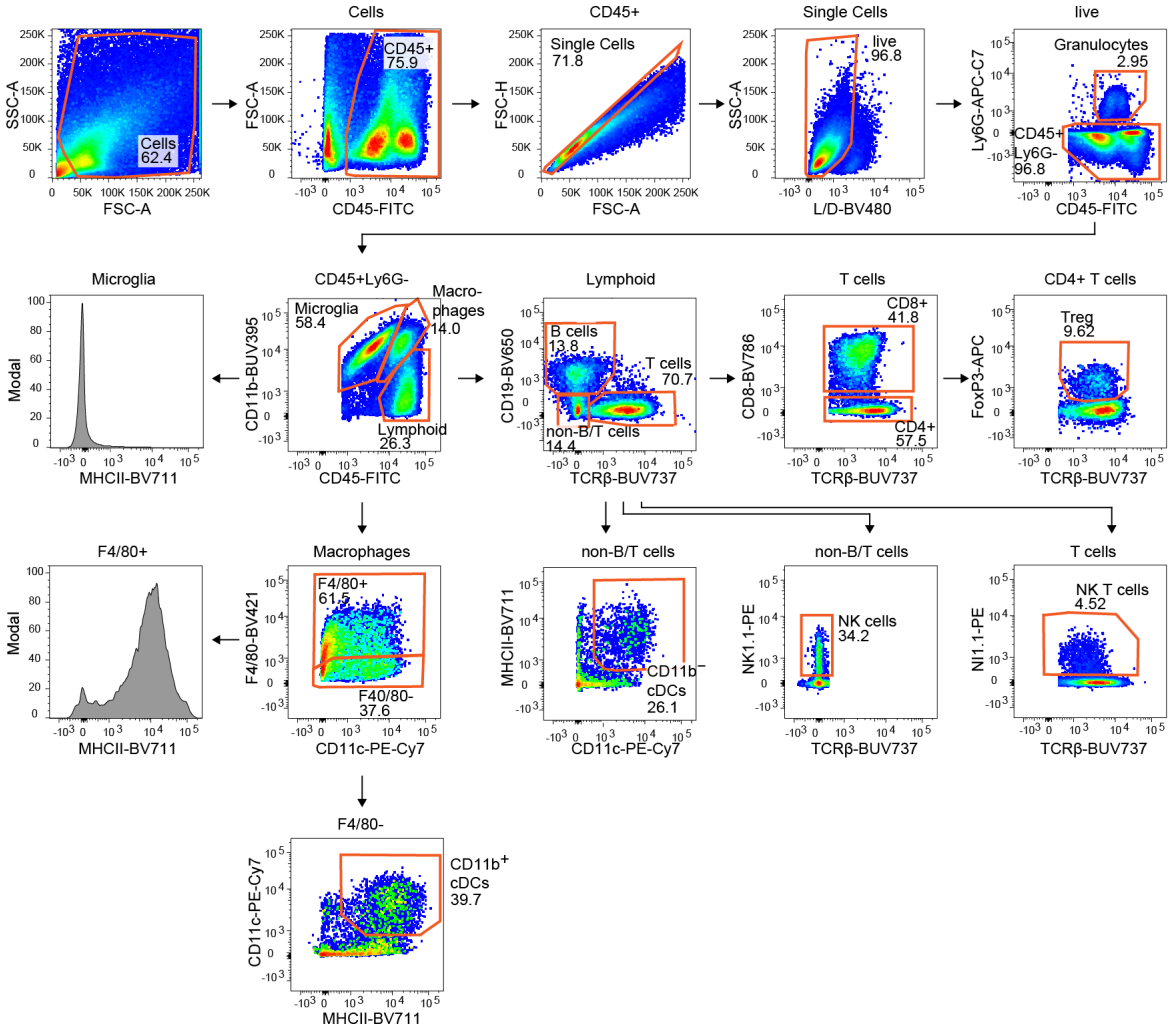

Figure 2.3: Gating Strategy for identification of immune cell subsets in broad phenotyping of CNS-infiltrating immune cells.
Lymphocytes were identified according to their size (FSC-A) and granularity (SSC-A). $CD45^+$ cells were gated as a reference gate for cell count calculation of immune cell subsets. Doublets were excluded by gating FSC height against area. Living cells were identified by excluding the dead stained cells. Further granulocytes were identified by gating $CD45^+Ly6G^+$ cells. Microglia were gated with $CD45^{low}CD11b^+$ and subsequently the MFI of MHCII analyzed. Macrophages were identified by gating $CD45^{high}CD11b^+$ and further excluding $F4/80^-$ cells. Subsequently the MFI of MHCII in macrophages was analyzed. $CD11b^+$cDCs were identified among $F4/80^-$ cells ($CD11c^+MHCII^+$). Lymphocytes were identified by gating $CD45^+CD11b^-$ cells, which were further discriminated in B cells ($CD19^+TCR\beta^-$) and T cells ($CD19^-TCR\beta^+$) and non-B/T cells ($CD19^-TCR\beta^-$). Among the non-B/T cells NK cells ($TCR\beta^-NK1.1^+$) and $CD11b^-$cDCs ($CD11c^+MHCII^+$) were identified. T cells were subdivided in $CD4^+$ T cells ($TCR\beta^+CD8^-$) and $CD8^+$ T cells ($TCR\beta^+CD8^-$). NKT cells ($TCR\beta^+NK1.1^+$) were gated in the T cells. Moreover, Treg ($TCR\beta^+FoxP3^+$) were gated in $CD4^+$ T cells.

2.2.12 Specific T cell phenotyping

Single cell suspensions of isolated CNS-infiltrating immune cells, splenocytes and lymphocytes were generated as described in 2.2.9 and stained as described in 2.2.10. The

single cell suspensions were generated under sterile conditions because the following analysis of the T cell polarization status included an incubation step. For all tissues, 10% of the sample was used for cell quantification with Precision Count Beads. For CNS-infiltrating immune cells 450 µl were used each for analyzing the T cell activation status or the T cell polarization status. For the lymphocytic single cell suspension, 1×10^6 cells were used for analyzing the T cell activation status and 300,000 cells in 100 µl per well for analyzing the T cell polarization status.

Precision Count Bead-based cell quantification: To quantify immune cell counts of CNS-infiltrating immune cells, spleen, and lymph nodes 10% of the generated single cell suspensions, were washed with 2 ml PBS and transferred to a FACS tube. Cells were centrifuged (1500*g*, 5 min, RT) and resuspended in 100 µl of primary labelled anti-CD45-FITC (1:200) antibody and Fc receptor block in PBS for 30 min at 4 °C in the dark. Cells were centrifuged (1500*g*, 5 min, RT) and diluted with 250 µl FACS buffer and 50 µl of Precision Count Beads. The total number of $CD45^+$ cells in the respective tissue was quantified as follows: $CD45^+$ cells = (total beads per tube / acquired beads) × (acquired $CD45^+$ cells × dilution factor of 10).

Phenotyping of T cell activation status: From the single cell suspensions 1×10^6 cells were stained to identify immune cells subsets according to the protocol for flow cytometry surface staining, followed by the protocol for intranuclear staining. $CD4^+$ and $CD8^+$ T cells were identified as shown in Figure 2.3.

Phenotyping of T cell polarization status: Two wells per sample were seeded into a 96-well U-shape plate in 100 µl T cell medium and stimulated at 37 °C for 5 h with 100 µl of 40 ng ml^{-1} PMA, 2 µg ml^{-1} Ionomycin and 2× Brefeldin A in T cell medium. The cells were transferred to a 5 ml FACS tube and stained as described in 2.2.10. $CD4^+$ and $CD8^+$ T cells were identified as shown in Figure 2.3.

2.2.13 Antigen recall assay

EAE mice at day 9 post induction were anesthetized with CO_2/O_2 gas mixture (80% CO_2, 20% O_2), killed with a lethal dose of 100% CO_2 and intracardially perfused with 10 ml ice-cold PBS, prior to harvesting the inguinal lymph nodes and generating single cell suspensions as described in 2.2.9. under sterile conditions. The cells were diluted 1:20 with filtered Trypan-Blue in PBS (1:10) to visualize dead cells, counted with a disposable hemocytometer. The concentration adjusted to 3×10^6 living cells ml^{-1} in T cell medium and 100 µl of this suspension added to a U-shaped 96-well plate with four stimulation conditions for each mouse. An

unstimulated control, a low concentration of 2 µg ml^{-1} MOG_{35-55}, a high concentration of 20 µg ml^{-1} MOG_{35-55} and a positive control containing 1 µg ml^{-1} anti-CD3 and 1 µg ml^{-1} anti-CD28, were incubated with the isolated lymphocytes for 54 h at 37 °C. The surrounding wells were filled with PBS to prevent evaporation. The cells were pulsed with BrdU with a final concentration of 1 µg ml^{-1} 16 h prior to harvesting into a FACS tube with 2 ml of cold PBS. After centrifugation (1500*g*, 5 min, RT), the supernatant was discarded, and the cells resuspended in 100 µl master mix of live/dead APC-Cy7 (1:1000) and Fc-Block (1:500) in PBS, followed by a washing step with 2 ml FACS buffer after 20 min incubation at 4 °C and subsequent centrifugation (1500*g*, 5 min, RT). The cells were permeabilized with 500 µl 0.5% Triton-X 100, vortexed and incubated for 15 min at RT. The samples were washed with 2 ml PBS with Ca^{2+} and Mg^{2+}, centrifuged (1500*g*, 5 min, RT) and resuspended in 500 µl DNase I solution (20 µg DNase I/tube). The tubes were sealed with parafilm and incubated at 37 °C for 60 min. After washing the samples with 1× Perm buffer and centrifugation (1500*g*, 5 min, RT), the cells were resuspended in anti-BrdU-FITC staining master mix in Perm buffer (1:20) and incubated for 60 min at RT in the dark. After another washing step with Perm buffer and centrifugation (1500*g*, 5 min, RT), the cells were resuspended in 300 µl FACS buffer and analyzed with the with the BD FACSymphony A3 analyzer.

2.2.14 Immunocytochemistry

Sample preparation: For immunocytochemistry stainings, 24-well plates with coverslips were coated with PDL in PBS (1:500) overnight, washed twice with PBS, filled with 500 µl cell culture medium per well, and pre-warmed at 37 °C. Cell seeding and culturing was performed according to the respective cell type as previously described.

ICC surface staining: Coverslips with the cells were carefully washed twice with cold PBS, taken out of the well with forceps and placed on a piece of parafilm upside up. The primary antibody master mix in 10% NDS in PBS was added directly on the coverslip and incubated for 30–45 min at 4 °C in the dark. The coverslips were placed back into their well and washed gently two times with cold PBS.

ICC whole cell staining: After washing the cells twice with cold PBS, the cells were fixed by adding 4% PFA in PBS for 15 min at RT. The cells were washed twice with PBS and permeabilized with 500 µl 0.5% Triton-X100 per well for 2.5 min at RT. After washing two times with PBS, a blocking solution of 10% NDS in PBS was added for 30 min incubation at RT in the dark. The coverslips were placed upside down on 35 µl primary antibody master mix in 10% NDS in PBS on parafilm and incubated for 2 h at RT in the dark. After washing two times

with PBS in the 24-well plate, the secondary antibody staining was performed as described for the primary antibody by placing the coverslips upside down on 35 µl secondary antibody master mix in 10% NDS in PBS on parafilm, followed by incubation for 1 h at RT in the dark. After washing two times with PBS and an additional washing step with ddH_2O, coverslips were mounted face down on a glass slide with Immu Mount, let dry overnight at RT and stored at 4 °C until imaging with a confocal microscope (Zeiss, LSM 700) equipped with a 405 nm, 488 nm, 555 nm, and 647 nm laser. Pictures were generated under 40× or 63× magnification, using the ZEN2012 software. The Images were further processed with ImageJ.

2.2.15 Immunohistochemistry

Tissue preparation: Mice were intraperitoneally anesthetized with an overdose (15 µl g^{-1} bodyweight) of Ketamine/Xylazine (12 mg ml^{-1}/ 1.6 mg ml^{-1}) in PBS. Toe reflexes were tested after 5 – 15 min before intracardial perfusion to ensure sufficient anesthesia. Mice were perfused for 2 min with cold PBS (~ 10 ml), followed by 5 min with 4% PFA in PBS (~25 ml). Complete brain and cervical spinal cords were dissected carefully and post-fixed in a 15 ml tube with cold 4% PFA in PBS for 30 min on ice. The PFA was discarded and replaced with 30% saccharose in PBS for 2 days at 4 °C for dehydration and cryo-protection. The tissue was frozen in embedding solution (Tissue-Tek® O.C.T.™ compound) at −80 °C and cut into 12 µm thick transversal cryosections with a cryostat and stored at −80 °C until staining.

Staining procedure and imaging: After warming to RT and drying, cryosections on the same glass slide were separated with a liquid blocker pen, to allow simultaneous staining of different marker combinations. Following permeabilization and blocking for 45 min in 5% NDS with 0.25% Triton-X100 at RT, the blocking solution was removed, and slices were washed with PBS for 5 min, and incubated with the primary antibody master mix overnight at 4 °C (2.5% NDS in PBS with 0.1% Triton-X100). After washing three times with PBS for 5 min, the cryosections were incubated for 3 h with the secondary antibody master mix (2.5% NDS in PBS with 0.1% Triton-X100). The slices were washed three times with PBS for 5 min and once with ddH_2O and mounted with Immu Mount, let dry overnight at RT and stored at 4 °C until imaging with a confocal microscope (Zeiss, LSM 700) equipped with a 405 nm, 488 nm, 555 nm, and 647 nm laser. Pictures were generated under 40× or 63× magnification, using the ZEN2012 software. The Images were further processed with ImageJ.

2.2.16 ELISA

Sample generation: To analyze IL-10 protein levels from cortical tissue lysates and EDTA-plasma samples, mice were anesthetized with CO_2/O_2 gas mixture (80% CO_2, 20% O_2), killed

with a lethal dose of 100% CO_2. Prior to perfusion with 10 ml ice-cold PBS, blood was drawn from the vena cava, transferred into blood collection micro tube. Plasma samples were generated by centrifugation (10,000*g*, 10 min 4 °C) and the supernatant was stored at −80 °C until analysis. After the perfusion the prefrontal cortex (PFC) was collected into a 1.5 ml tube, snap frozen in liquid nitrogen and stored at −80 °C until analysis.

Cortical tissue lysates: Cortical tissue lysates from snap frozen tissue were generated by dissociation in ELISA tissue extraction buffer in a 2 ml tube. Tissue weight was determined, and the volume of extraction buffer was adjusted to 500 µl/100 µg tissue. After mechanic dissociation with a 7 mm stainless steel bead and homogenization at 50 Hz for 2 min, the samples were centrifuged (16,000*g*, 10 min, 4 °C) and the supernatant was stored at −80 °C until analysis.

IL-10 ELISA: The IL-10 protein levels in tissue and plasma were determined by using the ELISA MAX™ Deluxe Set Mouse IL-10 Kit, according to the manufacturer's instructions. All washing steps were performed by addition of 300 µl ELISA wash buffer four times under shaking. Incubation times were conducted at RT under shaking unless indicated otherwise. One day prior to analysis, the capture antibody was diluted in 1×Coating Buffer B, added to a flat-bottomed 96-well plate and incubated overnight at 4 °C. Plates were washed and unspecific binding sites blocked with 200 µl 1×Assay Diluent A per well for 1 h. Plates were washed, and IL-10 standard or samples added to the appropriate wells and incubated for 2 h. After another washing step 100 µl of diluted detection antibody were added to each well and incubated for 1 h. Plates were washed and 100 µl Avidin-HRP were added to each well and incubated for 30 min. The plates were washed five times and incubated with 100 µl TMB substrate solution in the dark for 20 min. The reaction was stopped by addition of 100 µl ELISA stop solution and the absorbance at 450 nm and 570 nm was measured within 15 min on a multi-well plate reader (Tecan). IL-10 protein levels below the detection limit were plotted with a value of 0.

GDF-15 ELISA: The GDF-15 protein levels in tissue and plasma were determined by using the kit for human GDF-15 (R&D system) analogous to the IL-10 ELISA protocol. The detection antibody was replaced by an in-house generated GDF-15 antibody (Jörg Wischhusen, UK Würzburg). GDF-15 protein levels below the detection limit were plotted with a value of 0.

2.2.17 Western blot

Sample generation from N2a cells: N2a cells were seeded in 6-well plates at a density of 50,000 cells cm^{-2} and transiently transfected the following day. The transfected cells were harvested 24 h later by washing them twice with cold PBS, followed by incubation with PBS supplemented with 1 mM EDTA for 5 min. The cells were transferred into a 1.5 ml tube and centrifuged (5000*g*, 5 min, 4 °C). The cell pellet was quickly frozen on dry ice and stored at −80 °C until cell lysis. For cell lysis, 200 µl RIPA buffer were added to the cell pellet. The samples were homogenized by sonification and incubated for 30 min at 4 °C on a rotating wheel. After centrifugation the supernatant was transferred to a new 1.5 ml tube and stored at −80 °C until analysis.

BCA assay for determination of protein concentration: To determine the sample protein concentration the Pierce™ BCA Protein Assay Kit was used. 10 µl of standard (Pierce™ Bovine Serum Albumin Standard Ampules, 2 mg ml^{-1}) and diluted samples were added onto a flat-bottomed 96-well plate as well as 200 µl BCA reagent (196 µl Reagent A+ 4 µl Reagent B). The plate was incubated at 37 °C for 30 min in the dark and the absorbance at 562 nm measured on a multi-well plate reader (Tecan).

Sample generation from PFA fixed tissue: Cortical tissue of mice that was initially intended for IHC analysis and therefore fixed with 4% PFA and embedded in tissue tek, was used for WB analysis according to a modified protocol for protein detection from fixed brain tissue (Thacker *et al.* 2020). As the modified tissue lysis buffer for fixed tissue is incompatible with protein determination by BCA assay, similar protein concentrations per sample were achieved by adjusting the volume of lysis buffer to 500 µl/ 100 µg tissue. After mechanic dissociation with a 7 mm stainless steel bead and homogenization at 50 Hz for 2 min, the samples were centrifuged (1000*g*, 10 min, 4 °C). The supernatant was transferred to a new 1.5 ml tube and stored at −80 °C until analysis.

Western blot: The samples were reduced by heating them to 70 °C for 10 min with reducing agent and sample buffer. For N2a cell lysates the reducing mix was adjusted to 1 µg $µl^{-1}$ and of tissue lysates from fixed tissues 10 µl/ 100 µl reducing mix were used. 10 µl of each reduced sample was loaded onto a 4–12% Bis Tris Plus Gel with 10 wells. Proteins were separated at 165 V for 1 h and subsequently transferred onto a PVDF membrane for staining at 10 V for 1 h. Unspecific binding of the membrane was blocked with blocking solution, consisting of 5% BSA in TBS-T for 1 h at RT under shaking. The membrane was cut along the 65 kDa band and the upper membrane part was stained for the housekeeping protein vinculin, while the

lower membrane part was used for staining PD-L1 and incubated in the primary antibody master mix overnight at 4 °C (5% BSA in TBS-T) under rotation in a 50 ml falcon. The membrane was washed with TBS-T 4 times for 5 min under shaking and incubated at RT for 1 h in secondary antibody in blocking solution (5% BSA in TBS-T) under shaking. The washing step was repeated, and the membrane was imaged with a CCD camera (ImageQuant™LAS4000mini) using a mixture of 1:1 chemiluminescence substrate in 15 s increment exposure times.

2.2.18 Computational and statistical analysis

Cloning strategies and annealing of sequencing data was done in Benchling (Benchling Inc.). Flow cytometry data was recorded with FACS DIVA and analyzed with FlowJo, Confocal images were recorded with ZEN Black and processed with Fiji software (NIH). Data analysis was done in R within R Studio (Posit Software). The statistical analyses in this study were performed with GraphPad Prism. The error bars represent the standard error of the mean (s.e.m.).

Differences of two experimental groups were determined with a two-tailed Student's *t*-test or with a Mann-Whitney *U* test. Differences in disease incidence were identified with a Fisher's exact test and differences in probability of survival were calculated with a log-rank test. Differences between three or more experimental groups were determined with a one-way analysis of variance (ANOVA) with Tukey's post hoc test. Differences of two or more experimental groups that depend on two variables were determined with a two-way ANOVA with Šidák's post hoc test, in case of comparison to a control condition within each column a two-way ANOVA with Dunnett's post hoc test was used. Significant differences are indicated as $*P < 0.05$; $**P < 0.01$; $***P < 0.001$. *n* represents the number of samples that were used for statistical analyses.

3 Results

3.1 rAAV-based neuronal gene delivery

Targeting the CNS to study the biological role and therapeutic potential of proteins of interest in a neuroinflammatory disease such as MS, remains challenging to date, due to the restrictive nature of the BBB, which is functioning to maintain brain homeostasis. To screen for the capacity of therapeutical effector proteins to protect against neuroinflammatory damage in the EAE mouse model, the two novel serotypes AAV-PHP.eB and AAV.CAP-B10 were compared for their capacity to facilitate neuron-specific transgene delivery *in vivo* after intravenous administration. To deliver neuroprotection to the majority of neurons, the aim was to reach a neuronal transduction efficiency of over 50%.

3.1.1 AAV-PHP.eB serotype for neuronal gene delivery

AAV-PHP.eB is a CNS trophic serotype, which transduces a broad spectrum of CNS resident cell types like neurons, astrocytes, oligodendrocytes, and endothelial cells after intravenous administration[163–165]. To enable neuron-specific targeting, a delivery plasmid was developed that contained a nuclear enhanced green fluorescent protein (EGFP) and the respective effector candidate, separated by a 2A peptide from porcine teschovirus-1 (P2A). This allowed for separate expression of both proteins by ribosomal skipping of the glycyl-prolyl peptide bond formation at the C-terminus of the P2A[247]. To express EGFP in the nucleus, the EGFP was flanked with two nuclear localization sequences (NLS), specifically an N-terminal nucleoplasmin NLS and a C-terminal SV-40 NLS. The delivery plasmid was designed with the neuron-specific human synapsin 1 (*hSyn1)* promoter, to ensure neuron-specific expression (AAV-PHP.eB:*hSyn1*). *hSyn1* was selected due to its relatively small size of 448 bp, compared to other neuron-specific promoters like the *CaMKIIα* promoter with 1289 bp, which is an important factor, considering the limited AAV packaging size of 4.7 kb. Moreover, to explore the general AAV-PHP.eB transduction profile and visualize off-target infection in non-neuronal cells in the CNS and in peripheral organs, an rAAV was generated which expressed NLS-EGFP under the control of the ubiquitous chicken beta-actin (*CAG*) promoter (AAV-PHP.eB:*CAG*).

As a first step, AAV expression tests were conducted by transduction of primary cortical neuronal cultures, followed by immunocytochemistry co-staining of microtubule-associated protein 2 (MAP2) to visualize the dendritic network and the neuronal marker NeuN for neuronal soma. While transduction with AAV-PHP.eB:*hSyn1* resulted in neuron-restricted expression of EGFP (Figure 3.1A), cultures that were transduced with AAV-PHP.eB:*CAG* also displayed EGFP expression in $NeuN^-$ cells, that were most likely astrocytes due to their morphological features (Figure 3.1B).

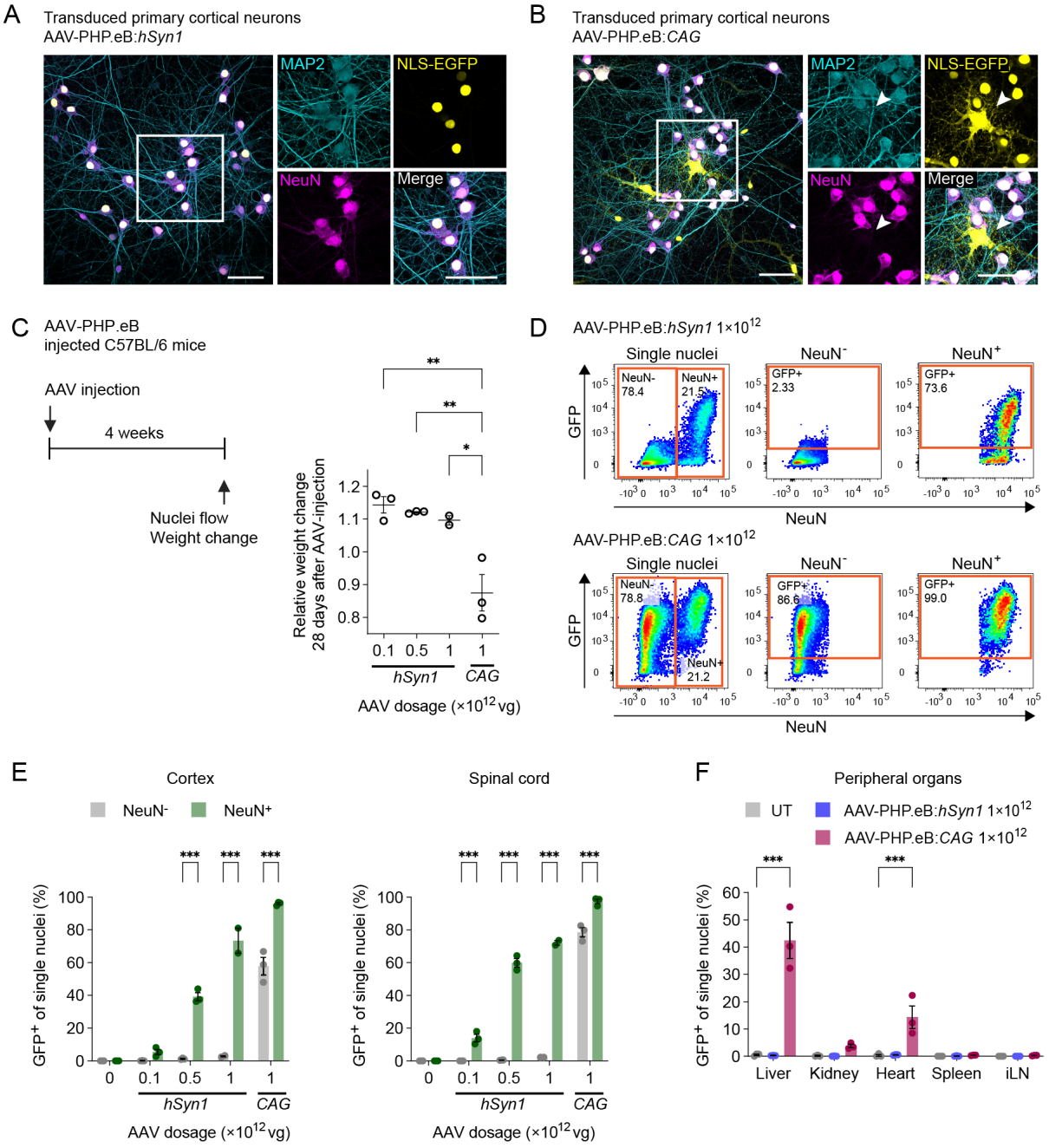

Figure 3.1: Dose dependent, robust, and neuron-specific transduction with AAV-PHP.eB in combination with the *hSyn1* promoter.

(**A**) Immunocytochemistry of primary cortical neurons transduced with AAV-PHP.eB:*hSyn1*-NLS-EGFP (AAV-PHP.eB:*hSyn1*) at a MOI of 50k on DIV7 and stained on DIV14. Co-staining of NeuN (neuronal soma) and MAP2 (dendrites) with endogenous expression of NLS-EGFP. Scale bar, 50 µm. (**B**) Immunocytochemistry of primary cortical neurons transduced with AAV-PHP.eB:*CAG*-NLS-EGFP (AAV-PHP.eB:*CAG*) at a MOI of 50k on DIV7 and stained on DIV14. Co-staining of NeuN (neuronal soma) and MAP2 (dendrites) with endogenous expression of NLS-EGFP. Scale bar, 50 µm. Arrows indicate NeuN$^-$EGFP$^+$ cells. (**C**) Experimental scheme to assess the ideal AAV-PHP.eB dosage for most efficient neuron-specific transduction in C57BL/6 wild type mice. Relative weight change 28 days after AAV injection. Viral titers of 1×10^{11} vg (n = 3), 5×10^{11} vg (n = 3) and 1×10^{12} vg (n = 2) for AAV-PHP.eB:*hSyn1* and 1×10^{12} vg (n = 3) for AAV-PHP.eB:*CAG* were used. (**D**) Representative flow cytometry gating to assess transduction efficiency. The transduction efficiency was determined by gating EGFP$^+$ in NeuN$^+$ and NeuN$^-$ nuclei. (**E**) Flow cytometry analysis of transduction efficiency in NeuN$^+$ and NeuN$^-$ nuclei in cortex and spinal cord 21 days (AAV-PHP.eB:*CAG*) or 28 days (AAV-PHP.eB:*hSyn1*) after AAV injection. (**F**) Flow cytometry analysis of transduction efficiency of peripheral organs. UT, untreated. Data is shown as mean values ± s.e.m. Statistical analyses were performed by one-way ANOVA with Tukey's post hoc test in **C** and two-way ANOVA with Šidák's post hoc test in **E** and two-way ANOVA compared to UT with Dunnett's post hoc test in **F**. *P < 0.05; **P < 0.01; ***P < 0.001.

Next, viral titers in the range of 1×10^{11}–1×10^{12} vg/animal of AAV-PHP.eB:*hSyn1* were titrated *in vivo*, while AAV-PHP.eB:*CAG* was tested at 1×10^{12} vg/animal as a positive control. The weight was monitored daily. While mice that received AAV-PHP.eB:*hSyn1* did not display any weight loss or signs of other detrimental effects, AAV-PHP.eB:*CAG* treatment caused over 10% of their starting weight. Consequently, mice that displayed weight loss were sacrificed and analyzed at day 22 after AAV injection (Figure 3.1C). The transduction efficiency and neuronal specificity were analyzed by quantifying $EGFP^+$ in $NeuN^+$ and $NeuN^-$ nuclei via flow cytometry 21 days after AAV-injection (Figure 3.1D). Regarding the efficiency, a robust, dose dependent transduction of up to 100% was observed with AAV-PHP.eB:*CAG,* and up to 75% with AAV-PHP.eB:*hSyn1*, measured as the frequency of $EGFP^+$ in $NeuN^+$ nuclei in the cortex and spinal cord. The two lower AAV titers of 1×10^{11} vg and 5×10^{11} vg, showed a ~3-fold higher transduction efficiency in $NeuN^+$ nuclei of the spinal cord than of the cortex. This difference was not detectable in mice that received the highest AAV dosage of 1×10^{12} vg. This indicates, that with lower AAV dosages, spinal cord neurons were preferentially targeted compared to cortical neurons. While AAV-PHP.eB:*CAG* also transduced 60%–80% of $NeuN^-$ nuclei, AAV-PHP.eB:*hSyn1* displayed a neuron-specific transduction pattern in all investigated dosages, as no EGFP signal in $NeuN^-$ nuclei was detected (Figure 3.1E). To control for potential off-target transduction in the periphery, the expression of nuclear EGFP was tested in a selection of peripheral organs. While no peripheral transgene expression was detected with AAV-PHP.eB:*hSyn1*, animals that were infected with AAV.PHP-*CAG*, ~40% of liver, ~5% of kidney, and ~15% of heart cells showed peripheral off-target transduction, evident as a nuclear EGFP signal. Notably, none of the tested lymphoid organs, spleen and lymph nodes showed off-target transduction, regardless which of both promoters was used (Figure 3.1F).

3.1.2 AAV.CAP-B10 serotype for neuronal gene delivery

The AAV.CAP-B10 serotype was described to yield a CNS-specific transduction pattern with decreased liver targeting and a predominant neuronal transduction at a viral dosage of $1x10^{11}$ vg/animal after intravenous administration[170]. Because the previous experiment revealed the AAV-PHP.eB serotype to be dependent on a neuron-specific promoter to compensate for its broad transduction pattern, AAV.CAP-B10 was next evaluated for neuron-specific transgene delivery. To follow the transduction efficiency, *CAG*-NLS-EGFP, which served as a positive control in the AAV-PHP.eB titration experiment, was used as a transfer plasmid (AAV.CAP-B10:*CAG*). AAV.CAP-B10:*CAG* was tested in primary neuronal cultures, where most transduced cells co-localized with NeuN, however also $NeuN^-$ cells were detected that expressed EGFP, indicating limited neuronal specificity *in vitro* (Figure 3.2A).

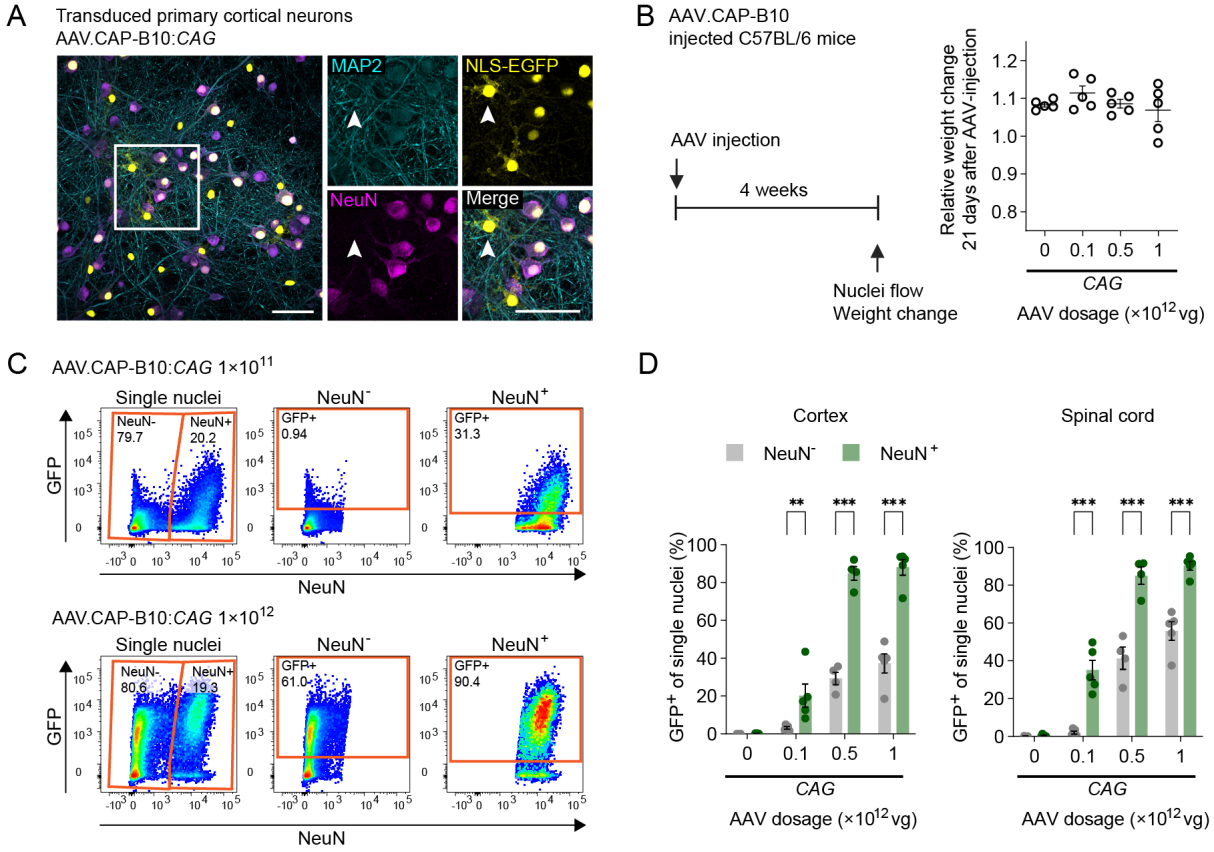

Figure 3.2: **Dose dependent, robust, and neuronally biased transduction with AAV.CAP-B10.** (**A**) Immunocytochemistry of primary cortical neurons transduced with AAV.CAP-B10:*CAG*-NLS-EGFP (AAV.CAP-B10:*CAG*) the respective AAV at a MOI of 50k on DIV7 and stained on DIV14. Co-staining of NeuN (neuronal soma) and MAP2 (dendrites) with endogenous expression of NLS-EGFP. Scale bar, 50 µm. Arrows indicate non-neuronal EGFP expression. (**B**) Experimental scheme to assess ideal AAV.CAP-B10 dosage for most efficient neuron-specific transduction in 8-week-old female C57BL/6 wild type mice and relative weight change 28 days after AAV injection. Viral titers of 1×10^{11} vg (n = 5), 5×10^{11} vg (n = 5) and 1×10^{12} vg (n = 5) were used. (**C**) Representative flow cytometry gating to assess transduction efficiency. The transduction efficiency was determined by gating EGFP$^+$ in NeuN$^-$ and NeuN$^+$ nuclei. (**D**) Transduction efficiency in NeuN$^+$ and NeuN$^-$ nuclei in spinal cord 21 days after AAV injection. Data is shown as mean values ± s.e.m. Statistical analyses were performed by one-way ANOVA with Tukey's post hoc test in **B** and two-way ANOVA with Šidák's post hoc test in **D**.

Next, AAV.CAP-B10:*CAG* was titrated *in vivo* with viral titers in the range of 1×10^{11}–1×10^{12} vg/animal. The weight was monitored daily, and the transduction efficiency and neuronal specificity analyzed by quantifying EGFP$^+$ in NeuN$^+$ and NeuN$^-$ nuclei via flow cytometry, 21 days after AAV-injection. Mice did not display any weight loss or signs of other detrimental effects (Figure 3.2B). By using the medium and high AAV doses of 5×10^{11} and 1×10^{12} vg/animal, up to 90% of NeuN$^+$ nuclei in cortical and spinal cord tissue were targeted, whereas also 40%–60% of non-neuronal cells exhibited a nuclear EGFP signal. Yet only the lowest tested AAV titer of 1×10^{11} vg/animal showed a neuron-specific transduction pattern, however with limited efficiency of ~20% of NeuN$^+$ cells in the cortex and ~30% of NeuN$^+$ cells in the spinal cord. This did not match with the goal of targeting at least 50% NeuN$^+$ cells. (Figure 3.2D).

Based on these systematic AAV titrations, the AAV-PHP.eB serotype in combination with the *hSyn1* promoter in the highest titrated dosage of 1×10^{12} vg/animal, displayed a neuron-

specific and efficient transduction pattern with the least off-target properties and was therefore chosen as default for the following experiments to deliver neuroprotection in the EAE mouse model. An rAAV, expressing *hSyn1*-NLS-EGFP served here as a negative control (AAV-*hSyn1*-NLS-EGFP) and an rAAV, that additionally expressed the respective effector protein, separated by a 2A peptide (AAV-*hSyn1*-NLS-EGFP-P2A-Effector) was used to deliver immune evasion mechanisms to neurons and establish a local immune tolerance.

3.2 Surface proteins as mediator of immune tolerance in the CNS

3.2.1 Delivery of PD-L1 in EAE

To address the neuroprotective potential of the transmembrane protein PD-L1, an overexpression plasmid was generated by molecular cloning to enable neuronal PD-L1 delivery (*hSyn1*-NLS-EGFP-P2A-PDL1). Correct protein localization and sufficient delivery were tested by transient transfection of N2a cells by flow cytometry and western blot.

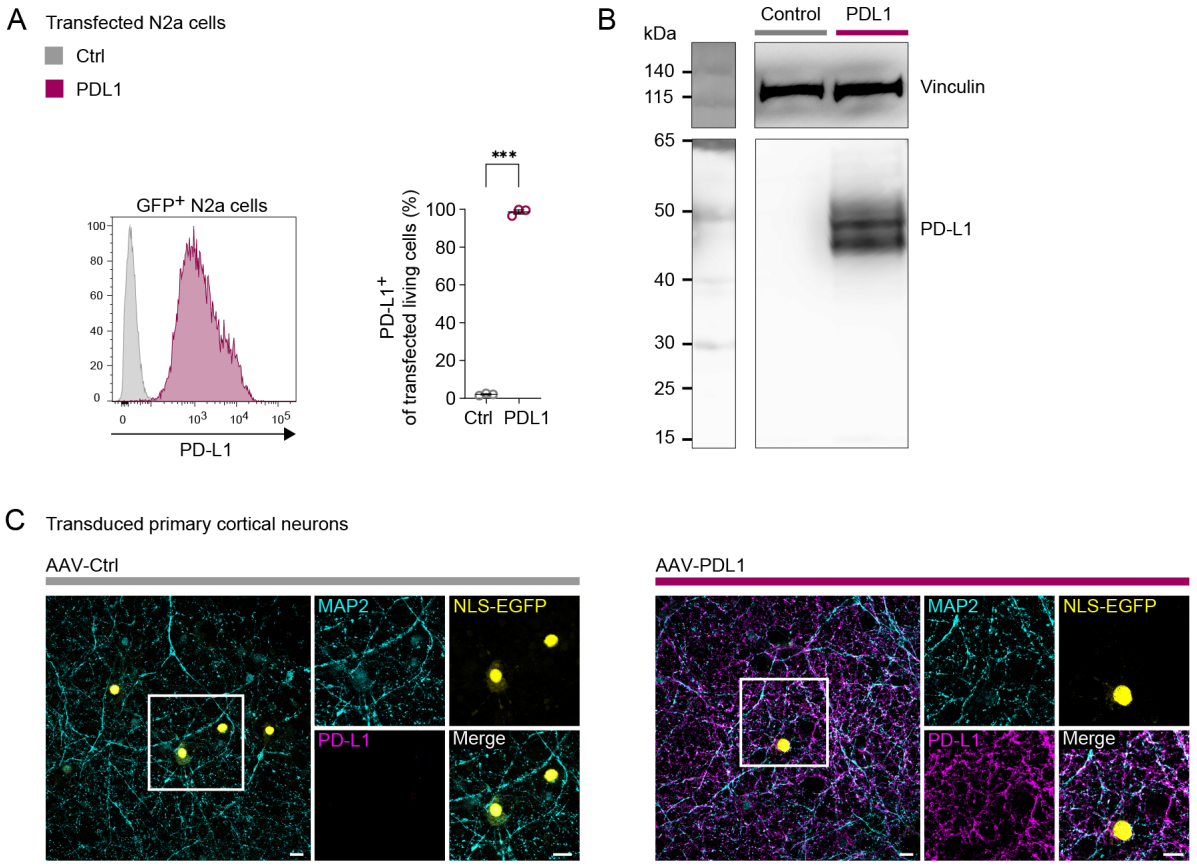

Figure 3.3: Validation of PD-L1 surface expression in N2a cells and primary cortical neurons.
(**A**) Flow cytometry analysis of PD-L1 surface expression 24 h after transient transfection of N2a cells with either *hSyn1*-NLS-EGFP (Ctrl) or *hSyn1*-NLS-EGFP-P2A-PDL1 (PDL1), *n* = 3 per group. (**B**) Western blot of N2a cell lysates 24 h after transfection with Ctrl- or PDL1-delivery plasmid. (**C**) Immunocytochemistry of PD-L1 surface expression after transduction with AAV-Ctrl or AAV-PDL1 on DIV7 at a MOI of 50k and stained on DIV14.Co-staining of PD-L1 with MAP2 (dendrites) and endogenous expression of NLS-EGFP (transduced cell). Scale bar, 10 µm. Data is shown as mean values ± s.e.m. Statistical analysis was performed by paired Student's *t*-test in **A**. **P* < 0.05; ***P* < 0.01; ****P* < 0.001.

PD-L1 surface protein expression was detected in ~100% of transfected N2a cells in the experimental condition, while not present in the control condition (P = 0.002, Figure 3.3A). Moreover, sufficient expression levels of PD-L1 were found in western blot of transfected N2a cell lysates (Figure 3.3B). After the validation of the PD-L1 overexpression plasmid, AAVs were generated. To verify the PD-L1 surface expression after AAV-PD-L1 delivery in primary cortical neurons, an immunocytochemistry surface staining was performed, prior to fixation and subsequent intracellular staining. This revealed a surface expression of PD-L1, which co-localized with dendritic MAP2 staining and was not present in the control condition (Figure 3.3C).

After validation of the correct transgene expression *in vitro*, the next step was to investigate the protective potential of PD-L1 delivery in the neuroinflammatory mouse model EAE. AAV-Ctrl and AAV-PDL1 were injected 28 days before EAE induction in 8-week-old female C57BL/6 wild type mice, to allow full protein expression (Figure 3.4A). The animal weight and health were monitored daily until EAE induction to discover possible detrimental effects of neuronal PD-L1 delivery.

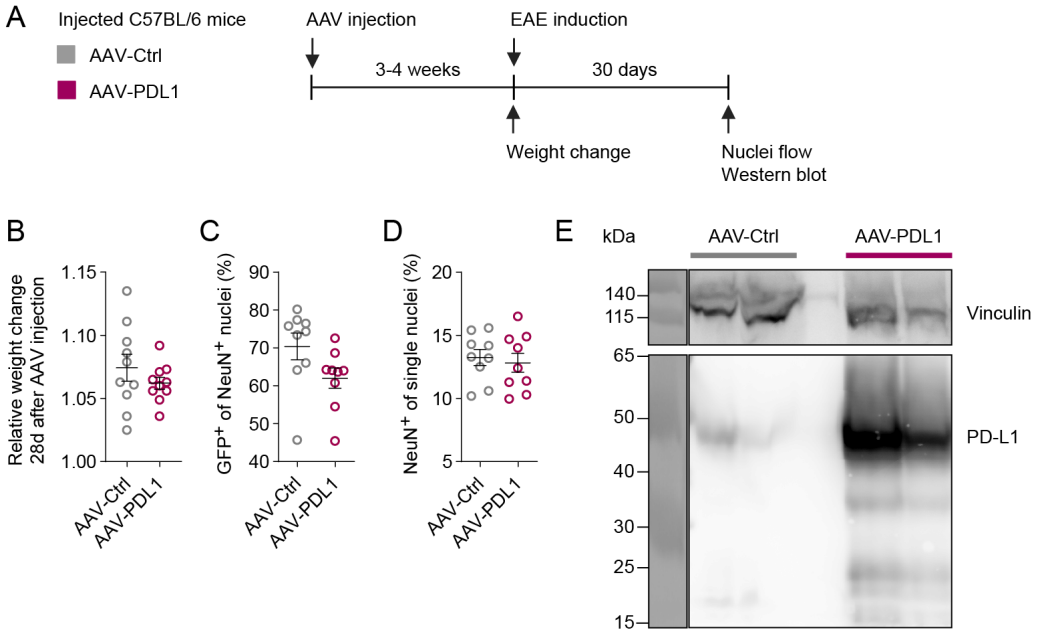

Figure 3.4: Validation of neuronal PD-L1 delivery in d30 EAE animals.
(**A**) Scheme for experimental setup to assess effects of AAV-mediated neuronal PD-L1 delivery. C57BL/6 wild type mice were injected with either AAV-*hSyn1*-NLS-EGFP (AAV-Ctrl) or AAV-*hSyn1*-NLS-EGFP-P2A-PDL1 (AAV-PDL1). Viral titers of 1×10^{12} vg were used (n = 10 mice per group). (**B**) Relative weight change, 28 days after AAV injection. (**C**) Flow cytometry analysis of transduction efficiency, measured as the frequency of EGFP$^+$ in NeuN$^+$ nuclei. (**D**) Flow cytometry analysis of NeuN$^+$ of single nuclei in thoracic spinal cord. (**E**) Western blot of two representative animals per group of cortical tissue lysates. Data is shown as mean values ± s.e.m. Statistical analyses were performed by unpaired Student's *t*-tests in **B**–**D**. *P < 0.05; **P < 0.01; ***P < 0.001.

However, the mice did not display any weight loss or signs of other detrimental effects (Figure 3.4B). To control for comparable transduction efficiency of the two experimental groups, the frequency of EGFP$^+$ in NeuN$^+$ nuclei was quantified in the spinal cord at the end of the

experiment on day 30 after EAE induction. Mice showed a consistent neuronal transduction efficiency of 60–70% (Figure 3.4C). Moreover, the frequency of $NeuN^+$ neuronal nuclei was similar in both groups (~13–14%), which excludes profound neuronal loss by PD-L1 delivery (Figure 3.4D). Further western blot validation of the PD-L1 delivery in two representative mice of each group, showed a strong PD-L1 expression in the mice which received AAV-PDL1, but only low expression in AAV-Ctrl mice (Figure 3.4E). In summary, a robust PD-L1 delivery was observed without indication of detrimental side effects of the AAV treatment.

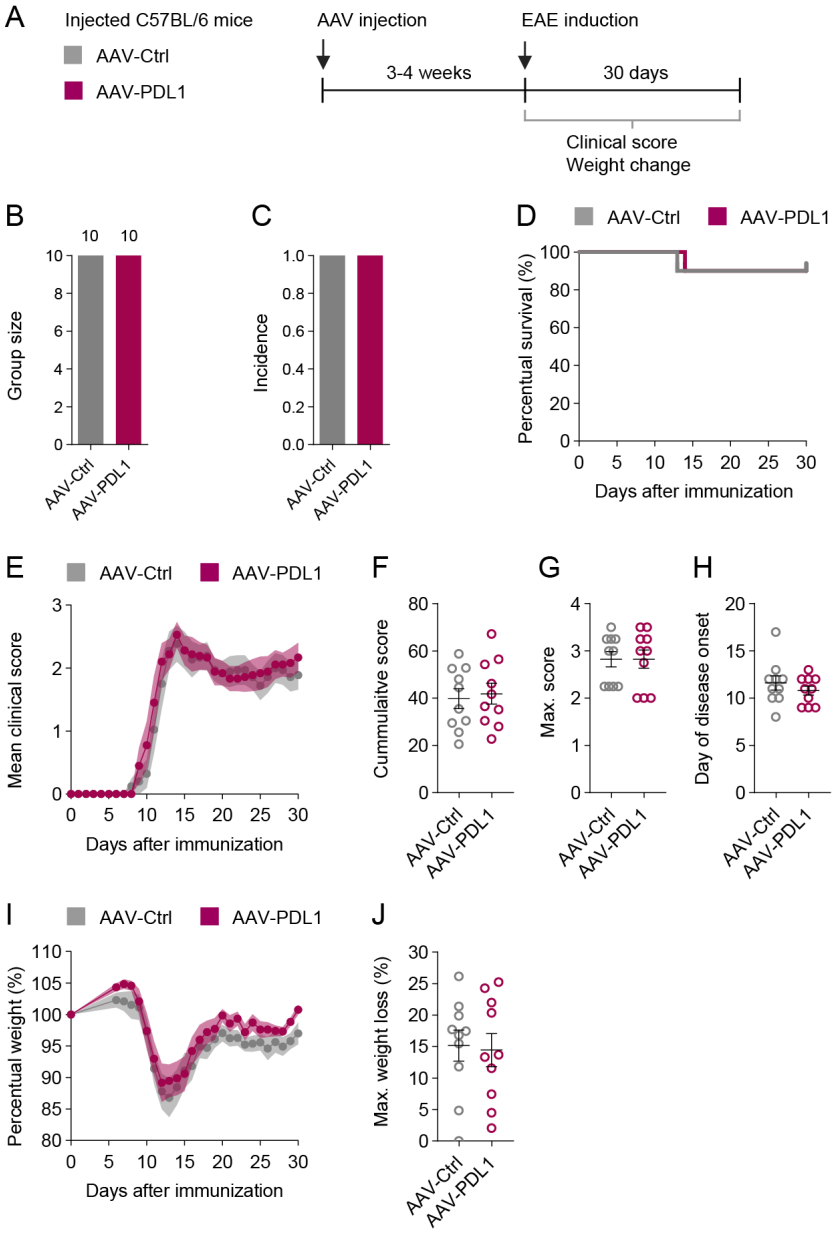

Figure 3.5: Neuronal PD-L1 delivery does not rescue EAE phenotype.
(**A**) Experimental setup to test protective potential of neuronal PD-L1 delivery in EAE. C57BL/6 wild type mice were injected with either AAV-*hSyn1*-NLS-EGFP (AAV-Ctrl) or AAV-*hSyn1*-NLS-EGFP-P2A-PDL1 (AAV-PDL1). Viral titers of 1×10^{12} vg were used. (**B**) Group size (AAV-Ctrl, $n = 10$; AAV-PDL1, $n = 10$). One representative experiment of two with similar results is shown. (**C**) Disease incidence. (**D**) Kaplan Meier plot of probability of survival in percent during EAE course. (**E**) Clinical disease course. (**F**) Cumulative scores. (**G**) Maximal EAE score. (**H**) Day of disease onset. (**I**) Change of bodyweight. (**J**) Maximal weight loss relative to start weight. Data is shown as mean values ± s.e.m. Statistical analyses were performed by Fisher's exact test in **C,** log-rank test in **D**, Mann-Whitney *U* test in **F** and **G** and Student's *t*-test in **H** and **J**. $^*P < 0.05$; $^{**}P < 0.01$; $^{***}P < 0.001$.

To assess the therapeutic potential of PD-L1 delivery, the clinical disability score and the weight of each animal were monitored daily for 30 days after EAE-induction (Figure 3.5). However, no differences in disease incidence ($P > 0.999$, Figure 3.5C) and probability of survival ($P = 0.942$, Figure 3.5D) were observed. Moreover, neither the mean clinical score (Figure 3.5E), the cumulative score ($P = 0.754$, Figure 3.5F), the maximum score ($P = 0.885$, Figure 3.5G) the day of disease onset ($P = 0.376$, Figure 3.5H), the percentual body weight change (Figure 3.5I) nor the maximal weight loss ($P = 0.846$, Figure 3.5J) were changed. In summary, despite effective delivery of PD-L1 to neurons in the CNS, no clinical benefits were observed in the EAE mouse model.

3.2.2 Delivery of CD200 in EAE

Further, the neuroprotective potential of antiphagocytic signaling by the transmembrane protein CD200, was addressed. After generating the overexpression plasmid by molecular cloning (*hSyn1*-NLS-EGFP-P2A-CD200), the correct protein localization and sufficient delivery were tested by transient transfection of N2a cells. CD200 surface expression was detected in ~100% of transfected N2a cells in the experimental condition, while not present in the control condition ($P < 0.001$, Figure 3.6A). Moreover, immunocytochemistry stainings revealed a localization of CD200 at the cell membrane (Figure 3.6B). After the validation of the CD200 delivery plasmid in N2a cells, AAVs were generated and tested in primary cortical neuronal cultures. To verify the CD200 surface expression after AAV-CD200 delivery in primary cortical neurons, an immunocytochemistry surface staining was performed, prior to fixation and subsequent intracellular staining. Surface expression of CD200, which was co-localizing with the dendritic MAP2 signal, was observed after the treatment with AAV-CD200. The confocal images also showed a dim signal for CD200 in the control condition, which is consistent with the literature, as neurons express CD200 at base level. However, the CD200 signal in the experimental condition was strongly increased (Figure 3.6C).

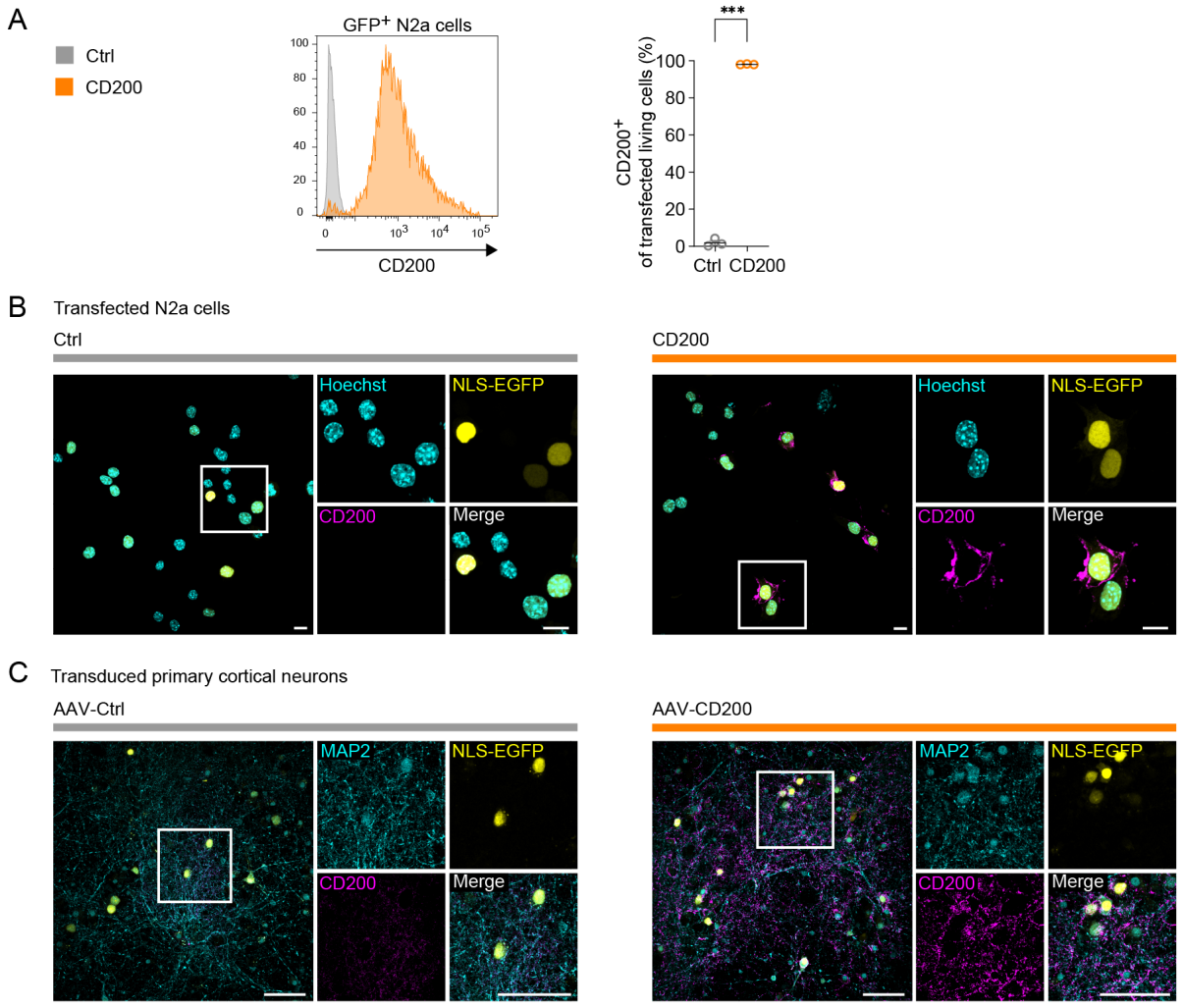

Figure 3.6: **Validation of CD200 surface expression in N2a cells and primary cortical neurons.** (**A**) Flow cytometry analysis of CD200 surface expression 24 h after transient transfection of N2a cells with either NLS-EGFP (Ctrl) or *hSyn1*-NLS-EGFP-P2A-CD200 (CD200), *n* = 3 per group. (**B**) Immunocytochemistry of *hSyn1*-CD200 expression 24 h after transfection of N2a cells. Co-staining of CD200 with Hoechst (nuclei) and endogenous expression of NLS-EGFP (transfected cell). Scale bar, 10 µm. (**C**) Immunocytochemistry of CD200 surface expression after transduction with AAV-Ctrl or AAV-CD200 on DIV7 at a MOI of 50k and stained on DIV14. Co-staining with MAP2 (dendrites) and endogenous expression of NLS-EGFP (transduced cell). Scale bar, 50 µm. Data is shown as mean values ± s.e.m. Statistical analysis was performed by paired Student's *t*-test in **A**. **P* < 0.05; ***P* < 0.01; ****P* < 0.001.

To evaluate the protective potential of neuronal CD200 delivery in a neuroinflammatory disease setting, 8-week-old female C57BL/6 wild type mice were either injected with AAV-Ctrl or AAV-CD200, 25 days prior to EAE induction (Figure 3.7A). Daily weight and health monitoring did not indicate any detrimental effects of the AAV treatment itself, as the mice gained the same amount of weight in both groups (Figure 3.7B). To control for comparable transduction efficiency of the two experimental groups, the frequency of $EGFP^+$ in $NeuN^+$ nuclei was quantified in the spinal cord at the end of the experiment on day 30 after EAE induction. Neither the transduction efficiency (Figure 3.7C) nor the frequency of $NeuN^+$ neuronal nuclei showed differences (Figure 3.7D). The transgene expression was further validated by immunohistochemistry in day 30 EAE motor neurons of the cervical spinal cord. While AAV-CD200 treated animals showed a strong CD200 expression, a dim endogenous CD200 signal

was observed in the control group, consistent with the observations *in vitro* (Figure 3.7E). In summary, robust CD200 delivery was observed without indication of detrimental side effects of the AAV treatment.

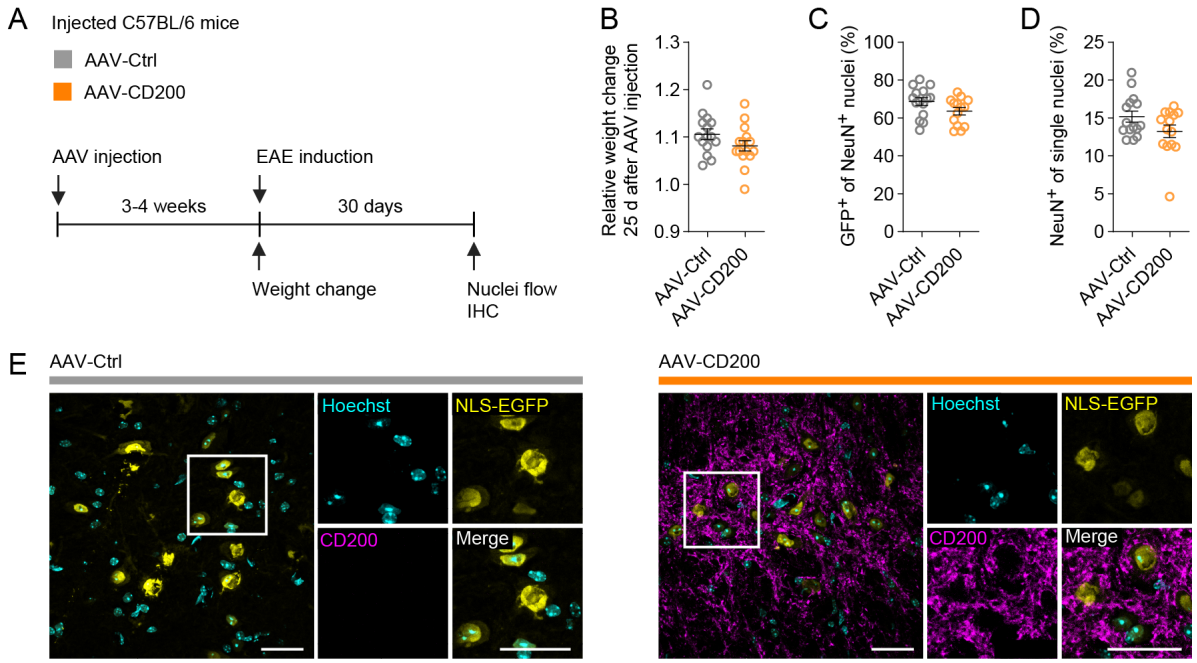

Figure 3.7: **Validation of neuronal CD200 delivery in d30 EAE animals.**
(**A**) Scheme for experimental setup to assess effects of AAV-mediated neuronal CD200 delivery. C57BL/6 wild type mice were injected with either AAV-*hSyn1*-NLS-EGFP (AAV-Ctrl) or AAV-*hSyn1*-NLS-EGFP-P2A-CD200 (AAV-CD200). Viral titers of 1×10^{12} vg were used (n = 15 mice per group). (**B**) Relative weight change, 25 days after AAV injection. (**C**) Flow cytometry analysis of transduction efficiency, measured as the frequency of $EGFP^+$ in $NeuN^+$ nuclei in thoracic spinal cord. (**D**) Flow cytometry analysis of $NeuN^+$ of single nuclei in thoracic spinal cord. (**E**) Immunohistochemistry of cervical spinal cord samples. Co-staining of CD200 with Hoechst (nuclei) and endogenous EGFP (enhanced by EGFP staining). Scale bar, 50 µm. Data is shown as mean values ± s.e.m. Statistical analyses were performed by Student's *t*-tests in **B**–**D**. *P < 0.05; **P < 0.01; ***P < 0.001.

For clinical assessment during EAE, the clinical disability score and the weight of animals were monitored daily for 30 days after EAE-induction (Figure 3.8A). No significant differences were observed regarding disease incidence (P > 0.999, Figure 3.8C) or probability of survival (P = 0.317, Figure 3.8D). The mean clinical score (Figure 3.8E), the cumulative score (P = 0.628, Figure 3.8F), the maximum score (P = 0.283, Figure 3.8G), the day of disease onset (P = 0.264, Figure 3.8H), as well as the percentual body weight change (Figure 3.8I) and the maximal weight loss (P = 0.225, Figure 3.8J) showed a slight protective effect of CD200 delivery, which however did not reach statistical significance. In summary, despite effective delivery of CD200 to neurons in the CNS, no significant clinical benefits were observed in the EAE mouse model.

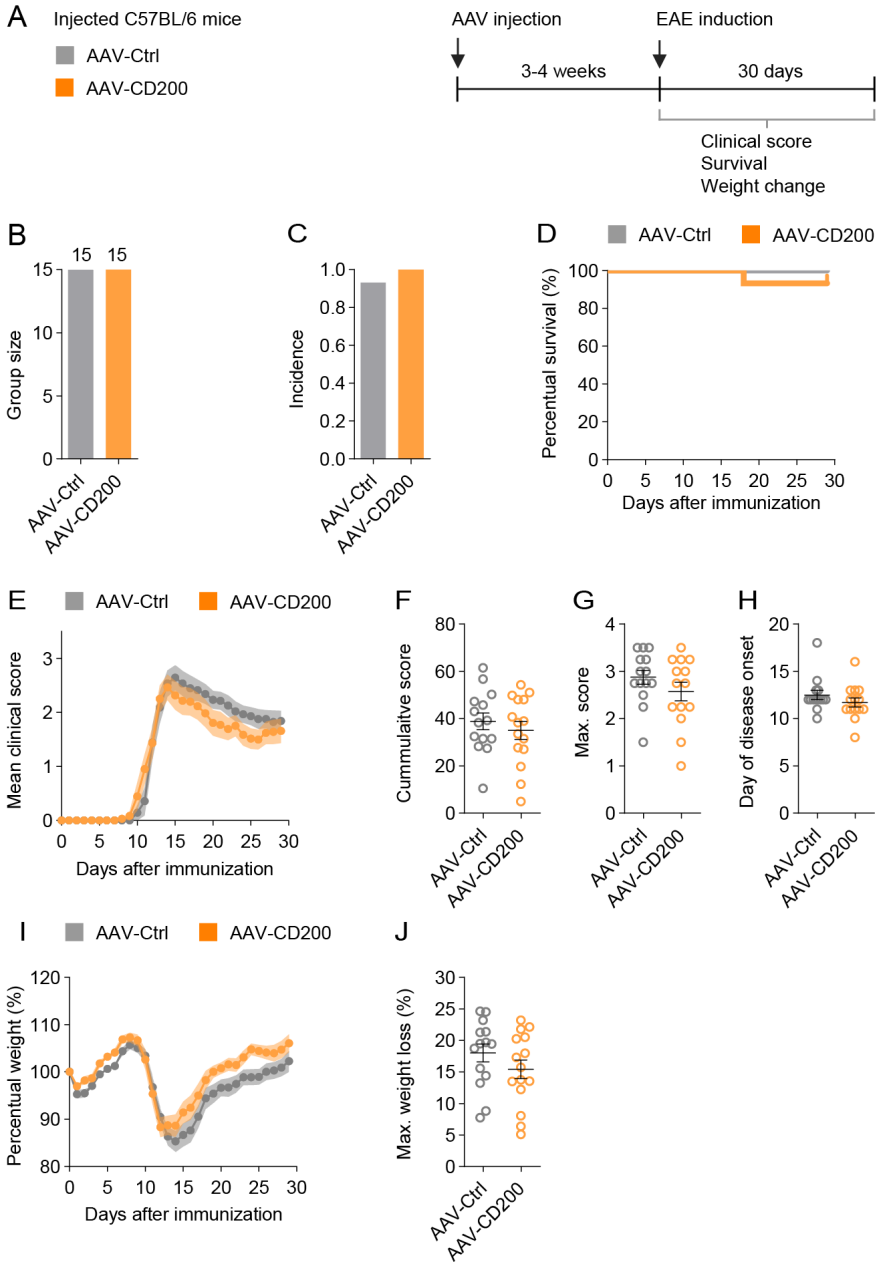

Figure 3.8: **Neuronal CD200 delivery does not rescue EAE phenotype.**
(**A**) Experimental setup to test protective potential of neuronal CD200 delivery in EAE. C57BL/6 wild type mice were injected with either AAV-*hSyn1*-NLS-EGFP (AAV-Ctrl) or AAV-*hSyn1*-NLS-EGFP-P2A-CD200 (AAV-CD200). Viral titers of 1×10^{12} vg were used. (**B**) Group size (AAV-Ctrl, n = 15; AAV-CD200, n = 15). (**C**) Disease incidence. (**D**) Kaplan Meier plot of probability of survival in percent during EAE course. (**E**) Clinical disease course. (**F**) Cumulative scores. (**G**) Maximal EAE score. (**H**) Day of disease onset. (**I**) Change of bodyweight. (**J**) Maximal weight loss relative to start weight. Data is shown as mean values ± s.e.m. Statistical analyses were performed by Fisher's exact test in **C,** log-rank test in **D**, Mann-Whitney *U* test in **F** and **G** and Student's *t*-test in **H** and **J**. **P* < 0.05; ***P* < 0.01; ****P* < 0.001.

3.3 Secreted proteins as mediator of immune tolerance in the CNS

As neither the neuronal delivery of PD-L1 nor of CD200, resulted in a meaningful protection in EAE, a possible explanation was that immune modulation close to the neuronal cell membrane might not be sufficient to interfere with inflammatory EAE activity. Indeed, it is unclear whether direct cell–cell contact between immune cells and neurons needs to be established in order to drive neurodegeneration[1]. Alternatively, proinflammatory cytokines and hostile changes to the

local microenvironment including tissue acidification, reactive oxygen species and excitotoxic levels of extracellular glutamate might suffice to trigger neuronal demise[248]. To target neuroinflammation in a broader sense independent of direct cell–cell contact, neuronal delivery of secreted proteins was next exploited.

3.3.1 Delivery of GDF-15 in EAE

To address more distant inflammatory processes from the neuron within the CNS, the secreted protein GDF-15 was tested for the potential to mediate CNS-restricted immune tolerance. An overexpression plasmid was generated by molecular cloning (*hSyn1*-NLS-EGFP-P2A-GDF15), and GDF-15 delivery was tested by transient transfection of N2a cells. An intracellular immunofluorescent staining was performed 24 h after transient transfection, which showed a specific intracellular GDF-15 signal in the experimental condition, which was not present in the control condition (Figure 3.9A). Moreover, GDF-15 secretion was validated by measurement of the protein levels in the N2a cell culture supernatant by ELISA (P = 0.076, Figure 3.9B).

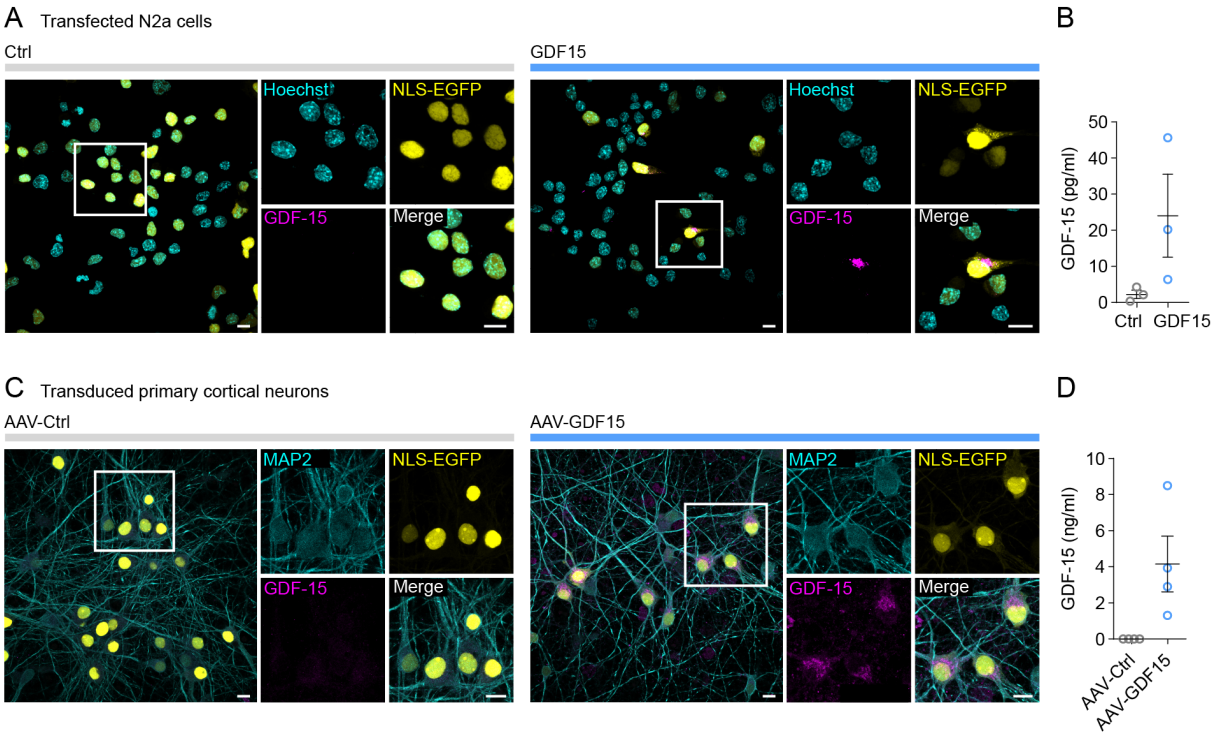

Figure 3.9: Validation of GDF-15 secretion in N2a cells and primary cortical neurons.
(**A**) Immunocytochemistry of transfected N2a cells 24 h after transient transfection with either *hSyn1*-NLS-EGFP (Ctrl) or *hSyn1*-NLS-EGFP-P2A-GDF15 (GDF15). Co-staining of GDF-15 with Hoechst (nuclei) and endogenous expression of NLS-EGFP (transfected cell). Scale bar, 10 µm. (**B**) GDF-15 protein levels in cell culture supernatant measured by ELISA 24 h after transient transfection of N2a cells (n = 3 per group). (**C**) Immunocytochemistry after transduction with AAV-Ctrl or AAV-GDF15 on DIV7 at a MOI of 50k and stained on DIV14. Co-staining of GDF-15 with MAP2 (dendrites) and endogenous expression of NLS-EGFP (transduced cell). Scale bar, 10 µm. (**D**) GDF-15 protein levels in cell culture supernatant of primary cortical neurons at DIV14 measured by ELISA 7 days after transduction (n = 4 per group). Data is shown as mean values ± s.e.m. Statistical analyses were performed by paired Student's t-tests in **B** and **D**. *P < 0.05; **P < 0.01; ***P < 0.001.

Next, AAVs were generated and validated by transduction of primary cortical neurons. An intracellular immunofluorescent staining was performed, which showed a somatic GDF-15 signal (Figure 3.9C). Sufficient secretion was validated by measurement of protein levels in the cell culture supernatant by ELISA (P = 0.074, Figure 3.9D).

After validating the correct delivery of GDF-15 *in vitro*, the next step was to address the protective potential of neuronal GDF-15 delivery in the EAE mouse model. Due to the greater mobility of secreted proteins, the AAV dosage was reduced to 5×10^{11} vg, which showed ~60% transduction efficiency in the rAAV titration experiment (Figure 3.1E). Next, 8-week-old female C57BL/6 wild type mice were injected with either AAV-Ctrl or AAV-GDF15, 26 days prior to EAE induction to allow full transgene expression (Figure 3.10A). However, despite the reduced doses, mice in the GDF-15 group lost weight, starting at day 7 after AAV injection, probably due to metabolic off-target effects of GDF-15 on the GFRAL receptor[218] (Figure 3.10C). While serving as a positive control for the biological activity of GDF-15, five animals showed more than 10% weight loss compared to their starting weight and one animal had to be sacrificed due to reaching the termination criteria of more than 25% weight loss at day 24 after AAV injection (P < 0.001, Figure 3.10D). Consequently, only animals that lost less than 10% of weight, were included in the EAE experiment, which was run until day 15 after immunization to perform a phenotyping of CNS infiltrating immune cells at the acute phase of EAE. Successful delivery of GDF-15 was examined 15 days after EAE induction by measurement of protein levels in cortical tissue lysates and EDTA plasma samples by ELISA. One animal was excluded from the analysis, due to no detectable transgene expression. All the other animals showed substantial levels of GDF-15 in cortical tissue lysates (P = 0.005, Figure 3.10E), as well as in the peripheral blood (P = 0.003, Figure 3.10E). Thus, a total group size of 6 vs 4 animals was included for the final EAE analysis (Figure 3.10F).

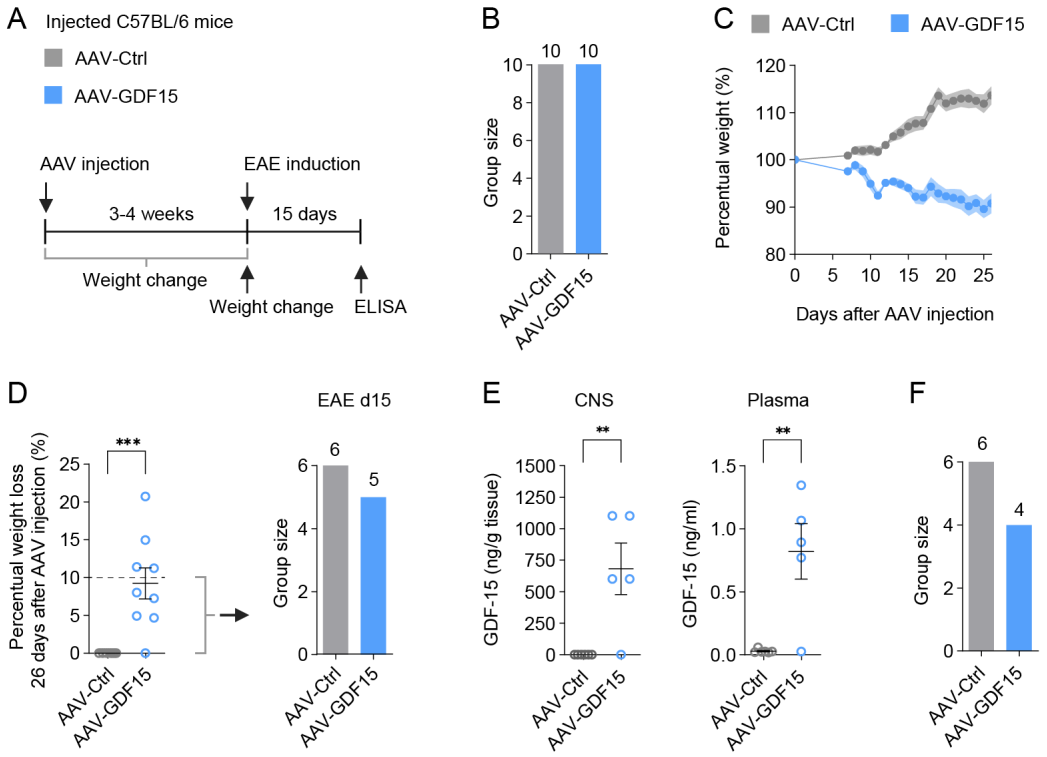

Figure 3.10: **Neuronal GDF-15 delivery leads to significant weight loss**.
(**A**) Scheme for experimental setup to assess effects of AAV-mediated neuronal GDF-15 delivery. C57BL/6 wild type mice were injected with either AAV-*hSyn1*-NLS-EGFP (AAV-Ctrl) or AAV-*hSyn1*-NLS-EGFP-P2A-GDF15 (AAV-GDF15). Viral titers of 5×10^{11} vg were used. (**B**) Group size (AAV-Ctrl, *n* = 10; AAV-GDF15, *n* = 10). (**C**) Weight change after AAV-injection relative to start weight. (**D**) Percentual weight loss 26 days after AAV injection, only animals with less than 10% weight loss were used for the EAE experiment (AAV-Ctrl, *n* = 6; AAV-GDF15, *n* = 5). (**E**) GDF-15 protein levels in cortical tissue lysates and EDTA plasma samples measured by ELISA. (**F**) Group size for final EAE analysis (AAV-Ctrl, *n* = 6; AAV-GDF15, *n* = 4). Data is shown as mean values ± s.e.m. Statistical analyses were performed by unpaired Student's *t*-test in **D** and **E**. **P* < 0.05; ***P* < 0.01; ****P* < 0.001.

For clinical assessment during EAE, the clinical disability score and the weight of each animal were monitored daily for 15 days after EAE-induction (Figure 3.11A). No animals had to be sacrificed during the EAE course and the survival did not differ between the animals (Figure 3.11C). Neuronal GDF-15 delivery protected the mice from developing a clinical disease score and showed a significantly reduced incidence (*P* = 0.048, Figure 3.11D). None of the AAV-GDF15 treated mice developed a clinical score (*P* = 0.081, Figure 3.11E). While animals which received AAV-Ctrl, displayed a typical EAE weight course where the maximal weight loss correlated with the maximum disease score at day 13 after EAE induction, animals that received AAV-GDF15 steadily lost weight until day 6 and then gained weight again, without developing a clinical disease score. Yet, the maximum weight loss did not differ. After EAE induction no additional animal showed a weight loss of over 25%, compared to the starting weight and therefore no animal had to be sacrificed due to weight loss (*P* = 0.810, Figure 3.11F).

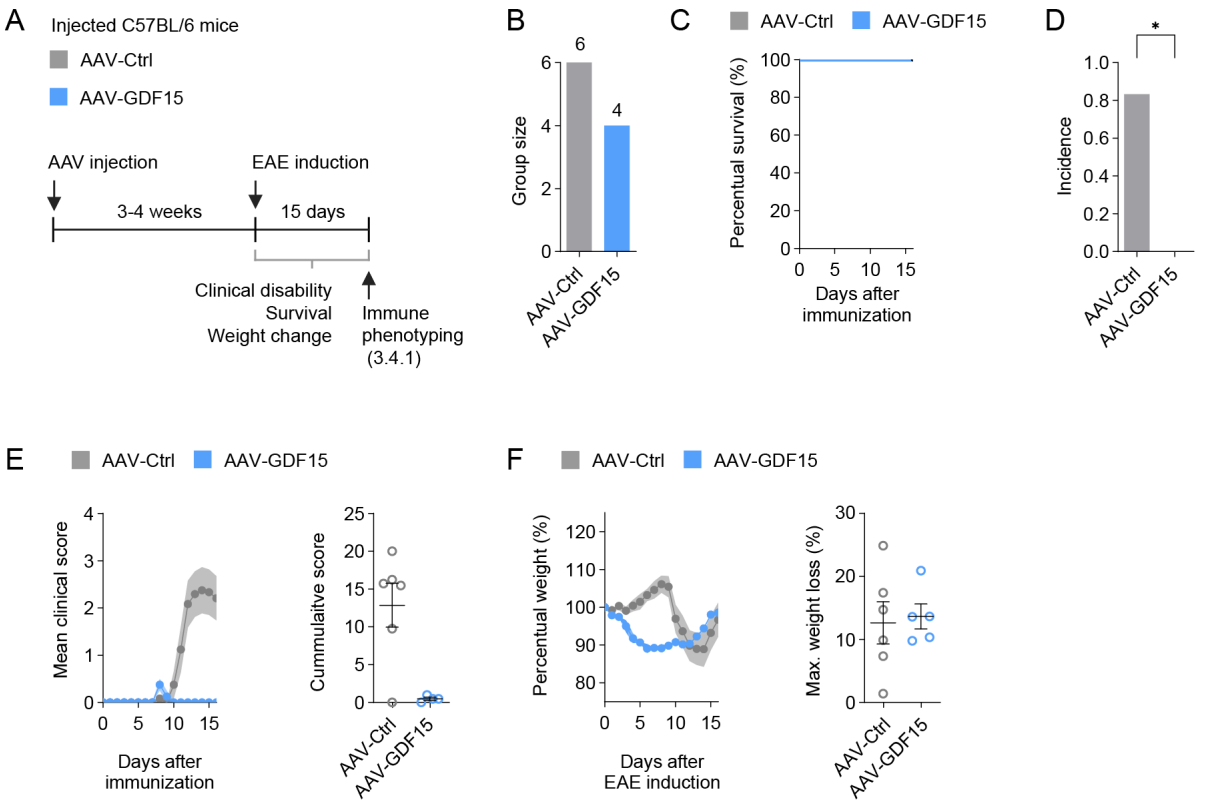

Figure 3.11: **Neuronal GDF-15 delivery rescues EAE phenotype.**
(**A**) Experimental setup to test protective potential of neuronal GDF-15 delivery in EAE. C57BL/6 wild type mice were injected with either AAV-*hSyn1*-NLS-EGFP (AAV-Ctrl) or AAV-*hSyn1*-NLS-EGFP-P2A-GDF15 (AAV-GDF15). Viral titers of 5×10^{11} were used. (**B**) Group size (AAV-Ctrl, n = 6; AAV-GDF15, n = 4). (**C**) Kaplan Meier plot of probability of survival in percent during EAE course. (**D**) Disease incidence. (**E**) Clinical disease course and cumulative scores. (**F**) Change of bodyweight and maximal weight loss relative to start weight. Data is shown as mean values ± s.e.m. Statistical analyses were performed by log-rank test in **C**, Fisher's exact test in **D,** Mann-Whitney *U* test in **E,** and Student's *t*-test in **F**. **P* < 0.05; ***P* < 0.01; ****P* < 0.001.

3.3.2 Delivery of IL-10 in EAE

Next, neuroprotective potential of the secreted effector candidate IL-10 with pleiotropic anti-inflammatory activity, was investigated. Neuronal IL-10 production was achieved by generating an overexpression plasmid by molecular cloning (*hSyn1*-NLS-EGFP-P2A-IL10) and was validated in transiently transfected N2a cells by intracellular flow cytometry analysis. Cells were treated with Brefeldin A for 5 hours prior to cell harvest and staining, which inhibits protein trafficking from the endoplasmic reticulum (ER) to the Golgi apparatus. Consequently IL-10 secretion was inhibited. An intracellular staining via flow cytometry revealed elevated IL-10 levels in ~25% of transfected N2a cells (P = 0.1594, Figure 3.12A). In an additional condition without Brefeldin A treatment, sufficient secretion was verified by measurement of protein levels in the cell culture supernatant by ELISA (P = 0.1458, Figure 3.12B). After validation of correct protein delivery, AAVs were generated and tested by transduction of primary cortical neurons. An intracellular immunofluorescent staining was performed, which showed a cytosolic IL-10 signal in transduced neurons (Figure 3.12C). Successful IL-10 secretion was validated

by measurement of protein levels in the cell culture supernatant by ELISA (P = 0.1392, Figure 3.12D).

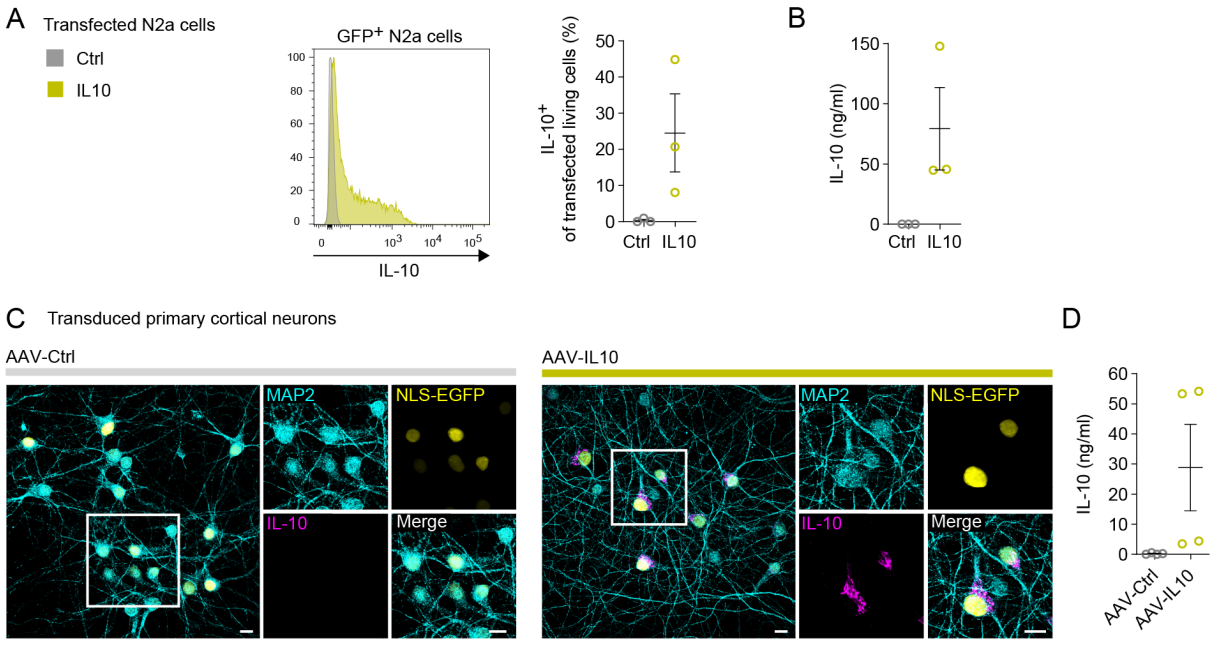

Figure 3.12: **Validation of IL-10 secretion in N2a cells and primary cortical neurons.**
(**A**) Flow cytometry analysis 24 h after transient transfection of N2a cells, cells were treated with Brefeldin A for 4 h before harvesting the cells to accumulate intracellular IL-10 with either *hSyn1*-NLS-EGFP (Ctrl) or *hSyn1*-NLS-EGFP-P2A-IL10 (IL10), n = 3 per group. (**B**) IL-10 protein levels in cell culture supernatant measured by ELISA 24 h after transient transfection of N2a cells (n = 3 per group). (**C**) Immunocytochemistry of DIV14 primary cortical neurons 7 days after transduction with AAV-Ctrl or AAV-IL10 at a MOI of 50k. Co-staining of IL-10 with MAP2 (dendrites) and endogenous expression of NLS-EGFP (transduced cell). Scale bar, 10 µm. (**D**) IL-10 protein levels in cell culture supernatant of primary cortical neurons at DIV14 measured by ELISA 7 days after transduction (n = 4 per group). Data is shown as mean values ± s.e.m. Statistical analyses were performed by paired Student's t-tests in **A**, **B** and **D**. *P < 0.05; **P < 0.01; ***P < 0.001.

To evaluate the protective potential of neuronal IL-10 delivery in a neuroinflammatory disease setting, 8-week-old female C57BL/6 wild type mice were either injected with AAV-Ctrl or AAV-IL10, 28 days prior to EAE induction (Figure 3.13A). Daily weight and health monitoring did not indicate any detrimental effects of the AAV treatment itself (Figure 3.13B). To control for comparable transduction efficiency of the two experimental groups, the frequency of $EGFP^+$ in $NeuN^+$ nuclei was quantified in the spinal cord at the end of the experiment 30 days after EAE induction. Neither transduction efficiency nor the frequency of $NeuN^+$ neuronal nuclei differed between the groups (Figure 3.13C,D). IL-10 transgene expression was validated by immunohistochemistry stainings of motor neurons of the cervical spinal cord on day 30 after EAE induction. Neurons that were transduced with AAV-IL10 showed a cytoplasmic IL-10 signal, while no IL-10 signal was observed in the control group (Figure 3.13E). In summary, AAV-IL10 treatment led to a robust IL-10 delivery without indication of detrimental side effects.

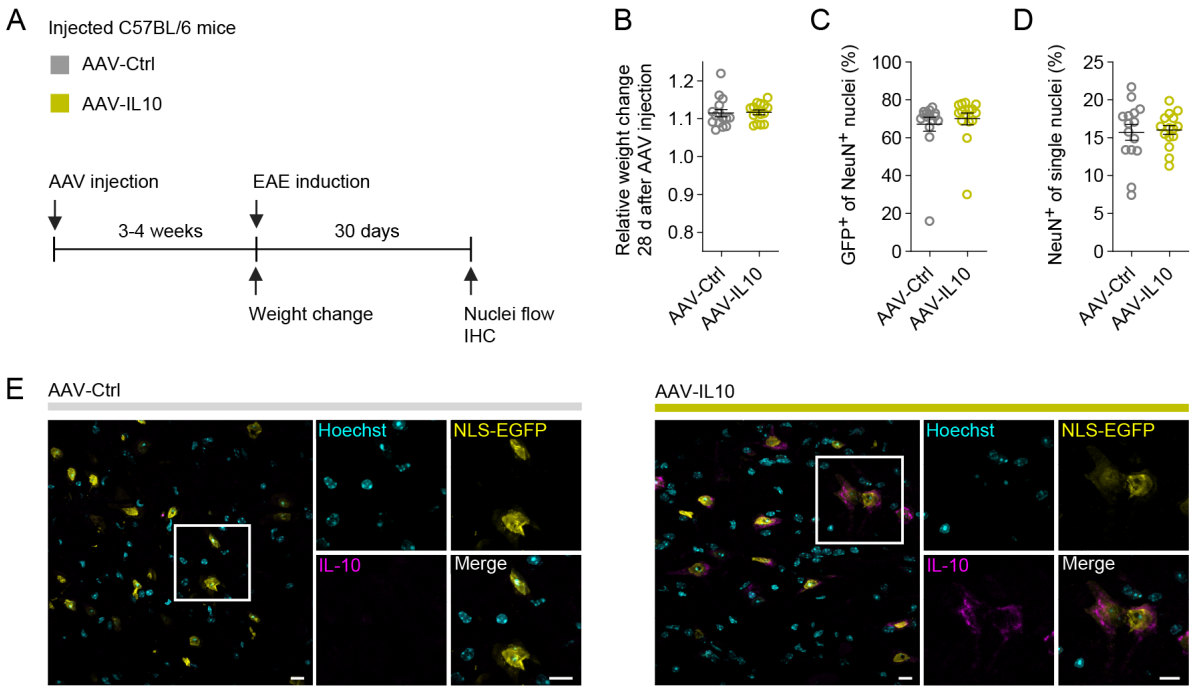

Figure 3.13: **Validation of neuronal IL-10 delivery in d30 EAE animals.**
(**A**) Scheme for experimental setup to assess effects of AAV-mediated neuronal IL-10 delivery. C57BL/6 wild type mice were injected with either AAV-*hSyn1*-NLS-EGFP (AAV-Ctrl) or AAV-*hSyn1*-NLS-EGFP-P2A-IL10 (AAV-IL10). Viral titers of 1×10^{12} vg were used (n = 15 mice per group). (**B**) Relative weight change, 28 days after AAV injection (**C**) Flow cytometry analysis of transduction efficiency, measured as the frequency of $EGFP^+$ in $NeuN^+$ nuclei in thoracic spinal cord. (**D**) Flow cytometry analysis of $NeuN^+$ of single nuclei in thoracic spinal cord. (**E**) Immunohistochemistry analysis of cervical spinal cord samples. Co-staining of IL-10 with Hoechst (nuclei) and endogenous EGFP (enhanced by EGFP staining). Scale bar, 10 µm. Data is shown as mean values ± s.e.m. Statistical analyses were performed by unpaired Student's *t*-tests in **B**–**D**. *P < 0.05; **P < 0.01; ***P < 0.001.

For clinical assessment during EAE, the clinical disability score and the weight were monitored daily for 30 days after EAE induction. (Figure 3.14). The percentual survival of the experimental group and the control group did not differ (P < 0.459, Figure 3.14D). However, animals that received AAV-IL10 showed a lower disease incidence (P < 0.001, Figure 3.14C), cumulative score (P < 0.001, Figure 3.14F) and maximum score (P < 0.001, Figure 3.14G), a later day of disease onset in the four animals that did get sick (P = 0.222, Figure 3.14H) and a lower maximum weight loss (P < 0.001, Figure 3.14J). Thus, neuronal delivery of IL-10 was found to act protective against neuroinflammatory damage in EAE.

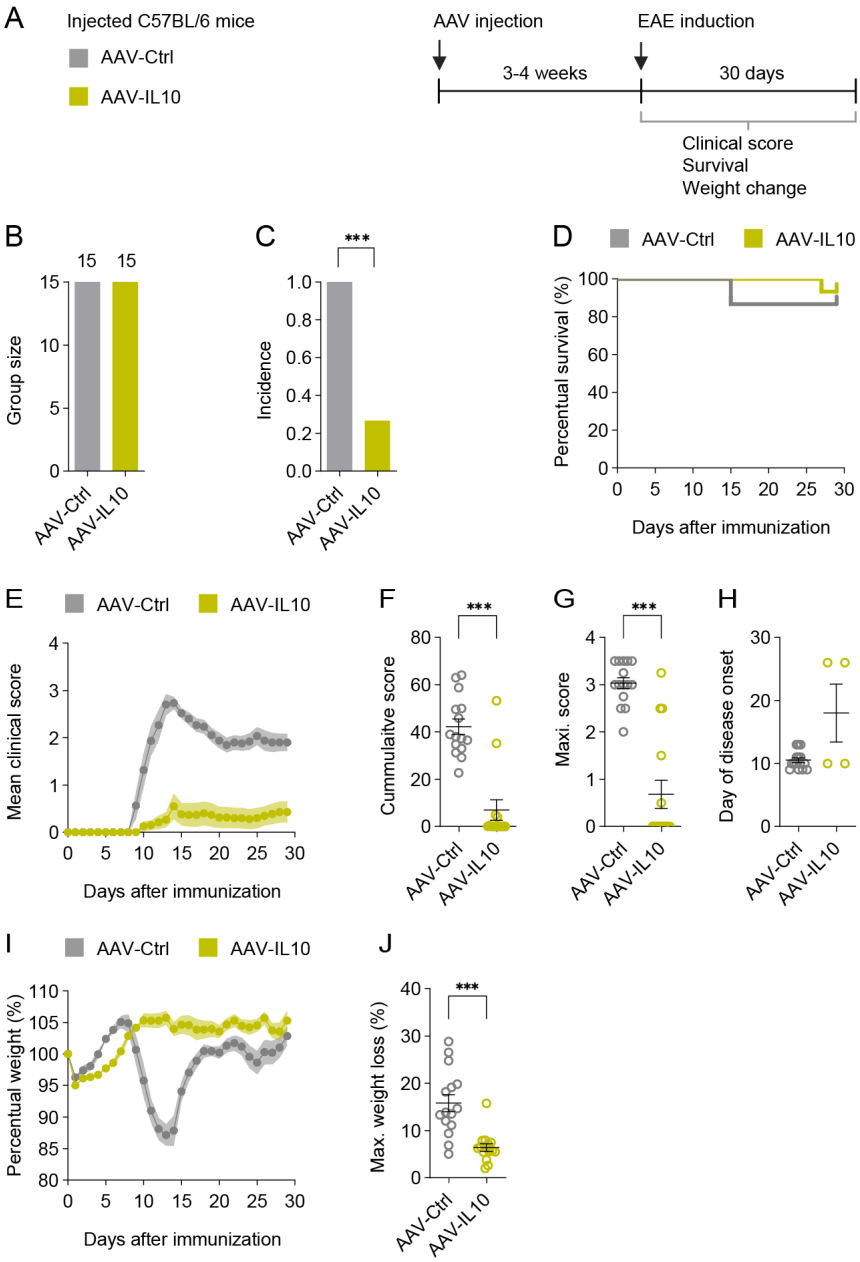

Figure 3.14: **Neuronal IL-10 delivery rescues EAE phenotype.**
(**A**) Experimental setup to test protective potential of neuronal IL-10 delivery in EAE. C57BL/6 wild type mice were injected with either AAV-*hSyn1*-NLS-EGFP (AAV-Ctrl) or AAV-*hSyn1*-NLS-EGFP-P2A-IL10 (AAV-IL10). Viral titers of 1×10^{12} vg were used. (**B**) Group size (AAV-Ctrl, n = 15; AAV-IL10, n = 15). (**C**) Disease incidence. (**D**) Kaplan Meier plot of probability of survival in percent during EAE course. (**E**) Clinical disease course. (**F**) Cumulative scores. (**G**) Maximal EAE score. (**H**) Day of disease onset. (**I**) Change of bodyweight. (**J**) Maximal weight loss relative to start weight. Data is shown as mean values ± s.e.m. Statistical analyses were performed by Fisher's exact test in **C,** log-rank test in **D**, Mann-Whitney *U* test in **F, G** and **H** and Student's *t*-test in **J**. **P* < 0.05; ***P* < 0.01; ****P* < 0.001.

3.4 Immune response modulation through GDF-15 and IL-10

The neuronal delivery of both soluble effector candidates GDF-15 and IL-10, led to a rescue of the EAE phenotype, while the surface proteins PD-L1 and CD200 did not significantly protect against neuroinflammatory damage. To better understand how this rescue was mediated, a flow cytometry-based broad phenotyping of the CNS-infiltrating immune cells was conducted at the acute phase of EAE. The question was whether a general immune cell reduction, or

specific changes in the infiltrate composition were responsible for the rescue of the EAE phenotype.

3.4.1 Modulation of CNS-infiltrating immune cells by GDF-15

To address the changes in the immune cell infiltrate at the acute phase of EAE after neuronal GDF-15 delivery, mice were intracardially perfused with PBS, immune cells isolated from the CNS and analyzed via flow cytometry (Figure 3.15A). This experiment was conducted in the animal cohort, in which the protective EAE phenotype was identified (3.3.1).

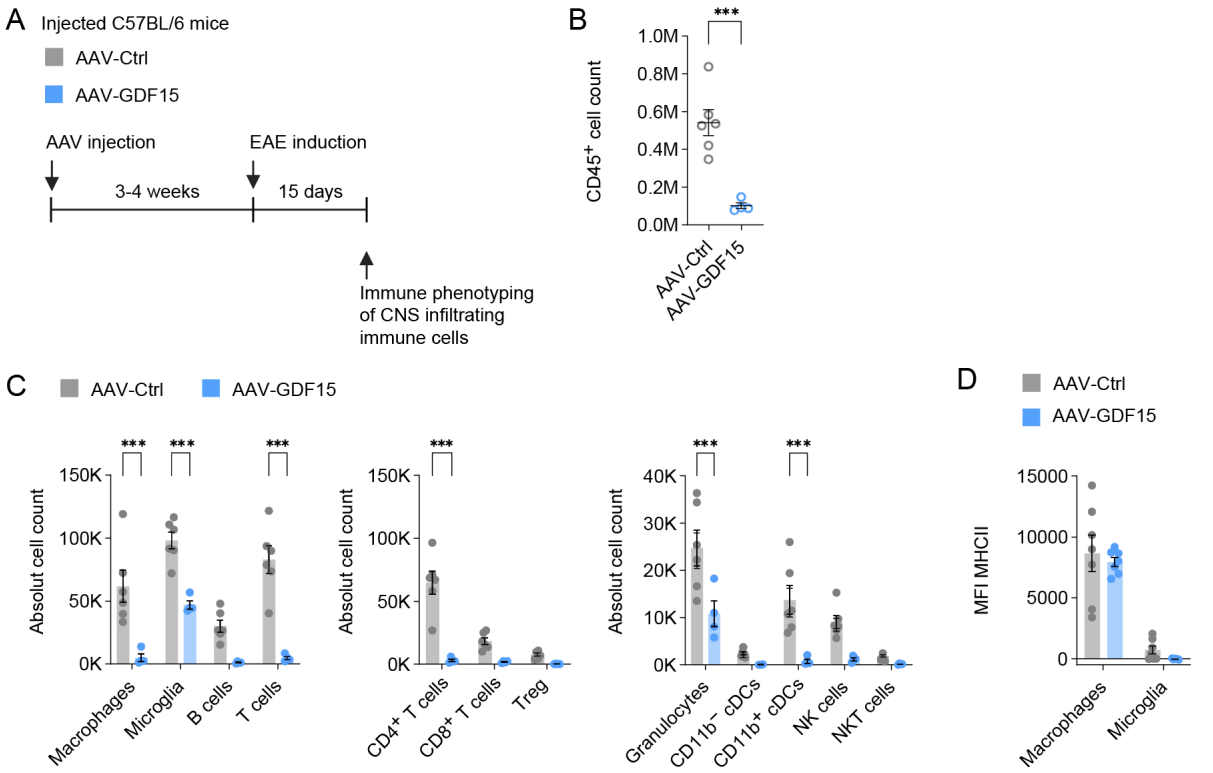

Figure 3.15: Neuronal GDF-15 delivery significantly reduces CNS immune cell infiltration in acute phase of EAE.
(**A**) Experimental setup to address changes in composition in CNS-infiltrating immune cells in the acute phase of EAE. C57BL/6 wild type mice were injected with either AAV-*hSyn1*-NLS-EGFP (AAV-Ctrl) or AAV-*hSyn1*-NLS-EGFP-P2A-GDF15 (AAV-GDF15). Viral titers of 5×10^{11} vg were used (AAV-Ctrl, n = 6; AAV-GDF15, n = 4). (**B**) Flow cytometry analysis of total CNS-infiltrating CD45$^+$ immune cells. (**C**) Flow cytometry analysis of immune cell counts. (**D**) Flow cytometry analysis of median fluorescence intensity (MFI) of MHCII on macrophages and microglia within the CNS. Data is shown as mean values ± s.e.m. Statistical analyses were performed by unpaired Student's *t*-test in **B** or two-way ANOVA with Šidák's post hoc test in **C** and **D**. *P < 0.05; **P < 0.01; ***P < 0.001.

The total amount of CNS-infiltrating CD45$^+$ immune cells was quantified and revealed a 5.3-fold significant reduction in the AAV-GDF15 receiving mice, compared to AAV-Ctrl treatment (Figure 3.15B). This decrease was reflected by all immune cell populations and not only a specific subset (Figure 3.15C). While the majority of immune cell populations were hardly detectable, microglia and granulocytes were only reduced by 2-fold in the AAV-GDF15 treated mice compared to the control animals. Moreover, the activation status of microglia and macrophages, which was measured by MHCII expression, was not altered (Figure 3.15D).

Overall, the immune cell infiltrate in AAV-GDF15 treated mice, was hardly present in acute EAE, which suggests that high CNS levels of GDF-15 prevented the infiltration of immune cells or interfered with the induction of EAE.

3.4.2 Modulation of CNS-infiltrating immune cells by IL-10

The influence of neuronal IL-10 delivery on infiltrating immune cells in the acute phase of EAE, was investigated in a second EAE experiment (Figure 3.16A). Mice were intracardially perfused with PBS, immune cells isolated from the CNS and analyzed via flow cytometry. Neuronal IL-10 delivery led to a 1.7-fold reduction of CNS-infiltrating $CD45^+$ immune cells, which however did not reach statistical significance (P = 0.062, Figure 3.16B). More specifically, this tendency was mainly driven by a reduction of brain infiltrating macrophages which contributed 24.6%, and $CD4^+$ T cells which contributed 12.9% of the total immune cell reduction. Granulocytes and $CD11b^+$cDCs were also significantly reduced (Figure 3.16C). The activation status of microglia and macrophages, which was measured by MHCII expression was not altered (Figure 3.16D).

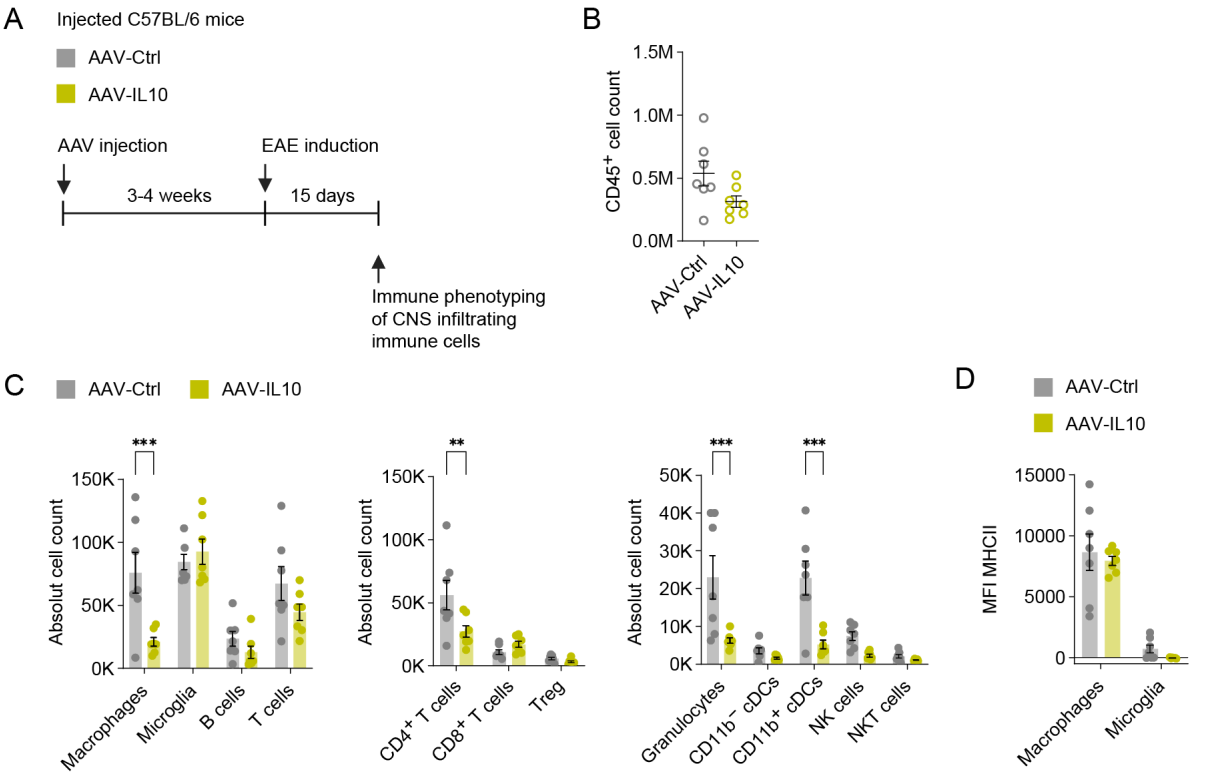

Figure 3.16: **Neuronal IL-10 delivery leads to significant changes in composition of CNS-infiltrating immune cells in acute phase of EAE.**
(**A**) Experimental setup to address changes in composition in CNS-infiltrating immune cells in the acute phase of EAE. C57BL/6 wild type mice were injected with either AAV-*hSyn1*-NLS-EGFP (AAV-Ctrl) or AAV-*hSyn1*-NLS-EGFP-P2A-IL10 (AAV-IL10). Viral titers of 1×10^{12} vg were used (n = 7 mice per group). (**B**) Flow cytometry analysis of total CNS-infiltrating $CD45^+$ immune cells. (**C**) Flow cytometry analysis of immune cell population counts. (**D**) Flow cytometry analysis of median fluorescence intensity (MFI) of MHCII on infiltrating macrophages and microglia. Data is shown as mean values ± s.e.m. Statistical analyses were performed by unpaired t-test in **B** or two-way ANOVA with Šidák's post hoc test in **C** and **D**. *P < 0.05; **P < 0.01; ***P < 0.001.

In conclusion, neuronal IL-10 delivery led to a significant reduction of multiple CNS-infiltrating immune cell populations, which contributed to the reduction of clinical EAE symptoms. The fact that the presence of immune cells was reduced in the CNS, however not as strikingly as observed for AAV-GDF15 treatment, suggests that the EAE induction was successful and high CNS levels of IL-10 were not sufficient to completely prevent immune cell infiltration.

3.4.3 Priming of autoreactive T cells in EAE

The two secreted effector molecules GDF-15 and IL-10 potently suppressed the EAE phenotype, while reducing the number of CNS-infiltrating immune cells. However, the previous finding of high protein levels of GDF-15 after neuronal gene delivery, not only in cortical tissue lysates but also in the periphery, suggested a potential interference with the T cell priming against $MOG_{35–55}$ (Figure 3.10E). Hence, an antigen recall assay was performed before the clinical disease onset, 9 days after EAE induction for AAV-GDF15 or AAV-IL10 in individual experiments. To assess whether neuronally produced IL-10 was also detectable in the periphery comparable to GDF-15, the protein levels for both cytokines were measured in the CNS and in the blood plasma by ELISA. To address these questions, 8-week-old female C57BL/6 wild type mice were injected with the respective AAV, 28 days prior to EAE induction, and peripheral T cells from the inguinal lymph nodes were isolated at day 9 after EAE induction (Figure 3.17A). A single cell suspension of the lymph nodes was then cultured for 3 days at 37 °C, re-stimulated with $MOG_{35–55}$ or CD3 in combination with CD28 as a positive control. At 16 h prior to analysis, cells were pulsed with bromodeoxyuridine (BrdU), a compound which integrates into the DNA upon cell division. T cell proliferation was measured by flow cytometry as the frequency of $BrdU^+$ cells in living lymphocytes.

First, the lymphocyte proliferation after neuronal GDF-15 delivery was analyzed by BrdU incorporation via flow cytometry. Lymphocytes in the AAV-GDF15 group did not proliferate after $MOG_{35–55}$ re-stimulation, except for one sample. However, also in the AAV-Ctrl group the lymphocytes only showed slight proliferation even with the higher $MOG_{35–55}$ concentration (Figure 3.17B). This indicates that in general the T cells in this EAE cohort were not strongly primed, however the peripheral GDF-15 levels, which were increased compared to AAV-Ctrl potentially contributed to this impairment. Also, cortical tissue lysates showed significantly increased GDF-15 proteins levels, which provides evidence for the successful neuronal GDF-15 delivery ($P = 0.001$, Figure 3.17C).

Next, the influence of AAV-IL10 treatment on T cell proliferation was assessed. The lymphocytes in both, the AAV-IL10 group and the AAV-Ctrl group, proliferated after $MOG_{35–55}$ re-stimulation in a dose dependent manner and did not differ between the groups. This indicates that the T cells were sufficiently primed against the $MOG_{35–55}$ antigen (Figure 3.17D) and the significantly elevated peripheral IL-10 protein levels did not interfere with this process

(*P* = 0.038, Figure 3.17E). Additionally, IL-10 protein levels of cortical tissue lysates were significantly elevated (*P* < 0.001, Figure 3.17E), which validates successful neuronal IL-10 delivery.

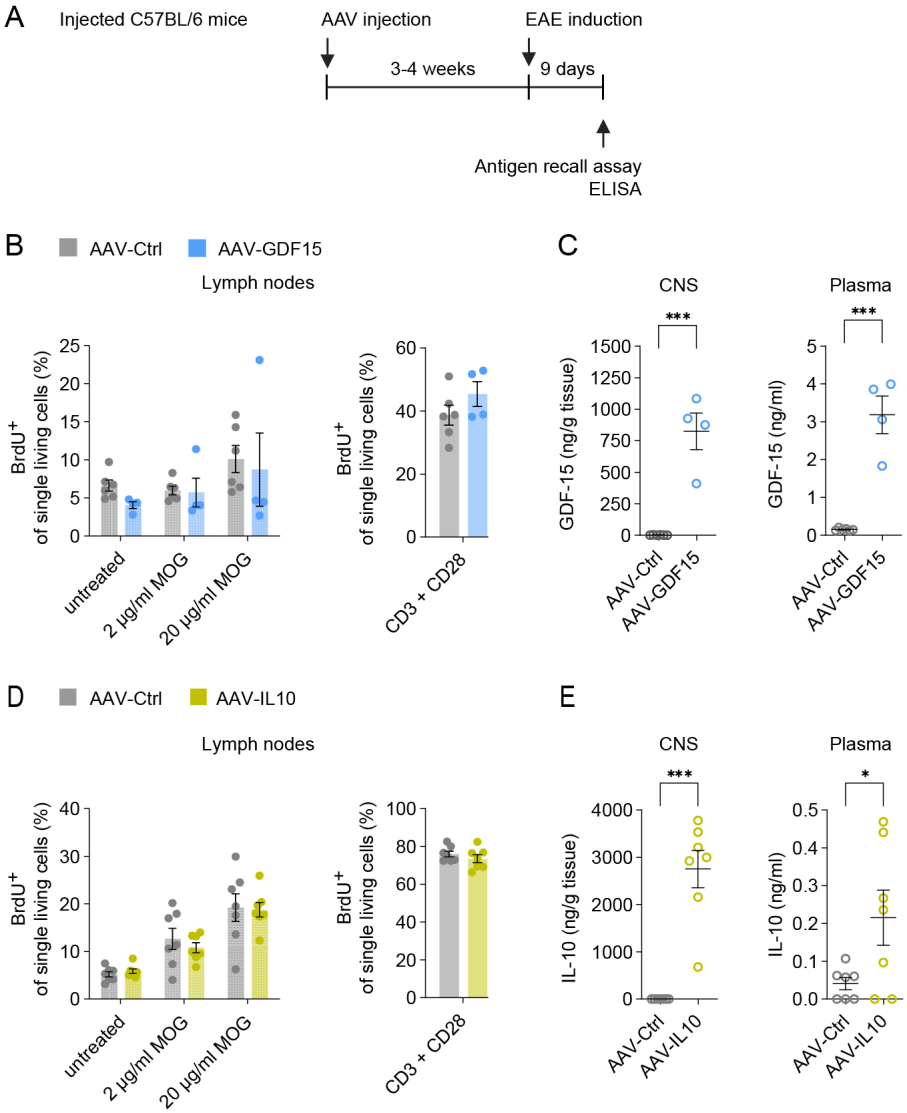

Figure 3.17: **Neuronal GDF-15 delivery results in impairment of T cell priming in EAE, while IL-10 delivery does not.**
(**A**) Experimental setup for antigen recall assay to assess T cell priming in the EAE mouse model at day 9 after EAE induction after neuronal GDF-15 or IL-10 delivery. (**B**) Flow cytometry analysis of lymphocyte proliferation after neuronal GDF-15 delivery, measured by BrdU incorporation after culturing lymphocytes for 3 days with the indicated stimuli. C57BL/6 wild type mice were injected with either AAV-*hSyn1*-NLS-EGFP (AAV-Ctrl) or AAV-*hSyn1*-NLS-EGFP-P2A-GDF15 (AAV-GDF15). Viral titers of 5×10^{11} vg were used. (AAV-Ctrl, *n* = 6; AAV-GDF15, *n* = 4). UT, untreated. (**C**) GDF-15 protein levels in cortical tissue lysates and EDTA plasma samples measured by ELISA. (**D**) Flow cytometry analysis of lymphocyte proliferation after neuronal IL-10 delivery, measured by BrdU incorporation after culturing lymphocytes for 3 days with the indicated stimuli. C57BL/6 wild type mice were injected with either AAV-*hSyn1*-NLS-EGFP (AAV-Ctrl) or AAV-*hSyn1*-NLS-EGFP-P2A-IL10 (AAV-IL10). Viral titers of 1×10^{12} vg were used (*n* = 7 mice per group). UT, untreated. (**E**) IL-10 protein levels in cortical tissue lysates and EDTA plasma samples measured by ELISA. Data is shown as mean values ± s.e.m. Statistical analyses were performed by two-way ANOVA with comparison to UT condition within each column and with Šidák's post hoc test in **B** and **D** and unpaired Student's *t*-tests in **C** and **E**. **P* < 0.05; ***P* < 0.01; ****P* < 0.001.

In summary the present results verify a sufficient neuronal delivery of both secreted effector proteins, which however were not restricted to the CNS, but also leaked into the periphery.

As the focus of this thesis was to establish a local immune tolerance in the CNS, based on the collected data, GDF-15 was not pursued as an effector candidate to establish a local immune tolerance in EAE. The observations that AAV-GDF15 receiving mice exhibited reduced T cell priming and a striking absence of CNS-infiltrating immune cells in acute EAE, hinted towards a peripheral cause of the EAE rescue rather than a CNS-specific effect. Moreover, the GDF-15 mediated weight loss added substantial burden to the animals. Unlike GDF15, neuronal IL-10 delivery did not interfere with the T cell priming. AAV-IL10 treatment led to a decrease of CNS-infiltrating immune cells, which was mainly driven by a reduction of macrophage and $CD4^+$ T cell infiltration, while the number of brain resident microglia was not altered. Based on these results the underlying mechanism of the protective effect of neuronal IL-10 delivery in the EAE mouse model was further investigated in subsequent experiments.

3.5 Mechanistic investigation of IL-10-mediated EAE rescue

Although T cell infiltration was reduced in acute EAE after AAV-IL10 treatment, ~60% of T cells were still able to reach the CNS compared to control mice, which however did not cause clinical symptoms. A possible explanation was that an IL-10-mediated alteration of the T cell activation status, might have contributed to the protective phenotype. To decipher potential peripheral immunological effects of IL-10 exposure from CNS-specific effects, a detailed T cell phenotyping was conducted in healthy mice as well as at the acute phase of EAE.

3.5.1 Modulation of T cells in lymph nodes and spleen by IL-10 in healthy animals

Due to the fact that the BBB gets impaired during EAE development, it was explored whether neuronally produced IL-10 was also detectable in the blood plasma of healthy mice or if a leakage into the periphery was dependent on an impairment of the BBB. To address how potential peripheral IL-10 protein levels modulate immune cells in healthy animals, 8-week-old female C57BL/6 wild type mice were injected with either AAV-Ctrl or AAV-IL10 and the T cell phenotype in lymph nodes and spleen was analyzed. A detailed flow cytometry-based analysis was focused on surface activation marker expression on T cells (Figure 3.18A). The transduction efficiency was quantified by flow cytometry as the frequency of $EGFP^+$ nuclei in $NeuN^+$ nuclei. Moreover, IL-10 transgene expression was measured by ELISA of cortical tissue lysates and EDTA plasma samples.

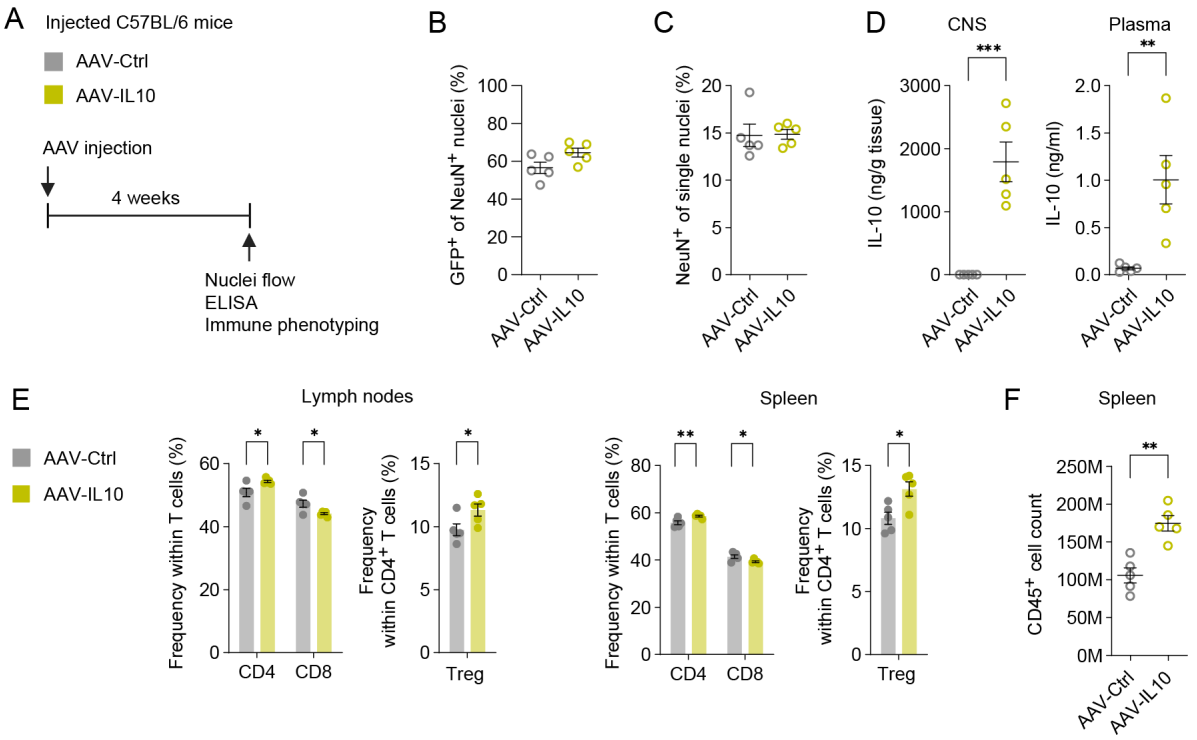

Figure 3.18: **Peripheral levels of IL-10 lead to an increase in Treg in peripheral lymphoid organs after neuronal delivery in healthy mice.**
(**A**) Experimental setup to evaluate IL-10 effects on peripheral immune cell frequencies in healthy mice. C57BL/6 wild type mice were injected with either AAV-*hSyn1*-NLS-EGFP (AAV-Ctrl) or AAV-*hSyn1*-NLS-EGFP-P2A-IL10 (AAV-IL10). Viral titers of 1×10^{12} vg were used (n = 5 mice per group). (**B**) Flow cytometry analysis of transduction efficiency, measured as the frequency of $EGFP^+$ in $NeuN^+$ nuclei in thoracic spinal cord. (**C**) Flow cytometry analysis of $NeuN^+$ of single nuclei in thoracic spinal cord. (**D**) IL-10 protein levels in cortical tissue lysates and EDTA plasma samples measured by ELISA. (**E**) Flow cytometry analysis of T cell subpopulations in lymph nodes and spleen. (**F**) Flow cytometry analysis of immune cell count in the spleen. Detailed plasmid description listed in Table 2.14. Data is shown as mean values ± s.e.m. Statistical analyses were performed by unpaired Student *t*-tests in **B**, **C, D** and **F** and two-way ANOVA with Šidák's post hoc test and unpaired Student *t*-tests in **E**. *P < 0.05; **P < 0.01; ***P < 0.001.

Neither the transduction efficiency (Figure 3.18B) nor the frequency of $NeuN^+$ neuronal nuclei differed between the groups (Figure 3.18C). Moreover, elevated IL-10 protein levels in cortical tissue lysates (P = 0.001, Figure 3.18D) and plasma samples (P = 0.007, Figure 3.18D) were observed, which were comparable to the IL-10 levels measured on day 9 after EAE induction. The fact that peripheral IL-10 levels were also detected in healthy mice, indicates the capacity of IL-10 to cross into the periphery without an impairment of the BBB. Due to the fact that the spleen of AAV-IL10 treated mice appeared enlarged, the total $CD45^+$ immune cell count in the spleen was quantified, which revealed a significant increase (P = 0.001, Figure 3.18E). Moreover, Treg increased in frequencies after neuronal IL-10 treatment in the spleen (P = 0.015, Figure 3.18E) and lymph nodes (P = 0.048, Figure 3.18E), which potentially contributed to shaping a tolerogenic peripheral environment.

Next, the activation status of $CD4^+$ and $CD8^+$ T cells in the lymph nodes after IL-10 exposure was addressed by analyzing the surface marker expression of CD25, CD44, CD69, LFA-1 and PD-1. All markers showed comparable expression level, with the exception of LFA-1, which was significantly upregulated in $CD4^+$ T cells (P = 0.021, Figure 3.19B) and in $CD8^+$

T cells ($P < 0.001$, Figure 3.19B). LFA-1, which is important for T cell activation by regulating the interaction between T cells and APCs, also facilitates T cell adhesion to endothelial cells and consequently T cell migration over the BBB[145]. Therefore, the increase of LFA-1 treated mice, might indicate a more activated T cell phenotype.

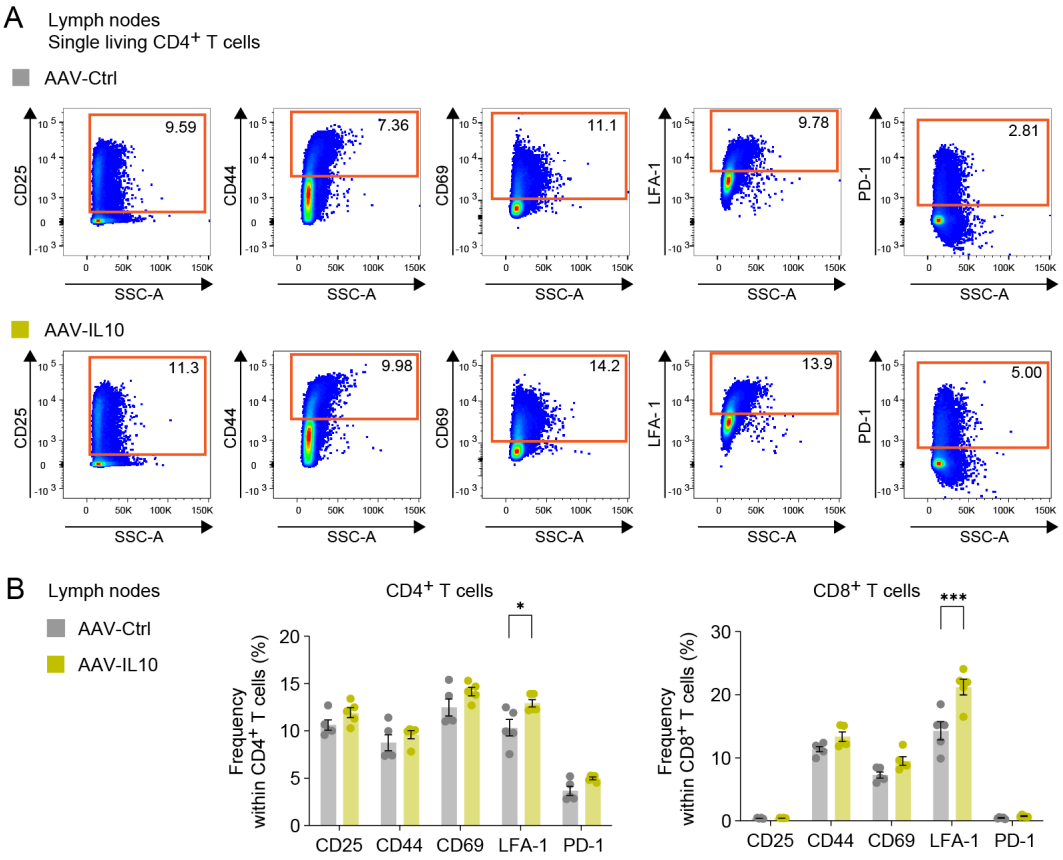

Figure 3.19: **Peripheral levels of IL-10 increase LFA-1 on CD4⁺ and CD8⁺ T cells in the lymph nodes in healthy mice.**
(**A**) Representative gating of surface markers on CD4⁺ T cells in lymph nodes in healthy mice. C57BL/6 wild type mice were injected with either AAV-*hSyn1*-NLS-EGFP (AAV-Ctrl) or AAV-*hSyn1*-NLS-EGFP-P2A-IL10 (AAV-IL10). Viral titers of 1×10^{12} vg were used ($n = 5$ mice per group). (**B**) Flow cytometry analysis of surface markers on CD4⁺ and CD8⁺ T cells in lymph nodes. Data is shown as mean values ± s.e.m. Statistical analyses were performed by two-way ANOVA with Šidák's post hoc test in B. *$P < 0.05$; **$P < 0.01$; ***$P < 0.001$.

3.5.2 Modulation of T cells in CNS, lymph nodes and spleen in acute EAE

Based on the finding that the peripheral T cell phenotype after IL-10 exposure was altered in healthy mice, the next step was to investigate if these changes were also present in CNS-infiltrating T cells, and whether the phenotype was further modulated after the encounter of high IL-10 protein levels in the CNS. Hence, the T cell modulation by IL-10 within the CNS and in the periphery were investigated in more detail, by conducting a dedicated flow cytometry-based T cell phenotyping at the acute phase of EAE (Figure 3.20A). The total infiltrating CD45⁺ immune cell count was similar to the first immune cell phenotyping, however this time a significant difference was detected between the groups due to the increased sample size ($P <$

0.001, Figure 3.20B). While the immune cell count in the inguinal lymph nodes did not differ (P = 0.425, Figure 3.20B), the cell count in the spleen was significantly increased (P < 0.001, Figure 3.20B), consistent to the finding in healthy mice. Interestingly, in contrast to healthy mice that received AAV-IL10, the Treg frequencies did not differ between the groups in lymph nodes (P = 0.298, Figure 3.20C), spleen (P = 0.486, Figure 3.20C), and CNS (P = 0.088, Figure 3.20C) at the acute phase of EAE.

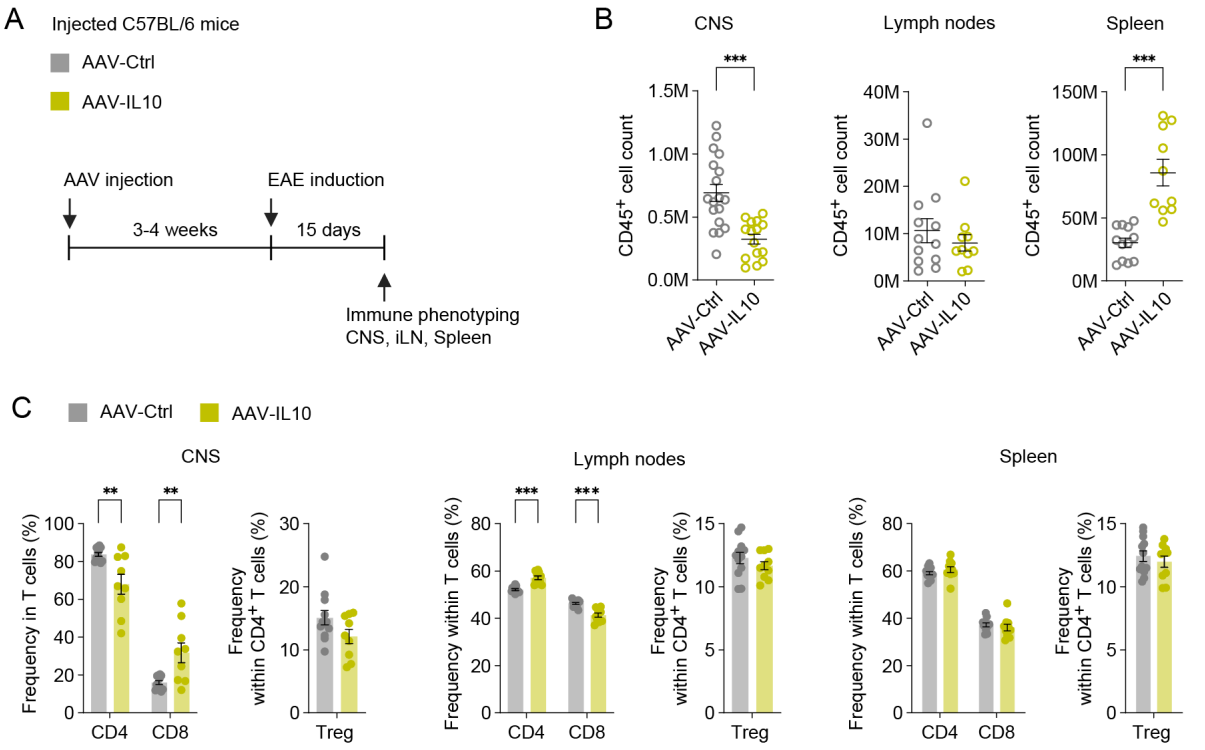

Figure 3.20: Neuronal IL-10 delivery leads to a decreased immune cell infiltrate in the CNS and an increased number of immune cells in the spleen in acute phase of EAE.
(**A**) Experimental setup for detailed T cell phenotyping in acute phase of EAE. Results pooled from 3 independent EAE cohorts. C57BL/6 wild type mice were injected with either AAV-*hSyn1*-NLS-EGFP (AAV-Ctrl) or AAV-*hSyn1*-NLS-EGFP-P2A-IL10 (AAV-IL10). Viral titers of 1×10^{12} vg were used. (**B**) Flow cytometry analysis of immune cell counts in CNS (AAV-Ctrl, n = 18; AAV-IL10, n = 15), lymph nodes (AAV-Ctrl, n = 12; AAV-IL10, n = 10) and spleen (AAV-Ctrl, n = 12; AAV-IL10, n = 10). (**C**) Flow cytometry analysis of T cell subpopulations in CNS (AAV-Ctrl, n = 18; AAV-IL10, n = 15), lymph nodes (AAV-Ctrl, n = 12; AAV-IL10, n = 10) and spleen (AAV-Ctrl, n = 12; AAV-IL10, n = 10). Data is shown as mean values ± s.e.m. Statistical analyses were performed by two-way ANOVA with Šidák's post hoc test **C** and unpaired Student t-tests in **B** and **C** for Treg comparison. *P < 0.05; **P < 0.01; ***P < 0.001.

To identify whether an altered T cell effector function, contributed to the IL-10-mediated EAE rescue, the activation status and cytokine production of $CD4^+$ and $CD8^+$ T cells were further analyzed in the CNS and the inguinal lymph nodes via flow cytometry (Figure 3.21A). Here, a reduction of ~50% in CD44 expression was observed on $CD4^+$ T cells that infiltrated the CNS (P < 0.001, Figure 3.21B). The fact that the frequency of $CD44^+CD4^+$ T cells was not altered in the lymph nodes in the AAV-IL10 group, indicates that this phenotype derived potentially from the exposure to the high IL-10 levels in the CNS. $CD8^+$ T cells significantly upregulated CD69 (P < 0.001, Figure 3.21B) and LFA-1 (P = 0.040, Figure 3.21B). The upregulation of

LFA-1 in lymph node CD4⁺ T cells, which was observed in healthy animals, was not present at the acute phase of EAE (P = 0.959, Figure 3.21B). CD8⁺ T cells in the lymph nodes also showed significantly elevated LFA-1 in the AAV-IL10 treated group (P < 0.001, Figure 3.21C).

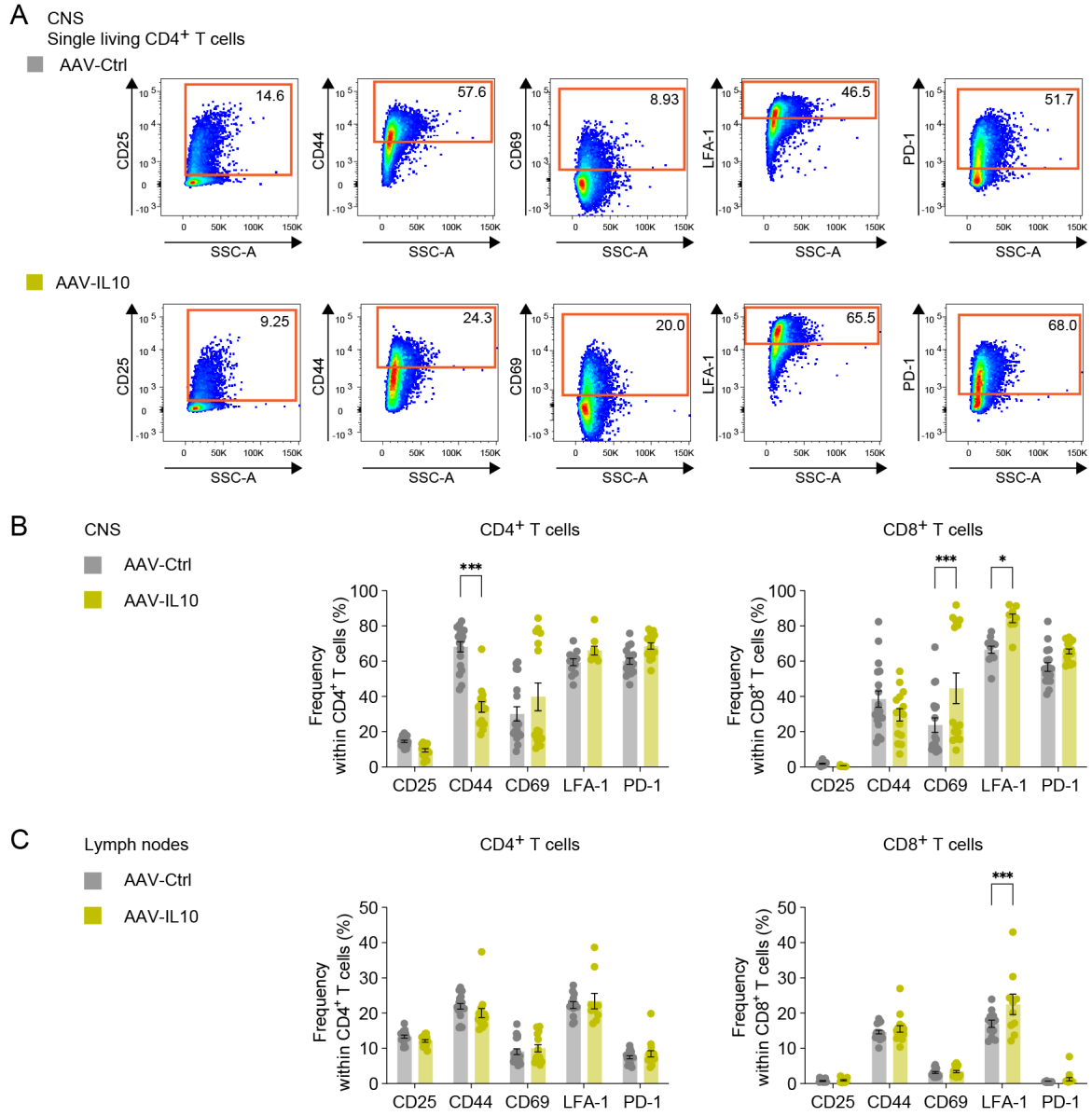

Figure 3.21: Changes in T cell activation status in CNS-infiltrating T cells in acute phase of EAE.
(**A**) Representative gating for flow cytometry analysis of surface markers on CD4⁺ T cells in the CNS in acute phase of EAE. C57BL/6 wild type mice were injected with either AAV-*hSyn1*-NLS-EGFP (AAV-Ctrl) or AAV-*hSyn1*-NLS-EGFP-P2A-IL10 (AAV-IL10). Viral titers of 1×10^{12} vg were used. Results pooled from 3 independent EAE cohorts. (**B**) Flow cytometry analysis of surface markers on CD4⁺ and CD8⁺ T cells in the CNS (AAV-Ctrl, n = 12; AAV-IL10, n = 10). (**C**) Flow cytometry analysis of surface markers CD4⁺ and CD8⁺ T cells in the lymph nodes (AAV-Ctrl, n = 12; AAV-IL10, n = 10). Data is shown as mean values ± s.e.m. Statistical analyses were performed by two-way ANOVA with Šidák's post hoc test in **B** and **C**. *P < 0.05; **P < 0.01; ***P < 0.001.

To test for changes in cytokine expression profile of T cells, single cell suspensions of CNS-infiltrating immune cells and lymphocytes were cultured for 5 h at 37 °C with Brefeldin A and PMA/Ionomycin. The capacity of IFN-γ, IL-17a and TNF-α production was then analyzed by performing an intracellular flow cytometry analysis (Figure 3.22A). CNS-infiltrating CD8⁺ T cells

produced IL-17a at a significantly reduced frequency (P = 0.011, Figure 3.22B), while no significant differences in cytokine production were present in CD4$^+$ T cells in the CNS infiltrate and lymph nodes (Figure 3.22C).

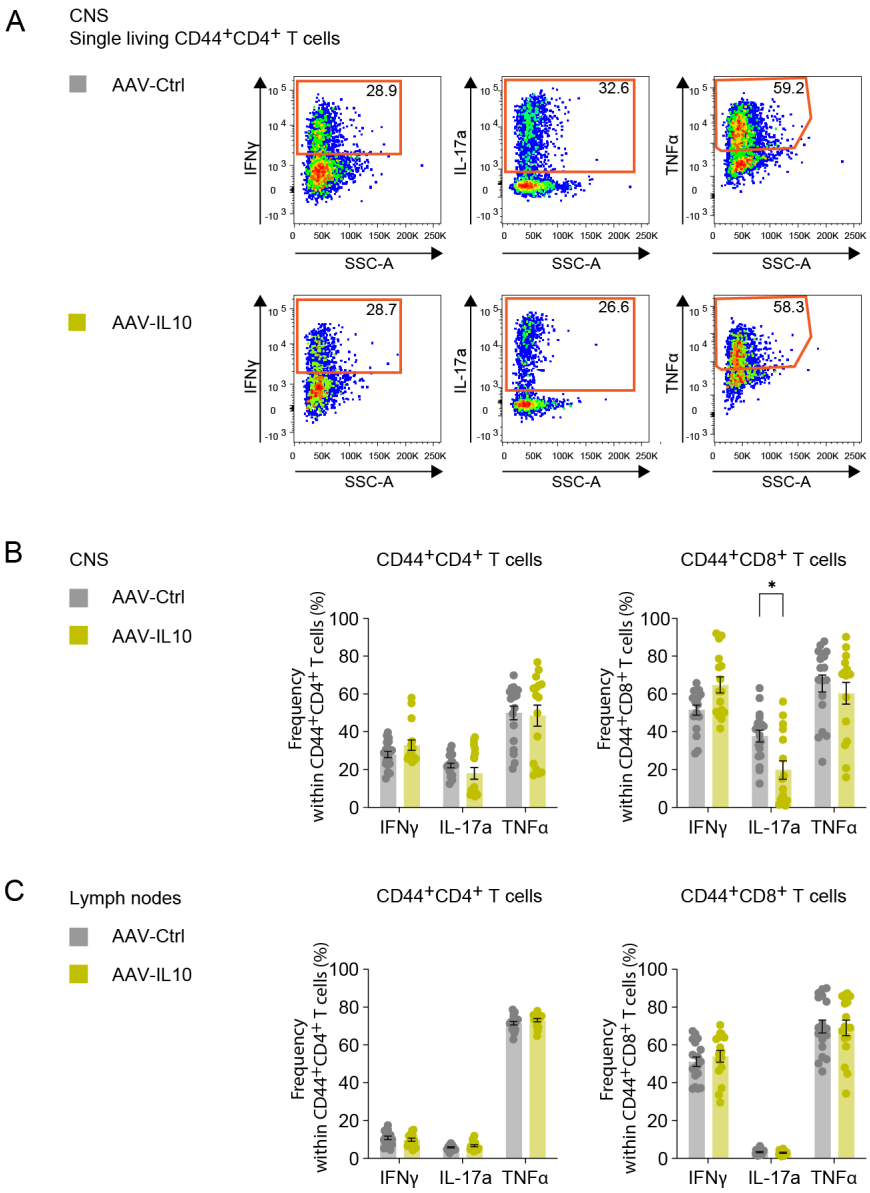

Figure 3.22: Changes in cytokine expression profile in CNS-infiltrating T cells in acute phase of EAE. (**A**) Representative gating of flow cytometry analysis cytokine production of CD44$^+$CD4$^+$ and CD44$^+$CD8$^+$ T cell in the CNS in acute phase of EAE. CD44$^+$ T cells were identified as shown in Figure 3.21. C57BL/6 wild type mice were injected with either AAV-*hSyn1*-NLS-EGFP (AAV-Ctrl) or AAV-*hSyn1*-NLS-EGFP-P2A-IL10 (AAV-IL10). Viral titers of 1×10^{12} vg were used. Results pooled from 3 independent EAE cohorts. (**B**) Flow cytometry analysis of produced cytokines by CD44$^+$CD4$^+$ and CD44$^+$CD8$^+$ T cells in the CNS. (AAV-Ctrl, n = 18; AAV-IL10, n = 15). (**C**) Flow cytometry analysis of produced cytokines by CD4$^+$ and CD8$^+$ T cells in the lymph nodes. (AAV-Ctrl, n = 12; AAV-IL10, n = 10). Data is shown as mean values ± s.e.m. Statistical analyses were performed by two-way ANOVA with Šidák's post hoc test in **B** and **C**. *P < 0.05; **P < 0.01; ***P < 0.001.

In conclusion, the detailed T cell phenotyping in healthy mice and at the acute phase of EAE, revealed a significant increase of Treg in healthy mice, but not at the acute phase of EAE after IL-10 exposure. Moreover, IL-10 treatment led to an increase of LFA-1, especially on CD8$^+$ T cells at both time points. Two findings that were unique to CNS-infiltrating T cells at the acute

phase of EAE, were a reduction of $CD4^+CD44^+$ T cells and a decrease of IL-17a production by $CD8^+$ T cells and therefore likely to derive from neuronal IL-10 production inside the CNS.

3.6 Biotechnological engineering of IL-10 delivery

While AAV-IL10 treatment potently suppressed clinical EAE symptoms, unwanted treatment effects were observed like the enlargement of the spleen, accompanied by an increased cell count. Potentially this was caused by peripheral IL-10 protein levels and prolonged exposition to IL-10 over three to four weeks prior to inducing EAE. To minimize the treatment exposure time and explore the therapeutic potential of IL-10 at the start of clinical symptoms, an inducible TetOn system was implemented to gain temporal control of neuronal IL-10 expression (3.6.1). Moreover, a membrane-bound version of the IL-10 protein was developed to restrict biological activity to the CNS and thereby reduce peripheral protein levels (3.6.2).

3.6.1 Temporal control of IL-10 delivery via inducible TetOn system

The TetOn system was implemented to achieve temporal control of IL-10 delivery and induce protein expression with occurrence of the first clinical symptoms, as this would be the timepoint of treatment in a clinical disease setting. A tetracycline responsive element (*TRE*), which consists of multiple tetracycline operator (TetO) sequences fused to a minimal promoter, activates gene transcription after binding of the TetO sequences to a reverse tetracycline-controlled transactivator (rtTA) in the presence of tetracycline (Tc) or its derivates doxycycline (Dox) or minocycline (Mc)[249] (Figure 3.23A). in addition to time-controlled induction of expression by administration of Tc, this system also allows to turn off protein expression upon withdrawal of Tc. In this thesis rtTA-V10 (TetOn3G) was used, which is an rtTA with increased sensitivity to Dox[249,250]. While Dox is most commonly used to induce gene expression, to date there is only sparse data on the responsiveness of different rtTAs to Mc. Mc is an interesting candidate for the development of new drugs for therapy of neurodegenerative diseases, due to its permeability for the blood–brain barrier and neuroprotective capacity via the suppression of microglial activation in traumatic brain injury (TBI)[251,252]. Therefore, Mc was included in the following validation experiments.

First, the response vector *TRE*-EGFP was generated, which like the constitutive control construct *hSyn1*-NLS-EGFP, consisted of an EGFP, flanked by two NLS to detect induction of transgene expression in the nucleus via nuclei flow cytometry. To ensure neuronal specificity, a dual vector system was employed that expressed rtTA under the control of a *hSyn1* promoter in an additional plasmid (*hSyn1*-rtTA). The rtTA was either expressed under the constitutive *hSyn1* promoter or with the self-enhancing *ihSyn1* promoter. The *ihSyn1* promoter can amplify its own gene expression under Tc treatment via two additional TetO sequences downstream

of the *hSyn1* promoter, potentially allowing reduced viral titers to reach sufficient rtTA expression (Figure 3.23A). *hSyn1*-rtTA and *ihSyn1*-rtTA were designed with a nuclear mScarlet protein (mSc) to follow transduction efficiency and validate neuronal rtTA expression.

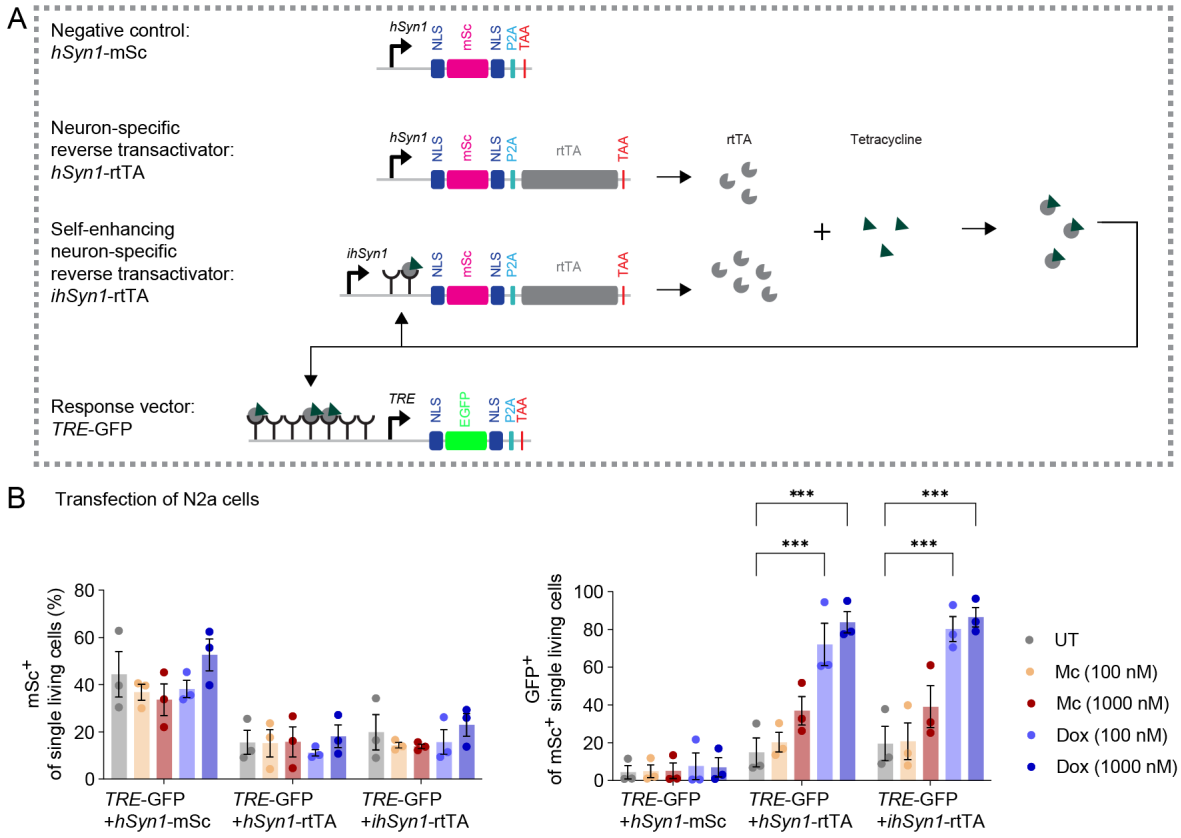

Figure 3.23: **Doxycycline-inducible protein expression in N2a cells by using a TetOn system.**
(**A**) Schematic representation of TetOn system, consisting of response vector *TRE*-NLS-EGFP (*TRE*-GFP) and *hSyn1*-NLS-mSc (*hSyn1*-mSc), *hSyn1*-NLS-mSc-P2A-rtTA (*hSyn1*-rtTA) or *ihSyn1*-NLS-mSc (*ihSyn1*-rtTA). (**B**) Flow cytometry analysis of co-transfected N2a cells with respective plasmid combinations, which were stimulated with indicated compounds 24 h after transfection and then analyzed 24 h later (n = 3 per group). UT, untreated. Data is shown as mean values ± s.e.m. Statistical analyses were performed by two-way ANOVA with comparison to UT and Dunnett's post hoc test in **B**. *P < 0.05; **P < 0.01; ***P < 0.001.

First, the induction of EGFP expression by using the TetOn System was tested *in vitro* by transient co-transfection of N2a cells of the response vector *TRE*-EGFP in combination with one of the rtTA expression plasmids *hSyn1*-rtTA and *ihSyn1*-rtTA, or in combination with *hSyn1*-NLS-mSc as a negative control. The mScarlet frequency was analyzed to control for similar transfection efficiency of the rtTA. Thereby variability in rtTA expression was excluded as a possible confounder of the induction of EGFP expression (Figure 3.23B). Co-expression of the response vector (*TRE*-EGFP) with the negative control plasmid (*hSyn1*-mSc), led to a baseline activity of *TRE*-EGFP of up to 10%, which did not change upon treatment with Dox or Mc. The additional presence of rtTA (*hSyn1*-rtTA or *ihSyn1*-rtTA) without any treatment, increased the EGFP signal up to 20%. Nevertheless, when the cells were treated with Dox, the EGFP expression was induced in a dose dependent manner up to 85% with both, *hSyn1*-rtTA and *ihSyn1*-rtTA. Treatment with 1,000 nM of Mc, induced EGFP expression up to ~40%

with both, *hSyn1*-rtTA and *ihSyn1*-rtTA (Figure 3.23B), thereby being less efficient than Dox treatment. In summary, this indicates, that rtTA-V10 is responsive to Mc, but concentrations need to be increased, as it acts not as potently in this experimental setting as Dox. Moreover, the response vector *TRE*-EGFP displayed a baseline leakiness of gene expression, which was increased with rtTA present. Because both, the *hSyn1* and the self-enhancing *ihSyn1* induced EGFP to the same extend, *ihSyn1* was employed, as this promoter potentially requires lower AAV dosages to reach sufficient rtTA expression, due to its self-enhancing nature.

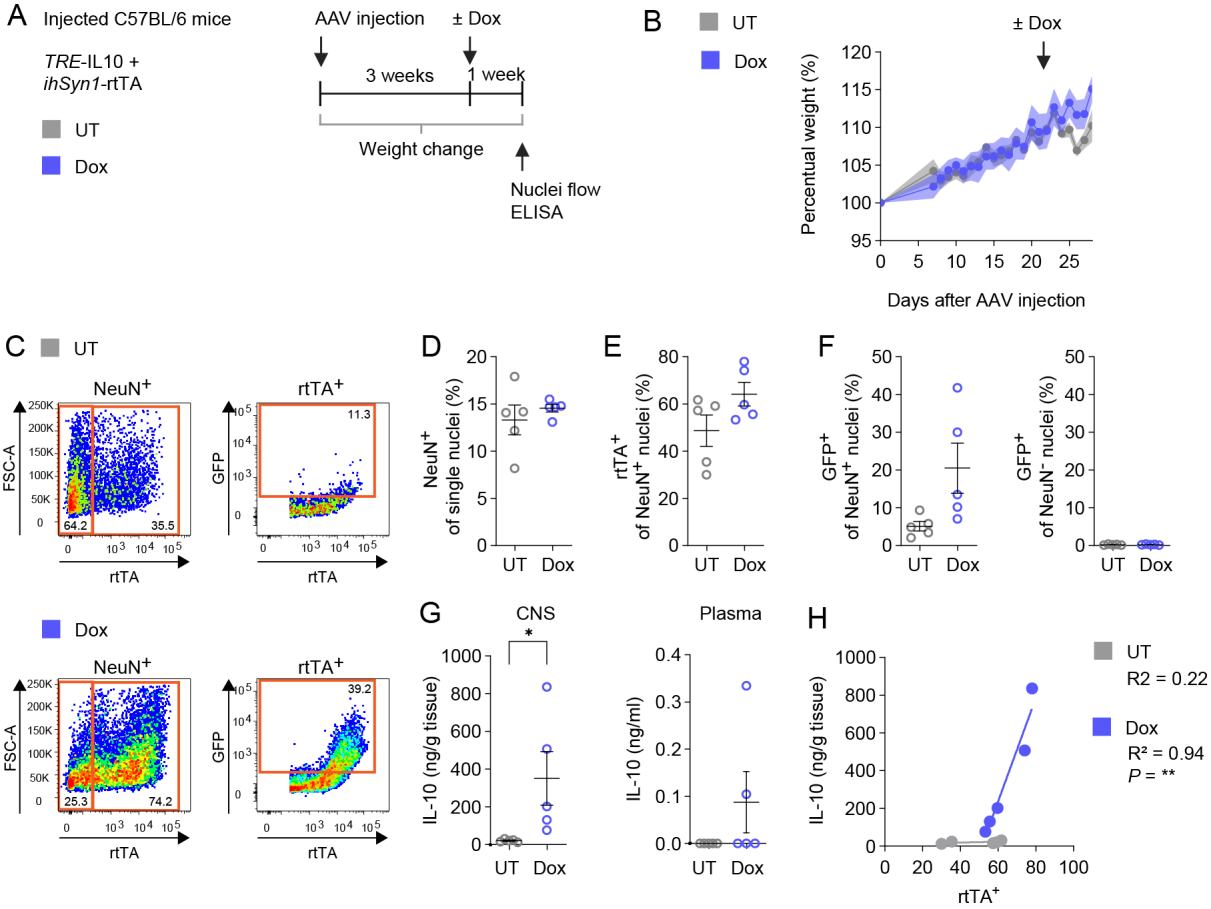

Figure 3.24: **Validation of doxycycline-inducible IL-10 expression *in vivo* by using TetOn system.**
(**A**) Experimental setup for *in vivo* validation of TetOn system. C57BL/6 wild type mice were injected with either AAV-*TRE*-NLS-EGFP-P2A-IL10 (AAV-*TRE*-IL10) or AAV-*ihSyn1*-NLS-mSc-P2A-rtTA (AAV-*ihSyn1*-rtTA). Viral titers of 1×10^{12} vg for AAV-*TRE*-IL10 and 5×10^{11} vg for AAV-*ihSyn1*-rtTA were used (n = 10 mice per group). UT, untreated. (**B**) Weight change after AAV injection. (**C**) Representative gating for flow cytometry analysis of transduction efficiency of rtTA and response vector in the untreated and doxycycline receiving group, measured as the frequency of EGFP$^+$ in NeuN$^+$ nuclei in thoracic spinal cord. (**D**) Flow cytometry analysis of NeuN$^+$ of single nuclei in thoracic spinal cord. (**E**) Flow cytometry analysis of transduction efficiency of AAV-*ihSyn1*-rtTA, measured as the frequency of mSc$^+$ in NeuN$^+$ nuclei in thoracic spinal cord. (**F**) Flow cytometry analysis of AAV-*TRE*-IL10 induction, measured as the frequency of EGFP$^+$ in NeuN$^+$ nuclei in thoracic spinal cord. (**G**) IL-10 protein levels in cortical tissue lysates and EDTA plasma samples measured by ELISA. (**E**) Correlation plot of rtTA expression with IL-10 protein levels in cortical tissue lysates. Data is shown as mean values ± s.e.m. Statistical analyses were performed by unpaired Student's *t*-test in **D**–**G,** and simple linear regression in **H**. **P* < 0.05; ***P* < 0.01; ****P* < 0.001.

After validating the TetOn system *in vitro*, inducible gene expression was tested *in vivo*. Here, the IL-10 overexpressing response vector *TRE*-IL10 was used, to evaluate whether the produced IL-10 levels reach comparable amounts to the constitutive delivery. 8-week-old

female C57BL/6 wild type mice were injected with AAV-*TRE*-IL10 at a dosage of 1×10^{12} vg, and with AAV-*ihSyn1*-rtTA at a dosage of 5×10^{11} vg. The animal diet was changed to doxycycline food pellets for one week for half of the mice, while the other half remained with the regular diet. The animal weight and health were monitored daily until EAE induction to discover possible detrimental effects of the TetOn system (Figure 3.24A). However, mice did not display any signs of weight loss or impaired health (Figure 3.24B). Moreover, the frequency of $NeuN^+$ nuclei did not differ between the groups (P = 0.100, Figure 3.24D). Successful neuronal rtTA transduction was then measured as mSc^+ in $NeuN^+$ nuclei after 7 days of Dox treatment. Both treatment groups showed a sufficient AAV-*ihSyn1*-rtTA transduction efficiency between 50-60%. However, the Dox-treated mice showed higher rtTA expression levels, compared to the untreated control group (P = 0.100, Figure 3.24E). This difference reflects the self-enhancing nature of the *ihSyn1* promoter after Dox treatment. Moreover, the EGFP frequency was analyzed in $NeuN^-$ and $NeuN^+$ nuclei to address the induction of the response vector, the potential baseline activity in untreated control animals, and the neuronal specificity of effector protein expression. The frequency of EGFP expression was induced up to ~20% of $NeuN^+$ nuclei compared to $NeuN^-$ nuclei (P = 0.052, Figure 3.24F). This Dox treatment-induced response vector expression, however, did not reach the same levels of ~70%, that were reached with the constitutive IL-10 overexpression system. Moreover, a base leakiness of ~8% $EGFP^+$ in $NeuN^+$ nuclei was observed in untreated animals. None the treatment groups expressed EGFP in $NeuN^-$ nuclei, which indicates neuronal specificity of the dual vector TetOn system (Figure 3.24F). Next, IL-10 protein levels were measured in the CNS and in the plasma by ELISA, to assess whether this expression pattern was also detectable for IL-10 protein expression. While no IL-10 was detected in untreated animals, mice that received the Dox diet showed significantly elevated IL-10 levels in cortical tissue lysates (P = 0.049, Figure 3.24G), which significantly correlated to rtTA expression in Dox treated animals (P = 0.007, Figure 3.24H). This was not the case for the untreated condition (P = 0.420, Figure 3.24H). This finding indicates, that high rtTA expression is primarily responsible for the induction of IL-10 expression. However, these experimental conditions resulted in only 10% of the IL-10 protein levels that were achieved with the constitutive neuronal IL-10 delivery in cortical tissue lysates. Taken together, inducible neuronal IL-10 expression was achieved by the implementation of a TetOn system *in vivo*, however the experimental setup requires further optimization to reach robust and sufficient response vector induction.

3.6.2 Spatial control of IL-10 delivery by membrane-bound IL-10

Another approach to reduce peripheral side effects and direct the anti-inflammatory effect of IL-10 closer to the neurons, was the development of a membrane-bound version of IL-10 (memIL-10). The goal was to establish a local immune tolerance in the direct proximity of the

neurons by anchoring IL-10 to the neuronal cell surface. This biotechnological modification aimed to reduce peripheral IL-10 protein levels and thereby ameliorate systemic side effects, like the observed splenomegaly following IL-10 treatment. Moreover, facilitating CNS-restricted IL-10 expression might minimize the risk of a potentially impaired clearance of peripheral infections due to peripheral anti-inflammatory activity. To anchor IL-10 to the neuronal cell membrane, three different approaches were explored. The first approach was to employ a GPI anchor to efficiently express proteins on the cellular surface. Two additional delivery plasmids were generated that either contained the transmembrane domains of the surface proteins PD-L1 (tmPDL1) or IL-2Ra (tmIL2Ra) to anchor IL-10 to the outer neuronal cell membrane. Next, the extracellular domain was designed based a patent, that utilizes a membrane-bound version of IL-10 on Treg to increase their tolerogenic capacity (patent number: WO/2019/180724). Specifically, a long glycine-serine peptide (GS) linker was fused to the GPI anchor or the transmembrane domains via a connecting peptide to express IL-10 on the neuronal cell surface. By this means, the GS linker allowed flexible binding of IL-10 to its receptor on target cells, while assuring CNS-restricted expression. IL-10 was either expressed directly as a dimer (2×IL10) connected by a linker, or as a monomer (1×IL10) to then dimerize at the neuronal cell surface to become biologically active. The different combinations of one of the three transmembrane domains in combination with dimeric or monomeric IL-10, resulted in a total of six different constructs, which were generated by molecular cloning (Figure 3.25A).

First, the efficiency of the cellular trafficking to the cell surface was addressed. N2a cells were transiently transfected for 24 h with the respective delivery construct and the frequency as well as the MFI of IL-10 surface expression was analyzed. While the N2a cells that were transduced with the control and soluble IL-10 delivery constructs did not show an IL-10 signal, all memIL-10 constructs expressed IL-10 on the cell surface. The three constructs expressing a dimeric IL-10 protein, reached close to 100% surface expression within transfected N2a cells. However, the constructs expressing a monomeric IL-10 protein showed an overall lower frequency of IL-10 surface expression within transfected cells. Here, GPI-1×IL10 performed the most efficient with ~90%, compared to tmPDL1-1×IL10 with ~60% and tmIL2Ra-1×IL10 with ~20% surface expression (Figure 3.25B). This might partially be explained by less IL-10 protein synthesis per co-expressed EGFP in the individual cells, by potentially impaired cellular trafficking to the cell surface, or by insufficient subsequent dimerization of the IL-10 monomers on the cellular surface. Moreover, culture supernatant of the transfected N2a cells was tested for memIL-10 protein shedding by ELISA. IL-10 shedding was most prominently observed with GPI-2×IL10. However, the protein levels were still three-times lower in comparison to the expression of secreted IL10. The other five tested constructs caused negligible shedding (Figure 3.25C). As the dimeric memIL-10 reached more efficient surface expression than the respective monomeric versions, further validation experiments

were conducted with the three dimeric memIL-10 versions GPI-2×IL10, tmPDL1-2×IL10 and tmIL2Ra-2×IL10.

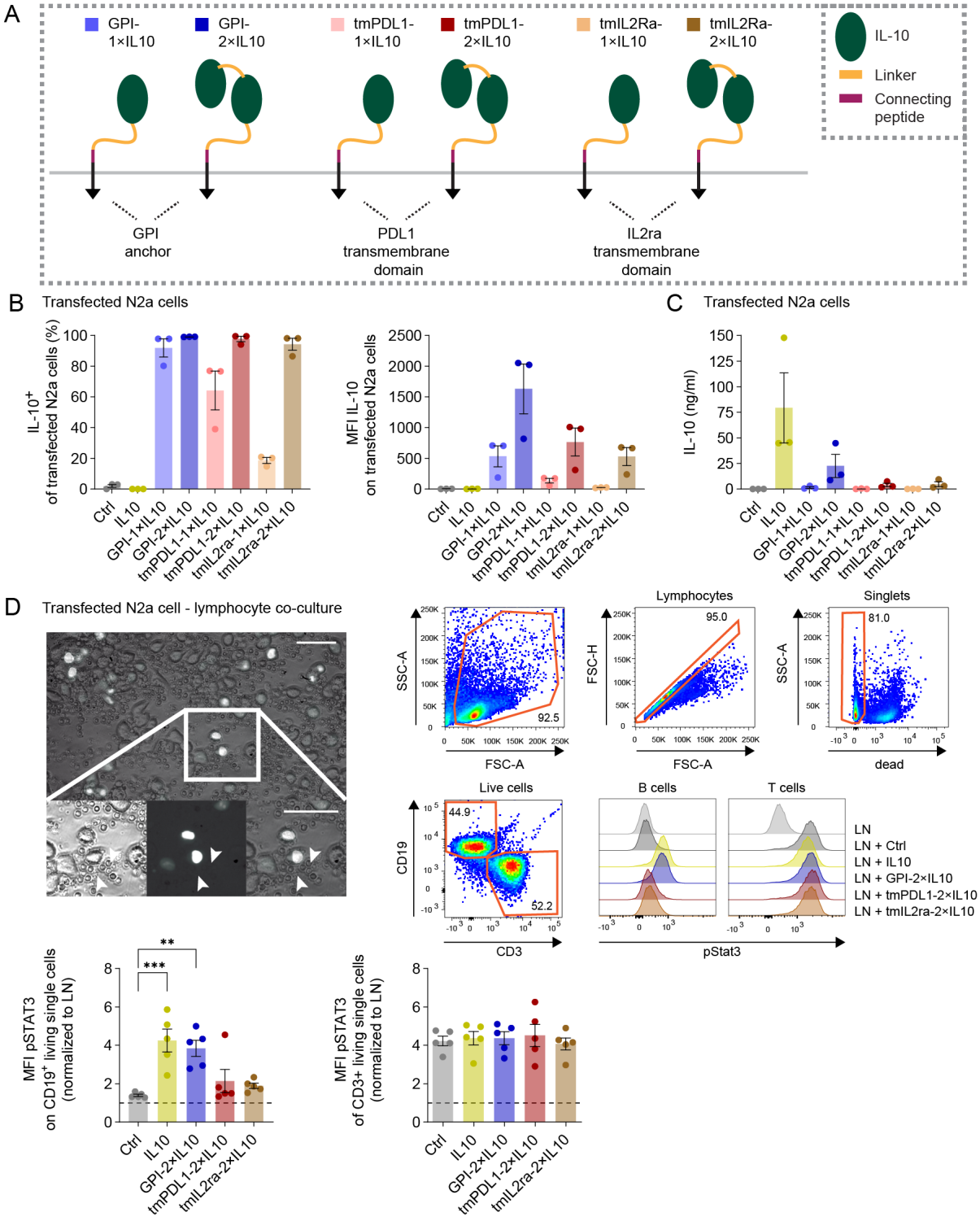

Figure 3.25: Functional IL-10 surface expression by engineering membrane-bound IL-10 in N2a cells. (**A**) Schematic representation of memIL-10, consisting of IL-10 monomer or IL-10 dimer connected by a linker that is bound on the neuronal cell surface via a long GS linker and a connecting peptide with either a GPI anchor or the transmembrane domain of PD-L1 or the IL-2a receptor, resulting in the 6 different plasmid combinations. (**B**) Flow cytometry analysis of IL-10 surface expression or IL-10 median fluorescent intensity (MFI) 24 h after transient transfection of N2a cells with either with either *hSyn1*-NLS-EGFP (Ctrl), *hSyn1*-NLS-EGFP-P2A-IL10 (IL10), *hSyn1*-NLS-EGFP-P2A-GPI-1×IL10 (GPI-1×IL10), *hSyn1*-NLS-EGFP-P2A-GPI-2×IL10 (GPI-2×IL10), *hSyn1*-NLS-EGFP-P2A-tmPDL1-1×IL10 (tmPDL1-1×IL10), *hSyn1*-NLS-EGFP-P2A-tmPDL1-2×IL10 (tmPDL1-2×IL10), *hSyn1*-NLS-EGFP-P2A-IL2ra-1×IL10 (IL2ra-1×IL10), *hSyn1*-NLS-EGFP-P2A-IL2ra-2×IL10 (IL2ra-2×IL10) (*n* = 3 per group). (**C**)

IL-10 protein levels in cell culture supernatant measured by ELISA 24 h after transient transfection of N2a cells (*n* = 3 per group). (**D**) Median fluorescent intensity (MFI) on B cells ($CD19^+CD3^-$) or T cells ($CD19^-CD3^+$) after co-culture with for 24 h transiently transfected N2a cells with the respective delivery plasmid for 30 min (*n* = 5 per group). Scale bar, 50 µm. Data is shown as mean values ± s.e.m. Statistical analyses were performed by one-way ANOVA, comparison to Ctrl with Dunnett's post hoc test in **C** and **D**. **P* < 0.05; ***P* < 0.01; ****P* < 0.001.

To control for the biological activity of memIL-10 and exclude conformational changes of IL-10 due to anchoring to the cell surface, IL-10 downstream pSTAT3 signaling was tested in B and T cells upon encounter with memIL-10 expressing N2a cells. N2a cells were transiently transfected with the dimeric memIL-10 variants and co-cultured with primary murine lymphocytes 24 h later for 30 min. Subsequently, the cells were fixed and the MFI of pSTAT3 was analyzed via flow cytometry. To compensate for intercultural variations, values were normalized to the MFI of pSTAT3 in lymphocytes that were cultured without N2a cells present, as it represents the baseline of endogenous STAT3 phosphorylation in the present experimental conditions. Secreted IL-10 served as a positive control, as the signaling is not dependent on cell–cell contact. T cells already showed elevated pSTAT3 levels in the negative control condition, which did not increase with secreted IL-10, or any of the memIL-10 constructs. However, a significant increase of pSTAT3 was observed in the co-culture with IL-10 secreting N2a cells compared to the control condition in B cells. The pSTAT3 MFI was significantly increased in the co-culture with GPI-2×IL10 (*P* = 0.002, Figure 3.25D). Notably, these findings reflected the amount of shed IL-10 in transfected N2a cell culture supernatants (Figure 3.25C).

In conclusion, this result indicates that the biological activity of memIL-10 in the N2a-mynphocyte co-culture, was most likely not contact dependent but mediated by shed IL-10 present in the culture. Nevertheless, the observed signaling of memIL-10 in B cells, indicate a biological activity of the engineered IL-10 dimer and rule out major conformational changes due to the design of the expression construct. Therefore, two constructs were selected for AAV generation. GPI-2×IL10 was selected as it showed the strongest surface expression as well as the highest pSTAT3 signaling. Due to the fact, that the generation of memIL-10 aimed to restrict IL-10 expression selectively to the neuronal surface, tmPDL1-2×IL10 with a more stable surface expression than with the GPI anchor, was included for further validation. rAAVs were generated and an immunocytochemistry surface staining was performed, prior to fixation and subsequent intracellular staining to verify memIL-10 surface expression after AAV-memIL10 delivery in primary cortical neurons. AAV-GPI-2×IL10 and AAV-tmPDL1-2×IL10 both showed robust IL-10 surface expression, while AAV-Ctrl and AAV-IL10 did not (Figure 3.26A).

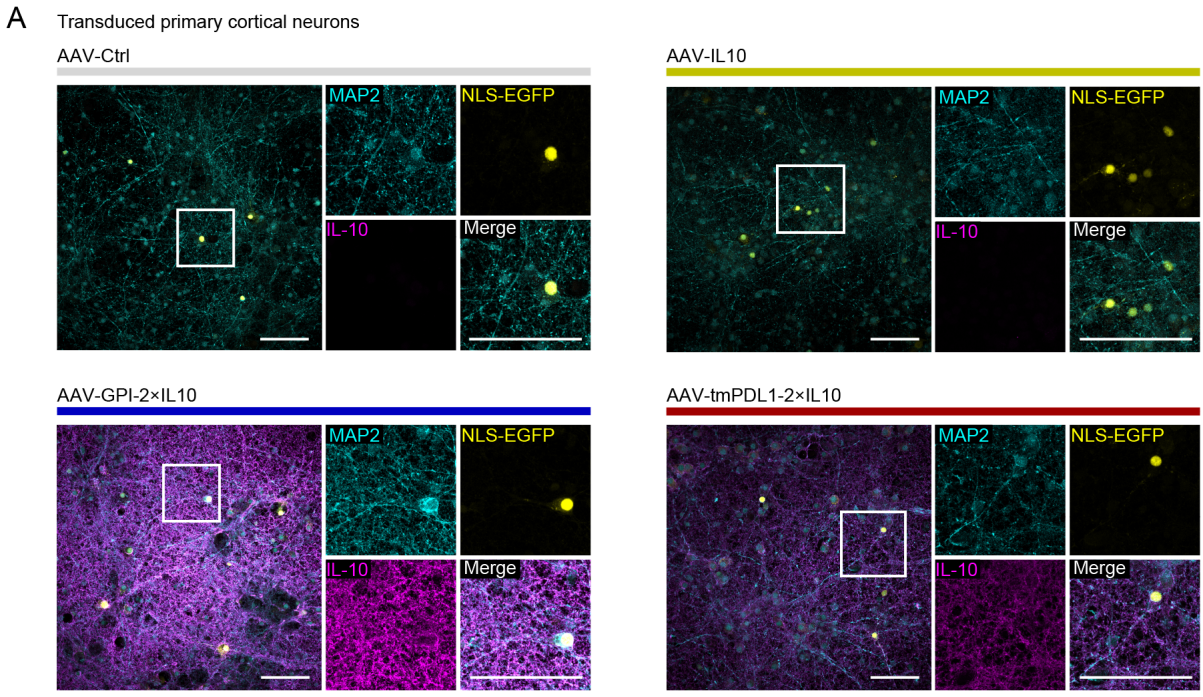

Figure 3.26: **IL-10 surface expression in primary cortical neurons with engineered memIL-10.**
(**A**) Immunocytochemistry of DIV14 primary cortical neurons 7 days after transduction with either AAV-*hSyn1*-NLS-EGFP (AAV-Ctrl), AAV-*hSyn1*-NLS-EGFP-P2A-IL10 (AAV-IL10), AAV-*hSyn1*-NLS-EGFP-P2A-GPI-2×IL10 (AAV-GPI-2×IL10) or AAV-*hSyn1*-NLS-EGFP-P2A-tmPDL1-2×IL10 (AAV-tmPDL1-2×IL10) at a MOI of 50k. Co-staining of IL-10 with MAP2 (dendrites) and endogenous expression of NLS-EGFP (transduced cell). Scale bar, 50 µm.

3.6.3 Delivery of membrane-bound IL-10 in EAE

After the *in vitro* validation of robust and functional surface expression of neuronal memIL-10 the next step was to evaluate its protective potential in the neuroinflammatory disease model EAE. 8-week-old female C57BL/6 wild type mice were either injected with AAV-Ctrl, AAV-GPI-2×IL10 or AAV-tmPDL1-2xIL10, 25 days prior to EAE induction (Figure 3.27A). Daily weight and health monitoring did not indicate any detrimental effects of the AAV treatment, as the mice gained the same amount of weight in both groups (Figure 3.27B). To control for comparable transduction efficiency of the two experimental groups, the frequency of $EGFP^+$ in $NeuN^+$ nuclei was quantified in the spinal cord at the end of the experiment at day 30 after EAE induction. No differences in the frequency of $NeuN^+$ nuclei were detected between the three groups (Figure 3.27C). However, although animals of the control group displayed a stable neuronal transduction efficiency of ~60%, no $EGFP^+$ of $NeuN^+$ nuclei signal was detected in animals, which received AAV-GPI-2×IL10 and AAV-tmPDL1-2×IL10. This finding indicates a general impairment of the transgene expression *in vivo* (Figure 3.27D). As this result was inconsistent with the *in vitro* validation, which showed sufficient nuclear EGFP signal in primary neuronal cultures for both memIL-10 expressing AAVs, the IL-10 protein levels were measured in cortical tissue lysates and EDTA plasma samples via ELISA. In cortical samples, AAV-tmPDL1-2×IL10 treated mice showed significantly elevated IL-10 levels compared to AAV-Ctrl, which were however ~50-fold lower than the protein levels that were reached with AAV-IL10

treatment, the secreted IL-10. AAV-GPI-2×IL10 treated mice did not show increased cortical IL-10 levels (Figure 3.27E). Interestingly, plasma samples revealed elevated IL-10 levels in AAV-GPI-2×IL10 treated mice but not in AAV-tmPDL1-2×IL10 treated mice (Figure 3.27E). This finding suggests that the GPI anchor enables less stable surface expression of IL-10, possibly due to shedding.

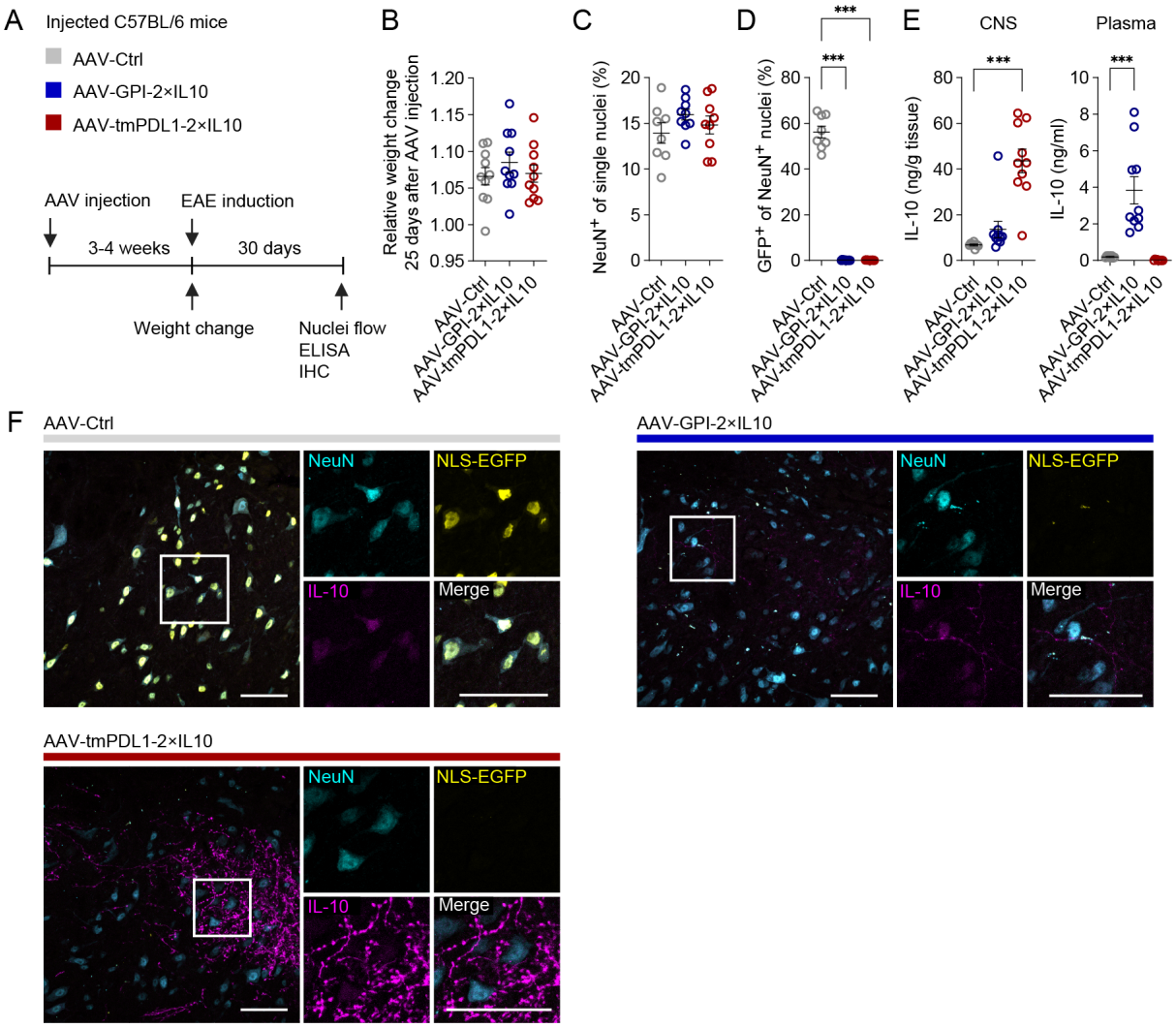

Figure 3.27: **Validation of neuronal memIL-10 delivery in d30 EAE animals.**
(**A**) Experimental setup to test protective potential of neuronal memIL-10 delivery in EAE. C57BL/6 wild type mice were injected with either AAV-*hSyn1*-NLS-EGFP (AAV-Ctrl), AAV-*hSyn1*-NLS-EGFP-P2A-GPI-2×IL10 (AAV-GPI-2×IL10) or AAV-*hSyn1*-NLS-EGFP-P2A-tmPDL1-2×IL10 (AAV-tmPDL1-2×IL10). (*n* = 10 mice per group). (**B**) Relative weight change, 25 days after AAV-injection. (**C**) Flow cytometry analysis of transduction efficiency, measured as the frequency of EGFP$^+$ in NeuN$^+$ nuclei in thoracic spinal cord. (**D**) Flow cytometry analysis of NeuN$^+$ of single nuclei in thoracic spinal cord. (**E**) IL-10 protein levels in cortical tissue lysates and EDTA plasma samples measured by ELISA. (**F**) Immunohistochemistry analysis of cervical spinal cord samples. Co-staining of IL-10 with NeuN (neuronal soma) endogenous EGFP (enhanced by EGFP staining). Scale bar, 50 µm. Data is shown as mean values ± s.e.m. Statistical analyses were performed by one-way ANOVA, Comparison to Ctrl with Dunnett's post hoc test in **B**–**E**. **P* < 0.05; ***P* < 0.01; ****P* < 0.001.

These observations were confirmed in an immunohistochemistry staining in d30 EAE motor neurons of the cervical spinal cord. In agreement with the flow cytometry data, it showed no EGFP signal in NeuN$^+$ nuclei for the two AAV-memIL10 experimental groups. However,

neuronal IL-10 signal was detected in AAV-tmPDL1-2×IL10 but not in AAV-GPI-2×IL10 and AAV-Ctrl (Figure 3.27F). In summary, although EGFP as a reporter for successful transduction was not detectable in NeuN$^+$ nuclei, IL-10 protein levels were still upregulated. Based on these results, both AAV-memIL10 delivery constructs need further optimization, however AAV-tmPDL1-2×IL10 appears to be better suited to restrict IL-10 expression to the CNS.

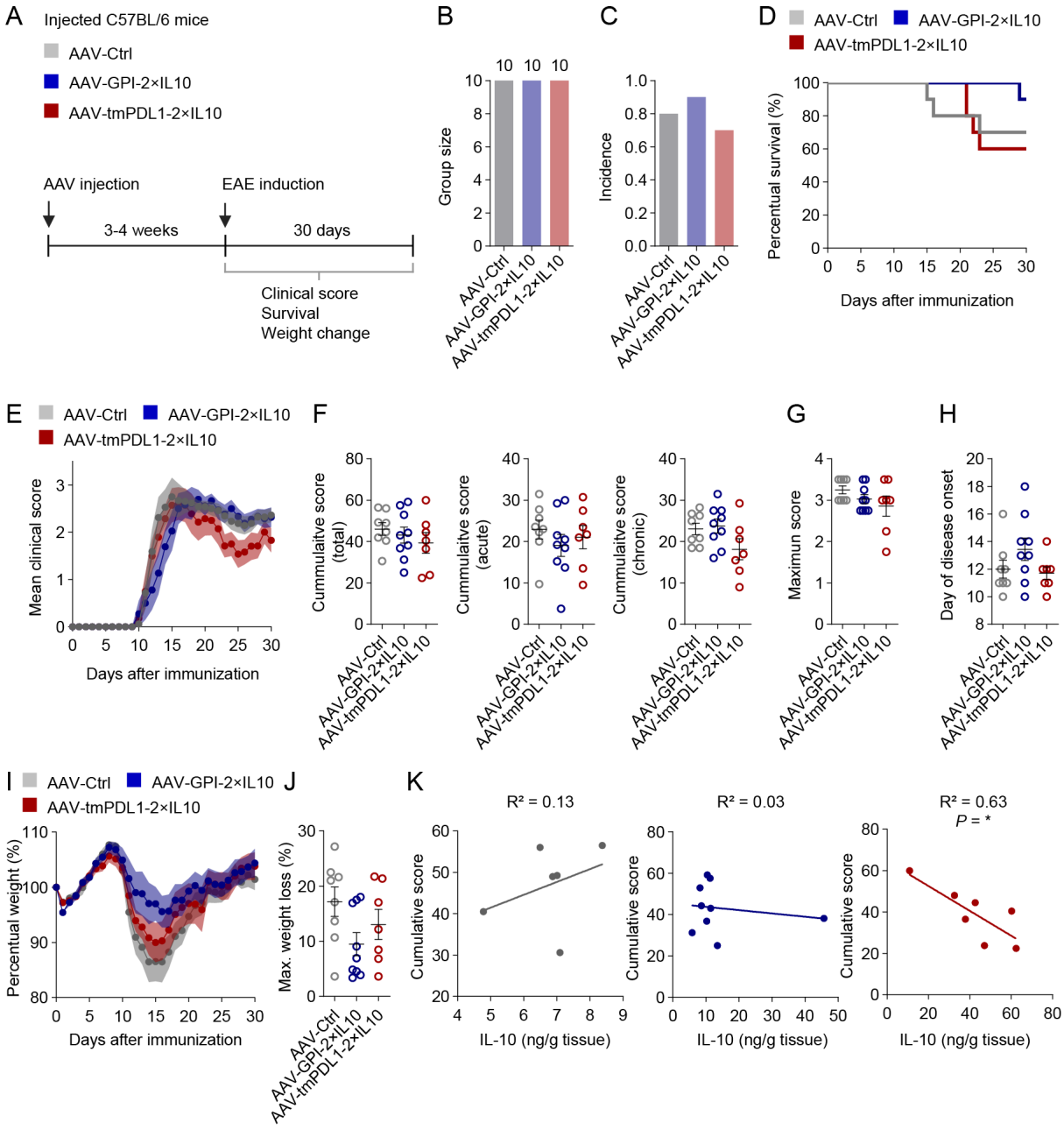

Figure 3.28: **Surface expression of tmPDL1-2×IL10 negatively correlates with cumulative score in EAE.** (**A**) Experimental setup to test protective potential of neuronal memIL-10 delivery in EAE. C57BL/6 wild type mice were injected with either AAV-*hSyn1*-NLS-EGFP (AAV-Ctrl), AAV-*hSyn1*-NLS-EGFP-P2A-GPI-2×IL10 (AAV-GPI-2×IL10) or AAV-*hSyn1*-NLS-EGFP-P2A-tmPDL1-2×IL10 (AAV-tmPDL1-2×IL10). Viral titers of 1×10^{12} vg were used. (**B**) Group size (AAV-Ctrl, *n* = 10; AAV-GPI-2×IL10, *n* = 10; AAV-tmPDL1-2×IL10, *n* = 10). (**C**) Disease incidence. (**D**) Kaplan Meier plot of probability of survival in percent during EAE course. (**E**) Clinical disease course. (**F**) Cumulative scores (acute = d11-d21, chronic = d21-d30). (**G**) Maximal EAE score. (**H**) Day of disease onset. (**I**) Change of bodyweight. (**J**) Maximal weight loss relative to start weight. (**K**) Correlation plots of cumulative scores and IL-10 protein levels of cortical tissue lysates. Data is shown as mean values ± s.e.m. Statistical analyses were performed by Fisher's exact test in **C,** log-rank test in **D,** Kruskal-Wallis test in **F** and **G**, one-way ANOVA with Dunnett's post hoc test in **H** and **J,** and simple linear regression in **K**. **P* < 0.05; ***P* < 0.01; ****P* < 0.001.

To evaluate how these detected IL-10 protein levels after neuronal memIL-10 delivery affect the EAE phenotype, the clinical disability score and the weight of each animal were monitored daily for 30 days (Figure 3.28A). No significant differences were observed in disease incidence (Figure 3.28C) or probability of survival (Figure 3.28D). Moreover, neither the mean clinical score, the cumulative score, the maximum score, the day of disease onset, the percentual body weight change, nor the maximal weight loss were significantly affected (Figure 3.28E-J). However, AAV-tmPDL1-2×IL10 treatment and especially the cumulative scores in the chronic phase appeared to be slightly protective (P = 0.271, Figure 3.28F). To address, if IL-10 protein level in the CNS influenced the EAE phenotype, IL-10 levels in cortical tissue lysates were correlated with the cumulative score to identify a potential causality between neuronal IL-10 surface expression and the clinical outcome. While there was no correlation in the AAV-Ctrl and the AAV-GPI-2×IL10 groups, AAV-tmPDL1-2×IL10 treated mice showed a significant negative correlation between IL-10 protein levels present in cortical tissue lysates and the cumulative EAE score (P = 0.034, Figure 3.28K). In summary, the clinical assessment of EAE after AAV-memIL10 treatment showed no statistically significant benefit in alle analyzed clinical parameters for both of the tested constructs. However, although AAV-GPI-2×IL10 and AAV-tmPDL1-2×IL10 only showed poor transduction efficiency, AAV-tmPDL1-2×IL10 treatment led to IL-10 expression that was restricted to the CNS. The fact, that the cortical IL-10 protein levels correlated to a reduced clinical score, indicates that the neuronal surface expression of IL-10 can indeed pose a promising treatment strategy to counteract neuroinflammation.

4 Discussion

Based on the hypothesis that treatments need to act directly in the CNS to resolve chronic neuroinflammation in MS, an experimental workflow was developed to realize robust neuron-specific targeting for the delivery of different types of effector proteins. The present data provides evidence for the feasibility of mediating neuroprotection in the EAE mouse model, by directly enabling neurons to evade the immune system and thereby limiting resulting neurological impairments. In this context, information was collected on the technical and biological aspects of rAAV-mediated neuronal gene delivery in mice, the therapeutical potential of membrane-bound proteins in comparison to secreted effector candidates and their clinical implication for MS treatment, which will be discussed in the following sections.

4.1 Clinical potential of CNS-directed DMTs

Immune cell accumulation inside the CNS is a main characteristic of MS immunopathology. However, current treatments predominantly act on the peripheral immune system. Although effective in treating relapses, few drugs address disease progression, and interfere with the resulting irreversible neurological impairment[71]. Hence, directing treatments specifically to the CNS holds significant promise for improving the efficacy of anti-inflammatory therapies for MS. Existing DMTs limit CNS-inflammation for example by restricting lymphocyte migration across different physiological barriers, including their egress from the lymph nodes into the blood stream or their crossing of the BBB to infiltrate the CNS. S1PR-modulators including fingolimod trap the lymphocytes inside the lymph node[78]. This mechanism reduces circulating activated immune cells including T and B cells, but also reduces the number of circulating Treg, which are important for maintaining peripheral tolerance[78]. The monoclonal antibody natalizumab inhibits immune cell infiltration of the CNS by binding to the integrin VLA-4, which is localized on endothelial cells of the BBB and assists immune cells to cross[81,92]. Consequently, T cells are trapped in the periphery and CNS inflammation is cut off from a resupply of immune cells from the periphery. However, none of these treatments have the potential to resolve chronic, persistent CNS inflammation, which is a hallmark of progressive MS.

Due to their ability to penetrate the BBB, new therapeutics are currently subject of clinical trials for MS treatment and are interesting candidates to show effectiveness against progredient forms of MS. Two examples are Bruton tyrosine kinase (BTK)-inhibitors and CD19-directed chimeric antigen receptor (CAR)-T cell therapies. BTK-inhibitors unfold their anti-inflammatory potential based on the regulation of maturation, survival, migration and activation of B cells and microglia[253]. B cell depletion therapy with ocrelizumab has already proven to be effective for progredient MS, however with limited efficacy. This is potentially resulting from the poor BBB penetration of monoclonal antibodies[80]. Moreover, the ability to control microglia

activation adds to their potential to resolve persistent inflammation and encouraging data was collected in preclinical and clinical trials[65,253,254]. BTK-inhibitors showed a good safety profile in clinical trials for MS and other autoimmune diseases such as rheumatoid arthritis and systemic lupus erythematosus[255]. Yet, a phase 3 trial for the BBB permeable BTK-inhibitor evobrutinib to treat RRMS, did not result in desired clinical endpoint in comparison to teriflunomide[256].

The second example for CNS-penetrating treatment candidates are CAR-T cells, which are directed against the B cell surface protein CD19[257]. CAR-T cells are engineered by retrieving T cells from individual patients, and their re-administration after equipment with an artificial T cell receptor, which recognizes specific epitopes. In clinical practice, CD19-directed CAR-T cells are commonly used to treat B cell lymphoma, and function by initiating B cell depletion[258]. Because B cell reduction poses an effective target for MS therapy, anti-CD19 CAR-T cell treatment was also tested in a B cell driven EAE mouse model, that relies on immunization with recombinant human MOG protein. The study detected B cell depletion in peripheral tissues and in the CNS[259] and first individual treatments with anti-CD19 CAR-T cell therapy in two patients with progressive MS resulted in an acceptable safety profile[260]. These findings make CAR-T cell therapy a promising candidate for the treatment of progressive MS.

Also, for the delivery of IL-10, which was one of the effector candidates, investigated in this thesis, previous reports highlight the importance for IL-10 to reach the CNS, to biologically influence the EAE outcome and ameliorate clinical symptoms[246,261]. Although IL-10 is a cytokine with pleiotropic immunomodulatory effects, peripheral IL-10 treatment was not sufficient to mediate a protective effect in EAE[262,246]. Preclinical studies identified the localization and timing of IL-10 application to be crucial. Cua *et al.* systematically analyzed different expression systems and administration routes of IL-10 in EAE. They reported an inhibition of the EAE phenotype upon the CNS expression of IL-10[246]. The overexpression of human IL-10 with adenoviral vectors rescued the EAE phenotype after intracerebral but not intravenous administration. Moreover, they reported peripheral IL-10 levels after intracerebral injection that interfered with the T cell priming, when administered before EAE immunization but not later on[246]. While a potent protective effect of IL-10 delivery into the CNS was observed, peripheral T cell priming was found to be unaffected despite detectable IL-10 levels in the serum. In another study, recombinant human IL-10 rescued the EAE phenotype, after intracerebral but not after subcutaneous administration[246]. Due to its short half-life, the recombinant IL-10 had to be administered daily for 5 days. A different study showed that intrathecal injection of rat-IL10 pDNA rescues EAE[263]. Summarizing these findings, IL-10 is a potent inhibitory agent to rescue the EAE phenotype, however several parameters like the administration route, frequency and timepoint have to be tightly regulated to assure the presence of biologically active IL-10 inside the CNS to achieve a beneficial effect.

4.2 AAV-mediated neuron-specific targeting

Effector proteins often act on a multitude of biological pathways across different organs and cell types. Therefore, it is crucial to limit potential organism-wide off-target effects by directing the expression of effector proteins to a specific target cell population. In the previous section, the importance of active therapeutical agents to reach the CNS to treat progredient MS was highlighted. Despite the recent development of promising CNS accessible drug candidates such as BTK-inhibitors and CAR-T cells, these agents still require peripheral administration and therefore are likely to compromise the systemic immune response against pathogens. By using rAAVs to directly express the effector proteins by CNS resident cells, the aim was to minimize their systemic side effects. Neurons were chosen as the target cell population to deliver protection directly to the cell type that suffers continuous degeneration in progredient MS. This was realized by first establishing neuron-specific gene delivery *in vitro* and *in vivo,* before addressing the therapeutic effects of the effector candidates PD-L1, CD200, GDF-15 and IL-10 in the EAE mouse model.

This targeted, efficient delivery was a central corner stone of the gene therapy approaches employed in this work. It was achieved by the establishment of a nuclei flow cytometry-based protocol to routinely validate sufficient efficiency of transgene delivery *in vivo* as a quality control measure for each individual animal. Transfer plasmids were equipped with EGFP, flanked by two NLS, which allowed to identify transduced neurons via the frequency of $EGFP^+$ in $NeuN^+$ nuclei. During the nuclei isolation process, a critical step was to post fixate the tissue for at least 24 h in 4% PFA to preserve the EGFP protein within the nucleus. Compared to previously reported immunohistochemical methods for transduction efficiency analyses, the protocol used here provided significant benefits, including higher sensitivity and sample throughput[171].

In principle, neuronal specificity can be achieved by using a neuron-specific promoter, a neuron-specific AAV serotype, or a combination of both. Here, two CNS-trophic AAV serotypes were systematically studied, namely AAV-PHP.eB and AAV.CAP-B10. Using AAV-PHP.eB in combination with a *hSyn1* promoter resulted in neuron-specific transgene delivery in 70% of neurons and below 1% in non-neuronal cells. The neuronally biased serotype AAV.CAP-B10 in combination with a *CAG* promoter reached similar neuronal efficiency but also revealed significantly higher off-target expression in up to 40% of non-neuronal cells. A more thorough titration of AAV.CAP-B10 between 1×10^{11} vg and 5×10^{11} vg might help to identify a condition that optimally balances transduction efficiency with neuronal specificity. When using AAV-PHP.eB:*hSyn1,* up to 75% of $NeuN^+$ cells were targeted, compared to 90–100% with AAV-PHP.eB:*CAG*. This indicates that despite identical serotypes and thus identical infection patterns, the promoter is taking considerable influence on the overall efficiency. The difference can only be explained by an overall weaker expression of the *hSyn1* promoter, and

/or by its activity in only a subset of $NeuN^+$ cells. Moreover, peripheral rAAV off-target transduction was analyzed, which revealed that AAV-PHP.eB:*CAG* also transduced the peripheral organs liver, kidney, and heart. However, no off-target transduction was detected in the secondary lymphoid organs, spleen, and lymph node. In contrast to this observation, AAV-PHP.eB:*hSyn1* did not cause peripheral transgene expression, which was therefore negligible in this experimental setup.

Moreover, the delivery construct was specifically designed with an N-terminal EGFP, due to the higher expression rate of promoter proximal proteins[247]. This composition ensured a strong EGFP signal that is readily detectable in neuronal nuclei via flow cytometry. The P2A peptide that induces ribosomal skipping of glycyl-prolyl peptide bond formation at the C-terminus, leaves 7 amino acids at the C-terminus of the protein upstream of it while only a single proline at the N-terminus of the downstream protein remains. Therefore, the effector proteins were positioned downstream of the P2A to modify the effector protein as little as possible and limit potential conformational changes. This composition was especially beneficial for secreted proteins as their signal peptide is cleaved off in the ER[264]. This way also the remaining proline from the P2A peptide was removed together with the signal peptide and was not part of the mature secreted protein. One argument to favor C-terminal EGFP, however, is the fact that the effector protein might benefit from higher expression rates when being closer to the promoter. This in turn could allow lower virus titers for sufficient biological activity as it might shift protein expression from EGFP to the effector protein. Moreover, the EGFP protein itself can cause toxicity making lower EGFP expression a desirable feature. Indeed, EGFP toxicity might provide a possible explanation for the observed weight loss in the high dose AAV-PHP.eB:*CAG* injected mice, as this treatment resulted in a very strong EGFP expression in nearly 100% of $NeuN^+$, and 80% of $NeuN^-$ cells. However, no toxicity was observed with the *hSyn1* promoter and importantly sufficient expression of effector proteins with clinically relevant rescue effects was achieved. Finally, for each effector protein it needs to be experimentally evaluated, whether an N- or C-terminal EGFP position is better suited. In general, proteins show differential susceptibility to conformational protein changes due to modifications at the two positions, which can impair protein function. For all plasmids with the N-terminal EGFP used in this study, the correct cellular localization and sufficient expression of the encoded effector proteins were successfully validated.

Delivering a transgene to the CNS via rAAVs not only allowed a neuron-restricted treatment delivery, but also allowed the utilization of C57BL/6 wild type mice to investigate the therapeutic potential of the effector candidates. Traditionally researching the biological function of a protein of interest largely relies on the generation of a genetically modified mouse line, that overexpresses the respective protein. This requires the breeding of high numbers of animals, many of which are needed just to generate, expand, and maintain the line in order to

generate experimental animals. Using the rAAV-based approach relying on wild type animals not only enabled a quicker experimental timeline, but also reduced the total number of required animals. Moreover, rAAV administration in adult mice circumvented developmental effects in mice due to lifelong protein overexpression, thus minimizing animal burden. For constitutive delivery of transgenes, 3–4 weeks were sufficient to reach complete, robust transgene expression. However, in future experiments, the rAAV-pretreatment time might be further reduced to 2–3 weeks as weight loss and therefore sufficient biological activity of GDF-15 were observed starting at day 10 after rAAV injection.

The present investigations rely on harnessing the neuroprotective potential of equipping neurons with immune evasive mechanisms and externally downregulating inflammatory activity. The concept of neuron-specific delivery of transgenes can further be expanded for equipping neurons with intracellular protective effector candidates to strengthen neuronal resilience. Due to their post mitotic nature, targeting the neurons could be most valuable for long-term protection after a single rAAV administration. Nevertheless, sustained expression could potentially result in adverse effects by disrupting neuronal function, raising concerns regarding treatment activity persisting beyond the resolution of the disease. Depending on the research question, rAAV mediated gene delivery can also be used to target other CNS resident cell populations[166]. For example, astrocytes might be a promising target population due to their ability to regenerate, unlike post-mitotic neurons. The specific astrocytic transduction could be facilitated by switching the promoter to the astrocytic glial fibrillary acidic protein (*GFAP)* promoter[265]. Moreover, the fact that the *GFAP* promoter expression increases in activated astrocytes and might therefore enable enhanced gene expression in inflammation[266]. This concept of astrocytic gene delivery was for example explored, by Yshii e*t al*. to combat neuroinflammation, by locally producing IL-2, which served as a survival signal for brain-resident anti-inflammatory Treg[166].

4.3 Creating a tolerogenic neuronal microenvironment

After the successful establishment of neuron-specific gene delivery following peripheral administration, the goal was to direct the anti-inflammatory activity as close as possible to the site of neuronal damage, while avoiding spillover into the systemic compartment. This aim was addressed by following two different strategies. The first approach was to express the anti-inflammatory proteins PD-L1 or CD200 on the neuronal cell surface and thereby counteracting inflammatory activity in the direct vicinity of neurons. This local treatment approach limits off-target activity of the effector proteins but might also limit therapeutical activity due to the spatial restriction. The surface expression of anti-inflammatory proteins requires direct cellular interaction of the neurons with a cell that expresses the cognate receptor. In case of PD-L1, mainly antigen activated T cells express the PD-1 receptor[192], in case of CD200, the

prospective target cells mainly consist of myeloid cells and microglia that prominently express CD200R1[201]. The second approach was to enable the neurons to secrete the anti-inflammatory molecules GDF-15 and IL-10 and thereby target immune cells more distant from the neurons. The neuron derived secretion of the cytokines established an anti-inflammatory gradient around the neurons, with highest activity closest to the neurons. However due to CNS draining fluids and an impairment of the BBB in EAE, this approach harbored a greater risk of peripheral leakage and therefore of causing systemic side effects.

Despite successful delivery of PD-L1 surface expression *in vitro* and *in vivo*, no protection was observed in the EAE mouse model. As a lack of PD-L1 was reported to worsen the EAE phenotype[194] and the peripheral administration of a PD-L1 Fc fusion protein was shown to act beneficially[198], this result was unexpected. Two different hypotheses might explain this observation. Firstly, the neuronal cell surface might be a suboptimal localization of PD-L1 expression in this disease context. In the EAE mouse model the T cells are primed against $MOG_{35–55}$, which marks oligodendrocytes as the primary target cell population in the CNS. Therefore, a PD-L1 mediated antiproliferative effect on T cells, might be more effective when expressed by oligodendrocytes or astrocytes to facilitate a broader effector candidate distribution also including the white matter. A positive control experiment could be by ubiquitously expressing PD-L1 in the CNS with the *CAG* instead of the *hSyn1* promoter. Addressing the therapeutic potential of a CNS-wide delivery of PD-L1 could identify if the neuron-restricted PD-L1 expression resulted in limited protective potential. The second possible explanation is based on the observations that PD-L1 is already upregulated in the CNS during inflammation[68]. Therefore, the additional expression, which was validated via western blot, might not have an additional protective effect, because down-stream signaling cascades are already fully activated.

Similar to the effector candidate PD-L1, the neuronal surface delivery of CD200 did not result in an ameliorated EAE phenotype. In previous preclinical studies, a lack of CD200 led to more severe EAE and the administration of a CD200 Fc fusion protein indicated the potential of CD200 to resolve inflammation and prevent neuronal damage[205,206]. Also in this thesis, AAV-CD200 treatment showed slight beneficial effects that were not significant due to the small effect sizes. To proof the robustness of these findings, the next step would be to repeat the EAE experiment and address whether a larger group size is required to show significant protection. A possible reason for limited efficacy of AAV-CD200 treatment could be, that the EAE is a T cell driven mouse model and macrophages and microglia, which are the major target cell population of CD200, play a subordinate role in EAE disease development[86].

In summary, neither of the initial strategies to protect neurons by surface expression of the co-inhibitory proteins PD-L1 and CD200, resulted in significant amelioration of the EAE course. Therefore, the next step was to investigate whether the establishment of a wider anti-

inflammatory microenvironment around the neurons and consequently targeting a broader spectrum of inflammatory immune cells, results in a more successful protection. Neuronal GDF-15 as well as IL-10 delivery led to a rescue of the EAE phenotype, accompanied by a significant reduction of CNS-infiltrating immune cells. To control for the CNS restriction of secreted GDF-15 or IL-10, peripheral protein levels were measured. Significant peripheral leakage was detected for both secreted effector proteins. While the T cell priming for AAV-IL10 treated mice remained intact, impaired T cell priming was observed for neuronal GDF-15 delivery. Another striking observation of AAV-GDF15 treatment was a significant weight loss, which caused additional animal burden during the EAE experiment. Two major points need to be addressed to pinpoint the capacity of GDF-15 of mediating neuroprotection during EAE directly to CNS-specific expression and not systemic presence of the protein. Firstly, the function of GDF-15 to cause substantial weight loss, poses a confounding factor for interpreting the lack of clinical EAE symptoms, because intermittent fasting is reported to ameliorate the EAE phenotype and to suppress the secretion of IFN-γ and TNF-α, which was accompanied by increased IL-10 production in splenocytes[267]. Secondly, the potentially impaired T cell priming requires experimental adjustments. These issues can be addressed by a reduction of the rAAV dosage per animal. Resulting lower GDF-15 levels in the CNS might also reduce the metabolic GDF-15 effect and therefore result in less weight loss. Moreover, this might lead to lower peripheral GDF-15 levels and allow intact T cell priming against $MOG_{35–55}$. Impaired T cell priming could further be addressed by a later rAAV administration timepoint or by using the inducible TetOn system. After successful reduction of GDF-15-mediated adverse effects, the next step would be to assess if thereby resulting lower GDF-15 proteins levels, still have the capacity to resolve neuroinflammation in EAE.

Similar to the observations for GDF-15, neuronal delivery of IL-10 led to a profound rescue of the EAE phenotype, accompanied by a significant reduction of CNS-infiltrating immune cells. However, in contrast to GDF-15, the T cell priming remained intact after neuronal IL-10 delivery despite increased peripheral levels of IL-10. The characterization of the immune cell phenotype in peripheral and CNS-infiltrating immune cells at the acute phase of EAE, revealed an alteration of a variety of immune cell subsets in their frequency and their inflammatory potency. CNS-infiltrating macrophages, $CD4^+$ T cells, granulocytes and DCs were significantly reduced in AAV-IL10 treated mice. In the CNS $CD4^+$ T cells of AAV-IL10 treated mice were not only lower in frequency but also downregulated CD44, which implied less $CD4^+$ T cell activation and a potentially reduced effector function. Moreover, CNS-infiltrating $CD8^+$ T cells produced less IL-17, and were therefore contributing to an overall decreased inflammatory activity of the infiltrate[268]. Healthy animals showed increased Treg frequencies in secondary peripheral lymphoid organs after AAV-IL10 treatment, which might partially contribute to the ameliorated EAE phenotype after neuronal IL-10 delivery. During the

acute phase of EAE the Treg frequencies did however no longer differ in all analyzed tissues. Due to the rather multifaceted changes in number and phenotype of infiltrating immune cell subtypes, more detailed investigation is needed to identify which of the observed immune effects of AAV-IL10 treatment is causal for the EAE rescue. The question of which immune cell population is mainly responsible to mediate the protective effect in this experimental setting, could be addressed by using cell type specific *Il10ra*$^{-/-}$ animals. More specifically, knocking out IL10Ra in T cells (CD4-Cre), myeloid cells (LysM-Cre), Treg (FoxP3-Cre) and Th17 cells (IL-17a-Cre) would allow to disentangle the contribution of each of these cell types to the IL-10 mediated rescue of EAE disease activity.

While the two surface proteins PD-L1 and CD200 did not mediate the desired effect, the two secreted effector candidates GDF-15 and IL-10 rescued the EAE phenotype. The collected data indicates a peripheral suppression of EAE induction by neuronal GDF-15 delivery, while for AAV-IL-10 treatment a diverse modulation of different immune cell subsets was observed. As neuronal delivery of secreted IL-10 showed a protection against EAE, but also caused peripheral immunological side effects, a membrane-bound IL-10 protein was engineered to restrict the IL-10 activity to the CNS. Neuronal surface expression of IL-10 correlated with a reduced EAE score. A possible explanation might provide the broader spectrum of target immune cells of IL-10, compared to PD-L1 or CD200. Therefore, the neuronal cell surface can be the correct localization of anti-inflammatory treatments in general, PD-L1 and CD200 however, potentially did not address the correct target cell population in an efficient manner.

4.4 Temporal and spatial control of IL-10 delivery

The fact that previous studies reported that IL-10 presence in the CNS was needed to ameliorate EAE disease severity[246], hints towards a direct effect of IL-10 on cells within the CNS including both CNS-infiltrating and CNS-resident cells. Two biotechnological approaches were realized to direct the anti-inflammatory activity of IL-10 more specifically towards the CNS. The first approach was to implement the inducible TetOn system to activate neuronal IL-10 expression at first occurrence of clinical symptoms, after immune cell infiltration. The second approach was to spatially restrict IL-10 expression to the neuronal cell surface to prevent protein leakage into the periphery. This was achieved by development of a membrane-bound version of IL-10.

TetOn systems present an effective tool to facilitate inducible gene expression. Sufficient protein induction upon Dox treatment and a minimal baseline leakiness without Dox treatment were validated *in vitro* and *in vivo*. Prior to applying the technology *in vivo*, the TetOn system was characterized for efficiency and potential leakiness *in vitro*. *TRE*-EGFP displayed a baseline activity of up to 10% without the presence of the rtTA, which did not increase under

the influence of Dox or Mc treatment. This suggests that a general base leakiness of the *TRE* promoter occurs independently of rtTA binding and of the drug treatment and needs to be considered. Nevertheless, also the addition of rtTA, increased the base line protein expression by another 10% without Dox treatment.

When applying this technology *in vivo*, IL-10 levels after Dox treatment in cortical tissue lysates were significantly elevated, however still ~10-fold lower than with the constitutive AAV-IL10 delivery. The cortical IL-10 levels correlated with the percentage of rtTA expressing $NeuN^+$ nuclei. Thus, a possibility to amplify the IL-10 protein induction, is by increasing rtTA dosage in future experiments. However, the *in vitro* characterization suggested that an increase of rtTA levels, could also create more leakiness of the *TRE* promoter in untreated mice. Moreover, using the TetOn system, caused reduced peripheral IL-10 levels compared to the constitutive delivery, which might contribute to reduced peripheral off-target effects. This can be explained by lower *TRE* promoter strength or the shorter expression time of 7 days, compared to 28 days of constitutive neuronal IL-10 expression. Another benefit of the application of an inducible system, is the possibility to also turn off protein expression upon withdrawal of the Dox treatment when the inflammation of the CNS is resolved. This could ultimately provide the experimental setup to start treatment at the beginning of clinical symptoms and therefore mainly act on CNS inflammation rather than causing peripheral immune cell alterations. Of note, this concept to mimic neuronal gene therapy as a treatment for acute symptoms, could also be transferred to other effector candidates like memIL-10 in the future.

Despite the fact, that the TetOn system presented a robust tool to achieve inducible gene expression, it was dependent on administration of two individual rAAVs. This resulted in a higher total virus load per mouse of 1.5×10^{12} vg/animal, compared to the constitutive delivery with 1×10^{12} vg/animal, which in turn could result in a stronger inflammatory response of the host immune system to the rAAV[269–271]. Moreover, it requires additional Dox administration to induce transgene expression, which itself can cause adverse effects such as gastrointestinal symptoms and phototoxicity[272]. An alternative biotechnological solution to finetune IL-10 expression and restrict it to the timepoint of clinical symptom development, is to employ a self-inducing system, which is responsive to inflammation. One example for such a promoter system was published by Greensphan *et al.*, which induces gene expression upon recognition of inflammatory cytokines[273]. Here, the transgene is encoded under the control of a minimal promoter which initiates transcription after the binding of IFN-y and TNF-α to a responsive genetic element upstream of the promoter. The employment of this self-inducing promoter in the EAE mouse model has the capacity to initiate neuronal gene expression by the CNS-infiltrating immune cells themselves, and their release of inflammatory cytokines. Once the inflammation is successfully cleared, the promoter becomes inactive again, and the gene expression is silenced. This would allow a very tight dose-regulation of IL-10 treatment. The

self-inducing promoter that has been developed by Greensphan *et al.,* is however not cell-type specific and would require the delivery with an rAAV with neuronal tropism.

As an alternative approach to address neuroinflammation in a CNS-restricted manner a membrane-bound IL-10 was developed. Although AAV-memIL10 showed sufficient surface expression in primary cortical neurons and a beneficial tendency in the EAE mouse model with both AAV-GPI-2×IL10 and AAV-tmPDL1-2×IL10, the lack of nuclear neuronal EGFP signal and therefore low transduction efficiency remains a technical issue, which needs to be resolved. The discrepancy of rAAV transduction efficiency between *in vitro* and *in vivo* might be explained by three possible hypotheses. The first reason for insufficient transduction might be a less potent rAAV preparation, that comprised less functional viral particles. This can happen for example when the viral preparation consists of a high amount of empty rAAV capsids. A second reason for the generation of impaired rAAVs is recombination of the transfer plasmid due to the two repetitive IL-10 sequences. Yet, this massive reduction of transduction efficiency to only 1% of $NeuN^+$ cells, should have already been visible *in vitro*, if it was caused by non-functional rAAVs. The third hypothesis is a possible ITR recombination after the plasmid preparation for rAAV production. Despite a routine performance of a control digest with the restriction enzyme SmaI, which cuts within the ITRs, minor changes that do not affect the restriction sites would be hard to detect. Undetected mutations could potentially interfere with concatemerization to form more stable endosomes by the rAAV *in vivo*[154]. Troubleshooting of this issue would include whole plasmid sequencing to verify the ITR integrity and construct optimization by diversification of one of the repetitive IL-10 coding sequences, to circumvent possible recombination of the IL-10 dimer.

Although the treatment of mice with AAV-memIL10 reached only a very low transduction efficiency, IL-10 protein levels in the CNS and the plasma were analyzed to address whether neuronal surface expression of IL-10 results in CNS-restricted protein expression. Interestingly, AAV-GPI-2×IL10 treated mice showed elevated peripheral IL-10 levels, while in AAV-tmPDL1-2×IL10 treated mice, the elevated IL-10 levels were restricted to the CNS. This indicated that, AAV-GPI-2×IL10 was more prone for shedding from the neuronal cell surface than AAV-tmPDL1-2×IL10. Moreover, the cumulative EAE score of AAV-tmPDL1-2×IL10 treated mice correlated with IL-10 levels present in the CNS, which was not true for AAV-GPI-2×IL10 treatment. The fact that only few transduced cells were already able to influence the clinical EAE score, hints towards a potent protective potential of AAV-tmPDL1-2×IL10 against neuroinflammatory damage in EAE. In summary this data suggests that by neuronal delivery of memIL-10 with AAV-tmPDL1-2×IL10, neurons can be equipped with biologically active IL-10 on the cell surface, which needs however further optimization.

4.5 From proof of concept to clinical care

Before a new treatment can be approved for clinical use in humans, it must undergo several phases of clinical studies. Preclinical studies investigate the treatment potential of a therapeutic drug or strategy and establish safety and dosage parameters. The next step is the progression of investigational treatments to phase 1 clinical trials, where their safety and dosage are further evaluated in a small group of healthy human volunteers. Phase 2 trials then assess the treatment's efficacy in a larger cohort, while phase 3 trials confirm its effectiveness and monitor for adverse effects in a diverse patient population[274]. These trials conclude in regulatory review, where successful outcomes pave the way for approval and widespread availability.

The majority of preclinical studies rely on the utilization of animals to model the human situation and provide mechanistic proof of concept for disease pathophysiology or therapeutic potential of novel treatment approaches. A key aspect here is to investigate the required treatment dosage to observe the desired biological effect *in vivo*, while recording evidence concerning possible side effects of the treatment. In this work, based on the systematic titration experiments, 1×10^{12} vg/animal was identified as the required rAAV dosage to target the majority of neurons in the CNS. Although the systemic delivery in humans can go up to 1.5×10^{17} vg this would translate to immense titers in humans, which might cause substantial side effects, such as host immune responses towards the rAAV and hepatotoxicity as well as high production costs for clinical rAAV treatments[275]. Potential side effects can either be caused by off-target activity of the treatment or by the rAAV itself. Within the present experimental conditions, one detrimental effect was the weight loss upon treatment with AAV-*CAG*-EGFP*,* which led to early termination of these animals. Based on the fact that up to 100% of neuronal and up to 80% of non-neuronal cells were targeted by using the strong *CAG* promoter, a possible explanation might be toxicity due to high EGFP levels[276]. Yet, other groups used even higher titers of AAV-*CAG*-EGFP with 5×10^{12} vg/animal without reporting detrimental effects[171]. However, rAAV titers might not be directly comparable, as they can vary depending on the primers, which are used for qPCR-based quantification[277]. Moreover, rAAV preparations contain between 20% to over 98% empty capsids and therefore the viral activity can differ between preparations[278].

Since the 80s not only rAAVs have been harnessed for DNA delivery[150], but also several other viruses such as retrovirus[279,280], adenovirus[281] and herpesvirus vectors[282]. Although the immunotoxicity of rAAVs is lower in comparison to adenoviral or lentiviral vectors, high rAAV doses still resulted in deaths in clinical trials. One example is a patient that was treated with rAAV carrying dSaCas9-VP64 to up-regulate cortical dystrophin in an attempt to treat Duchenne's Muscular Dystrophy[283]. However, it is impossible to disentangle, whether adverse effects are caused by the rAAV itself or by the cargo. Nevertheless, rAAV treatments

can activate the innate immune system via PRRs, TLR9 and TLR2[269]. Moreover, also the adaptive immune system can get activated as seen in the killing of transduced cells by cytotoxic T lymphocytes that were activated via MHCI[270]. Also, humoral responses to the wild type AAV in humans such as neutralizing antibodies (NAbs) play a role. NAbs were either described to trigger an overshooting immune response to treatment but also to diminish vector efficacy[271]. Therefore, evidence of pre-existing NAbs is a common exclusion criterion in clinical studies which are based on viral delivery[284]. In addition to immunogenic reactions to the rAAV treatment, hepatotoxicity poses another major side effect that led to a patient's death in the treatment of X-linked myotubular myopathy due to cholestatic liver failure following gene therapy[285]. Besides viral vectors, other delivery routes to target the CNS have been developed and applied in clinical treatments. One example are liposomes, which comprise of lipid bilayers, that are used to enrich small molecules, peptides, proteins, and nucleic acids in the brain[286]. They can carry both hydrophilic as well as hydrophobic molecules and can cross the BBB endothelial cells by carrier-/ receptor- or adsorptive-mediated transcytosis, depending on the liposomal surface design[287–290]. Another strategy applied in the clinic are cyclodextrins, which are cyclic, non-reducing oligosaccharides composed of glucopyranose units[291] that are used for delivery of the Parkinson's disease drug L-DOPA[292].

Despite immunological effects on the host, rAAVs were the first viruses that were approved for human therapy with tiparvovec in 2012, designed to reverse lipoprotein lipase deficiency[293]. Since then, other gene therapies have been approved like abeparvovec for the treatment of spinal muscular atrophy by intravenous administration of AAV9 carrying the *SMN1* gene[294]. The exogenous delivery of genes is a straightforward approach for gene therapy, as it does not interfere with endogenous genomic material and can either be harnessed as genome replacement of a missing or malfunctioning gene, or by the introduction of a new protein to deliver protection to receiving cell. Nonetheless, DNA editing with clustered regularly interspaced short palindromic repeats (CRISPR), or RNA editing with antisense oligonucleotides (ASOs) are also being developed[295]. Gene therapy is appealing because it only requires a single injection for long term effects, however it needs a careful consideration of the advantages and the risks as the administration is irreversible.

Another major aim of preclinical animal studies is the identification of the efficacy of the potential new treatments. In addition to providing a technical workflow to address the therapeutic potential of effector proteins in neurological diseases, this thesis investigated the potential to ameliorate the EAE phenotype by equipping neurons with immune evasive mechanisms. Both blocking and stimulation of immune checkpoints have shown immense potential to clinically treat inflammatory diseases[296,297]. Inhibiting immune checkpoints with monoclonal antibodies emerged to be a potent immunotherapy of cancer, including anti-PD-1 agents like nivolumab and pembrolizumab, anti-PD-L1 agents like atezolizumab, and anti-

CTLA4 agents like ipilimumab and tremelimumab[296]. These inhibitors target molecules expressed by immune cells, preventing their deactivation, and enabling them to remain active against tumors. More recently, a combination therapy of anti-LAG3 (relatlimab) and anti-PD-1 (nivolumab) received approval for the treatment of unresectable or metastatic melanoma[298]. While not yet approved for clinical use, checkpoint inhibitors targeting myeloid cells directly or the interaction between T cells and myeloid cells, are under investigation in clinical trials. For instance, a phase 1 study of anti-CD200 treatment (samalizumab) for chronic lymphocytic leukemia and multiple myeloma demonstrated a reduction in circulating $CD200^{+}CD4^{+}$ T cells[299].

The present thesis on equipping neurons with immune evasive defense strategies to combat neuroinflammation in the EAE mouse model, revealed IL-10 as a promising candidate, while PD-L1, CD200 and GDF-15 showed limited potential. However, in addition to observing a rescue of clinical symptoms, peripheral off-target effects were detected as a result of neuronal IL-10 delivery, such as an enlargement of the spleen together with a total increase of splenic immune cells. Cardoso *et al.* propose a possible explanation for this finding, as they describe increased myelopoiesis to cause splenomegaly upon IL-10 treatment[300]. In addition to IL-10 specific aspects, general off-target effects of systemic anti-inflammatory treatments pose a significant risk for impaired clearance of infections by the immune system this kind of side effect needs to be addressed in peripheral and CNS infection models before moving into clinical trials.

Due to its pleiotropic effects in fine tuning the immune system, IL-10 has been subject of various clinical trials for disease with immune system contribution, such as Crohn's disease, rheumatoid arthritis (RA), psoriasis and solid tumors[301]. Based on the knowledge that *Il10*$^{-/-}$ and *Il10r*$^{-/-}$ mice develop colitis[302], and its contribution to inflammatory bowels disease (IBD), human recombinant IL-10 has been subject of clinical studies for Crohn's disease (CD) in the early 2000s. The administration of recombinant IL-10 was reported to be safe and well tolerated[303]. Yet, the clinical benefit has been conflicting[304–306], most likely due to the heterogeneity of already elevated IL-10 serum levels in people with CD[307]. To harness IL-10 for the treatment of RA, F8 a human antibody against fibronectin was fused to IL-10. F8-IL10 has been tested in a phase 1 clinical trial for rheumatoid arthritis and is currently subject of a phase 2 trial. However approvals of new agents for the same indication have significantly slowed down the recruitment of probands[308]. The stimulating effect of IL-10 on $CD8^{+}$ T cells is subject of drug development for cancer treatment. PEGylated IL-10 induces systemic immune activation, $CD8^{+}$ T cell invigoration and polyclonal T cell expansion in people with cancer[309]. A phase 1 study was successful in combination with anti-PD-1 treatment[310]. In addition to its immunological function, IL-10 also has neuroprotective effects like the promotion of tissue regeneration after spinal cord injury[311,312]. However, in transgenic animals chronically

overexpressing IL-10 by astrocytes, a disruption of the microglia-neuron dialogue was observed, which resulted in impaired hippocampal neurogenesis and spatial memory[313].

4.6 Conclusion and outlook

In this work, neurons were equipped with mechanisms to evade neuroinflammation. IL-10 was identified as a promising effector candidate to limit neuronal damage in EAE and potentially MS. To leverage IL-10 treatments for the clinic, more mechanistic data has to be compiled and the precise mode of action of the IL-10-mediated EAE rescue has to be unraveled. Neuronal IL-10 treatment in cell type specific *Il10ra*$^{-/-}$ animals, is suited to address the contribution of different immune cell populations. After the establishment of proof of concept for inducible IL-10 delivery with the TetOn system in this work, a possible next step is to conduct an EAE with different Dox treatment regimens to explore which phase of the disease most prominently benefits from IL-10 delivery. Moreover, the implementation of a self-inducing gene expression system, would allow for autonomous and needs-based regulation of effector protein expression during inflammation of the CNS. Although AAV-memIL10 still needs further optimization to secure sufficient neuronal transduction, the present data indicates a high potential as a treatment strategy for combating neuroinflammation. However, these findings need to be addressed in an additional EAE experiment, after successful optimization of neuronal memIL-10 delivery. Moreover, a detailed characterization of the immune cell infiltrate by flow cytometry at the acute phase of EAE after AAV-memIL10 treatment will further identify which immune cells are the most affected and are therefore directly attacking neurons in EAE. The results of the proposed experiments will aid the identification of the optimal delivery system and biological modification of neuronal IL-10 delivery to treat MS. After successful implementation of CNS-restricted IL-10 treatment, an essential additional control experiment is to address a possible impairment of infection clearance under AAV-IL10 treatment in animal models of peripheral and CNS infection. In summary, the results suggest that rAAV-mediated neuronal IL-10 expression has the potential to resolve persistent CNS inflammation and opens up possibilities for further research to harness the anti-inflammatory effects of IL-10 for MS treatment.

5 Summary

Multiple sclerosis (MS) is characterized by the irreversible demise of neurons, which leads to motor and cognitive impairments. This is believed to be triggered by autoreactive immune cells, infiltrating the central nervous system (CNS), which results in persistent neuroinflammation and consecutive neurodegeneration. Current pharmacological therapies primarily target the peripheral immune system to reduce relapses but inadequately address the neurodegeneration in the CNS that is underlying progressive MS. Therefore, therapies that locally protect affected neurons against autoreactive immune cells are urgently needed. Although transporting CNS-effective therapeutic substances across the blood–brain barrier represents a major technological challenge, the development of new CNS-permeable adeno-associated viruses (AAV) serotypes, such as AAV-PHP.eB, offers promising opportunities for efficient transduction of CNS-resident cells, including neurons.

The aim of this project was to equip neurons with anti-inflammatory proteins to establish local immune tolerance and provide protection against neurodegeneration while minimizing potential systemic side effects. Therefore, the neuroprotective potential of rAAV-mediated gene delivery of immunomodulatory molecules, including PD-L1, CD200, GDF-15, and IL-10 to neurons was tested in the experimental autoimmune encephalomyelitis (EAE) mouse model of MS. Equipping neurons with the surface proteins PD-L1 and CD200 did not lead to a significant improvement in the EAE phenotype. In contrast, neuronal secretion of GDF-15 and IL-10 ameliorated EAE symptoms and significantly reduced CNS-infiltrating immune cells. AAV-IL10 gene therapy resulted in peripheral induction of regulatory T cells. Moreover, CNS-infiltrating immune cells exhibited a less inflammatory phenotype, characterized by reduced CD44 expression on $CD4^+$ T cells and decreased IL-17 production by $CD8^+$ T cells. The establishment of a TetOn system and the development of membrane-bound IL-10, allowed tight temporal and spatial control over neuronal IL-10 expression. In conclusion, this work demonstrates the potential of rAAV-mediated neuronal IL-10 expression for alleviating chronic CNS inflammation and lays the foundation for further research to harness the anti-inflammatory properties of IL-10 for the treatment of MS.

6 Zusammenfassung

Multiple Sklerose (MS) ist durch den irreversiblen Untergang von Neuronen gekennzeichnet, welcher zu motorischen und kognitiven Beeinträchtigungen führt. Es wird angenommen, dass dies durch autoreaktive Immunzellen ausgelöst wird, die das Zentralnervensystem (ZNS) infiltrieren, was zu einer anhaltenden Neuroinflammation und anschließender Neurodegeneration führt. Aktuelle pharmakologische Therapien zielen in erster Linie auf das periphere Immunsystem ab, um Schübe zu reduzieren, bekämpfen jedoch nur unzureichend die Neurodegeneration im ZNS, die der progressiven MS zugrunde liegt. Daher sind Therapien, die betroffene Neurone lokal vor autoreaktiven Immunzellen schützen, dringend erforderlich. Obwohl der Transport ZNS-wirksamer therapeutischer Substanzen über die Blut-Hirn-Schranke eine große technologische Herausforderung darstellt, bietet die Entwicklung neuer ZNS-permeabler Adeno-assoziierter Viren (AAV)-Serotypen wie AAV-PHP.eB vielversprechende Möglichkeiten für eine effiziente Transduktion von ZNS-residenten Zellen, einschließlich Neuronen.

Das Ziel dieses Projekts war es, Neurone mit entzündungshemmenden Proteinen auszustatten, um eine lokale Immuntoleranz aufzubauen und Schutz vor Neurodegeneration zu bieten und gleichzeitig potenzielle systemische Nebenwirkungen zu minimieren. Daher wurde das neuroprotektive Potenzial des rAAV-vermittelten Gentransfers immunmodulatorischer Moleküle, einschließlich PD-L1, CD200, GDF-15 und IL-10, an Neurone in experimenteller autoimmunen Enzephalomyelitis (EAE), dem Mausmodell von MS, getestet. Die Ausstattung von Neuronen mit den Oberflächenproteinen PD-L1 und CD200 führte nicht zu einer signifikanten Verbesserung des EAE-Phänotyps. Im Gegensatz dazu linderte die neuronale Sekretion von GDF-15 und IL-10 die EAE-Symptome und reduzierte die ZNS-infiltrierenden Immunzellen signifikant. Die AAV-IL10-Gentherapie führte zu einer peripheren Induktion regulatorischer T-Zellen. Darüber hinaus zeigten ZNS-infiltrierende Immunzellen einen weniger entzündlichen Phänotyp, der durch eine verringerte CD44-Expression auf $CD4^+$ T-Zellen und eine verringerte IL-17-Produktion durch $CD8^+$ T-Zellen gekennzeichnet war. Die Etablierung eines TetOn-Systems und die Entwicklung von membrangebundenem IL-10 ermöglichten eine strenge zeitliche und räumliche Kontrolle der neuronalen IL-10-Expression. Zusammenfassend zeigt diese Arbeit das Potenzial der rAAV-vermittelten neuronalen IL-10-Expression zur Linderung chronischer ZNS-Entzündungen und legt den Grundstein für weitere Forschungen, um die entzündungshemmenden Eigenschaften von IL-10 für die Behandlung von MS zu nutzen.

III. Abbreviations

AAV	Adeno-associated virus
A, C, G, T	Adenine, Cytosine, Guanine, Thymine
AF	Alexa fluor
AIRE	Autoimmune regulator
ANOVA	Analysis of variance
APC	Antigen presenting cell
BBB	Blood–brain barrier
BCA	Bicinchoninic acid
Bcl-6	B-cell lymphoma 6 protein
BCR	B cell receptor
bp	Base pairs
BrdU	Bromodeoxyuridine
BTK	Bruton tyrosine kinase
BUV	Brilliant ultra violet
BV	Brilliant violet
CAG	Chicken beta-actin
CAR	Chimeric antigen receptor
CD	Cluster of differentiation
cDCs	Classical dendritic cells
cDNA	Complementary DNA
CFA	Complete Freund’s adjuvant
CNS	Central nervous system
CSF	Cerebrospinal fluid
CSIF	Cytokine synthesis inhibitory factor
cTECs	Cortical thymic epithelial cells
CTLA-4	Cytotoxic T-lymphocyte-associated Protein 4
DAMP	Damage-associated molecular patterns
DCs	Dendritic cells
DIV	Days *in vitro*
DMEM	Dulbecco's modified eagle medium
DMT	Disease modifying treatment
DNA	Deoxyribonucleic acid
Dox	Doxycycline
E16	Embryonic day 16
EAE	Experimental autoimmune encephalitis
EBNA1	Epstein–Barr nuclear antigen 1
EBV	Epstein–Barr Virus
E.Coli	*Escherichia Coli*
EDSS	Expanded disability status scale
EDTA	Ethylenediaminetetraacetic acid
EGFP	Enhanced green fluorescent protein
EGTA	Ethylene glycol-bis(2-aminoethylether)-N,N,N',N'-tetraacetic acid
ELISA	Enzyme-linked immunosorbent assay
ER	Endoplasmic reticulum
FACS	Fluorescence-activated cell sorting
FCS	Fetal calf serum
fwd	Forward
FoxP3	Forkhead-box protein P3
FSC	Forward scatter
GDF-15	Growth differentiation factor 15
GFAP	Glial fibrillary acidic protein

GM-CSF	Granulocyte-macrophage colony-stimulating factor
GPI	Glycosylphosphatidylinositol
GS	Glycine-serine peptide linker
HBSS	Hanks balanced salt solution
HLA	Human leukocyte antigen
HRP	Horseradish peroxidase
hSyn1	Human synapsin 1
IFN-β	Interferon beta
IFN-γ	Interferon gamma
Ig	Immunoglobulin
IL	Interleukin
INIMS	Institute for Neuroimmunology and Multiple Sclerosis
Iono	Ionomycin
i.p.	Intraperitoneal
ITR	Inverted terminal repeat
ITSM	Immunoreceptor tyrosine-based switch-motif
LAG3	Lymphocyte-activation gene 3
LB	Lysogeny broth
LFA-1	Lymphocyte function-associated antigen 1
LN	Lymph nodes
LP	Longpass
MAP2	Microtubule-associated protein 2
MCS	Multiple cloning site
mTECs	Medullary thymic epithelial cells
memIL-10	Membrane-bound interleukin 10
MFI	Median fluorescent intensity
MHC	Major histocompatibility complex
Mc	Minocycline
MOG	Myelin oligodendrocyte glycoprotein
MOI	Multiplicity of infection
MRI	Magnetic resonance imaging
MS	Multiple sclerosis
mSc	mScarlet
n	Number of individuals
N2a	Neuro-2a
NDS	Normal donkey serum
NEAA	Non-essential amino acids
NAbs	Neutralizing antibodies
NGM	Neuronal growth medium
NK cell	Natural killer cell
NLS	Nuclear localization sequence
nt	Nucleotides
PAMP	Pattern associated molecular pattern
PBS	Phosphate-buffered saline
PCR	Polymerase chain reaction
PD-1	Programmed cell death protein 1
PDL	Poly-D-Lysin
PD-L1	Programmed death-ligand 1
PFA	Paraformaldehyde
PFC	Prefrontal cortex
PMA	Phorbol 12-myristate 13-acetate
PML	Progressive multifocal leukoencephalopathy
PPMS	Primary progressive multiple sclerosis
PTX	Pertussis toxin

PRR	Pattern recognition receptor
R	Receptor
rAAV	Recombinant adeno-associated virus
rev	Reverse
RE	Restriction enzyme
RIPA	Radioimmunoprecipitation assay
RNA	Ribonucleic acid
RORγt	RAR-related orphan receptor gammat
Rpm	Rounds per minute
RRMS	Relapsing-remitting multiple sclerosis
RT	Room temperature
rtTA	Reverse tetracycline-controlled transactivator
S1PR	Sphingosine-1-phosphate receptor
SDS	Sodium dodecyl sulfate
s.e.m.	Standard error of the mean
SOC	Super optimal broth with catabolite repression
SPMS	Secondary progressive multiple sclerosis
SSC	Sideward scatter
SSC-A	Sideward scatter area
TAE	Tris-acetate-EDTA
T-bet	T-box transcription factor TBX21
TBI	Traumatic brain injury
Tc	Tetracycline
TCR	T cell receptor
TE	Tris-EDTA
Teff	Effector T cells
TetO	Tetracycline operator
TGF-β	Transforming growth factor β
Tfh	Follicular T helper cel
Th1	Type 1 T helper
Th2	Type 2 T helper
Th17	Type 17 T helper
TLR	Toll-like receptor
tm	Transmembrane
TMEV	Theiler's murine encephalomyelitis virus
TNF-α	Tumor necrosis factor alpha
TRE	Tetracycline responsive element
Treg	Regulatory T cells
UKE	University Medical Center Hamburg-Eppendorf
UV	Ultraviolet
vg	Viral genomes
VLA-4	Very late antigen 4
WB	Western blot
WPRE	Woodchuck hepatitis virus posttranscriptional regulatory element
ZNS	Zentralnervensystem
ZMNH	Center for Molecular Neurobiology Hamburg

IV. References

1. Attfield, K. E., Jensen, L. T., Kaufmann, M., Friese, M. A. & Fugger, L. The immunology of multiple sclerosis. *Nat. Rev. Immunol.* **22**, 734–750 (2022) 10.1038/s41577-022-00718-z.
2. Lunde, H. M. B., Assmus, J., Myhr, K.-M., Bø, L. & Grytten, N. Survival and cause of death in multiple sclerosis: a 60-year longitudinal population study. *J. Neurol. Neurosurg. Psychiatry* **88**, 621–625 (2017) 10.1136/jnnp-2016-315238.
3. Dendrou, C. A., Fugger, L. & Friese, M. A. Immunopathology of multiple sclerosis. *Nat. Rev. Immunol.* **15**, 545–558 (2015) 10.1038/nri3871.
4. Stys, P. K., Zamponi, G. W., van Minnen, J. & Geurts, J. J. G. Will the real multiple sclerosis please stand up? *Nat. Rev. Neurosci.* **13**, 507–514 (2012) 10.1038/nrn3275.
5. ’t Hart, B. A., Luchicchi, A., Schenk, G. J., Stys, P. K. & Geurts, J. J. G. Mechanistic underpinning of an inside-out concept for autoimmunity in multiple sclerosis. *Ann. Clin. Transl. Neurol.* **8**, 1709–1719 (2021) 10.1002/acn3.51401.
6. Walton, C. *et al.* Rising prevalence of multiple sclerosis worldwide: Insights from the Atlas of MS, third edition. *Mult. Scler. J.* **26**, 1816–1821 (2020) 10.1177/1352458520970841.
7. Filippi, M. *et al.* Assessment of lesions on magnetic resonance imaging in multiple sclerosis: practical guidelines. *Brain J. Neurol.* **142**, 1858–1875 (2019) 10.1093/brain/awz144.
8. Ghasemi, N., Razavi, S. & Nikzad, E. Multiple Sclerosis: Pathogenesis, Symptoms, Diagnoses and Cell-Based Therapy. *Cell J.* **19**, 1–10 (2017) 10.22074/cellj.2016.4867.
9. Joseph, F. G. *et al.* CSF oligoclonal band status informs prognosis in multiple sclerosis: a case control study of 100 patients. *J. Neurol. Neurosurg. Psychiatry* **80**, 292–296 (2009) 10.1136/jnnp.2008.150896.
10. Khalil, M. *et al.* Neurofilaments as biomarkers in neurological disorders. *Nat. Rev. Neurol.* **14**, 577–589 (2018) 10.1038/s41582-018-0058-z.
11. Paul, A., Comabella, M. & Gandhi, R. Biomarkers in Multiple Sclerosis. *Cold Spring Harb. Perspect. Med.* **9**, a029058 (2019) 10.1101/cshperspect.a029058.
12. Noseworthy, J. H., Vandervoort, M. K., Wong, C. J. & Ebers, G. C. Interrater variability with the Expanded Disability Status Scale (EDSS) and Functional Systems (FS) in a multiple sclerosis clinical trial. The Canadian Cooperation MS Study Group. *Neurology* **40**, 971–975 (1990) 10.1212/wnl.40.6.971.
13. Carassiti, D. *et al.* Neuronal loss, demyelination and volume change in the multiple sclerosis neocortex. *Neuropathol. Appl. Neurobiol.* **44**, 377–390 (2018) 10.1111/nan.12405.
14. Dobson, R. & Giovannoni, G. Multiple sclerosis – a review. *Eur. J. Neurol.* **26**, 27–40 (2019) 10.1111/ene.13819.

15. Cree, B. A. C. *et al.* Secondary Progressive Multiple Sclerosis: New Insights. *Neurology* **97**, 378–388 (2021) 10.1212/WNL.0000000000012323.
16. Orton, S.-M. *et al.* Sex ratio of multiple sclerosis in Canada: a longitudinal study. *Lancet Neurol.* **5**, 932–936 (2006) 10.1016/S1474-4422(06)70581-6.
17. Trojano, M. *et al.* Geographical Variations in Sex Ratio Trends over Time in Multiple Sclerosis. *PLoS ONE* **7**, e48078 (2012) 10.1371/journal.pone.0048078.
18. Gianfrancesco, M. A. *et al.* Obesity during childhood and adolescence increases susceptibility to multiple sclerosis after accounting for established genetic and environmental risk factors. *Obes. Res. Clin. Pract.* **8**, e435-447 (2014) 10.1016/j.orcp.2014.01.002.
19. Hedström, A., Olsson, T. & Alfredsson, L. Body mass index during adolescence, rather than childhood, is critical in determining MS risk. *Mult. Scler. J.* **22**, 878–883 (2016) 10.1177/1352458515603798.
20. Hawkes, C. H. Smoking is a risk factor for multiple sclerosis: a metanalysis. *Mult. Scler. J.* **13**, 610–615 (2007) 10.1177/1352458506073501.
21. Hedström, A. K., Bäärnhielm, M., Olsson, T. & Alfredsson, L. Tobacco smoking, but not Swedish snuff use, increases the risk of multiple sclerosis. *Neurology* **73**, 696–701 (2009) 10.1212/WNL.0b013e3181b59c40.
22. Hedström, A. K. *et al.* Smoking and two human leukocyte antigen genes interact to increase the risk for multiple sclerosis. *Brain* **134**, 653–664 (2011) 10.1093/brain/awq371.
23. Hedström, A., Olsson, T. & Alfredsson, L. Smoking is a major preventable risk factor for multiple sclerosis. *Mult. Scler. J.* **22**, 1021–1026 (2016) 10.1177/1352458515609794.
24. Confavreux, C., Hutchinson, M., Hours, M. M., Cortinovis-Tourniaire, P. & Moreau, T. Rate of pregnancy-related relapse in multiple sclerosis. Pregnancy in Multiple Sclerosis Group. *N. Engl. J. Med.* **339**, 285–291 (1998) 10.1056/NEJM199807303390501.
25. Ramien, C. *et al.* Sex effects on inflammatory and neurodegenerative processes in multiple sclerosis. *Neurosci. Biobehav. Rev.* **67**, 137–146 (2016) 10.1016/j.neubiorev.2015.12.015.
26. Kurtzke, J. F. Geography in multiple sclerosis. *J. Neurol.* **215**, 1–26 (1977) 10.1007/BF00312546.
27. Gale, C. R. & Martyn, C. N. Migrant studies in multiple sclerosis. *Prog. Neurobiol.* **47**, 425–448 (1995).
28. Munger, K. L., Levin, L. I., Hollis, B. W., Howard, N. S. & Ascherio, A. Serum 25-hydroxyvitamin D levels and risk of multiple sclerosis. *JAMA* **296**, 2832–2838 (2006) 10.1001/jama.296.23.2832.

29. Bäärnhielm, M. *et al.* Sunlight is associated with decreased multiple sclerosis risk: no interaction with human leukocyte antigen-DRB1*15. *Eur. J. Neurol.* **19**, 955–962 (2012) 10.1111/j.1468-1331.2011.03650.x.
30. Dankers, W. *et al.* Human Memory Th17 Cell Populations Change Into Anti-inflammatory Cells With Regulatory Capacity Upon Exposure to Active Vitamin D. *Front. Immunol.* **10**, 1504 (2019) 10.3389/fimmu.2019.01504.
31. Bjornevik, K. *et al.* Longitudinal analysis reveals high prevalence of Epstein-Barr virus associated with multiple sclerosis. *Science* **375**, 296–301 (2022) 10.1126/science.abj8222.
32. Parnell, G. P. & Booth, D. R. The Multiple Sclerosis (MS) Genetic Risk Factors Indicate both Acquired and Innate Immune Cell Subsets Contribute to MS Pathogenesis and Identify Novel Therapeutic Opportunities. *Front. Immunol.* **8**, 425 (2017) 10.3389/fimmu.2017.00425.
33. International Multiple Sclerosis Genetics Consortium. Multiple sclerosis genomic map implicates peripheral immune cells and microglia in susceptibility. *Science* **365**, eaav7188 (2019) 10.1126/science.aav7188.
34. Ebers, G. C. *et al.* A Population-Based Study of Multiple Sclerosis in Twins. *N. Engl. J. Med.* **315**, 1638–1642 (1986) 10.1056/NEJM198612253152603.
35. Westerlind, H. *et al.* Modest familial risks for multiple sclerosis: a registry-based study of the population of Sweden. *Brain J. Neurol.* **137**, 770–778 (2014) 10.1093/brain/awt356.
36. Fagnani, C. *et al.* Twin studies in multiple sclerosis: A meta-estimation of heritability and environmentality. *Mult. Scler. Houndmills Basingstoke Engl.* **21**, 1404–1413 (2015) 10.1177/1352458514564492.
37. Jersild, C. *et al.* Histocompatibility determinants in multiple sclerosis, with special reference to clinical course. *Lancet Lond. Engl.* **2**, 1221–1225 (1973) 10.1016/s0140-6736(73)90970-7.
38. Friese, M. A. *et al.* Opposing effects of HLA class I molecules in tuning autoreactive CD8+ T cells in multiple sclerosis. *Nat. Med.* **14**, 1227–1235 (2008) 10.1038/nm.1881.
39. International Multiple Sclerosis Genetics Consortium (IMSGC). Analysis of immune-related loci identifies 48 new susceptibility variants for multiple sclerosis. *Nat. Genet.* **45**, 1353–1360 (2013) 10.1038/ng.2770.
40. the International Multiple Sclerosis Genetics Consortium. Class II HLA interactions modulate genetic risk for multiple sclerosis. *Nat. Genet.* **47**, 1107–1113 (2015) 10.1038/ng.3395.
41. Jelcic, I. *et al.* Memory B Cells Activate Brain-Homing, Autoreactive CD4+ T Cells in Multiple Sclerosis. *Cell* **175**, 85-100.e23 (2018) 10.1016/j.cell.2018.08.011.

42. Sundqvist, E. *et al.* Epstein-Barr virus and multiple sclerosis: interaction with HLA. *Genes Immun.* **13**, 14–20 (2012) 10.1038/gene.2011.42.
43. Handel, A. E. *et al.* An updated meta-analysis of risk of multiple sclerosis following infectious mononucleosis. *PloS One* **5**, e12496 (2010) 10.1371/journal.pone.0012496.
44. Disanto, G. *et al.* Assessing interactions between HLA-DRB1*15 and infectious mononucleosis on the risk of multiple sclerosis. *Mult. Scler. J.* **19**, 1355–1358 (2013) 10.1177/1352458513477231.
45. Li, Q. *et al.* Epstein-Barr virus uses HLA class II as a cofactor for infection of B lymphocytes. *J. Virol.* **71**, 4657–4662 (1997) 10.1128/jvi.71.6.4657-4662.1997.
46. Angelini, G., Bani, A., Constantin, G. & Rossi, B. The interplay between T helper cells and brain barriers in the pathogenesis of multiple sclerosis. *Front. Cell. Neurosci.* **17**, 1101379 (2023) 10.3389/fncel.2023.1101379.
47. Ortiz, G. G. *et al.* Role of the blood-brain barrier in multiple sclerosis. *Arch. Med. Res.* **45**, 687–697 (2014) 10.1016/j.arcmed.2014.11.013.
48. Profaci, C. P., Munji, R. N., Pulido, R. S. & Daneman, R. The blood–brain barrier in health and disease: Important unanswered questions. *J. Exp. Med.* **217**, e20190062 (2020) 10.1084/jem.20190062.
49. Guttmann, C. R. *et al.* Multiple sclerosis lesion formation and early evolution revisited: A weekly high-resolution magnetic resonance imaging study. *Mult. Scler. Houndmills Basingstoke Engl.* **22**, 761–769 (2016) 10.1177/1352458515600247.
50. Kadry, H., Noorani, B. & Cucullo, L. A blood-brain barrier overview on structure, function, impairment, and biomarkers of integrity. *Fluids Barriers CNS* **17**, 69 (2020) 10.1186/s12987-020-00230-3.
51. Carrithers, M. D., Visintin, I., Kang, S. J. & Janeway, C. A. Differential adhesion molecule requirements for immune surveillance and inflammatory recruitment. *Brain J. Neurol.* **123 (Pt 6)**, 1092–1101 (2000) 10.1093/brain/123.6.1092.
52. Kebir, H. *et al.* Human TH17 lymphocytes promote blood-brain barrier disruption and central nervous system inflammation. *Nat. Med.* **13**, 1173–1175 (2007) 10.1038/nm1651.
53. Tahmasebinia, F. & Pourgholaminejad, A. The role of Th17 cells in auto-inflammatory neurological disorders. *Prog. Neuropsychopharmacol. Biol. Psychiatry* **79**, 408–416 (2017) 10.1016/j.pnpbp.2017.07.023.
54. Galli, E. *et al.* GM-CSF and CXCR4 define a T helper cell signature in multiple sclerosis. *Nat. Med.* **25**, 1290–1300 (2019) 10.1038/s41591-019-0521-4.
55. Wagner, C. A., Roqué, P. J. & Goverman, J. M. Pathogenic T cell cytokines in multiple sclerosis. *J. Exp. Med.* **217**, e20190460 (2020) 10.1084/jem.20190460.

56. Murphy, A. C., Lalor, S. J., Lynch, M. A. & Mills, K. H. G. Infiltration of Th1 and Th17 cells and activation of microglia in the CNS during the course of experimental autoimmune encephalomyelitis. *Brain. Behav. Immun.* **24**, 641–651 (2010) 10.1016/j.bbi.2010.01.014.
57. Lassmann, H. Multiple Sclerosis Pathology. *Cold Spring Harb. Perspect. Med.* **8**, a028936 (2018) 10.1101/cshperspect.a028936.
58. Shi, K. *et al.* Bone marrow hematopoiesis drives multiple sclerosis progression. *Cell* **185**, 2234-2247.e17 (2022) 10.1016/j.cell.2022.05.020.
59. Lassmann, H. Pathogenic Mechanisms Associated With Different Clinical Courses of Multiple Sclerosis. *Front. Immunol.* **9**, 3116 (2019) 10.3389/fimmu.2018.03116.
60. Kunkl, M., Frascolla, S., Amormino, C., Volpe, E. & Tuosto, L. T Helper Cells: The Modulators of Inflammation in Multiple Sclerosis. *Cells* **9**, 482 (2020) 10.3390/cells9020482.
61. Kebir, H. *et al.* Preferential recruitment of interferon-gamma-expressing TH17 cells in multiple sclerosis. *Ann. Neurol.* **66**, 390–402 (2009) 10.1002/ana.21748.
62. Frischer, J. M. *et al.* The relation between inflammation and neurodegeneration in multiple sclerosis brains. *Brain J. Neurol.* **132**, 1175–1189 (2009) 10.1093/brain/awp070.
63. Venken, K. *et al.* Compromised CD4+ CD25(high) regulatory T-cell function in patients with relapsing-remitting multiple sclerosis is correlated with a reduced frequency of FOXP3-positive cells and reduced FOXP3 expression at the single-cell level. *Immunology* **123**, 79–89 (2008) 10.1111/j.1365-2567.2007.02690.x.
64. Verma, N. D. *et al.* Multiple sclerosis patients have reduced resting and increased activated CD4+CD25+FOXP3+T regulatory cells. *Sci. Rep.* **11**, 10476 (2021) 10.1038/s41598-021-88448-5.
65. Kamma, E., Lasisi, W., Libner, C., Ng, H. S. & Plemel, J. R. Central nervous system macrophages in progressive multiple sclerosis: relationship to neurodegeneration and therapeutics. *J. Neuroinflammation* **19**, 45 (2022) 10.1186/s12974-022-02408-y.
66. Burda, J. E. & Sofroniew, M. V. Reactive gliosis and the multicellular response to CNS damage and disease. *Neuron* **81**, 229–248 (2014) 10.1016/j.neuron.2013.12.034.
67. Mayo, L. *et al.* Regulation of astrocyte activation by glycolipids drives chronic CNS inflammation. *Nat. Med.* **20**, 1147–1156 (2014) 10.1038/nm.3681.
68. Ortler, S. *et al.* B7-H1 restricts neuroantigen-specific T cell responses and confines inflammatory CNS damage: implications for the lesion pathogenesis of multiple sclerosis. *Eur. J. Immunol.* **38**, 1734–1744 (2008) 10.1002/eji.200738071.
69. Koning, N., Bö, L., Hoek, R. M. & Huitinga, I. Downregulation of macrophage inhibitory molecules in multiple sclerosis lesions. *Ann. Neurol.* **62**, 504–514 (2007) 10.1002/ana.21220.

70. Koning, N., Swaab, D. F., Hoek, R. M. & Huitinga, I. Distribution of the Immune Inhibitory Molecules CD200 and CD200R in the Normal Central Nervous System and Multiple Sclerosis Lesions Suggests Neuron-Glia and Glia-Glia Interactions: *J. Neuropathol. Exp. Neurol.* **68**, 159–167 (2009) 10.1097/NEN.0b013e3181964113.
71. Yang, J. H., Rempe, T., Whitmire, N., Dunn-Pirio, A. & Graves, J. S. Therapeutic Advances in Multiple Sclerosis. *Front. Neurol.* **13**, 824926 (2022) 10.3389/fneur.2022.824926.
72. Hemmer B. et al., Diagnose und Therapie der Multiplen Sklerose, Neuromyelitis-optica-Spektrum-Erkrankungen und MOG-IgG-assoziierten Erkrankungen, S2k-Leitlinie, 2023, in: Deutsche Gesellschaft für Neurologie (Hrsg.), Leitlinien für Diagnostik und Therapie in der Neurologie. Online: www.dgn.org/leitlinien (Retrieved March 20, 2024)
73. Interferon beta-1b is effective in relapsing-remitting multiple sclerosis. I. Clinical results of a multicenter, randomized, double-blind, placebo-controlled trial. The IFNB Multiple Sclerosis Study Group. *Neurology* **43**, 655–661 (1993) 10.1212/wnl.43.4.655.
74. Jacobs, L. D. *et al.* Intramuscular interferon beta-1a for disease progression in relapsing multiple sclerosis. The Multiple Sclerosis Collaborative Research Group (MSCRG). *Ann. Neurol.* **39**, 285–294 (1996) 10.1002/ana.410390304.
75. Linker, R. A. & Gold, R. Dimethyl fumarate for treatment of multiple sclerosis: mechanism of action, effectiveness, and side effects. *Curr. Neurol. Neurosci. Rep.* **13**, 394 (2013) 10.1007/s11910-013-0394-8.
76. Johnson, K. P. *et al.* Sustained clinical benefits of glatiramer acetate in relapsing multiple sclerosis patients observed for 6 years. Copolymer 1 Multiple Sclerosis Study Group. *Mult. Scler. Houndmills Basingstoke Engl.* **6**, 255–266 (2000) 10.1177/135245850000600407.
77. Miller, A. E. An updated review of teriflunomide's use in multiple sclerosis. *Neurodegener. Dis. Manag.* **11**, 387–409 (2021) 10.2217/nmt-2021-0014.
78. Hjorth, M., Dandu, N. & Mellergård, J. Treatment effects of fingolimod in multiple sclerosis: Selective changes in peripheral blood lymphocyte subsets. *PloS One* **15**, e0228380 (2020) 10.1371/journal.pone.0228380.
79. Hill-Cawthorne, G. A. *et al.* Long term lymphocyte reconstitution after alemtuzumab treatment of multiple sclerosis. *J. Neurol. Neurosurg. Psychiatry* **83**, 298–304 (2012) 10.1136/jnnp-2011-300826.
80. Montalban, X. *et al.* Ocrelizumab versus Placebo in Primary Progressive Multiple Sclerosis. *N Engl J Med* (2017).
81. Stüve, O. *et al.* Altered CD4+/CD8+ T-cell ratios in cerebrospinal fluid of natalizumab-treated patients with multiple sclerosis. *Arch. Neurol.* **63**, 1383–1387 (2006) 10.1001/archneur.63.10.1383.

82. Weissert, R. Progressive multifocal leukoencephalopathy. *J. Neuroimmunol.* **231**, 73–77 (2011) 10.1016/j.jneuroim.2010.09.021.
83. Kappos, L. *et al.* Siponimod versus placebo in secondary progressive multiple sclerosis (EXPAND): a double-blind, randomised, phase 3 study. *The Lancet* **391**, 1263–1273 (2018) 10.1016/S0140-6736(18)30475-6.
84. Brown, J. W. L. *et al.* Association of Initial Disease-Modifying Therapy With Later Conversion to Secondary Progressive Multiple Sclerosis. *JAMA* **321**, 175–187 (2019) 10.1001/jama.2018.20588.
85. Friese, M. A. *et al.* The value of animal models for drug development in multiple sclerosis. *Brain J. Neurol.* **129**, 1940–1952 (2006) 10.1093/brain/awl083.
86. Baxter, A. G. The origin and application of experimental autoimmune encephalomyelitis. *Nat. Rev. Immunol.* **7**, 904–912 (2007) 10.1038/nri2190.
87. Simmons, S. B., Pierson, E. R., Lee, S. Y. & Goverman, J. M. Modeling the heterogeneity of multiple sclerosis in animals. *Trends Immunol.* **34**, 410–422 (2013) 10.1016/j.it.2013.04.006.
88. Robinson, A. P., Harp, C. T., Noronha, A. & Miller, S. D. The experimental autoimmune encephalomyelitis (EAE) model of MS. in *Handbook of Clinical Neurology* vol. 122 173–189 (Elsevier, 2014). 10.1016/B978-0-444-52001-2.00008-X.
89. Lassmann, H. & Bradl, M. Multiple sclerosis: experimental models and reality. *Acta Neuropathol. (Berl.)* **133**, 223–244 (2017) 10.1007/s00401-016-1631-4.
90. Jilek, S. *et al.* CSF enrichment of highly differentiated CD8+ T cells in early multiple sclerosis. *Clin. Immunol. Orlando Fla* **123**, 105–113 (2007) 10.1016/j.clim.2006.11.004.
91. Yednock, T. A. *et al.* Prevention of experimental autoimmune encephalomyelitis by antibodies against alpha 4 beta 1 integrin. *Nature* **356**, 63–66 (1992) 10.1038/356063a0.
92. Baron, J. L., Madri, J. A., Ruddle, N. H., Hashim, G. & Janeway, C. A. Surface expression of alpha 4 integrin by CD4 T cells is required for their entry into brain parenchyma. *J. Exp. Med.* **177**, 57–68 (1993) 10.1084/jem.177.1.57.
93. Hohlfeld, R. & Steinman, L. T Cell-Transfer Experimental Autoimmune Encephalomyelitis: Pillar of Multiple Sclerosis and Autoimmunity. *J. Immunol. Baltim. Md 1950* **198**, 3381–3383 (2017) 10.4049/jimmunol.1700346.
94. Papenfuss, T. L. *et al.* Sex differences in experimental autoimmune encephalomyelitis in multiple murine strains. *J. Neuroimmunol.* **150**, 59–69 (2004) 10.1016/j.jneuroim.2004.01.018.
95. Maña, P. *et al.* Demyelination caused by the copper chelator cuprizone halts T cell mediated autoimmune neuroinflammation. *J. Neuroimmunol.* **210**, 13–21 (2009) 10.1016/j.jneuroim.2009.02.013.

96. Almuslehi, M. S. M., Sen, M. K., Shortland, P. J., Mahns, D. A. & Coorssen, J. R. CD8 T-cell Recruitment Into the Central Nervous System of Cuprizone-Fed Mice: Relevance to Modeling the Etiology of Multiple Sclerosis. *Front. Cell. Neurosci.* **14**, 43 (2020) 10.3389/fncel.2020.00043.
97. Tsunoda, I. & Fujinami, R. S. Neuropathogenesis of Theiler's murine encephalomyelitis virus infection, an animal model for multiple sclerosis. *J. Neuroimmune Pharmacol. Off. J. Soc. NeuroImmune Pharmacol.* **5**, 355–369 (2010) 10.1007/s11481-009-9179-x.
98. Pike, S. C., Welsh, N., Linzey, M. & Gilli, F. Theiler's virus-induced demyelinating disease as an infectious model of progressive multiple sclerosis. *Front. Mol. Neurosci.* **15**, 1019799 (2022) 10.3389/fnmol.2022.1019799.
99. Chaplin, D. D. Overview of the immune response. *J. Allergy Clin. Immunol.* **125**, S3-23 (2010) 10.1016/j.jaci.2009.12.980.
100. Cheng, H., Zheng, Z. & Cheng, T. New paradigms on hematopoietic stem cell differentiation. *Protein Cell* **11**, 34–44 (2020) 10.1007/s13238-019-0633-0.
101. Rock, F. L., Hardiman, G., Timans, J. C., Kastelein, R. A. & Bazan, J. F. A family of human receptors structurally related to *Drosophila* Toll. *Proc. Natl. Acad. Sci.* **95**, 588–593 (1998) 10.1073/pnas.95.2.588.
102. Ariza, M.-E., Glaser, R., Kaumaya, P. T. P., Jones, C. & Williams, M. V. The EBV-encoded dUTPase activates NF-kappa B through the TLR2 and MyD88-dependent signaling pathway. *J. Immunol. Baltim. Md 1950* **182**, 851–859 (2009) 10.4049/jimmunol.182.2.851.
103. Jimenez-Dalmaroni, M. J. *et al.* Soluble CD36 Ectodomain Binds Negatively Charged Diacylglycerol Ligands and Acts as a Co-Receptor for TLR2. *PLoS ONE* **4**, e7411 (2009) 10.1371/journal.pone.0007411.
104. Schrijver, I. A. *et al.* Bacterial peptidoglycan and immune reactivity in the central nervous system in multiple sclerosis. *Brain J. Neurol.* **124**, 1544–1554 (2001) 10.1093/brain/124.8.1544.
105. Pishesha, N., Harmand, T. J. & Ploegh, H. L. A guide to antigen processing and presentation. *Nat. Rev. Immunol.* **22**, 751–764 (2022) 10.1038/s41577-022-00707-2.
106. Eisenbarth, S. C. Dendritic cell subsets in T cell programming: location dictates function. *Nat. Rev. Immunol.* **19**, 89–103 (2019) 10.1038/s41577-018-0088-1.
107. Cyster, J. G. & Allen, C. D. C. B Cell Responses: Cell Interaction Dynamics and Decisions. *Cell* **177**, 524–540 (2019) 10.1016/j.cell.2019.03.016.
108. Crotty, S. T Follicular Helper Cell Biology: A Decade of Discovery and Diseases. *Immunity* **50**, 1132–1148 (2019) 10.1016/j.immuni.2019.04.011.
109. Zhu, J. & Paul, W. E. Heterogeneity and plasticity of T helper cells. *Cell Res.* **20**, 4–12 (2010) 10.1038/cr.2009.138.

110. Saravia, J., Chapman, N. M. & Chi, H. Helper T cell differentiation. *Cell. Mol. Immunol.* **16**, 634–643 (2019) 10.1038/s41423-019-0220-6.
111. Jones, E. Y. MHC class I and class II structures. *Curr. Opin. Immunol.* **9**, 75–79 (1997) 10.1016/s0952-7915(97)80162-8.
112. Wucherpfennig, K. W., Gagnon, E., Call, M. J., Huseby, E. S. & Call, M. E. Structural biology of the T-cell receptor: insights into receptor assembly, ligand recognition, and initiation of signaling. *Cold Spring Harb. Perspect. Biol.* **2**, a005140 (2010) 10.1101/cshperspect.a005140.
113. Wu, L. & Van Kaer, L. Natural killer T cells in health and disease. *Front. Biosci. Sch. Ed.* **3**, 236–251 (2011) 10.2741/s148.
114. Godfrey, D. I., Uldrich, A. P., McCluskey, J., Rossjohn, J. & Moody, D. B. The burgeoning family of unconventional T cells. *Nat. Immunol.* **16**, 1114–1123 (2015) 10.1038/ni.3298.
115. Crosby, C. M. & Kronenberg, M. Tissue-specific functions of invariant natural killer T cells. *Nat. Rev. Immunol.* **18**, 559–574 (2018) 10.1038/s41577-018-0034-2.
116. Hinks, T. S. C. & Zhang, X.-W. MAIT Cell Activation and Functions. *Front. Immunol.* **11**, 1014 (2020) 10.3389/fimmu.2020.01014.
117. Choi, J. & Crotty, S. Bcl6-Mediated Transcriptional Regulation of Follicular Helper T cells (TFH). *Trends Immunol.* **42**, 336–349 (2021) 10.1016/j.it.2021.02.002.
118. Szabo, S. J. *et al.* A novel transcription factor, T-bet, directs Th1 lineage commitment. *Cell* **100**, 655–669 (2000) 10.1016/s0092-8674(00)80702-3.
119. Walker, J. A. & McKenzie, A. N. J. TH2 cell development and function. *Nat. Rev. Immunol.* **18**, 121–133 (2018) 10.1038/nri.2017.118.
120. Capone, A. & Volpe, E. Transcriptional Regulators of T Helper 17 Cell Differentiation in Health and Autoimmune Diseases. *Front. Immunol.* **11**, 348 (2020) 10.3389/fimmu.2020.00348.
121. Shevyrev, D. & Tereshchenko, V. Treg Heterogeneity, Function, and Homeostasis. *Front. Immunol.* **10**, 3100 (2019) 10.3389/fimmu.2019.03100.
122. Xing, Y. & Hogquist, K. A. T-cell tolerance: central and peripheral. *Cold Spring Harb. Perspect. Biol.* **4**, a006957 (2012) 10.1101/cshperspect.a006957.
123. Klein, L., Kyewski, B., Allen, P. M. & Hogquist, K. A. Positive and negative selection of the T cell repertoire: what thymocytes see (and don't see). *Nat. Rev. Immunol.* **14**, 377–391 (2014) 10.1038/nri3667.
124. Kisielow, P. & Miazek, A. Positive selection of T cells: rescue from programmed cell death and differentiation require continual engagement of the T cell receptor. *J. Exp. Med.* **181**, 1975–1984 (1995) 10.1084/jem.181.6.1975.
125. Abramson, J., Giraud, M., Benoist, C. & Mathis, D. Aire's partners in the molecular control of immunological tolerance. *Cell* **140**, 123–135 (2010) 10.1016/j.cell.2009.12.030.

126. Giraud, M. *et al.* An RNAi screen for Aire cofactors reveals a role for Hnrnpl in polymerase release and Aire-activated ectopic transcription. *Proc. Natl. Acad. Sci. U. S. A.* **111**, 1491–1496 (2014) 10.1073/pnas.1323535111.
127. Anderson, M. S. & Su, M. A. AIRE expands: new roles in immune tolerance and beyond. *Nat. Rev. Immunol.* **16**, 247–258 (2016) 10.1038/nri.2016.9.
128. Oh, J. & Shin, J.-S. The Role of Dendritic Cells in Central Tolerance. *Immune Netw.* **15**, 111–120 (2015) 10.4110/in.2015.15.3.111.
129. Wirnsberger, G., Hinterberger, M. & Klein, L. Regulatory T-cell differentiation versus clonal deletion of autoreactive thymocytes. *Immunol. Cell Biol.* **89**, 45–53 (2011) 10.1038/icb.2010.123.
130. Owen, D. L., Sjaastad, L. E. & Farrar, M. A. Regulatory T Cell Development in the Thymus. *J. Immunol. Baltim. Md 1950* **203**, 2031–2041 (2019) 10.4049/jimmunol.1900662.
131. Chen, L. & Flies, D. B. Molecular mechanisms of T cell co-stimulation and co-inhibition. *Nat. Rev. Immunol.* **13**, 227–242 (2013) 10.1038/nri3405.
132. Ross, S. H. & Cantrell, D. A. Signaling and Function of Interleukin-2 in T Lymphocytes. *Annu. Rev. Immunol.* **36**, 411–433 (2018) 10.1146/annurev-immunol-042617-053352.
133. Martín, P. *et al.* CD69 Association with Jak3/Stat5 Proteins Regulates Th17 Cell Differentiation. *Mol. Cell. Biol.* **30**, 4877–4889 (2010) 10.1128/MCB.00456-10.
134. Cibrián, D. & Sánchez-Madrid, F. CD69: from activation marker to metabolic gatekeeper. *Eur. J. Immunol.* **47**, 946–953 (2017) 10.1002/eji.201646837.
135. Yu, L. *et al.* CD69 enhances immunosuppressive function of regulatory T-cells and attenuates colitis by prompting IL-10 production. *Cell Death Dis.* **9**, 905 (2018) 10.1038/s41419-018-0927-9.
136. Baaten, B. J. G., Tinoco, R., Chen, A. T. & Bradley, L. M. Regulation of Antigen-Experienced T Cells: Lessons from the Quintessential Memory Marker CD44. *Front. Immunol.* **3**, 23 (2012) 10.3389/fimmu.2012.00023.
137. Krummel, M. F. & Allison, J. P. CTLA-4 engagement inhibits IL-2 accumulation and cell cycle progression upon activation of resting T cells. *J. Exp. Med.* **183**, 2533–2540 (1996) 10.1084/jem.183.6.2533.
138. Dong, Y. *et al.* CD4+ T cell exhaustion revealed by high PD-1 and LAG-3 expression and the loss of helper T cell function in chronic hepatitis B. *BMC Immunol.* **20**, 27 (2019) 10.1186/s12865-019-0309-9.
139. Abbott, N. J., Patabendige, A. A. K., Dolman, D. E. M., Yusof, S. R. & Begley, D. J. Structure and function of the blood-brain barrier. *Neurobiol. Dis.* **37**, 13–25 (2010) 10.1016/j.nbd.2009.07.030.

140. Zihni, C., Mills, C., Matter, K. & Balda, M. S. Tight junctions: from simple barriers to multifunctional molecular gates. *Nat. Rev. Mol. Cell Biol.* **17**, 564–580 (2016) 10.1038/nrm.2016.80.
141. Kim, K.-A. *et al.* Autophagy-mediated occludin degradation contributes to blood-brain barrier disruption during ischemia in bEnd.3 brain endothelial cells and rat ischemic stroke models. *Fluids Barriers CNS* **17**, 21 (2020) 10.1186/s12987-020-00182-8.
142. Kaya, M. & Ahishali, B. Basic physiology of the blood-brain barrier in health and disease: a brief overview. *Tissue Barriers* **9**, 1840913 (2021) 10.1080/21688370.2020.1840913.
143. Mikitsh, J. L. & Chacko, A.-M. Pathways for small molecule delivery to the central nervous system across the blood-brain barrier. *Perspect. Med. Chem.* **6**, 11–24 (2014) 10.4137/PMC.S13384.
144. Wong, A. D. *et al.* The blood-brain barrier: an engineering perspective. *Front. Neuroengineering* **6**, 7 (2013) 10.3389/fneng.2013.00007.
145. Marchetti, L. & Engelhardt, B. Immune cell trafficking across the blood-brain barrier in the absence and presence of neuroinflammation. *Vasc. Biol. Bristol Engl.* **2**, H1–H18 (2020) 10.1530/VB-19-0033.
146. Atchison, R. W., Casto, B. C. & Hammon, W. M. ADENOVIRUS-ASSOCIATED DEFECTIVE VIRUS PARTICLES. *Science* **149**, 754–756 (1965) 10.1126/science.149.3685.754.
147. Hoggan, M. D., Blacklow, N. R. & Rowe, W. P. Studies of small DNA viruses found in various adenovirus preparations: physical, biological, and immunological characteristics. *Proc. Natl. Acad. Sci.* **55**, 1467–1474 (1966) 10.1073/pnas.55.6.1467.
148. Casto, B. C., Atchison, R. W. & Hammon, W. M. Studies on the relationship between adeno-associated virus type I (AAV-1) and adenoviruses. I. Replication of AAV-1 in certain cell cultures and its effect on helper adenovirus. *Virology* **32**, 52–59 (1967) 10.1016/0042-6822(67)90251-6.
149. Atchison, R. W. The role of herpesviruses in adenovirus-associated virus replication in vitro. *Virology* **42**, 155–162 (1970) 10.1016/0042-6822(70)90248-5.
150. Hermonat, P. L. & Muzyczka, N. Use of adeno-associated virus as a mammalian DNA cloning vector: transduction of neomycin resistance into mammalian tissue culture cells. *Proc. Natl. Acad. Sci.* **81**, 6466–6470 (1984) 10.1073/pnas.81.20.6466.
151. Dong, J. Y., Fan, P. D. & Frizzell, R. A. Quantitative analysis of the packaging capacity of recombinant adeno-associated virus. *Hum. Gene Ther.* **7**, 2101–2112 (1996) 10.1089/hum.1996.7.17-2101.
152. Foust, K. D. *et al.* Intravascular AAV9 preferentially targets neonatal neurons and adult astrocytes. *Nat. Biotechnol.* **27**, 59–65 (2009) 10.1038/nbt.1515.

153. Bevan, A. K. Systemic Gene Delivery in Large Species for Targeting Spinal Cord, Brain, and Peripheral Tissues for Pediatric Disorders. *Cell Ther.* **19**, (2011).
154. Yang, J. *et al.* Concatamerization of Adeno-Associated Virus Circular Genomes Occurs through Intermolecular Recombination. *J VIROL* **73**, (1999).
155. Greig, J. A. Integrated vector genomes may contribute to long-term expression in primate liver after AAV administration. *Nat. Biotechnol.*
156. Dudek, A. M. *et al.* GPR108 Is a Highly Conserved AAV Entry Factor. *Mol. Ther. J. Am. Soc. Gene Ther.* **28**, 367–381 (2020) 10.1016/j.ymthe.2019.11.005.
157. Pillay, S. *et al.* Adeno-associated Virus (AAV) Serotypes Have Distinctive Interactions with Domains of the Cellular AAV Receptor. *J. Virol.* **91**, (2017).
158. Jang, S., Shen, H. K., Ding, X., Miles, T. F. & Gradinaru, V. Structural basis of receptor usage by the engineered capsid AAV-PHP.eB. *Mol. Ther. Methods Clin. Dev.* **26**, 343–354 (2022) 10.1016/j.omtm.2022.07.011.
159. Zengel, J. *et al.* Hardwiring tissue-specific AAV transduction in mice through engineered receptor expression. *Nat. Methods* **20**, 1070–1081 (2023) 10.1038/s41592-023-01896-x.
160. Maguire, C. A. *et al.* Mouse Gender Influences Brain Transduction by Intravascularly Administered AAV9. *Mol. Ther.* **21**, 1470–1471 (2013) 10.1038/mt.2013.95.
161. Rumachik, N. G. *et al.* Methods Matter: Standard Production Platforms for Recombinant AAV Produce Chemically and Functionally Distinct Vectors. *Mol. Ther. - Methods Clin. Dev.* **18**, 98–118 (2020) 10.1016/j.omtm.2020.05.018.
162. Gessler, D. J., Tai, P. W. L., Li, J. & Gao, G. Intravenous Infusion of AAV for Widespread Gene Delivery to the Nervous System. *Methods Mol. Biol. Clifton NJ* **1950**, 143–163 (2019) 10.1007/978-1-4939-9139-6_8.
163. Chan, K. Y. *et al.* Engineered AAVs for efficient noninvasive gene delivery to the central and peripheral nervous systems. *Nat. Neurosci.* **20**, 1172–1179 (2017) 10.1038/nn.4593.
164. Deverman, B. E. *et al.* Cre-dependent selection yields AAV variants for widespread gene transfer to the adult brain. *Nat. Biotechnol.* **34**, 204–209 (2016) 10.1038/nbt.3440.
165. Jang, M. J. *et al.* Spatial transcriptomics for profiling the tropism of viral vectors in tissues. *Nat. Biotechnol.* (2023) doi:10.1038/s41587-022-01648-w 10.1038/s41587-022-01648-w.
166. Yshii, L. *et al.* Astrocyte-targeted gene delivery of interleukin 2 specifically increases brain-resident regulatory T cell numbers and protects against pathological neuroinflammation. *Nat. Immunol.* **23**, 878–891 (2022) 10.1038/s41590-022-01208-z.
167. Hordeaux, J. *et al.* The GPI-Linked Protein LY6A Drives AAV-PHP.B Transport across the Blood-Brain Barrier. *Mol. Ther.* **27**, 912–921 (2019) 10.1016/j.ymthe.2019.02.013.

168. Huang, Q. *et al.* Delivering genes across the blood-brain barrier: LY6A, a novel cellular receptor for AAV-PHP.B capsids. *PLOS ONE* **14**, e0225206 (2019) 10.1371/journal.pone.0225206.
169. Batista, A. R. *et al. Ly6a* Differential Expression in Blood–Brain Barrier Is Responsible for Strain Specific Central Nervous System Transduction Profile of AAV-PHP.B. *Hum. Gene Ther.* **31**, 90–102 (2020) 10.1089/hum.2019.186.
170. Goertsen, D. *et al.* AAV capsid variants with brain-wide transgene expression and decreased liver targeting after intravenous delivery in mouse and marmoset. *Nat. Neurosci.* **25**, 106–115 (2022) 10.1038/s41593-021-00969-4.
171. Finneran, D. J. *et al.* Toward Development of Neuron Specific Transduction After Systemic Delivery of Viral Vectors. *Front. Neurol.* **12**, 685802 (2021) 10.3389/fneur.2021.685802.
172. Chulanetra, M. & Chaicumpa, W. Revisiting the Mechanisms of Immune Evasion Employed by Human Parasites. *Front. Cell. Infect. Microbiol.* **11**, 702125 (2021) 10.3389/fcimb.2021.702125.
173. Damian, R. T. Molecular Mimicry: Antigen Sharing by Parasite and Host and Its Consequences. *Am. Nat.* **98**, 129–149 (1964) 10.1086/282313.
174. Ludin, P., Nilsson, D. & Mäser, P. Genome-Wide Identification of Molecular Mimicry Candidates in Parasites. *PLoS ONE* **6**, e17546 (2011) 10.1371/journal.pone.0017546.
175. García-Sastre, A. *et al.* Influenza A Virus Lacking the NS1 Gene Replicates in Interferon-Deficient Systems. *Virology* **252**, 324–330 (1998) 10.1006/viro.1998.9508.
176. Graef, K. M. *et al.* The PB2 Subunit of the Influenza Virus RNA Polymerase Affects Virulence by Interacting with the Mitochondrial Antiviral Signaling Protein and Inhibiting Expression of Beta Interferon. *J. Virol.* **84**, 8433–8445 (2010) 10.1128/JVI.00879-10.
177. Ahn, K. *et al.* Human cytomegalovirus inhibits antigen presentation by a sequential multistep process. *Proc. Natl. Acad. Sci.* **93**, 10990–10995 (1996) 10.1073/pnas.93.20.10990.
178. Salek-Ardakani, S., Arrand, J. R. & Mackett, M. Epstein–Barr Virus Encoded Interleukin-10 Inhibits HLA-Class I, ICAM-1, and B7 Expression on Human Monocytes: Implications for Immune Evasion by EBV. *Virology* **304**, 342–351 (2002) 10.1006/viro.2002.1716.
179. Jochum, S., Moosmann, A., Lang, S., Hammerschmidt, W. & Zeidler, R. The EBV Immunoevasins vIL-10 and BNLF2a Protect Newly Infected B Cells from Immune Recognition and Elimination. *PLoS Pathog.* **8**, e1002704 (2012) 10.1371/journal.ppat.1002704.
180. Huo, S. *et al.* EBV-EBNA1 constructs an immunosuppressive microenvironment for nasopharyngeal carcinoma by promoting the chemoattraction of Treg cells. *J. Immunother. Cancer* **8**, e001588 (2020) 10.1136/jitc-2020-001588.

181. Hedström, A. K. *et al.* High Levels of Epstein–Barr Virus Nuclear Antigen-1-Specific Antibodies and Infectious Mononucleosis Act Both Independently and Synergistically to Increase Multiple Sclerosis Risk. *Front. Neurol.* **10**, 1368 (2020) 10.3389/fneur.2019.01368.
182. Lanz, T. V. *et al.* Clonally expanded B cells in multiple sclerosis bind EBV EBNA1 and GlialCAM. *Nature* **603**, 321–327 (2022) 10.1038/s41586-022-04432-7.
183. Thompson, R. H. *et al.* Costimulatory B7-H1 in renal cell carcinoma patients: Indicator of tumor aggressiveness and potential therapeutic target. *Proc. Natl. Acad. Sci. U. S. A.* **101**, 17174–17179 (2004) 10.1073/pnas.0406351101.
184. Choe, D. & Choi, D. Cancel cancer: The immunotherapeutic potential of CD200/CD200R blockade. *Front. Oncol.* **13**, 1088038 (2023) 10.3389/fonc.2023.1088038.
185. Lichtenegger, F. S. *et al.* Targeting LAG-3 and PD-1 to Enhance T Cell Activation by Antigen-Presenting Cells. *Front. Immunol.* **9**, 385 (2018) 10.3389/fimmu.2018.00385.
186. Williams, L. M., Ricchetti, G., Sarma, U., Smallie, T. & Foxwell, B. M. J. Interleukin-10 suppression of myeloid cell activation--a continuing puzzle. *Immunology* **113**, 281–292 (2004) 10.1111/j.1365-2567.2004.01988.x.
187. Zong, J., Keskinov, A. A., Shurin, G. V. & Shurin, M. R. Tumor-derived factors modulating dendritic cell function. *Cancer Immunol. Immunother. CII* **65**, 821–833 (2016) 10.1007/s00262-016-1820-y.
188. Yang, Y. & Cao, Y. The impact of VEGF on cancer metastasis and systemic disease. *Semin. Cancer Biol.* **86**, 251–261 (2022) 10.1016/j.semcancer.2022.03.011.
189. Chihara, N. *et al.* Induction and transcriptional regulation of the co-inhibitory gene module in T cells. *Nature* **558**, 454–459 (2018) 10.1038/s41586-018-0206-z.
190. Dong, H., Zhu, G., Tamada, K. & Chen, L. B7-H1, a third member of the B7 family, co-stimulates T-cell proliferation and interleukin-10 secretion. *Nat. Med.* **5**, 1365–1369 (1999) 10.1038/70932.
191. Sharpe, A. H. & Pauken, K. E. The diverse functions of the PD1 inhibitory pathway. *Nat. Rev. Immunol.* **18**, 153–167 (2018) 10.1038/nri.2017.108.
192. Keir, M. E., Butte, M. J., Freeman, G. J. & Sharpe, A. H. PD-1 and Its Ligands in Tolerance and Immunity. *Annu. Rev. Immunol.* **26**, 677–704 (2008) 10.1146/annurev.immunol.26.021607.090331.
193. Nishimura, H., Nose, M., Hiai, H., Minato, N. & Honjo, T. Development of Lupus-like Autoimmune Diseases by Disruption of the PD-1 Gene Encoding an ITIM Motif-Carrying Immunoreceptor. *Immunity* **11**, 141–151 (1999) 10.1016/S1074-7613(00)80089-8.
194. Latchman, Y. E. *et al.* PD-L1-deficient mice show that PD-L1 on T cells, antigen-presenting cells, and host tissues negatively regulates T cells. *Proc. Natl. Acad. Sci.* **101**, 10691–10696 (2004) 10.1073/pnas.0307252101.

195. Salama, A. D. *et al.* Critical Role of the Programmed Death-1 (PD-1) Pathway in Regulation of Experimental Autoimmune Encephalomyelitis. *J. Exp. Med.* **198**, 71–78 (2003) 10.1084/jem.20022119.
196. Linnerbauer, M. *et al.* PD-L1 positive astrocytes attenuate inflammatory functions of PD-1 positive microglia in models of autoimmune neuroinflammation. *Nat. Commun.* **14**, 5555 (2023) 10.1038/s41467-023-40982-8.
197. Carter, L. L. *et al.* PD-1/PD-L1, but not PD-1/PD-L2, interactions regulate the severity of experimental autoimmune encephalomyelitis. *J. Neuroimmunol.* **182**, 124–134 (2007) 10.1016/j.jneuroim.2006.10.006.
198. Herold, M. *et al.* B7-H1 Selectively Controls TH17 Differentiation and Central Nervous System Autoimmunity via a Novel Non–PD-1–Mediated Pathway. *J. Immunol.* **195**, 3584–3595 (2015) 10.4049/jimmunol.1402746.
199. McCaughan, G. W., Clark, M. J. & Neil Barclay, A. Characterization of the human homolog of the rat MRC OX-2 membrane glycoprotein. *Immunogenetics* **25**, 329–335 (1987) 10.1007/BF00404426.
200. Wright, G. J., Jones, M., Puklavec, M. J., Brown, M. H. & Barclay, A. N. The unusual distribution of the neuronal/lymphoid cell surface CD200 (OX2) glycoprotein is conserved in humans. *Immunology* **102**, 173–179 (2001) 10.1046/j.1365-2567.2001.01163.x.
201. Kotwica-Mojzych, K., Jodłowska-Jędrych, B. & Mojzych, M. CD200:CD200R Interactions and Their Importance in Immunoregulation. *Int. J. Mol. Sci.* **22**, 1602 (2021) 10.3390/ijms22041602.
202. Pankratova, S. *et al.* Immunomodulator CD200 Promotes Neurotrophic Activity by Interacting with and Activating the Fibroblast Growth Factor Receptor. *Mol. Neurobiol.* **53**, 584–594 (2016) 10.1007/s12035-014-9037-6.
203. Hoek, R. M. *et al.* Down-Regulation of the Macrophage Lineage Through Interaction with OX2 (CD200). *Science* **290**, 1768–1771 (2000) 10.1126/science.290.5497.1768.
204. Valente, T., Serratosa, J., Perpiñá, U., Saura, J. & Solà, C. Alterations in CD200-CD200R1 System during EAE Already Manifest at Presymptomatic Stages. *Front. Cell. Neurosci.* **11**, 129 (2017) 10.3389/fncel.2017.00129.
205. Meuth, S. G. *et al.* CNS inflammation and neuronal degeneration is aggravated by impaired CD200–CD200R-mediated macrophage silencing. *J. Neuroimmunol.* **194**, 62–69 (2008) 10.1016/j.jneuroim.2007.11.013.
206. Liu, Y. *et al.* CD200R1 Agonist Attenuates Mechanisms of Chronic Disease in a Murine Model of Multiple Sclerosis. *J. Neurosci.* **30**, 2025 (2010) 10.1523/JNEUROSCI.4272-09.2010.
207. Xiong, Y. *et al.* Long-acting MIC-1/GDF15 molecules to treat obesity: Evidence from mice to monkeys. *Sci. Transl. Med.* **9**, eaan8732 (2017) 10.1126/scitranslmed.aan8732.

208. Böttner, M., Suter-Crazzolara, C., Schober, A. & Unsicker, K. Expression of a novel member of the TGF-β superfamily, growth/differentiation factor-15/macrophage-inhibiting cytokine-1 (GDF-15/MIC-1) in adult rat tissues. *Cell Tissue Res.* **297**, 103–110 (1999) 10.1007/s004410051337.
209. Bootcov, M. R. *et al.* MIC-1, a novel macrophage inhibitory cytokine, is a divergent member of the TGF-beta superfamily. *Proc. Natl. Acad. Sci. U. S. A.* **94**, 11514–11519 (1997) 10.1073/pnas.94.21.11514.
210. Lawton, L. N. *et al.* Identification of a novel member of the TGF-beta superfamily highly expressed in human placenta. *Gene* **203**, 17–26 (1997) 10.1016/S0378-1119(97)00485-X.
211. Tong, S. *et al.* Serum concentrations of macrophage inhibitory cytokine 1 (MIC 1) as a predictor of miscarriage. *The Lancet* **363**, 129–130 (2004) 10.1016/S0140-6736(03)15265-8.
212. Andersson-Hall, U. *et al.* Growth differentiation factor 15 increases in both cerebrospinal fluid and serum during pregnancy. *PloS One* **16**, e0248980 (2021) 10.1371/journal.pone.0248980.
213. Luan, H. H. *et al.* GDF15 Is an Inflammation-Induced Central Mediator of Tissue Tolerance. *Cell* **178**, 1231-1244.e11 (2019) 10.1016/j.cell.2019.07.033.
214. Roth, P. *et al.* GDF-15 Contributes to Proliferation and Immune Escape of Malignant Gliomas. *Clin. Cancer Res.* **16**, 3851–3859 (2010) 10.1158/1078-0432.CCR-10-0705.
215. Wischhusen, J., Melero, I. & Fridman, W. H. Growth/Differentiation Factor-15 (GDF-15): From Biomarker to Novel Targetable Immune Checkpoint. *Front. Immunol.* **11**, 951 (2020) 10.3389/fimmu.2020.00951.
216. Yang, L. *et al.* GFRAL is the receptor for GDF15 and is required for the anti-obesity effects of the ligand. *Nat. Med.* **23**, 1158–1166 (2017) 10.1038/nm.4394.
217. Emmerson, P. J. *et al.* The metabolic effects of GDF15 are mediated by the orphan receptor GFRAL. *Nat. Med.* **23**, 1215–1219 (2017) 10.1038/nm.4393.
218. Mullican, S. E. *et al.* GFRAL is the receptor for GDF15 and the ligand promotes weight loss in mice and nonhuman primates. *Nat. Med.* **23**, 1150–1157 (2017) 10.1038/nm.4392.
219. Benichou, O. *et al.* Discovery, development, and clinical proof of mechanism of LY3463251, a long-acting GDF15 receptor agonist. *Cell Metab.* **35**, 274-286.e10 (2023) 10.1016/j.cmet.2022.12.011.
220. Kempf, T. *et al.* GDF-15 is an inhibitor of leukocyte integrin activation required for survival after myocardial infarction in mice. *Nat. Med.* **17**, 581–588 (2011) 10.1038/nm.2354.
221. Zhou, Z. *et al.* Growth Differentiation Factor-15 Suppresses Maturation and Function of Dendritic Cells and Inhibits Tumor-Specific Immune Response. *PLoS ONE* **8**, e78618 (2013) 10.1371/journal.pone.0078618.

222. Wang, Z. *et al.* GDF15 induces immunosuppression via CD48 on regulatory T cells in hepatocellular carcinoma. *J. Immunother. Cancer* **9**, e002787 (2021) 10.1136/jitc-2021-002787.
223. Zhang, Y. *et al.* GDF15 Regulates Malat-1 Circular RNA and Inactivates NFκB Signaling Leading to Immune Tolerogenic DCs for Preventing Alloimmune Rejection in Heart Transplantation. *Front. Immunol.* **9**, 2407 (2018) 10.3389/fimmu.2018.02407.
224. Abulizi, P. *et al.* Growth Differentiation Factor-15 Deficiency Augments Inflammatory Response and Exacerbates Septic Heart and Renal Injury Induced by Lipopolysaccharide. *Sci. Rep.* **7**, 1037 (2017) 10.1038/s41598-017-00902-5.
225. Strelau, J. *et al.* Progressive Postnatal Motoneuron Loss in Mice Lacking GDF-15. *J. Neurosci.* **29**, 13640–13648 (2009) 10.1523/JNEUROSCI.1133-09.2009.
226. Nohara, S. GDF-15, a mitochondrial disease biomarker, is associated with the severity of multiple sclerosis. *J. Neurol. Sci.* (2019).
227. Amstad, A. *et al.* Growth differentiation factor 15 is increased in stable MS. *Neurol. Neuroimmunol. Neuroinflammation* **7**, e675 (2020) 10.1212/NXI.0000000000000675.
228. Fiorentino, D. F., Bond, M. W. & Mosmann, T. R. Two types of mouse T helper cell. IV. Th2 clones secrete a factor that inhibits cytokine production by Th1 clones. *J. Exp. Med.* **170**, 2081–2095 (1989) 10.1084/jem.170.6.2081.
229. Huhn, R. D. *et al.* Pharmacodynamics of subcutaneous recombinant human interleukin-10 in healthy volunteers. *Clin. Pharmacol. Ther.* **62**, 171–180 (1997) 10.1016/S0009-9236(97)90065-5.
230. Yogev, N. *et al.* CD4+ T-cell-derived IL-10 promotes CNS inflammation in mice by sustaining effector T cell survival. *Cell Rep.* **38**, 110565 (2022) 10.1016/j.celrep.2022.110565.
231. Huber, S. *et al.* Th17 Cells Express Interleukin-10 Receptor and Are Controlled by Foxp3− and Foxp3+ Regulatory CD4+ T Cells in an Interleukin-10-Dependent Manner. *Immunity* **34**, 554–565 (2011) 10.1016/j.immuni.2011.01.020.
232. Bedke, T., Muscate, F., Soukou, S., Gagliani, N. & Huber, S. IL-10-producing T cells and their dual functions. *Semin. Immunol.* **44**, 101335 (2019) 10.1016/j.smim.2019.101335.
233. Sawant, D. V. Adaptive plasticity of IL-10+ and IL-35+ Treg cells cooperatively promotes tumor T cell exhaustion. *Nat. Immunol.* **20**, (2019).
234. Wilke, C. M. *et al.* Endogenous interleukin-10 constrains Th17 cells in patients with inflammatory bowel disease. *J. Transl. Med.* **9**, 217 (2011) 10.1186/1479-5876-9-217.
235. Gagliani, N. *et al.* Th17 cells transdifferentiate into regulatory T cells during resolution of inflammation. *Nature* **523**, 221–225 (2015) 10.1038/nature14452.

236. Hanna, B. S. *et al.* Interleukin-10 receptor signaling promotes the maintenance of a PD-1int TCF-1+ CD8+ T cell population that sustains anti-tumor immunity. *Immunity* **54**, 2825-2841.e10 (2021) 10.1016/j.immuni.2021.11.004.
237. Wang, Z. *et al.* IL-10 Enhances Human Natural Killer Cell Effector Functions via Metabolic Reprogramming Regulated by mTORC1 Signaling. *Front. Immunol.* **12**, 619195 (2021) 10.3389/fimmu.2021.619195.
238. Mumm, J. B. *et al.* IL-10 elicits IFNγ-dependent tumor immune surveillance. *Cancer Cell* **20**, 781–796 (2011) 10.1016/j.ccr.2011.11.003.
239. Mumm, J. B. *et al.* IL-10 Elicits IFNg-Dependent Tumor Immune Surveillance. *Cancer Cell*.
240. Saraiva, M., Vieira, P. & O'Garra, A. Biology and therapeutic potential of interleukin-10. *J. Exp. Med.* **217**, e20190418 (2020) 10.1084/jem.20190418.
241. Wei, Y. *et al.* Low Serum Interleukin-10 Is an Independent Predictive Factor for the Risk of Second Event in Clinically Isolated Syndromes. *Front. Neurol.* **10**, 604 (2019) 10.3389/fneur.2019.00604.
242. Myhr, K.-M. *et al.* Interleukin-10 promoter polymorphisms in patients with multiple sclerosis. *J. Neurol. Sci.* **202**, 93–97 (2002) 10.1016/s0022-510x(02)00246-0.
243. Martinez-Forero, I. *et al.* IL-10 suppressor activity and ex vivo Tr1 cell function are impaired in multiple sclerosis. *Eur. J. Immunol.* **38**, 576–586 (2008) 10.1002/eji.200737271.
244. Kennedy, M. K., Torrance, D. S., Picha, K. S. & Mohler, K. M. Analysis of cytokine mRNA expression in the central nervous system of mice with experimental autoimmune encephalomyelitis reveals that IL-10 mRNA expression correlates with recovery. *J. Immunol. Baltim. Md 1950* **149**, 2496–2505 (1992).
245. Bettelli, E. *et al.* IL-10 is critical in the regulation of autoimmune encephalomyelitis as demonstrated by studies of IL-10- and IL-4-deficient and transgenic mice. *J. Immunol. Baltim. Md 1950* **161**, 3299–3306 (1998).
246. Cua, D. J., Hutchins, B., LaFace, D. M., Stohlman, S. A. & Coffman, R. L. Central Nervous System Expression of IL-10 Inhibits Autoimmune Encephalomyelitis. *J. Immunol.* **166**, 602–608 (2001) 10.4049/jimmunol.166.1.602.
247. Liu, Z. *et al.* Systematic comparison of 2A peptides for cloning multi-genes in a polycistronic vector. *Sci. Rep.* **7**, 2193 (2017) 10.1038/s41598-017-02460-2.
248. Friese, M. A., Schattling, B. & Fugger, L. Mechanisms of neurodegeneration and axonal dysfunction in multiple sclerosis. *Nat. Rev. Neurol.* **10**, 225–238 (2014) 10.1038/nrneurol.2014.37.

249. Zhou, X., Vink, M., Klaver, B., Berkhout, B. & Das, A. T. Optimization of the Tet-On system for regulated gene expression through viral evolution. *Gene Ther.* **13**, 1382–1390 (2006) 10.1038/sj.gt.3302780.
250. T. Das, A., Tenenbaum, L. & Berkhout, B. Tet-On Systems For Doxycycline-inducible Gene Expression. *Curr. Gene Ther.* **16**, 156–167 (2016) 10.2174/1566523216666160524144041.
251. Siopi, E. *et al.* Minocycline restores sAPPα levels and reduces the late histopathological consequences of traumatic brain injury in mice. *J. Neurotrauma* **28**, 2135–2143 (2011) 10.1089/neu.2010.1738.
252. Celorrio, M., Shumilov, K., Payne, C., Vadivelu, S. & Friess, S. H. Acute minocycline administration reduces brain injury and improves long-term functional outcomes after delayed hypoxemia following traumatic brain injury. *Acta Neuropathol. Commun.* **10**, 10 (2022) 10.1186/s40478-022-01310-1.
253. Krämer, J., Bar-Or, A., Turner, T. J. & Wiendl, H. Bruton tyrosine kinase inhibitors for multiple sclerosis. *Nat. Rev. Neurol.* **19**, 289–304 (2023) 10.1038/s41582-023-00800-7.
254. Arnold, D. L. *et al.* Effect of Evobrutinib on Slowly Expanding Lesion Volume in Relapsing Multiple Sclerosis: A Post Hoc Analysis of a Phase 2 Trial. *Neurology* **102**, e208058 (2024) 10.1212/WNL.0000000000208058.
255. Montalban, X. *et al.* Characterisation of the safety profile of evobrutinib in over 1000 patients from phase II clinical trials in multiple sclerosis, rheumatoid arthritis and systemic lupus erythematosus: an integrated safety analysis. *J. Neurol. Neurosurg. Psychiatry* **94**, 1–9 (2023) 10.1136/jnnp-2022-328799.
256. Schrimpf, G. (2023, December 5). Merck Provides Update on Phase III Results for Evobrutinib in Relapsing Multiple Sclerosis. https://www.merckgroup.com. Retrieved March 20, 2024 from https://www.merckgroup.com/en/news/evobrutinib-phase-lll.html
257. Mullard, A. CAR-T therapy for multiple sclerosis enters US trials for first time. *Nature* (2024) doi:10.1038/d41586-024-00470-5 10.1038/d41586-024-00470-5.
258. Brudno, J. N. & Kochenderfer, J. N. Chimeric antigen receptor T-cell therapies for lymphoma. *Nat. Rev. Clin. Oncol.* **15**, 31–46 (2018) 10.1038/nrclinonc.2017.128.
259. Gupta, S. *et al.* CAR-T Cell-Mediated B-Cell Depletion in Central Nervous System Autoimmunity. *Neurol. Neuroimmunol. Neuroinflammation* **10**, e200080 (2023) 10.1212/NXI.0000000000200080.
260. Fischbach, F. *et al.* CD19-targeted chimeric antigen receptor T cell therapy in two patients with multiple sclerosis. *Med N. Y. N* S2666-6340(24)00114–4 (2024) doi:10.1016/j.medj.2024.03.002 10.1016/j.medj.2024.03.002.

261. Kwilasz, A. J., Grace, P. M., Serbedzija, P., Maier, S. F. & Watkins, L. R. The therapeutic potential of interleukin-10 in neuroimmune diseases. *Neuropharmacology* **96**, 55–69 (2015) 10.1016/j.neuropharm.2014.10.020.
262. Cannella, B., Gao, Y. L., Brosnan, C. & Raine, C. S. IL-10 fails to abrogate experimental autoimmune encephalomyelitis. *J. Neurosci. Res.* **45**, 735–746 (1996) 10.1002/(SICI)1097-4547(19960915)45:6<735::AID-JNR10>3.0.CO;2-V.
263. Sloane, E. *et al.* Anti-inflammatory cytokine gene therapy decreases sensory and motor dysfunction in experimental Multiple Sclerosis: MOG-EAE behavioral and anatomical symptom treatment with cytokine gene therapy. *Brain. Behav. Immun.* **23**, 92–100 (2009) 10.1016/j.bbi.2008.09.004.
264. Liaci, A. M. *et al.* Structure of the human signal peptidase complex reveals the determinants for signal peptide cleavage. *Mol. Cell* **81**, 3934-3948.e11 (2021) 10.1016/j.molcel.2021.07.031.
265. Brenner, M., Kisseberth, W. C., Su, Y., Besnard, F. & Messing, A. GFAP promoter directs astrocyte-specific expression in transgenic mice. *J. Neurosci. Off. J. Soc. Neurosci.* **14**, 1030–1037 (1994) 10.1523/JNEUROSCI.14-03-01030.1994.
266. Sofroniew, M. V. Molecular dissection of reactive astrogliosis and glial scar formation. *Trends Neurosci.* **32**, 638–647 (2009) 10.1016/j.tins.2009.08.002.
267. Razeghi Jahromi, S. *et al.* Effects of Intermittent Fasting on Experimental Autoimune Encephalomyelitis in C57BL/6 Mice. *Iran. J. Allergy Asthma Immunol.* **15**, 212–219 (2016).
268. Huber, M. *et al.* IL-17A secretion by CD8+ T cells supports Th17-mediated autoimmune encephalomyelitis. *J. Clin. Invest.* **123**, 247–260 (2013) 10.1172/JCI63681.
269. Muhuri, M. *et al.* Overcoming innate immune barriers that impede AAV gene therapy vectors. *J. Clin. Invest.* **131**, e143780, 143780 (2021) 10.1172/JCI143780.
270. Mingozzi, F. *et al.* CD8+ T-cell responses to adeno- associated virus capsid in humans. *Nat. Med.* **13**, (2007).
271. Boutin, S. *et al.* Prevalence of serum IgG and neutralizing factors against adeno-associated virus (AAV) types 1, 2, 5, 6, 8, and 9 in the healthy population: implications for gene therapy using AAV vectors. *Hum. Gene Ther.* **21**, 704–712 (2010) 10.1089/hum.2009.182.
272. Goetze, S., Hiernickel, C. & Elsner, P. Phototoxicity of Doxycycline: A Systematic Review on Clinical Manifestations, Frequency, Cofactors, and Prevention. *Skin Pharmacol. Physiol.* **30**, 76–80 (2017) 10.1159/000458761.
273. Greenshpan, Y. *et al.* Synthetic promoters to induce immune-effectors into the tumor microenvironment. *Commun. Biol.* **4**, 143 (2021) 10.1038/s42003-021-01664-7.

274. Huang, W., Percie du Sert, N., Vollert, J. & Rice, A. S. C. General Principles of Preclinical Study Design. *Handb. Exp. Pharmacol.* **257**, 55–69 (2020) 10.1007/164_2019_277.
275. Au, H. K. E., Isalan, M. & Mielcarek, M. Gene Therapy Advances: A Meta-Analysis of AAV Usage in Clinical Settings. *Front. Med.* **8**, 809118 (2022) 10.3389/fmed.2021.809118.
276. Ansari, A. M. *et al.* Cellular GFP Toxicity and Immunogenicity: Potential Confounders in in Vivo Cell Tracking Experiments. *Stem Cell Rev. Rep.* **12**, 553–559 (2016) 10.1007/s12015-016-9670-8.
277. Shmidt, A. A. & Egorova, T. V. PCR-Based Analytical Methods for Quantification and Quality Control of Recombinant Adeno-Associated Viral Vector Preparations. *Pharm. Basel Switz.* **15**, 23 (2021) 10.3390/ph15010023.
278. Schnödt, M. & Büning, H. Improving the Quality of Adeno-Associated Viral Vector Preparations: The Challenge of Product-Related Impurities. *Hum. Gene Ther. Methods* **28**, 101–108 (2017) 10.1089/hgtb.2016.188.
279. Shimotohno, K. & Temin, H. M. Formation of infectious progeny virus after insertion of herpes simplex thymidine kinase gene into DNA of an avian retrovirus. *Cell* **26**, 67–77 (1981) 10.1016/0092-8674(81)90034-9.
280. Wei, C. M., Gibson, M., Spear, P. G. & Scolnick, E. M. Construction and isolation of a transmissible retrovirus containing the src gene of Harvey murine sarcoma virus and the thymidine kinase gene of herpes simplex virus type 1. *J. Virol.* **39**, 935–944 (1981) 10.1128/JVI.39.3.935-944.1981.
281. Solnick, D. Construction of an adenovirus-SV40 recombinant producing SV40 T antigen from an adenovirus late promoter. *Cell* **24**, 135–143 (1981) 10.1016/0092-8674(81)90509-2.
282. Spaete, R. R. & Frenkel, N. The herpes simplex virus amplicon: a new eucaryotic defective-virus cloning-amplifying vector. *Cell* **30**, 295–304 (1982) 10.1016/0092-8674(82)90035-6.
283. Lek, A. *et al.* Death after High-Dose rAAV9 Gene Therapy in a Patient with Duchenne's Muscular Dystrophy. *N Engl J Med* (2023).
284. Perocheau, D. P. *et al.* Age-Related Seroprevalence of Antibodies Against AAV-LK03 in a UK Population Cohort. *Hum. Gene Ther.* **30**, 79–87 (2019) 10.1089/hum.2018.098.
285. Shieh, P. B. *et al.* Safety and efficacy of gene replacement therapy for X-linked myotubular myopathy (ASPIRO): a multinational, open-label, dose-escalation trial. *Lancet Neurol.* **22**, 1125–1139 (2023) 10.1016/S1474-4422(23)00313-7.
286. Bangham, A. D., Standish, M. M. & Watkins, J. C. Diffusion of univalent ions across the lamellae of swollen phospholipids. *J. Mol. Biol.* **13**, 238–252 (1965) 10.1016/s0022-2836(65)80093-6.

287. Zheng, X. *et al.* Intranasal H102 Peptide-Loaded Liposomes for Brain Delivery to Treat Alzheimer's Disease. *Pharm. Res.* **32**, 3837–3849 (2015) 10.1007/s11095-015-1744-9.
288. Ullah, Z., Al-Asmari, A., Tariq, M. & Fatani, A. Preparation, characterization, and in vivo evaluation of intranasally administered liposomal formulation of donepezil. *Drug Des. Devel. Ther.* 205 (2016) doi:10.2147/DDDT.S93937 10.2147/DDDT.S93937.
289. Pawar, G. N., Parayath, N. N., Nocera, A. L., Bleier, B. S. & Amiji, M. M. Direct CNS delivery of proteins using thermosensitive liposome-in-gel carrier by heterotopic mucosal engrafting. *PLOS ONE* **13**, e0208122 (2018) 10.1371/journal.pone.0208122.
290. Hu, Y. *et al.* Core-shell lipoplexes inducing active macropinocytosis promote intranasal delivery of c-Myc siRNA for treatment of glioblastoma. *Acta Biomater.* **138**, 478–490 (2022) 10.1016/j.actbio.2021.10.042.
291. Szejtli, J. Introduction and General Overview of Cyclodextrin Chemistry. *Chem. Rev.* **98**, 1743–1754 (1998) 10.1021/cr970022c.
292. Trotta, F. *et al.* Molecularly imprinted cyclodextrin nanosponges for the controlled delivery of L-DOPA: perspectives for the treatment of Parkinson's disease. *Expert Opin. Drug Deliv.* **13**, 1671–1680 (2016) 10.1080/17425247.2017.1248398.
293. Ylä-Herttuala, S. Endgame: Glybera Finally Recommended for Approval as the First Gene Therapy Drug in the European Union. *Mol. Ther.* **20**, 1831–1832 (2012) 10.1038/mt.2012.194.
294. Mendell, J. R. *et al.* Single-Dose Gene-Replacement Therapy for Spinal Muscular Atrophy. *N. Engl. J. Med.* **377**, 1713–1722 (2017) 10.1056/NEJMoa1706198.
295. Sun, J. & Roy, S. Gene-based therapies for neurodegenerative diseases. *Nat. Neurosci.* (2021) doi:10.1038/s41593-020-00778-1 10.1038/s41593-020-00778-1.
296. Ribas, A. *et al.* Phase III randomized clinical trial comparing tremelimumab with standard-of-care chemotherapy in patients with advanced melanoma. *J. Clin. Oncol. Off. J. Am. Soc. Clin. Oncol.* **31**, 616–622 (2013) 10.1200/JCO.2012.44.6112.
297. Rech, J. *et al.* Abatacept inhibits inflammation and onset of rheumatoid arthritis in individuals at high risk (ARIAA): a randomised, international, multicentre, double-blind, placebo-controlled trial. *Lancet Lond. Engl.* **403**, 850–859 (2024) 10.1016/S0140-6736(23)02650-8.
298. Tawbi, H. A. *et al.* Relatlimab and Nivolumab versus Nivolumab in Untreated Advanced Melanoma. *N. Engl. J. Med.* **386**, 24–34 (2022) 10.1056/NEJMoa2109970.
299. Mahadevan, D. *et al.* Phase I study of samalizumab in chronic lymphocytic leukemia and multiple myeloma: blockade of the immune checkpoint CD200. *J. Immunother. Cancer* **7**, 227 (2019) 10.1186/s40425-019-0710-1.
300. Cardoso, A. *et al.* Interleukin-10 induces interferon-γ-dependent emergency myelopoiesis. *Cell Rep.* **37**, 109887 (2021) 10.1016/j.celrep.2021.109887.

301. Wang, X., Wong, K., Ouyang, W. & Rutz, S. Targeting IL-10 Family Cytokines for the Treatment of Human Diseases. *Cold Spring Harb. Perspect. Biol.* **11**, a028548 (2019) 10.1101/cshperspect.a028548.
302. Kühn, R., Löhler, J., Rennick, D., Rajewsky, K. & Müller, W. Interleukin-10-deficient mice develop chronic enterocolitis. *Cell* **75**, 263–274 (1993) 10.1016/0092-8674(93)80068-p.
303. van Deventer, S. J., Elson, C. O. & Fedorak, R. N. Multiple doses of intravenous interleukin 10 in steroid-refractory Crohn's disease. Crohn's Disease Study Group. *Gastroenterology* **113**, 383–389 (1997) 10.1053/gast.1997.v113.pm9247454.
304. Schreiber, S. *et al.* Safety and efficacy of recombinant human interleukin 10 in chronic active Crohn's disease. *Gastroenterology* **119**, 1461–1472 (2000) 10.1053/gast.2000.20196.
305. Colombel, J. F. *et al.* Interleukin 10 (Tenovil) in the prevention of postoperative recurrence of Crohn's disease. *Gut* **49**, 42–46 (2001) 10.1136/gut.49.1.42.
306. Braat, H. *et al.* A Phase I Trial With Transgenic Bacteria Expressing Interleukin-10 in Crohn's Disease. *Clin. Gastroenterol. Hepatol.* **4**, 754–759 (2006) 10.1016/j.cgh.2006.03.028.
307. Wang, A. H. *et al.* The effect of IL-10 genetic variation and interleukin 10 serum levels on Crohn's disease susceptibility in a New Zealand population. *Hum. Immunol.* **72**, 431–435 (2011) 10.1016/j.humimm.2011.02.014.
308. Galeazzi, M. *et al.* FRI0118 Dekavil (F8IL10) – update on the results of clinical trials investigating the immunocytokine in patients with rheumatoid arthritis. in *FRIDAY, 15 JUNE 2018* 603.2-604 (BMJ Publishing Group Ltd and European League Against Rheumatism, 2018). doi:10.1136/annrheumdis-2018-eular.5550 10.1136/annrheumdis-2018-eular.5550.
309. Naing, A. *et al.* PEGylated IL-10 (Pegilodecakin) Induces Systemic Immune Activation, CD8+ T Cell Invigoration and Polyclonal T Cell Expansion in Cancer Patients. *Cancer Cell* **34**, 775-791.e3 (2018) 10.1016/j.ccell.2018.10.007.
310. Tannir, N. M. *et al.* Pegilodecakin as monotherapy or in combination with anti-PD-1 or tyrosine kinase inhibitor in heavily pretreated patients with advanced renal cell carcinoma: Final results of cohorts A, G, H and I of IVY Phase I study. *Int. J. Cancer* **149**, 403–408 (2021) 10.1002/ijc.33556.
311. Ishii, H. *et al.* ifn-γ-dependent secretion of IL-10 from Th1 cells and microglia/macrophages contributes to functional recovery after spinal cord injury. *Cell Death Dis.* **4**, e710 (2013) 10.1038/cddis.2013.234.
312. Li, J. *et al.* Neuroprotective effects of interleukin 10 in spinal cord injury. *Front. Mol. Neurosci.* **16**, 1214294 (2023) 10.3389/fnmol.2023.1214294.

313. Sanchez-Molina, P., Almolda, B., Giménez-Llort, L., González, B. & Castellano, B. Chronic IL-10 overproduction disrupts microglia-neuron dialogue similar to aging, resulting in impaired hippocampal neurogenesis and spatial memory. *Brain. Behav. Immun.* **101**, 231–245 (2022) 10.1016/j.bbi.2021.12.026.

V. Acknowledgements

First of all, I would like to thank Prof. Dr. Manuel Friese for giving me the opportunity to conduct my PhD thesis at the INIMS, his support and inspiring scientific discussions.

I would like to thank my thesis committee, namely Prof. Dr. Hans-Willi Mittrücker and Prof. Dr. Boris Fehse for providing valuable feedback as well as for the evaluation of this thesis.

I am grateful to Dr. Dr. Jan Broder Engler, firstly for starting and acquiring funding for this project and allowing me to work on it. And secondly, I would like to thank him for the excellent supervision and constant availability for scientific and non-scientific discussions and the proofreading of my thesis.

Many thanks to Dr. Lars Binkle-Ladisch, who introduced me to molecular biology methods including molecular cloning and cell culture experiments and further contributed with troubleshooting and discussing most elegant approaches.

Moreover, I would like to thank Dr. Jana Sonner for collaborating on GDF-15 related experiments, as well as introducing me to immunological methods and supporting me in all kinds of technical emergencies.

Thanks to all members of the INIMS lab for creating a work environment that allowed and also constructively challenged me to grow at the same time. I am especially grateful for relying on this group of people during the Covid 19 pandemic to not only support each other scientifically but also on a personal level. Especially, I would like to thank Simone Bauer for technical assistance especially for tissue preparations and Ana Coneva for supporting me with EAE scoring.

I would like to thank the Gemeinnützige Hertie Stiftung for funding this project.

Thanks to Beatrice Haack from the AG Wischhusen in Würzburg, who conducted GDF-15 ELISA analyses for this project.

In the end, I am grateful for everybody, who supported and motivated me during the last years. I would especially like to thank my friends and family for their patience and constant encouragement.

VI. Curriculum vitae

Lebenslauf aus datenschutzrechtlichen Gründen nicht enthalten.

VII. Appendix

Sequences

hSyn1-2xNLS-EGFP-P2A-STOP

AGTGCAAGTGGGTTTTAGGACCAGGATGAGGCGGGGTGGGGGTGCCTACCTGACGAC
CGACCCCGACCCACTGGACAAGCACCCAACCCCCATTCCCCAAATTGCGCATCCCCTA
TCAGAGAGGGGGAGGGGAAACAGGATGCGGCGAGGCGCGTGCGCACTGCCAGCTTCA
GCACCGCGGACAGTGCCTTCGCCCCCGCCTGGCGGCGCGCGCCACCGCCGCCTCAG
CACTGAAGGCGCGCTGACGTCACTCGCCGGTCCCCCGCAAACTCCCCTTCCCGGCCAC
CTTGGTCGCGTCCGCGCCGCCGCCGGCCCAGCCGGACCGCACCACGCGAGGCGCGA
GATAGGGGGGCACGGGCGCGACCATCTGCGCTGCGGCGCCGGCGACTCAGCGCTGC
CTCAGTCTGCGGTGGGCAGCGGAGGAGTCGTGTCGTGCCTGAGAGCGCAGTCGAGAA
GGTACCGCCACCATGGTTAAAAGGCCGGCGGCCACGAAAAAGGCCGGCCAGGCAAAA
AAGAAAAAGACCGGTGTGAGCAAGGGCGAGGAGCTGTTCACCGGGGTGGTGCCCATC
CTGGTCGAGCTGGACGGCGACGTAAACGGCCACAAGTTCAGCGTGTCCGGCGAGGGC
GAGGGCGATGCCACCTACGGCAAGCTGACCCTGAAGTTCATCTGCACCACCGGCAAGC
TGCCCGTGCCCTGGCCCACCCTCGTGACCACCCTGACCTACGGCGTGCAGTGCTTCAG
CCGCTACCCCGACCACATGAAGCAGCACGACTTCTTCAAGTCCGCCATGCCCGAAGGC
TACGTCCAGGAGCGCACCATCTTCTTCAAGGACGACGGCAACTACAAGACCCGCGCCG
AGGTGAAGTTCGAGGGCGACACCCTGGTGAACCGCATCGAGCTGAAGGGCATCGACTT
CAAGGAGGACGGCAACATCCTGGGGCACAAGCTGGAGTACAACTACAACAGCCACAAC
GTCTATATCATGGCCGACAAGCAGAAGAACGGCATCAAGGTGAACTTCAAGATCCGCCA
CAACATCGAGGACGGCAGCGTGCAGCTCGCCGACCACTACCAGCAGAACACCCCCATC
GGCGACGGCCCCGTGCTGCTGCCCGACAACCACTACCTGAGCACCCAGTCCGCCCTG
AGCAAAGACCCCAACGAGAAGCGCGATCACATGGTCCTGCTGGAGTTCGTGACCGCCG
CCGGGATCACTCTCGGCATGGACGAGCTGTACAAGCAATTGCCCAAGAAAAAGCGGAA
GGTGGGCGCAACAAACTTCTCTCTGCTGAAACAAGCCGGAGATGTCGAAGAGAATCCT
GGACCATAA

GPI-1×IL10

CGTACGACGCCTGGCTCAGCACTGCTATGCTGCCTGCTCTTACTGACTGGCATGAGGA
TCAGCAGGGGCCAGTACAGCCGGGAAGACAATAACTGCACCCACTTCCCAGTCGGCCA
GAGCCACATGCTCCTAGAGCTGCGGACTGCCTTCAGCCAGGTGAAGACTTTCTTTCAAA
CAAAGGACCAGCTGGACAACATACTGCTAACCGACTCCTTAATGCAGGACTTTAAGGGT
TACTTGGGTTGCCAAGCCTTATCGGAAATGATCCAGTTTTACCTGGTAGAAGTGATGCC
CCAGGCAGAGAAGCATGGCCCAGAAATCAAGGAGCATTTGAATTCCCTGGGTGAGAAG
CTGAAGACCCTCAGGATGCGGCTGAGGCGCTGTCATCGATTTCTCCCCTGTGAAAATAA
GAGCAAGGCAGTGGAGCAGGTGAAGAGTGATTTTAATAAGCTCCAAGACCAAGGTGTC
TACAAGGCCATGAATGAATTTGACATCTTCATCAACTGCATAGAAGCATACATGATGATC
AAAATGAAATCCGGAGGTGGCGGGTCCGGCGGTGGATCTGGGGGAGGCAGTTCAAGC
GGTGGGGGCAGCGGAGGTGGCTCTGGGGGAGGAAGTACTAGTAGTAGTACAAACAAC
TCCAGCAAGAAATGCATCCCTGATCCTATAGCTATTGCATCTCTCTCCTTTTTGACCAGT
GTCATCATCTTTTCCAAAAGCAGAGTATAG

GPI-2×IL10

CGTACGACGCCTGGCTCAGCACTGCTATGCTGCCTGCTCTTACTGACTGGCATGAGGA
TCAGCAGGGGCCAGTACAGCCGGGAAGACAATAACTGCACCCACTTCCCAGTCGGCCA
GAGCCACATGCTCCTAGAGCTGCGGACTGCCTTCAGCCAGGTGAAGACTTTCTTTCAAA
CAAAGGACCAGCTGGACAACATACTGCTAACCGACTCCTTAATGCAGGACTTTAAGGGT
TACTTGGGTTGCCAAGCCTTATCGGAAATGATCCAGTTTTACCTGGTAGAAGTGATGCC

CCAGGCAGAGAAGCATGGCCCAGAAATCAAGGAGCATTTGAATTCCCTGGGTGAGAAG
CTGAAGACCCTCAGGATGCGGCTGAGGCGCTGTCATCGATTTCTCCCCTGTGAAAATAA
GAGCAAGGCAGTGGAGCAGGTGAAGAGTGATTTTAATAAGCTCCAAGACCAAGGTGTC
TACAAGGCCATGAATGAATTTGACATCTTCATCAACTGCATAGAAGCATACATGATGATC
AAAATGAAATCCGGAAGCACATCTGGATCTGGAAAAGGTAGTGGGGGATCCACCAAGG
GGAGCAGGGGCCAGTACAGCCGGGAAGACAATAACTGCACCCACTTCCCAGTCGGCC
AGAGCCACATGCTCCTAGAGCTGCGGACTGCCTTCAGCCAGGTGAAGACTTTCTTTCAA
ACAAAGGACCAGCTGGACAACATACTGCTAACCGACTCCTTAATGCAGGACTTTAAGGG
TTACTTGGGTTGCCAAGCCTTATCGGAAATGATCCAGTTTTACCTGGTAGAAGTGATGC
CCCAGGCAGAGAAGCATGGCCCAGAAATCAAGGAGCATTTGAATTCCCTGGGTGAGAA
GCTGAAGACCCTCAGGATGCGGCTGAGGCGCTGTCATCGATTTCTCCCCTGTGAAAATA
AGAGCAAGGCAGTGGAGCAGGTGAAGAGTGATTTTAATAAGCTCCAAGACCAAGGTGT
CTACAAGGCCATGAATGAATTTGACATCTTCATCAACTGCATAGAAGCATACATGATGAT
CAAAATGAAATCCGGAGGTGGCGGGTCCGGCGGTGGATCTGGGGGAGGCAGTTCAAG
CGGTGGGGGCAGCGGAGGTGGCTCTGGGGGAGGAAGTACTAGTAGTAGTACAAACAA
CTCCAGCAAGAAATGCATCCCTGATCCTATAGCTATTGCATCTCTCTCCTTTTTGACCAG
TGTCATCATCTTTTCCAAAAGCAGAGTATAG

tmPDL1

CACTGGGTGCTTCTGGGtTCCATCCTGTTGTTCCTCATTGTAGTGTCCACGGTCCTCCTC
TTCTTGAGAAAACAAGTGAGAATGCTAGATGTGGAGAAATGTGGCGTTGAAGATACAAG
CTCAAAAAACCGAAATGATACACAATTCGAGGAGACG

tmIL2ra

GTAGCAGTGGCCAGCTGCCTCTTCCTGCTCATCAGCATCCTCCTCCTGAGCGGGCTCA
CCTGGCAACACAGATGGAGGAAGAGCAGAAGAACCATC

VIII. Affidavit

Ich versichere ausdrücklich, dass ich die Arbeit selbständig und ohne fremde Hilfe verfasst, andere als die von mir angegebenen Quellen und Hilfsmittel nicht benutzt und die aus den benutzten Werken wörtlich oder inhaltlich entnommenen Stellen einzeln nach Ausgabe (Auflage und Jahr des Erscheinens), Band und Seite des benutzten Werkes kenntlich gemacht habe.

Ferner versichere ich, dass ich die Dissertation bisher nicht einem Fachvertreter an einer anderen Hochschule zur Überprüfung vorgelegt oder mich anderweitig um Zulassung zur Promotion beworben habe.

Ich erkläre mich einverstanden, dass meine Dissertation vom Dekanat der Medizinischen Fakultät mit einer gängigen Software zur Erkennung von Plagiaten überprüft werden kann.

Unterschrift: .....